Synthesis and Characterizations of ZnO Nanostructures for Field Emission Devices

Hamed Majdooa H Algarni

PhD

University of York

Department of Electronics

October 2013

ABSTRACT

The work presented in this thesis describes the growth and characterizations of ZnO nanostructures with a focus on studying their field emission properties. Successful synthesis of various doped and undoped ZnO nanostructures with different morphologies and compositions on different substrates (zinc foil, silicon, titanium and tungsten) via two different fabrication techniques (i.e. hydrothermal method and thermal evaporation process) were successfully accomplished. The morphological, structural, compositional and optical properties of as synthesized ZnO nanostructures were characterized by various analytical techniques. In addition, plausible growth mechanisms based on the crystallographic properties of the wurtzite hexagonal ZnO and the physical and chemical reactions involved in the growth process have been proposed for all prepared ZnO nanostructures.

The influence of the surface morphology on the field emission properties of ZnO nanostructures was also studied. It was found that, the turn-on and threshold voltages of the 2D ZnO nanosheets interconnect to be high compared to that in the ZnO nanorods. In the meantime, ZnO nanorods exhibits much more stable current than nanosheets and this is mainly due to the uniformity (i.e. shape and size) of the ZnO nanorods.

The doping also has significant effect on the morphology as well as the electrical properties of the grown ZnO nanostructures and thus the field emission properties. Different ratios of gallium doping led to two different types of morphologies (nanoneedles and multipods). A significant enhancement of the field emission performance of Ga-doped ZnO nanostructures (nanoneedles and multipods) is attained and this is due to the combined effect of the geometrical enhancement factor and the doping effect. Similarly, the In-doped ZnO nanopencils exhibits enhanced emission performance with very low turn on voltage which is related to both the distinctive geometrical configuration and the improvement in the electrical properties (i.e. conductivity and carrier concentration) due to indium doping.

Finally, an important goal/objective of this thesis is the application of the ZnO nanorods as alternative high brightness electron cathodes and for their use in harsh environment have been explored and presented. A new approach to fabricate novel a field emitter electron cathode based on ZnO nanostructures is reported. The preliminary results obtained are very encouraging but more experiments are needed before its use in either the field emission display or electron microscopy.

TABLE OF CONTENTS

ABSTRACT	i
TABLE OF CONTENTS	ii
LIST OF TABLES	vii
LIST OF FIGURES	viii
ACKNOWLEDGEMENT	xvi
DECLARATION	xvii
CHAPTER1: INTRODUCTION	1
1.1 General introduction of nanomaterials	1
1.2 General properties of zinc oxide nanomaterials	3
1.3 General synthetic methods of metal oxide Nanomaterials	5
1.3.1. Vapor phase growth process	5
1.3.1.1. Thermal evaporation process	6
1.3.1.2. Pulsed laser deposition process	7
1.3.1.3. Sputtering process	8
1.3.1.4. Metal organic chemical vapor deposition process (MOCVD)	9
1.3.2. Solution phase growth process	10
1.3.2.1 Sol-gel deposition technique	10
1.3.2.2. Electrochemical deposition process	10
1.3.2.3. Surfactant and capping agent assisted growth process	11
1.3.2.4. Sonochemical method	11
1.3.2.5. Hydrothermal deposition process	11
1.4 The choice of ZnO	12
1.4.1 Metals	12
1.4.2 Carbon nanotubes	12
1.4.3 Zinc oxide (ZnO) nanostructures	13
1.5 Research objectives	13
1.6 The organization of the thesis	15
CHAPTER2: THE THEORY OF ELECTRON EMISSION	17
2.1 The band theory of solids	17

2.2 The surface potential barrier 17
2.3 The electron emission and the work function 19
2.4 Modification of the surface potential barrier 22
2.5 Fowler-Nordheim theory 23
2.6 Electron emission sources 27
2.6.1 Thermionic emission source 27
2.6.2 Field emission electron source 29
2.7 Basic field emission characteristics 30
2.8 Conclusion 31

CHAPTER3: EXPERIMENTAL TECHNIQUES 32
3.1 Introduction 32
3.2 Synthesis techniques used for this work 32
3.1.1 Hydrothermal growth processs 32
3.1.2 Thermal evaporation process 33
3.3 Characterization techniques 35
3.3.1 Structural characterizations techniques 35
3.3.1.1 X-Ray diffraction pattern 35
3.3.1.2 Field emission scanning electron microscopy (FESEM) 36
3.3.1.3 Energy dispersive x-ray spectroscopy (EDS) 37
3.3.1.4 Transmission electron microscope (TEM) 38
3.3.2 Optical characterization techniques 40
3.3.2.1 *Room-temperature photoluminescence spectroscopy* 40
3.3.2.2 *Raman-scattering spectroscopy* 41
3.4 Field emission system 42
3.4.1 Vacuum system layout 42
3.4.2 Design of the sample holder and the field emission experimental setup 42
3.5 Conclusion 44
CHAPTER 4: ZnO NANOSHEETS INTERCONNECTS: GROWTH, CHARACTERIZATIONS AND FIELD EMISSION PROPERTIES 45
4.1 Introduction 45
4.2 Experimental work 46

4.2.1 Synthesis of nanocrystalline thin ZnO nanosheets interconnects on zinc foil 46
4.2.2 Characterization of nanocrystalline thin ZnO nanosheet interconnects on zinc foil 48
4.3 Results and discussion 48
4.3.1 Morphological, structural and compositional properties of grown ZnO nanosheets interconnects 48
4.3.2 Room-temperature photoluminescence (PL) properties of grown ZnO nanosheets interconnects 57
4.3.3 Room-temperature Raman-scattering properties of as-grown thin ZnO nanosheets interconnects 58
4.3.4 Plausible growth mechanism for as-grown thin ZnO nanosheets interconnects 60
4.3.5 Field emission studies 63
4.3.5.1 Current –voltage characteristic of ZnO nanosheets 63
4.3.5.2 Current emission stability of ZnO nanosheets 65
4.3.5.3 Field emission pattern of ZnO nanosheet at different voltages 67
4.4 Conclusion 68
CHAPTER 5: NON-CATALYTIC GROWTH OF HEXAGONAL SHAPED ZnO NANORODS ON TITANIUM SUBSTRATE: STRUCTURAL, OPTICAL AND FIELD EMISSION PROPERTIES 69
5.1 Introduction 69
5.2 Experimental details 70
5.3 Results and discussion 71
5.3.1 Morphological and structural properties 71
5.3.2 Optical properties 75
5.3.3 Plausible growth mechanism 77
5.3.4 Field emission studies 79
5.3.4.1 Current –voltage characteristic of ZnO nanorods 79
5.3.4.2 The field emission stability of ZnO nanorods 83
5.3.4.3 Field emission patterns from ZnO nanorods 84
5.4 Conclusion 86

CHAPTER6: GALLIUM-DOPED ZnO NANOSTRUCTURES: GROWTH, OPTICAL AND FIELD EMISSION PROPERTIES 87
6.1 Introduction 87
6.2 Experimental details 88
6.2.1 Synthesis of Ga-doped ZnO nanostructures on a Si(100) substrate 88
6.2.2 Characterization of Ga-doped ZnO nanostructures on Si (100) Substrate 90
6.3 Results and discussion 90
6.3.1 Morphological, compositional and structural properties of Ga-doped ZnO nanostructures grown on Si (100) substrate 90
6.3.2 Room-temperature photoluminescence (PL) properties of Ga-doped ZnO nanostructures grown on a Si (100) substrate 101
6.3.3 Field emission studies 104
6.3.3.1 Current –voltage characteristic of Ga-doped ZnO nanostructures 104
6.3.3.2 The field emission stability of the Ga-doped ZnO nanoneedles 108
6.3.3.3 Field emission patterns from Ga-doped ZnO nanoneedles 110
6.4 Conclusion 112
CHAPTER7: INDIUM-DOPED ZnO NANOPENCILS: GROWTH, CHARACTERIZATIONS AND FIELD EMISSION PROPERTIES 113
7.1 Introduction 113
7.2 Experimental details 113
7.3 Results and discussion 115
7.3.1 Morphological, compositional and structural properties of In-doped ZnO nanopencils 115
7.3.2 Optical and Raman-scattering properties of In-doped ZnO nanopencils 120
7.3.3 Plausible growth mechanism of In-doped ZnO nanopencils 122
7.3.4 Field emission properties of In-doped ZnO nanopencils 125
7.3.4.1 Current-voltage characteristics of In doped ZnO nanopencils 125
7.3.4.2 The field emission current stability of In doped ZnO nanopencils 127
7.3.4.3 Field emission patterns of In Doped ZnO nanopencils 128
7.4 Conclusion 129

CHAPTER8: GROWTH AND FIELD EMISSION STUDIES OF ZnO NANOSTRUCTURES GROWN ON MICROFABRICATED TUNGSTEN EMITTERS 130
8.1 Introduction 130
8.2 Direct growth of ZnO nanowires on micro-fabricated tungsten emitters 130
8.3 Experimental work of the growth of ZnO nanowires on the W emitters 131
8.3.1 The effect of temperature, the distance between the tip and source material and reaction time 134
8.3.2 Improving the alignment of the nanowires by adding an interface layer 138
8.3.3 The elimination of the overgrowth phenomenon 139
8.4 Discussion 142
8.5 Field emission properties of ZnO nanowires directly grown on micro-fabricated tungsten emitters provided by York Probe Sources (YPS), Ltd. York 144
8.5.1 Experimental design: sample holder layout 144
8.5.2 Field emission Results 148
8.6 Requirment for emission current stability of cold field emitter for electron microscopy 163
8.7 Conclusion 164
CHAPTER9: CONCLUSION 165
CHAPTER10: SUGGESTIONS AND FUTURE DIRECTIONS 169
10.1 Growth of ZnO nanomaterials 169
10.2 Field emission properties of ZnO nanomaterials 170
10.3 Theoretical studies 170
References 171

List of tables

Table 4.1 Summary of the growth parameters of ZnO nanosheet interconnects. 47

Table 5.1 Summary of the growth parameters of hexagonal shaped ZnO nanorods..... 71

Table 5.2 crystallite size and lattice constant of the ZnO nanorods grown on Ti substrate..... 73

Table 6.1 Summary of the growth parameters of Ga-doped ZnO nanoneedles with Ga concentration of 0.5%..... 89

Table 6.2 Summary of the growth parameters of Ga-doped ZnO thorny branched (multipods) nanostructures with Ga concentration of 2%..... 89

Table 6.3 crystallite size and lattice constants as-synthesized Ga-doped ZnO nanoneedles with Ga concentration of 0.5%.and multipods Ga-doped ZnO structures with Ga concentration of 2%..... 98

Table 7.1 Summary of the growth parameters of In-doped ZnO nanopencils.... 115

Table 7.2 crystallite size and lattice constant of the In-doped ZnO nanopencils grown on Si substrate..... 117

Table 8.1 Summary of the growth parameters for the growth of ZnO nanomaterials on YPS- tungsten (W) emitters..... 133

List of figures

Figure 1.1 Hexagonal wurtzite structure model of ZnO. Oxygen atoms are shown as larger yellow spheres while the zinc atoms are smaller white spheres..... 4

Figure1.2 Schematic of PLD system..... 7

Figure1.3 Schematic of typical RF sputtering system..... 8

Figure1.3 Schematic of typical vertical MOCVD system..... 9

Figure 2.1 The potential energy of an electron near an isolated nucleus..... 17

Figure 2.2 The potential energy of an electron along a line through two adjacent atoms..... 18

Figure 2.3 The potential energy of an electron along a line through a row of atoms..... 18

Figure 2.4 Schematic of one-dimensional potential well with a flat bottom. U_a is the surface potential barrier, E_v the vacuum level, E_F Fermi level, E_c the conduction band bottom and Φ is the work function..... 21

Figure 2.5 shows the surface potential barrier (a) without image potential and external field, (b) with image potential but without external field, (c) with external field but without image potential, and (d) with both image potential and external field..... 23

Figure 2.6 The configuration of thermionic electron gun..... 28

Figure 2.7 The configuration of field emission electron gun..... 29

Figure3.1 a representative image of different parts of the autoclave..... 32

Figure 3.2 Schematic for the instrumental setup for the thermal evaporation process used for the growth of ZnO nanostructures..... 34

Figure 3.3 Real photograph of the horizontal tube furnace used for the growth of ZnOnanostructures..... 34

Figure 3.4 Schematic diagram of field emission scanning electron microscope (FETEM)..... 37

Figure 3.5 Schematic diagram of transmission electron microscope (TEM)..... 39

Figure 3.6 A photograph of the Renta-Port system used for the field emission experiments..... 43

Figure 3.7 Schematic of the triode configuration stage for field emission..... 43

Figure 4.1 Typical (a and b) low-magnification, and (c and d) high-resolution FESEM images of the as-grown thin ZnO nanosheet interconnects on zinc foil at 110ºC..... 51

Figure 4.2 Low (a) and high (b) magnification FESEM images of flower-shaped structures composed of thin ZnO nanosheets, obtained from the edge portion of the zinc foil substrate at 110ºC..... 52

Figure 4.3 Typical (a) XRD pattern and (b) EDS spectrum of thin ZnO nanosheet interconnects grown on zinc foil at 110ºC..... 53

Figure 4.4 Typical (a) Low-magnification and (b) high-resolution TEM images of as-grown thin ZnO nanosheet interconnects grown on zinc foil at 110ºC..... 55

Figure 4.5 Typical (a and b) low-magnification, and (c and d) high-resolution FESEM images of the 200ºC annealed thin ZnO nanosheet interconnects grown on zinc foil at 110ºC..... 56

Figure 4.6 Typical room-temperature photoluminescence (PL) spectrum of thin ZnO nanosheet interconnects grown on zinc foil at 110ºC. A strong UV emission with a suppressed green emission confirmed the well-crystallinity of the prepared ZnO nanosheets interconnects..... 58

Figure 4.7 Typical room-temperature Raman-scattering spectrum of thin ZnO nanosheet interconnects grown on zinc foil at 110ºC showing a strong E_2 peak and a suppressed E_{1L} which are indicative of a good quality crystal..... 59

Figure 4.8 Plausible schematic for the growth mechanism for the synthesis of ZnO nanosheet interconnects grown on zinc foil at 110ºC..... 62

Figure 4.9 (a) The field emission electron *I-V* characteristic of ZnO nanosheets interconnects. (b) The corresponding F-N plot..... 64

Figure 4.10 Emission current stability curve of ZnO nanosheets interconnects as a function of time..... 66

Figure 4.11 Field emission patterns of ZnO nanosheets interconnects grown on Zn foil as a function of the applied voltage. The last image at an applied voltage of 5.8 kV shows the breakdown flash..... 67

Figure 5.1 Typical (a) low-magnification and (b) and (c) high-magnification FESEM images, and (d) EDS spectrum of as-grown ZnO nanorods on Ti substrate..... 72

Figure 5.2 Typical (a) low-magnification and (b) high-magnification TEM images of as-grown ZnO nanorods on Ti substrate. Inset (a) exhibits the corresponding SAED pattern..... 74

Figure 5.3 Typical (a) XRD pattern of as-grown ZnO nanorods on Ti substrate and (b) XRD for pure Ti substrate..... 74

Figure 5.4 Typical room-temperature PL spectrum of the as-grown ZnO nanorods on Ti substrate..... 75

Figure 5.5 Typical Raman-scattering spectrum of as-grown ZnO nanorods on Ti substrate..... 77

Figure 5.6 Schematic growth mechanism for the formation of the as-grown ZnO nanorods on Ti substrate..... 78

Figure 5.7 (a) Current-voltage (*I-V*) characteristic of the as-grown ZnO nanorods on Ti substrate (first scan black symbols) and (second scan red symbols). (b) The corresponding F-N plots..... 80

Figure 5.8 (a) Current-voltage (*I-V*) characteristic of as-grown ZnO nanorods on Ti substrate at different air pressures. (b) The corresponding F-N plots..... 82

Figure 5.9 the emission current stability profile of ZnO nanorods under a constant applied voltage of 2.7 kV..... 84

Figure 5.10 Field emission patterns of ZnO nanorods grown on titanium substrate. The patterns show the emission current as a function of increasing voltage: (a) 2.1 kV, (b) 2.4 kV, (c) 2.7 kV, (d) 3 kV, (e) 3.3 kV, (f) 3.9 kV and (g) shows the breakdown flash at 4.65 kV..... 85

Figure 6.1 Typical (a) low-magnification, (b and inset) high-resolution FESEM images and (c) the corresponding EDS spectrum of the as-grown Ga-doped ZnO nanoneedles with Ga concentration of 0.5%..... 92

Figure 6.2 Typical (a) low-magnification, (b) high magnification FESEM images and (c) the corresponding EDS spectrum of the as-grown Ga-doped ZnO multipodswith Ga concentration of 2%. The high magnification image (b) shows the presence of two groups; the small tips that result from the secondary growth (will be referred to as group1) and the big base needles (will be referred to as group2)..... 94

Figure 6.3 Typical (a) low-magnification, and (b and inset) high-resolution TEM images and (c) TEM-EDS of the as-grown Ga-doped ZnO nanoneedles with Ga concentration of 0.5%..... 96

Figure 6.4 Typical (a) low-magnification, and (b) high-resolution TEM images of the as grown Ga-doped ZnO multipods with nominal Ga concentration of 2%..... 97

Figure 6.5 Typical XRD pattern of as-synthesized; (a) Ga-doped ZnO nanoneedles with Ga concentration of 0.5%.and (b) multipods Ga-doped ZnO structures with Ga concentration of 2%..... 99

Figure 6.6 Typical room-temperature photoluminescence spectrum of the as-grown Ga-doped ZnO nanoneedles with Ga concentration of 0.5%..... 102

Figure 6.7 Typical room-temperature photoluminescence spectrum of the as-grown Ga-doped ZnO multipods with Ga concentration of 2%..... 103

Figure 6.8 (a) Current-voltage (*I*-*V*) characteristic of of the as-grown Ga-doped ZnO nanoneedles with Gaconcentration of 0.5%. (b) The corresponding F-N plot.. 105

Figure 6.9 (a) Current-voltage (*I*-*V*) characteristic of of the as-grown Ga-doped ZnO multipods with Ga concentration of 2%. (b) The corresponding F-N plot..... 107

Figure 6.10 the emission current stability profile of Ga-doped ZnO nanoneedles with Ga concentration of 0.5% under a constant applied voltage of 1.7 kV..... 109

Figure 6.11 the emission current stability profile of Ga-doped ZnO nanoneedles with Ga concentration of 0.5% under a constant applied voltage of 2 kV..... 110

Figure 6.12 Field emission patterns of Ga-doped ZnO nanoneedles with Ga concentration of 0.5% grown on Si substrate. 111

Figure 7.1 (a-c) FESEM images showing the morphology of the In-doped ZnO nanopencils on silicon substrate prepared by thermal evaporation process. Image (a) shows the dense growth of In-doped ZnO nanostructures. (b and c) images show that the In-doped ZnO nanostructures are made of two parts: ultra fine tip connected to a base of ZnO nanorods. (d) Shows the EDS spectrum showing the constituent elements found on the grown structures..... 116

Figure 7.2 XRD pattern of the as-grown In-doped ZnO nanopencils on silicon substrate prepared by thermal evaporation process showing a well crystalline wurtzite hexagonal phase of ZnO. The small peak at 54.5° indexed to In (112)..... 118

Figure7.3 (a) low magnification TEM image of the ultra fine tip (nanoneedle) of the as-grown In-doped ZnO nanopencil with a diameter in the range of 13-15 nm and (b) high-magnification TEM images of as-grown In-doped ZnO nanopencils on silicon substrate showing well-defined lattice fringes with *d* spacing equal to the lattice constant of crystalline ZnO (~0.52 nm)..... 119

Figure 7.4 Room-temperature photoluminescence (PL) spectrum of as-grown In-doped ZnO nanopencils on silicon substrate prepared by thermal evaporation process. See text for detailed discussion and assignments of the peaks..... 121

Figure 7.5 Raman-scattering spectrum of as-grown In-doped ZnO nanopencils on silicon substrate prepared by thermal evaporation process..... 122

Figure 7.6 Schematic growth mechanism for the formation of as-grown In-doped ZnO nanopencils on silicon substrate prepared by thermal evaporation process.... 124

Figure 7.7 (a) Current-voltage (*I-V*) characteristic of of the as-deposited In-doped ZnO nanopencils. (b) The corresponding F-N plot..... 126

Figure7.8 The emission current stability profile of In-doped ZnO nanopencils at fixed voltage of 1.5 kV..... 127

Figure 7.9 Field emission patterns of In-doped ZnO nanopencils grown on Si substrate as a function of applied voltage..... 128

Figure 8.1 Schematic for the direct growth of ZnO nanowires on pre-fabricated micro tungsten emitters provided by York Probe Sources (YPS) Ltd., York, UK.... 132

Figure 8.2 FESEM images of ZnO growth on the YPS tungsten emitters (Tip-1) (Reaction time: 3 hrs, Zn amount = 1.5 g; distance between source material and emitter: 5 cm; growth temperature: 600°C)..... 135

Figure 8.3 FESEM images of ZnO nanowires grown on the YPS micro tungsten emitters (Tip-2). (Reaction time 2.5 hrs, amount of metallic zinc powder =1.5 g,

reaction temperature 650°C; and distance between source material and emitter was set to 5 cm). The bent end-form has most likely been caused during handling the emitter while loading it in the furnace. This does not affect the experimental results discussed here, though as some nanorods are indeed grown along the optical axis of the tungsten emitter..... 137

Figure 8.4 FESEM images of ZnO nanowires grown on the ZnO film (200 nm) coated pre-fabricated micro tungsten emitters provided by YPS (Tip-3). (Reaction time 2 hrs, amount of metallic zinc powder =1.5 g, reaction temperature 650°C; and distance between source material and emitter was set to 5 cm)..... 139

Figure 8.5 FESEM images of ZnO nanowires grown on ZnO film (200 nm) coated pre-fabricated micro tungsten emitters provided by YPS (Tip-4). (Reaction time 1.5 hrs, amount of metallic zinc powder = 1.5 g, reaction temperature 700°C; and distance between source material and emitter was set to 5 cm)..... 140

Figure 8.6 FESEM images of ZnO nanowires grown on ZnO film (200 nm) coated pre-fabricated micro tungsten emitters provided by YPS (Tip-5). (Reaction time 1 hrs, amount of metallic zinc powder = 0.50 g, reaction temperature 750°C; and distance between source material and emitter was set to 3 cm). Note the ZnO nanowire, identified by the red circle in image (C), is significantly higher than the others grown on the tip's apex..... 141

Figure 8.7 Schematic diagram of the mounting plate showing the clearance hole through its centre for electrical connection purpose..... 145

Figure 8.8 Schematic diagram of the emitter holder showing (a) the emitter mounting ring (b) the axial and side view of the U shaped aluminum holder..... 145

Figure 8.9 Schematic diagram of the anode plate showing the 500 μm aperture hole at the centre of the plate for measuring the emission current from small spot through a Faraday cup connected to the back of the anode plate..... 146

Figure 8.10 Schematic diagram of the field emission assembly..... 147

Figure 8.11 (a) Current-voltage (*I-V*) characteristic of of ZnO nanowires grown on the ZnO film (200 nm) coated pre-fabricated micro tungsten emitters (Tip-3). (b) The corresponding F-N plot..... 150

Figure 8.12 The field emission pattern of ZnO nanowires grown on the ZnO film (200 nm) coated pre-fabricated micro tungsten emitters (Tip-3). This field emission pattern was obtained after several voltage ramps. (a) shows that the emission pattern starts as one circular spot at the centre of the phosphor screen. (b) and (c) images show that the emission pattern gets intense with increasing voltage and some other emission sites were also appeared. (d) shows the emission pattern from different angle at the centre of the phosphor screen facing the Faraday cup……..... 151

Figure 8.13 The emission current stability profile of ZnO nanowires grown on the ZnO film (200 nm) coated pre-fabricated micro tungsten emitters (Tip-3). (a) shows the total screen current as a function of time. (b) shows the field emission current stability of small spot (500 μm) measured by faraday cup through an opening hole at the centre of the viewing screen..... 152

Figure 8.14 The field emission pattern of ZnO nanowires grown on the ZnO film (200 nm) coated pre-fabricated micro tungsten emitters (Tip-4) as a function of applied voltages. (a) shows several emission patterns at an applied voltage of 2.5 kV. (b) and (c) images show that the emission patterns at 2.7 kV and 3 kV respectively. (d) shows the emission patterns from different angle. 154

Figure 8.15 (a) Current-voltage (*I-V*) characteristic of of ZnO nanowires grown on the ZnO film (200 nm) coated pre-fabricated micro tungsten emitters (Tip-4). (b) The corresponding F-N plot..... 155

Figure 8.16 The emission current stability profile of ZnO nanowires grown on the ZnO film (200 nm) coated pre-fabricated micro tungsten emitters (Tip-4). (a) shows the total emission current as a function of time for the first 11 hours of continues operation. (b) shows the stability of total emission current for span of another 50 hours..... 156

Figure 8.17 The emission current stability profile of the field emission pattern at the centre of the screen highlighted with the red arrow in figure 8.14(c). The emission current stability was measured through a Faraday cup for a span of more than 24 hours..... 157

Figure 8.18 (a) Current-voltage (*I-V*) characteristic of single ZnO nanowires grown on the ZnO film (200 nm) coated pre-fabricated micro tungsten emitters (Tip-5). (b) The corresponding F-N plot..... 160

Figure 8.19 The field emission pattern of single ZnO nanowires grown on the ZnO film (200 nm) coated pre-fabricated micro tungsten emitters (Tip-5) as a

function of applied voltages..... 161

Figure 8.20 The emission current stability profile of single ZnO nanwire grown on the ZnO film (200 nm) coated pre-fabricated micro tungsten emitters (Tip-5) as a function of time at fixed voltage of 3 kV over a period of about 34 hours..... 162

Acknowledgements

Several people have helped in various ways during the research work and in the preparation of this thesis. It is a pleasure, with the completion of this thesis to acknowledge the enormous help I received from them.

I would like to express my deep appreciation to my supervisor, Prof. Mohamed El-Gomati for his instantly inspiration, valuable guidance, encouragement and valuable advices, which led to the submission of this thesis.

I would like to thank the staff in the clean room for their help and guidance, particularly, Jonathan Cremer for his support. Sincere thanks go to Mr Torquil Wells for his support, scientific discussions and valuable suggestions especially on the field emission experiments.

I gratefully acknowledge The Promising centre for sensor and electronic devices, Najran University, Saudi Arabia for providing funding to this project and access to their facilities. In this regard, I would like to offer special thanks to Prof. Ali Al-Hajry and Prof. Mohamed Sultan for their unlimited support, advices, and encouragements. I am really thankful to them from the deep core of my heart for their friendly behavior and fatherly love.

I am in debt to Dr. Ahmad Umar for his all supports during my stay in Najran. I have learned from him a lot which will benefit to the rest of my life. I pray for his great success in his life.

I would like to thank Dr. Kim who has worked with me like friend and for his kind help and sharing his excellence experiences and his extraordinary help on the PL and Raman measurements of the samples.

I would like to thank my dear friends Dr. Sherif Bakush, Dr. Hassan Wahab, Mr Tariq Alhuwaymel, Mr Ranjdar Abdullah for their friendship and making the happy and enjoyable time of my stay throughout my PhD course.

I would like to extend very special thanks to all of the staff and students in the department of electronics at the University of York and to each and every person who helped and supported me during this research period.

Finally, I would like to deeply thank my parents, brothers, sisters for their endless support and encourgment. My life has been made made easier by my wife and daughters. Without their encourgment and sacrifices it would have been impossible for me to finish this work so (Thanks a lot).

Declarations

I declare that the work presented in this thesis, except where otherwise stated, is based purely on my own research. Parts of the work reported in this thesis have been previously published in:

Puplications:-

1. H. Algarni, M. El-Gomati, and M. S. Al-Assiri, "*Low-Temperature Growth and Properties of Nanocrystalline Thin ZnO Nanosheet Interconnects on Zinc Foil*" *Sci. Adv. Mater*. 4, 961-968 (2012)
2. H. Algarni, M. M. El-Gomati, and M. S. Al-Assiri, *"Effect of Gallium Concentrations on the Morphologies, Structural and Optical Properties of Ga-Doped ZnO Nanostructures" J. Nanosci. Nanotech*. 14, 5317-5323 (2014)
3. H. Algarni, M. El-Gomati, and M. S. Al-Assiri, *"Field emission properties of aligned ZnO nanorods on Ti substrate"* J. Phys. Conf. Ser, In Press (2013)
4. H. Algarni, M. El-Gomati, and M. S. Al-Assiri, *"Indium-doped ZnO nanopencils: structural and field emission properties" "* J. Phys. Conf. Ser, In Press (2013)

Hamed Algarni

CHAPTER1
INTRODUCTION

1.1 General introduction of nanomaterials

One widely accepted definition of nanostructures is to represent a system or an object with at least one dimension being 100 nm or less. The unique properties of nanomaterials over bulk material are due to their large number of grain boundaries, quantum confinement and its large surface area to volume ratio[1]. The impact of these significant changes on the intrinsic properties results in it exhibiting new physical phenomena, opening therefore new horizon to this field.

Several methods have been utilised and reported in the literature for the fabrication of nanomaterials. Generally, there are two approaches to produce these: a top down approach and a bottom up approach that play a very important role in modern industry and most likely in nanotechnology as well. For microelectronics fabrication, the top down approach is more practical in which small features are patterned in bulk materials by the combination of lithography, etching and deposition forming functional devices[2,3]. Nevertheless, in order to meet the demand of nanoscale of a lesser defects structures, more homogeneous chemical composition, the bottom-up approach is considered a powerful approach instead of the conventional methods[4].

Nanocrystalline materials can be classified into several groups according to their dimensional direction: nanoclusters, nanocrystals, or nanoparticles (quantum dots) are zero-dimensional nanomaterials, whereas, nanotubes, nanowires, nanorods and nanobelts are of 1-dimensional direction (1D) and finally, films and sheets are considered a 2-dimensional nanomaterials[5, 6].

Owing to their unique physical, chemical and mechanical properties over bulk materials, the study of 1D nanostructural materials is exceptionally active area in the scientific field. For instance its high physical aspect ratio, allows for it being utilised in field emission (FE) applications including vacuum microelectronics devices such as FE electron sources, FE display and X-ray sources. For their excellent field emission properties stemming from their high aspect ratio[7-9], the carbon nanotubes (CNTs) that

was discovered by Iijima in 1991 was by far the elite candidate to overtake the conventional tungsten cold field emission (CFE) cathode. However, being comprehensively examined and studied over the last decade, CNTs turned out to be less practical mainly because of two reasons. Firstly, their emission is sensitive to the surrounding environment, predominantly H_2O and O_2 adsorbates which lead to low stability[10-12]. Secondly, being highly influenced by the fabrication technique i.e. how it is rolled, results in voltage drop variations across the conducting and semiconducting CNTs. The voltage drop then varies the electric field along with the electron emission from the CNTs[13].

Recently, a rapidly growing interest in investigating other novel nanomaterials as alternative potential cold FE cathodes in vacuum devices is discernible. The wide band-gap inorganic semiconductor nanostructures were among the investigated candidates which exhibited desirable field emission properties similar to that of the CNTs[14]. Owing to high aspect ratio, high mechanical stability and oxidation resistance, high chemical and thermal stability and with the rolling problem being eliminated, **metal oxide nanostructures** are predominantly attractive alternative for field emission applications[15].The Growth as well as field emission brilliance of 1D structure of several metal oxides and particularly zinc oxide has been reported in the literature. Zinc oxides present themselves as a promising material for the fabrication of effective nanodevices due to its exceptional properties such as wide band gap (3.37 eV), high exciton binding energy (60 meV) at room-temperature, low electron affinity, high mechanical strength and chemical and thermal stability[16].

Hitherto, a variety of ZnO nano- and microstructures have been synthesized using various fabrication techniques and their optical and FE properties have been examined in the literature[16]. The conclusive trend suggests that the morphologies, the density and the alignment of the nanostructures are significantly influential on the FE and optical properties of these nanostructures.

1.2 General properties of zinc oxide nanomaterials

This section will cover some of the fundamental properties of ZnO nanostructures.

Zinc oxide (ZnO) is one of II-VI compounds with some exceptional properties[17-19]. As mentioned before (section 1.1) the ZnO is a direct and a wide band gap (3.37 eV) which is highly influential on some of the material's properties such as, the optical absorption, electrical conductivity and field emission[16]. More over ZnO has large exciton binding energy of 60 meV at room temperature, in addition, the crystalline ZnO nanoscale, has a wurtzite structure which is the ultimately stable and thus most common at ambient conditions (temperature and pressure)[16].

The wurtzite structure is of a hexagonal unit cell with two lattice parameters a=3.25Å and c=5.2065Å and their ratio c/a ~ 1.6 which is close to the ideal value of hexagonal cell c/a = 1.633. As figure 1.1 shows, the structure consists of two interpenetrating hexagonal close packed (*hcp*) sub-lattices, in which each has one type of atom (Zn or O) stacked alternatively along the threefold of c-axis[20]. Such structure can be simply described as a number of alternating planes stacked layer by layer along the c-axis direction and composed of tetrahedrally coordinated Zn^{2+} and O^{2-} ions.

The tetrahedral coordination of ZnO also exhibits non-centrosymmetric behaviour, two polar surfaces on opposite sides and each terminated with one type of ions only. Depending on the bonds nature along the c-axis, two types of polarity can be distinguished: Zn polarity when the bonds along the c-axis are from cation (Zn) to anion (O) and oxygen polarity when the bonds along the c-axis are from anion (O) to cation (Zn). The polarity is an essential factor in the crystal growth, defect generation, plasticity, etching etc. additionally; the polarity is correspondingly responsible for a number of properties of ZnO such as spontaneous polarization and piezoelectricity. In addition to polar surfaces, it also has non polar surfaces[16].

ZnO wurtzite structure has four common facets theses are, the polar Zn-terminated- (0001) and O-terminated- $(000\bar{1})$ faces (c-axis oriented), and the non polar $(2\bar{1}\bar{1}0)$ (a-axis) and $(01\bar{1}0)$ faces which contain an equal number of Zn and O atoms[21].

In wurtzite hexagonal ZnO, where each anion is surrounded by four cation at the corners of the tetrahedron, shows the tetrahedral coordination and hence exhibits the sp^3 covalent bonds. Because of the strong ionic bond between Zn and O, the ionicity of the ZnO resides at the borderline of the ionic and covalent semiconductors with an ionicity of f_i=0.616 on Phillips ionicity scale[22].

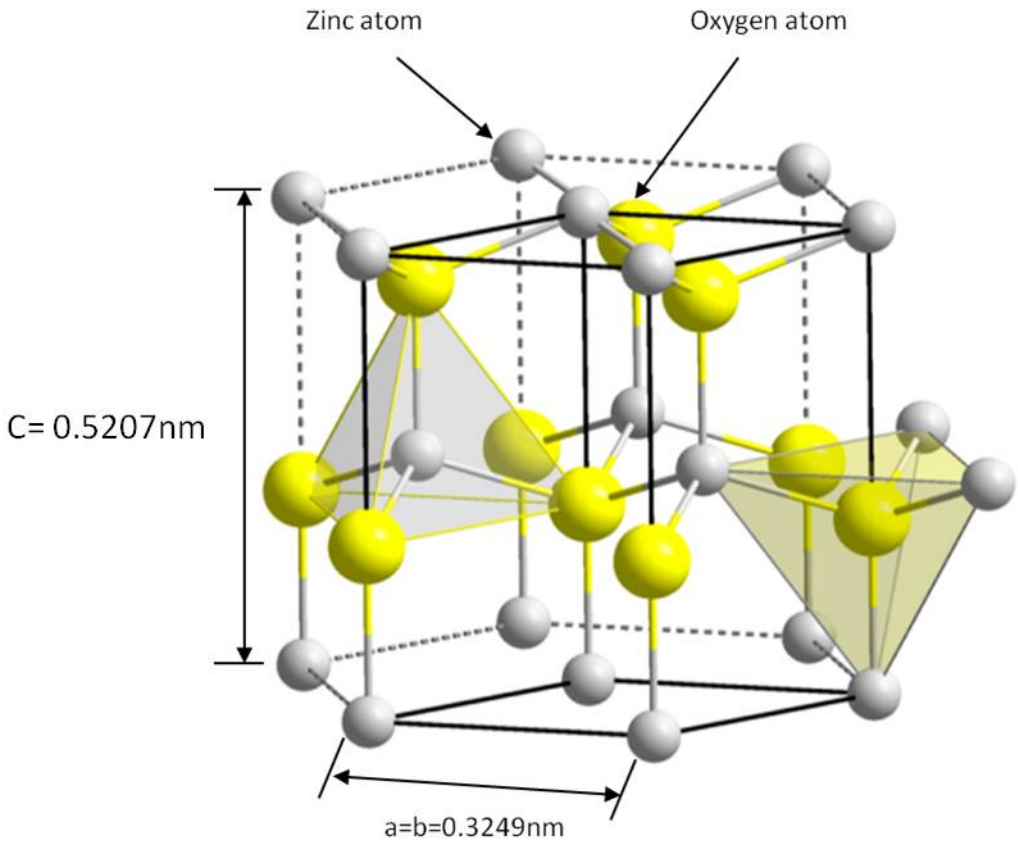

Figure 1.1 Hexagonal wurtzite structure model of ZnO. Oxygen atoms are shown as larger yellow spheres while the zinc atoms are smaller white spheres[23].

1.3 General synthetic methods of metal oxide nanomaterials

Significant research efforts have been dedicated recently to fabricate efficient miniaturized devices to be applied to various nanoelectronics and photonics technology. Depending on the synthesis environment, the various fabrication techniques that have been utilized for synthesising metal oxides nanostructures are divided into two categories: (1) vapour phase growth; (2) solution phase growth process.

1.3.1 Vapour phase growth process

The vapour phase deposition is the most versatile technique for the growth of multipurpose group of nanostructures. It is based on the reaction between the metal vapour and oxygen gas, in which the vapour species of the source materials are generated first at high temperatures, and then condense, nucleate and grow at lower temperature respectively.

In order to control the diameter, aspect ratio and crystallinity, various techniques have been explored including the thermal evaporation, pulse laser deposition (PLD), metal organic chemical vapour deposition (MOCVD), sputtering process, thermal chemical vapour deposition etc. Nevertheless, in general, two growth mechanisms for the formation of these metal oxide nanostructures are associated with the former techniques: vapour-liquid-solid (VLS) and vapour-solid (VS) process.

i) Vapour-liquid solid mechanism: Vapour-liquid solid mechanism that was firstly proposed by Wagner and Ellis in 1964[24] is one of the most successful techniques which is used for the growth of crystalline one-dimensional nanostructures. The growth of silicon whiskers was eventually implemented and observed later[25]. Wu *et al*. demonstrated the direct Ge nanowire growth by the vapour liquid solid mechanism observed by the means of real time *in situ* transmission electron microscope[26].

The VLS mechanism is a catalyst assisted process in which the metal nanoclusters or metal nanoparticals are utilised as nucleation sites for the growth of one-dimensional nanostructures. In this process, the gaseous reactants dissolve within the catalytic particles and form the alloy droplets which play an important role in the growth of one-dimensional nanostructures. Precipitation occurs when the liquid droplet

becomes supersaturated with the source material and under appropriate gas flow with increasing the time, the precipitation increases leading to the formation of corresponding metal oxide crystals. Normally the resulting crystal is grown along one particular crystallographic orientation which corresponds to the minimum atomic stacking energy forming eventually the one-dimensional structure. So far selections of metal oxide nanostructures have been synthesized using this mechanism (i.e. VLS mechanism) such as ZnO, MgO, CdO, TiO_2, SnO_2, In_2O_3, Fe_2O_3, WO_3, Ga_2O_3 etc[27-30]. However, the major drawback of the VLS technique is not being applicable to metals. The necessary use of a metal as the catalyst may also contaminate the semiconductor nanowires and thus potentially change their properties.

ii) Vapour-solid mechanism: The vapour solid mechanism is another important mechanism for the formation of nanostructures. This process occurs in many catalyst-free growth processes. Although, an in depth understanding of the VS process is absent in the literature, it is generally accepted that the control of supersaturation is a prime consideration to obtain nanostructures especially the one dimensional form. The degree of the supersaturation is an important factor of determining the dominant growth morphology. Accordingly, a low supersaturation can give whiskers growth whereas a medium supersaturation is desirable for bulk growth and for the powder growth high supersaturation is necessary[31]. Some experimental and theoretical studies have reported that the minimization of surface free energy primarily governs VS process. Under high temperature, the source materials are vaporized and then directly condensed onto the substrate placed at low temperature region. After initial condensation, the condensed molecules form seed crystals serving as nucleation sites facilitate directional growth to minimize the surface energy. Several metal oxides have been formed using VS process such as ZnO, Ga_2O_3, SnO_2, TiO_2 etc[17].

1.3.1.1 Thermal evaporation process

The nanostructures grown by the thermal evaporation are diverse and the resultant nanowires are practically used in several semiconductors materials[17]. The thermal evaporation instrument consists of a high temperature thermal furnace, typically operated at low pressures, to heat and evaporate the source material. The vapour is

transferred to relatively lower a temperature region for the deposition of the nanostructure. This method is considered in more details in chapter 3.

1.3.1.2 Pulsed laser deposition process

By implementing the laser ablation technique, the Pulsed Laser Deposition (PLD) is a highly efficient method to produce thin films[32]. The PLD technique was first used by Smith and Turner in 1965 for the preparation of the semiconductors and dielectric thin films. However, the PLD is advantageous over previous growth methods as it can be applied to a wide range of materials, especially to compounds that are difficult or impossible to produce in thin-film form. The typical set-up includes an ultrahigh vacuum chamber, solid target and high power laser as shown in figure 1.2. The fundamental principle of PLD is simple, in which a pulsed laser beam is focused onto the surface of a solid target. The strong absorption of the electromagnetic radiation by the solid surface leads to rapid evaporation of the target materials. A plume of material with stoichiometry similar to the target will be generated in front of the target surface. Finally the ablated species condense on the substrate placed opposite to the target forming thin film. Indeed, PLD is probably the simplest among all thin film growth techniques as only a few parameters, such as laser energy density and pulse of repetition rate, need to be controlled during the process. This technique has been used for the synthesis of a variety of 1D nanostructure including complex compounds and core shell structured nanostructures[32-35].

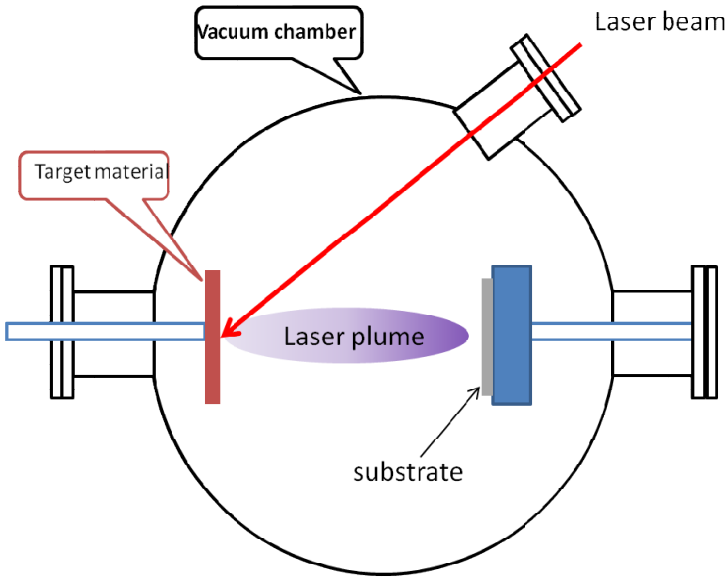

Figure1.2 Schematic of PLD system.

1.3.1.3 Sputtering process

Sputtering is a physical vapour deposition (PVD) method whereby atoms in a solid target material are ejected into the gas phase due to bombardment of the material by energetic ions and eventually deposited on a substrate to be coated. It is largely driven by momentum exchange between the ions and atoms in the material due to collisions. Surface diffusion is usually used for explanation of the nanoscale islands or rods' growth during the sputtering process. Although there are different types of sputter deposition techniques, however, they all have the same principle for the evaporation. A schematic diagram of a typical RF sputtering system is shown in the figure 1.3. Recently, the sputtering technologies have been employed to synthesise a variety of nanostructures for instance ZnO, W, Si, B, CN etc[36-38].

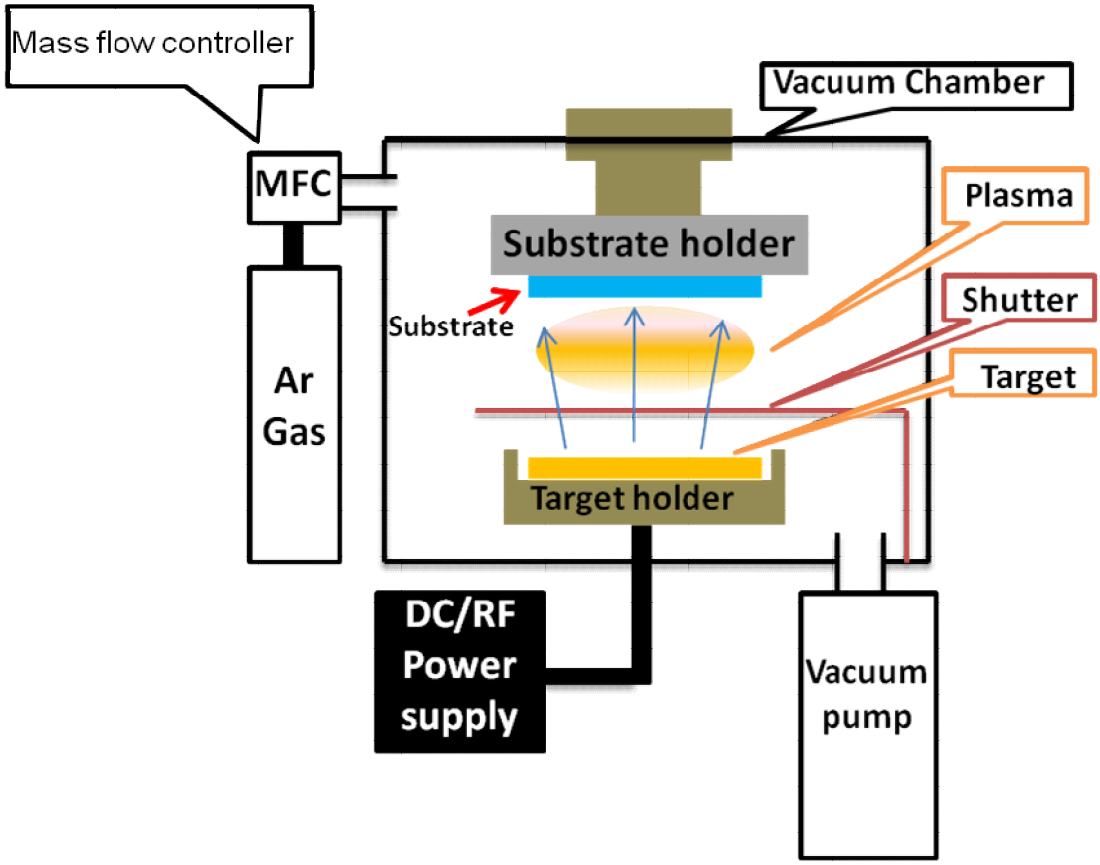

Figure1.3 Schematic of typical RF sputtering system.

1.3.1.4 Metal organic chemical vapour deposition (MOCVD) process

Metal organic chemical vapour deposition (MOCVD) also known as metal organic vapour phase epitaxy (MOVPE) is used for preparing thin films by depositing atoms on a wafer substrate. It has been extensively utilized in academic research and semiconductors industry for several thin films growth.

For specific crystal growth, the desired atoms are combined with complex organic gas molecules and passed over a hot semiconductor wafer. The heat breaks the molecules and deposits these atoms layer by layer onto the substrate surface. The undesired remnant are then removed or deposited on the walls of the reactor. By varying the composition of the gas, the crystal properties at almost atomic scale can be changed. Using this technique, layers of precisely controlled thickness can be built, which is essential in creating a material with specific optical and electrical properties. The MOCVD facilitate the building of a range of semiconductor photo detectors and lasers. In addition to the growth of thin films growth, scientists recently were motivated to grow nanostructures by this technique. Their efforts have fruitfully resulted in synthesizing selections of semiconductor nanostructures that is reported in the literature[39-41].

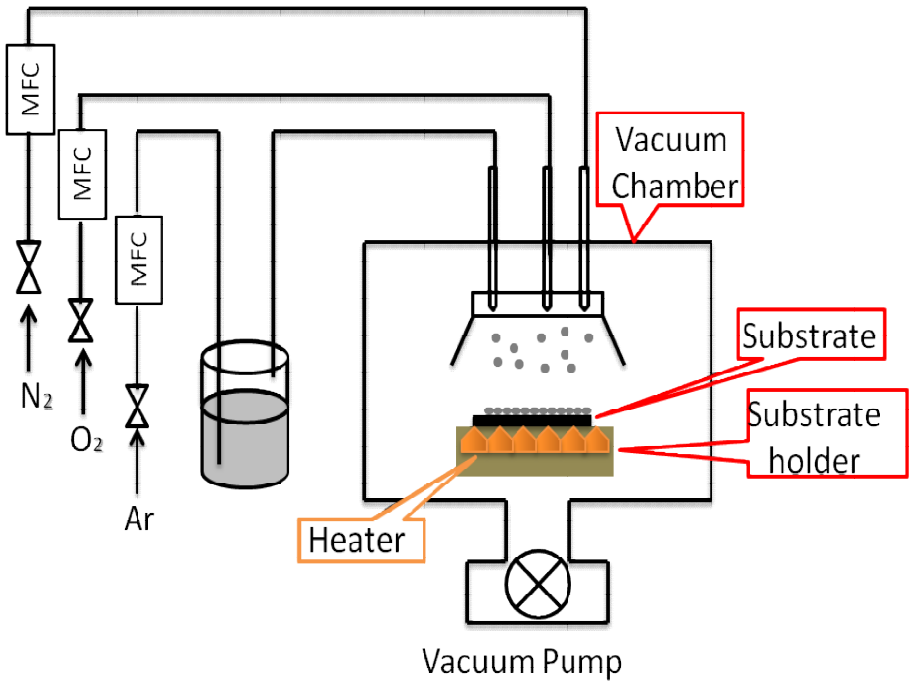

Figure1.3 Schematic of typical vertical MOCVD system.

1.3.2 Solution phase growth process

A solution phase growth process is a common method to synthesize many nanostructures, as it is advantages in numerous aspects over the vapour phase synthesis. In addition to its high yield growth, it provides multi environmental growth process, low cost and low temperature.

On the other hand, large amount of impurities are inherently present in the final products, hindering therefore their applications. Several approaches stem from the solution growth of nanostructures; these are the sol-gel technique, electrochemical deposition, and surfactant assisted growth processes, sonochemical method, hydrothermal and solvothermal methods and so on.

1.3.2.1 sol-gel deposition technique

The sol-gel process is a versatile solution process for making ceramic and glass materials. Generally, the sol-gel process involves the transition of a system from a liquid "sol" (mostly colloidal) into a solid "gel" phase. As a first step, colloidal suspension (sol) of the desired particles is prepared from the solution of the precursor molecules. As the appropriate reaction time is elapsed, the final product is obtained after a thermal treatment to remove the gel. Several nanostructures have recently been synthesized by this method such as ZnO, MnO_2, ZrO_2, TiO, CuO and V_2O_5[42,43].

1.3.2.2 Electrochemical deposition process

In addition to being a convenient method to synthesize metal oxide nanostructures, the electrochemical deposition (ECD) process is dedicated to fabricate metallic nanowires in the porous structures. The ECD method, from dissolved precursors, especially in aqueous solutions, is a low-cost and scalable method that is usually well suited for mass production of semiconductor thin films. Different material nanostructures are reported in the literature as synthesized using the porous or non-porous structures and substrates and metal foil etc. The materials include ZnO, NiO, Cu_2O and Fe_2O_3 and so on[44,45].

1.3.2.3 Surfactant and capping agent assisted growth process

Surfactant-assisted growth is considered an effective way to synthesize nanostructures. In order to obtain an appropriate nanostructure, careful selection of precursor and surfactant species and other parameters such as pH, concentration and temperature of the reactants are necessary. In this regard, the surfactant-assisted method is a trial and error based procedure, which requires much endeavour to choose proper capping agents and reaction environment.

The capping reagents are used to confine the lateral growth of the desired material. It serves as a soft template which can change the free energies of the various surfaces and thus alter their growth rates. This method was initially used to synthesize and control the morphology of the nanoparticles and presently it is extensively used for the synthesis of nanomaterials. The ZnO, SnO_2, NiO, $PbCrO_4$, CeO_2, etc nanostructures are synthesized by this process[46,47].

1.3.2.4 Sonochemical method

Sonochemical processing has been proven as a useful technique for generating novel materials with unusual properties. Sonochemistry arises from acoustic cavitation phenomenon which involves the formation, growth, and collapse of many bubbles in aqueous solution[48]. Under extreme reaction conditions, for instance extremely high temperatures more than 5000 K, pressures larger than 500 atm, and very high cooling rates that is higher than 10^{10} K/s attained during cavity collapse. The method yields many unique properties in the irradiated solution and results the formation of nanostructures via chemical reaction. A variety of nanostructures are already prepared and reported in the literature by this method.

1.3.2.5 Hydrothermal deposition process

The hydrothermal process is well known technique for the synthesis of a variety of nanostructures. This term (hydrothermal process) refers to the growth process that begins with the aqueous mixture of soluble metal salt (metal and/or metal organic) of the precursor material under high pressure and temperature conditions. Typically, the precursor's solutions are mixed and placed in an autoclave under elevated temperature and pressure in order to dissolve and recrystallise materials that are relatively insoluble

at ambient conditions. Nanostructures such as ZnO, CuO, CeO_2, TiO_2, In_2O_3, Fe_3O_4, MnO_2, Ga_2O_3 etc, can be obtained with or without use of capping reagents[49,50].

1.4 The choice of ZnO

As explained in the section (1.1), the material properties and geometry are the most important parameters influencing the performance and the quality of a field emission electron source. In this section, a brief review about the materials commonly used as field emission sources, sheds light as to why the ZnO nanomaterial is chosen to be a potential futuristic field emitter source.

1.4.1 Metals

The fabrication of metal emitters has been well developed whereby several techniques have been employed to create the optimum geometry.

The single crystal tungsten emitter with a tip radius of approximately ≤100nm has been fabricated through electrochemical etching of a fine tungsten wire and operated at ultrahigh vacuum (~10^{-11} mbar) to limit contamination/oxidation and enhance the stability and extend emitter lifetime[51]. Such stringent vacuum was somewhat a considerable challenge few decades ago which limited the applications of the tungsten field emission source. Even though, today's cutting-edge vacuum technology advancement has facilitated a widespread use of such emitter, at least two orders of magnitude gap between in what the next alternative is still vacant. Molybdenum (Mo) has offered a good opportunity to FE research, because of the high reproducible cone arrays it was hoped to instead implement it as an alternative. However, being flashed at high temperature to clean the surface from adsorbed species resulted in failure. As the molybdenum emitter is heated to sufficiently high temperatures, surface and geometrical damage occurs and thus its use is eliminated[52].

1.4.2 Carbon nanotubes

Carbon nanotubes (CNTs) were considered by many groups as one of the most promising field emitters because of their excellent properties such as metallic conductivity, very high aspect ratio. However, CNTs is very sensitive to the environment, particularly H_2O and O_2 absorbates which leads to high field emission

instability. Moreover, high interfacial resistance between CNTs and the substrate may lead to substantial interface temperature and detach the CNT emitter from the substrate or holder[53,54].

1.4.3 Zinc oxide (ZnO) nanostructures

Although ZnO does not have the ideal material's properties for field emission application i.e. work function being ≈5.3eV and melting point ≈1975ºC, the attractive properties of the ZnO nanostructures i.e. high mechanical stability and oxidation resistance, high chemical and thermal stability suggest the ZnO nanostructure as a potential candidate for the fabrication of efficient field emission sources[16]. Moreover, being n-type semiconductor ZnO's electronic properties such as the conductivity could be increased by doping and/or post growth treatment such as annealing. Increasing the conductivity will lower the work function and enhance the field emission properties of the ZnO nanostructures. In addition, fabricating ZnO nanostructures with enviable geometry and tuning its electronic properties is attainable using bottom-up techniques. Therefore, ZnO nonomaterials are considered a competitive candidate of realizing the practical application as futuristic field emitter source.

1.5 Research objectives

As highlighted throughout this chapter, metal oxide nanostructures of several morphologies such as, but not limited to, rods, tubes, wires, belts, needles, cones, pyramids, nails, pins can be prepared by different chemical and physical growth methods. These metal oxides and particularly the ZnO nanostructures could exhibit excellent field emission properties. Therefore, this section will summarize the main objectives of this research as follow:-

• ***Direct and controlled growth of pure and doped zinc oxide nanostructures for field electron emission applications.***

The first and most important objective of this research work is the direct and controlled growth of undoped and doped zinc oxide nanostructures by different synthesis techniques. The growth of undoped and doped zinc oxide nanostructures will be prepared in terms of their high aspect ratio with uniform morphology (height and

diameter) well aligned to the substrate in a reliable and reproducible way. To achieve this objective, several experiments were performed by changing various reaction parameters such as reactants, reaction time, temperature, different substrate etc.

• ***Enhancement of field electron emission properties of undoped and doped 1D zinc oxide nanostructures.***

There are many strategies to enhance the field emission properties of a material.

- The field emission properties of the emitter could be enhanced by enlarging the field enhancement factor which is determined by the morphology of the emitter. 2D and 1D ZnO nanostructures were successfully synthesized. The results show that the surface morphology and the Field enhancement factor 'β' have high impact on the field emission properties of the prepared ZnO nanostructures.
- Designing the ZnO nanostructures with particular geometrical configuration (e.g. nanoneedle and pencil like morphologies shapes) is also very efficient way for further enhancing in the field emission performance
- As the field emission property strongly depends upon the work function of the material, hence the field emission performance can be enhanced by lowering the work function. This objective can be achieved by doping the ZnO nanostructures.

• ***Fabrication of 1D zinc oxide nanorods based field emitters***

The fabrication of zinc oxide nanorods for their effective use as an electron source in the electron microscope is the scope of this thesis.

• ***Study of field electron emission mechanism based on the morphologies of ZnO nanomaterials***

The field electron emission properties of doped and undoped ZnO nanostructures with different morphologies will be carried out. The as grown ZnO emitters will be characterized in term of their *I-V* characteristics, current stability and vacuum requirements in the field emission measurement system.

1.6 The organization of the thesis

A brief introduction and review about the nanostructures and their field emission properties based on various semiconductor nanomaterials is presented in the start of the thesis. ZnO is chosen as material model for this thesis. Therefore, the general properties of a ZnO and its various synthesis techniques are presented in the first chapter. Also, why ZnO is chosen instead of metal or carbon nanotubes for field emission application is also discussed in length in this chapter. At the closing of the first chapter, the research objectives and organization of thesis have been presented.

The second chapter demonstrates the theory of electron emission in which various topics such as the band theory of solids, the surface potential barrier, the electron emission and the work function, modification of the surface potential barrier, Fowler-Nordheim theory, electron emission sources and basic field emission characteristics are discussed in length.

Two important synthesis techniques, i.e. hydrothermal process and thermal evaporation process, to prepare the ZnO nanomaterials are used in this work. Various characterization techniques, such as X-ray diffraction (XRD), field emission scanning electron microscopy (FESEM) equipped with energy dispersive spectroscopy (EDS), field emission transmission electron microscopy (FETEM), room-temperature photoluminescence (PL) spectroscopy, Raman-scattering spectroscopy were used to characterize the synthesized ZnO based nanomaterials. Finally, field emission measurements of all the prepared ZnO based nanomaterials are examined. These all experimental and characterization details are discussed in chapter 3.

Successful synthesis of various undoped and doped ZnO nanostructures with different morphologies and compositions on different substrates such as zinc foil, silicon, titanium and tungsten substrates via two different synthesis techniques i.e. hydrothermal process and thermal evaporation process were accomplished and presented in chapters 4 to 8. Finally, plausible growth mechanisms based on the crystallographic habits of the wurtzite hexagonal ZnO have also been proposed for the growth of all the ZnO based nanomaterials.

Chapter 4 describes the synthesis, detailed characterizations and field emission application of ZnO nanosheets interconnects grown on zinc foil by facile hydrothermal process. Besides, chapter 5 presents the non-catalytic growth and structural, optical and

field emission properties of hexagonal shaped ZnO nanorods grown on bare titanium substrate.

As the doping has significant effect on the morphology as well as the electrical properties and thus the field emission properties of the ZnO nanostructures. Therefore, chapter 6 demonstrates the growth of gallium (Ga)-doped ZnO nanostructures. Two kinds of Ga-doped ZnO were prepared, i.e. nanoneedles and multipods and their detailed characterizations (structural, optical and field emission) are presented in chapter 6. Chapter 7 describes the In-doped ZnO nanopencils and their details structural, optical and field emission properties.

To follow the ultimate goal of this thesis, I have explored the application of the ZnO nanorods as alternative electron source for high brightness electron cathodes and for their use in harsh environment and presented in chapter 8. A new approach to fabricate novel field emitter based on ZnO nanostructures is reported.

Finally, the obtained and presented results are concluded and future prospects of our work are highlighted in chapters 9 and 10.

CHAPTER2
THE THEORY OF ELECTRON EMISSION

2.1 The band theory of solids

As atoms in solid are brought close together, their energy levels interact with each other forming bands of energy states. These are separated by forbidden regions that relate to the gaps between the atomic levels. Once the bands are formed, their energy states are filled with electrons according to the exclusion principle[55]. The highest and the next higher energy filled band are termed the valence band and the conduction band respectively and the energy separation between them is termed the energy gap, E_g. Electrons which are bound to the nucleus (valence electrons), can jump from one atom to another but cannot move from a valence band to a conduction band without being excited or energised. Although, these electrons are free in the sense of not being attached to a particular atom, they are not free to escape from substance to vacuum due to the lattice's attractive force that acts as a whole[55].

2.2 The surface potential barrier

In isolated atom electrons have discrete energy levels with large gaps among them; an electron of the outmost conduction band is influenced by the nuclei's electrostatic attraction force that is inversely proportional to the square distance of electron to nuclei. The inverse square law approximately governs the relation between the electron's potential energy with respect to its atom. In figure 2.1 the horizontal broken line indicates the electron's potential at infinite distance.

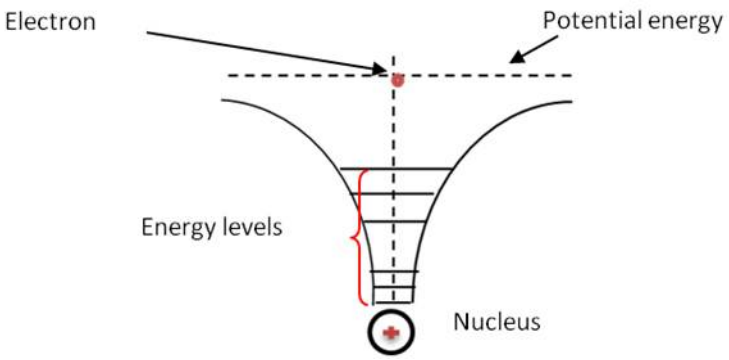

Figure 2.1 the potential energy of an electron near an isolated nucleus.

Considering the case of two neighbouring atoms, the presence of one atom decreases the potential energy on the adjacent side of the other as figure 2.2 shows.

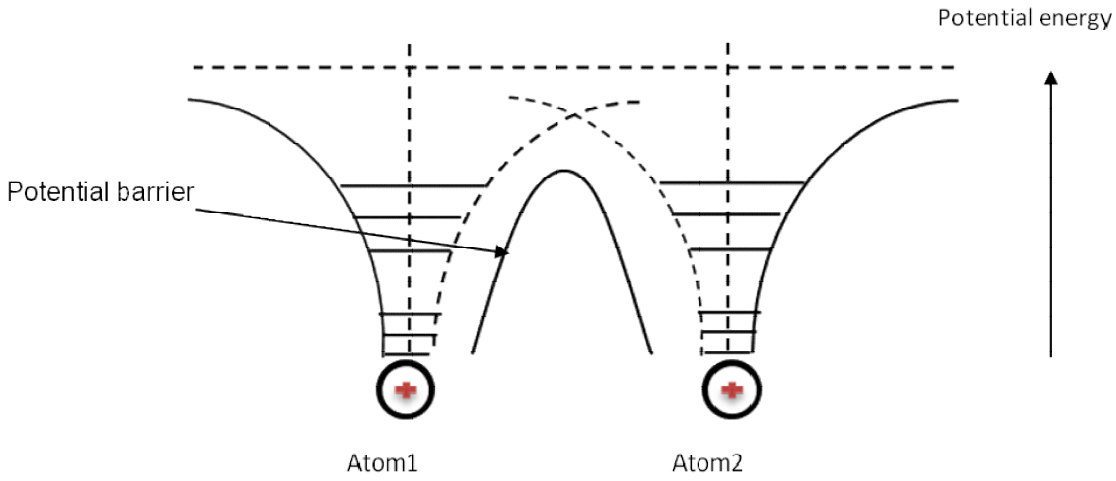

Figure 2.2 The potential energy of an electron along a line through two adjacent atoms.

This mutual effect of decreasing the potential barrier is even more noticeable with continuous lattice of atoms and results in a series of potential energy humps between the atoms as figure 2.3 shows. Nevertheless, the potential encounters an increase at surface atom (last atom) in very much the same way as in the case of the isolated atom.

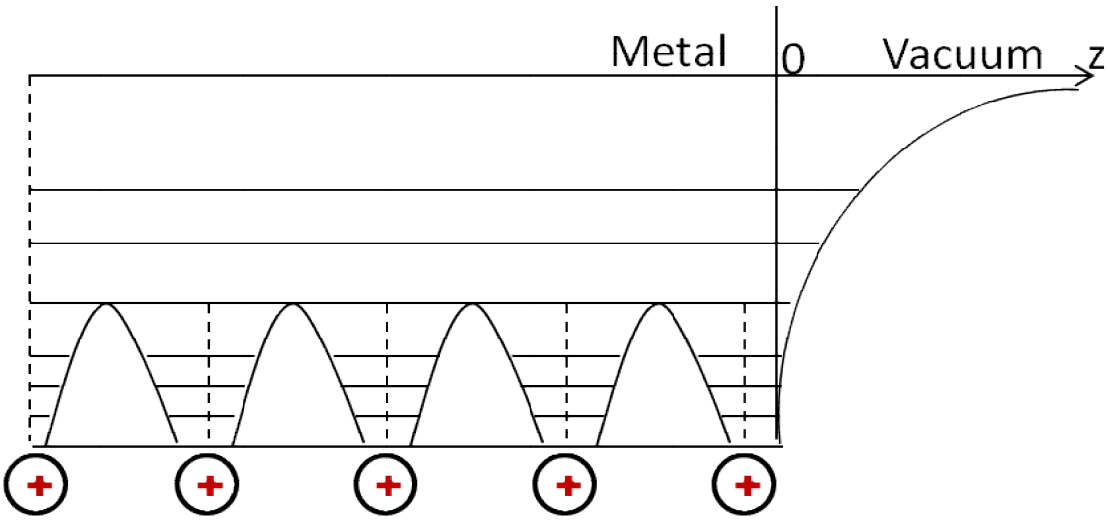

Figure 2.3 The potential energy of an electron along a line through a row of atoms.

Therefore, there are two main grounds for forming the surface potential barrier in metals. *The first one is the electric double layer* which is caused due to the asymmetric

distribution of electrons around the surface ions. The electron density is equivalent to the positive charge density in the deep interior of the bulk metal, but the electron density falls gradually toward the surface whereas the positive charge density remains constant up to the surface. This charge density alteration yields a double layer which produces an electrostatic potential to prevent electrons from escaping[56].

The second factor is the image force by which an electron at a distance z from the metal surface creates a positive charge on the metal surface which attracts the electron to it. The image force also prevents an electron from escaping the surface[57].

2.3 The electron emission and the work function

The theory of electron emission assumes that metals obey the Sommerfeld free-electron model[55] and the electron distribution follows the Fermi-Dirac statistics. Accordingly, at zero Kelvin temperature the electron distribution function is a step function and the probability for electron to occupy a quantum state below the Fermi level is equal to the unity and zero Probability to occupy a quantum state above the Fermi energy. Whereas at temberature greater than absoulute zero, the thermal distribution of electrons is given by[58]:

$$F(E,T) = \frac{1}{\exp(E - E_F / kT) + 1} \qquad (2.1)$$

where, E is the energy of the corresponding single-particle, k is Boltzmann's constant, 8.62×10^{-5}eV/K, T is the temperature in degrees Kelvin, and E_F is the Fermi energy or Fermi level. This is determined as the energy point where the probability of occupancy by an electron is exactly 50%.

For simplification, the free electrons distribution in the metal can be described as a 1D potential well with a flat bottom as can be seen in figure 2.4. The surface potential barrier (U_a) is defined as the difference between the vacuum level E_v and the bottom energy level in the potential well E_c (conduction band bottom) as follow.

$$U_a = E_v - E_c \qquad (2.2)$$

As can be seen from figure2.4 electrons at the Fermi level cannot escape the metal surface freely due to the surface potential barrier force. At the Fermi level, electrons require an amount of energy (Φ) to overcome the barrier. This energy is

equivalent to the difference in energy between the vacuum level and the Fermi level and termed the material's work function.

$$\Phi = U_a - E_F \tag{2.3}$$

The work function is defined to be the minimum energy required for an electron at the Fermi level to escape to the surrounding vacuum.

Two general means are utilised to liberate electrons from the surface potential barrier. The first is via raising the electrons' energy by external energy to surpass the surface potential barrier and escape to vacuum. Such energy transformation is accomplished by three different ways, these are:

i) *Thermionic emission:* In this process electrons gain excess energy through the thermal excitation (heat energy) to overcome the barrier. This will be discussed in detailed in section (2.6.1).

ii) *Photoelectric emission:* Electrons can be ejected from metals by the exposure to electromagnetic radiation such as x-ray or visible light. Electrons then absorb the photons through what is known as the photoelectric effect gaining therefore the sufficient energy to overcome the potential barrier force[59].

iii) *Secondary emission:* As a metal is bombarded with high energy electrons, some or all the kinetic energy of these electrons is transferred to the metal's free electrons and raise their energy to escape the barrier

The second means is the field emission process which involves lowering the surface potential barrier "Schottky effect" and narrowing its width via applying high electric field.

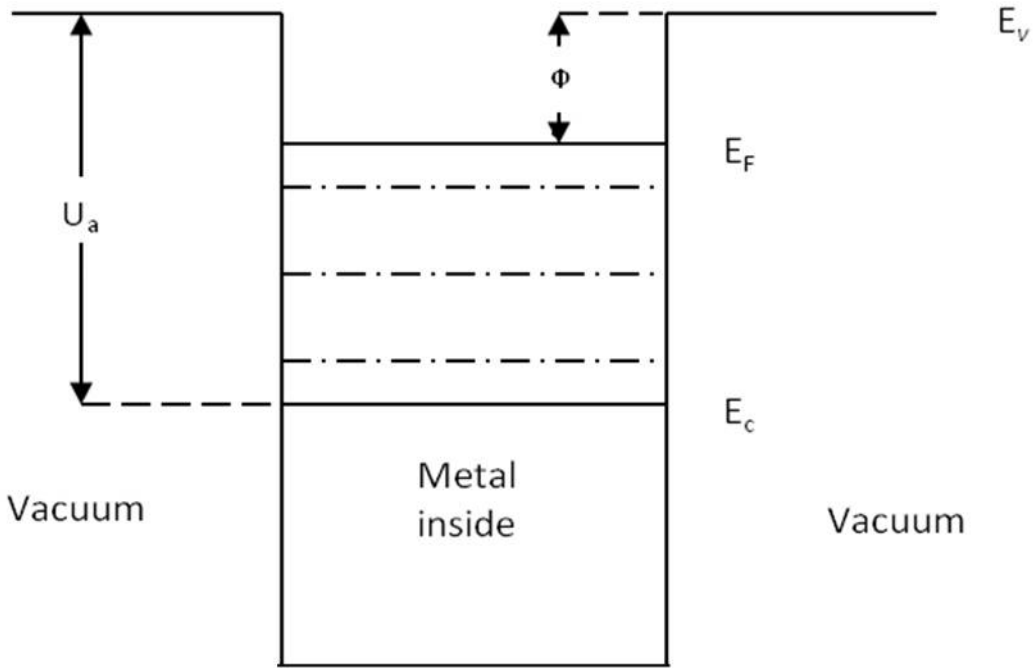

Figure 2.4 Schematic of one-dimensional potential well with a flat bottom. U_a is the surface potential barrier, E_v the vacuum level, E_F Fermi level, E_c the conduction band bottom and Φ is the work function.

2.4 Modification of the surface potential barrier

Regarding the second approach of liberating electrons from to the vacuum via applying intensive electric field, the form of the potential well will be considered in detail to enhance the understanding of the field emission process. Inside the metal ($z < 0$) $U(z)$ = constant for simplification, and in the vacuum side, $z>0$.

Considering the presence of the image force phenomenon at the surface of the emitting material, which is explained in section (2.2), such force is given by equation 2.4:

$$f = \frac{-e^2}{4z^2} \tag{2.4}$$

The electron energy (E) of an electron transferred from infinity to a distance z from the surface is given by:

$$E(z) = \int_x^{\infty} f.dz = -\frac{e^2}{4z} \tag{2.5}$$

Under an intense electric field for a planar emitter, the potential energy $U(z)$ near the surface for an electron outside a metal surface is described as

$$U(z) = \Phi + E_F - \frac{e^2}{4z} - eFz \tag{2.6}$$

Figure 2.5 illustrates the effect of the image potential and external field upon the surface barrier. As illustrated, the effect of the image force is that the step potential at the surface is rounded. This is the initiation of Schottky lowering effect[60] when electric field is applied. A simple calculation can give the lowering to be

$$\Delta\Phi = -\sqrt{e^3 F} \tag{2.7}$$

At the position

$$z = \frac{1}{2}\sqrt{\frac{e}{F}} \tag{2.8}$$

The resultant barrier is thinner and lower which leads to the possibility of the tunnelling phenomenon to occur.

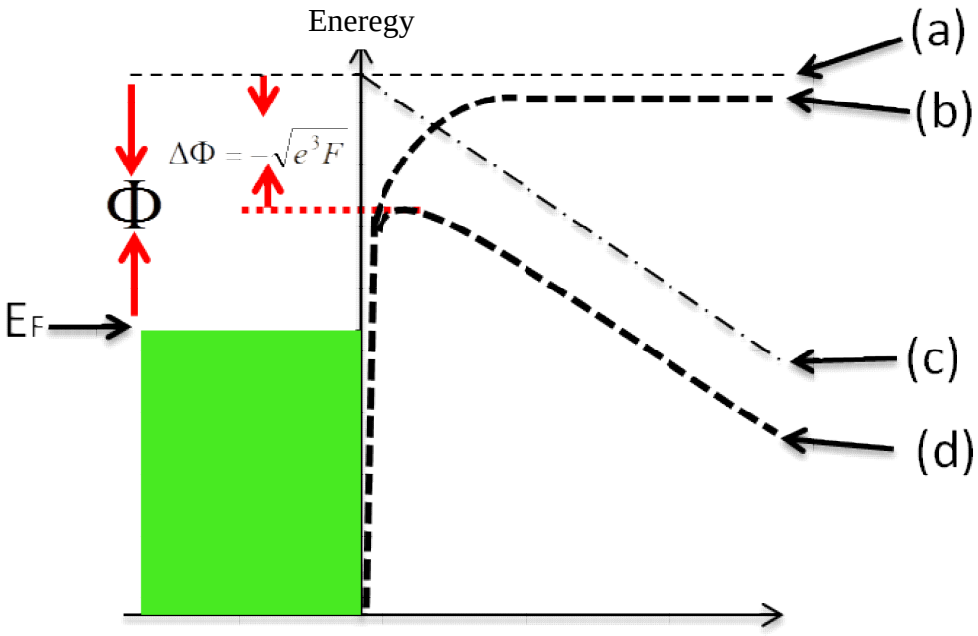

Figure 2.5 Shows the surface potential barrier (a) without image potential and external field, (b) with image potential but without external field, (c) with external field but without image potential, and (d) with both image potential and external field.

2.5 Fowler-Nordheim theory

To determine the effective potential barrier, the zero point is set at vacuum level, E_v =0, that means E_F=-Φ and the bottom of the conduction band E_c=-U_a. Based on these assumptions the effective potential barrier is:

$$U(z) = \begin{cases} -U_a, & \text{for } z<0 \\ -e^2/4z - eFz, & \text{for } z>0 \end{cases} \qquad (2.9)$$

The Fowler-Nordheim theory (F-N theory) is a quantitative description of field emission process for metals, which requires calculating the FE current density as a function of the electric field. F-N theory is based on the following main assumptions:

- The metal is assumed to obey the Sommerfeld free-electron model with the Fermi-Dirac statistics.
- The metal surface is taken to be planar, that is, the 1D problem considered. This assumption is valid because in most cases the thickness of the potential barrier in

fields of 10^7-10^8 V/cm is several orders of magnitude less than the emitter radius. Thus, the external field can be taken to be uniform along the surface for the finite surface without considering surface distortion effects.

- The potential $U(z)$ within the metal is considered a constant ($U(z)$=const=-U_a). Outside the metal the potential barrier is regarded as entirely due to the image force U_z=-e^2/4z with the externally applied electric field having no effect on the electron states inside the metal, which means the effect of the surface charge distribution can be neglected, leaving only the surface dipole distribution.
- The calculation is performed for the temperature T=0K.

Under these assumptions, E_z is defined to be the z-component of the electron energy:

$$E_z = E - \frac{P_x^2}{2m} - \frac{P_y^2}{2m} = \frac{P_z^2}{2m} + U(z), \tag{2.10}$$

where, E is the electron energy and P_x, P_y *and* P_z are the x, y and z components of the electron's momentum and m *i*ts mass.

If $N(E_z)d(E_z)$ is the number of electrons per unit area per second with the z-component at their energy within dE_z of E_z and $D(E_z)$ is the transmission coefficient, the electric current density, J_c, is:

$$J_c = e\int_{-U_a}^{\infty} D(E_z)N(E_z)dE_z \tag{2.11}$$

where, e is the electron charge and $N(E_x)$ is called the supply function.

The supply function can be calculated to be

$$N(E_z) = \frac{4\pi mkT}{h}\ln\left(1+\exp\left(-\frac{E_z - E_F}{kT}\right)\right) \text{ where } E_F=-\Phi \tag{2.12}$$

Using the WKB approximation, the transmission coefficient is

$$D(E_z) = \exp\left(-\frac{4\sqrt{2m|E_z|^3}}{3heF}v(y)\right) \tag{2.13}$$

where F is the applied electric field. The Nordheim function, v (y), is

$$v(y) = 2^{-\frac{1}{2}}\sqrt{1+\sqrt{1-y^2}}\,E(k) - (1-\sqrt{1-y^2})K(k) \tag{2.14}$$

$$E(k) = \int\sqrt{1-k^2\sin^2\varphi}\,d\varphi \tag{2.15}$$

$$K(k) = \int_0^{\frac{\pi}{2}} \frac{dU_a}{\sqrt{1-k^2\sin^2\varphi}} \tag{2.16}$$

$$k^2 = \frac{2\sqrt{1-y^2}}{1+\sqrt{1-y^2}} \tag{2.17}$$

$$y = \frac{\sqrt{e^3F}}{|E_z|} \tag{2.18}$$

The FE current density at zero temperature is described by F-N formula

$$J_c = \frac{e^3F^2}{8\pi ht^2(y)\Phi}\exp\left(-\frac{4\sqrt{2m}\Phi^{3/2}}{3\hbar eF}v(y)\left(\frac{\sqrt{e^3F}}{\Phi}\right)\right) \tag{2.19}$$

If the work function Φ is represented in eV, F in V/cm and J_c in A/cm^2 equation (2.19) results in:

$$J_c = 1.54\times10^{-6}\frac{F^2}{t^2(y)\Phi}\exp\left(-6.83\times10^7\frac{\Phi^{2/3}}{F}v(y)\right) \tag{2.20}$$

t usually is set equal to unity for simplification because t^{-2} varies between 1 and 0.81. Spindl *et al* proposed a close approximation of $t(y)$ and $v(y)$ as follows[52]:

$$t^2(y) = 1.1, \qquad v(y) = 0.95 - y^2 \qquad \text{where, } y = 3.79\times10^{-4}\frac{F^{1/2}}{\Phi}$$

Equation (2.20) assumes planar emitter in which the local field equal to the macroscopic field. The Fowler-Nordheim treatment was developed by Sommerfield and Bethe to include a factor known as the field enhancement factor[61]. For nanostructural emitters, the field enhancement factor reflects the degree of the FE enhancement of any tip over a flat surface. The field enhancement factor value is inversely proportional to the apex curvature radius of the tips and the local electric field F will be enhanced by:

$$F = \beta E \tag{2.21}$$

where, β is the field enhancement factor, and E is the applied electric field.

The Fowler-Nordheim formula for sharp emitter will be as follow:

$$J_c = 1.54\times10^{-6}\frac{(\beta E)^2}{t^2(y)\Phi}\exp\left(-6.83\times10^{7}\frac{\Phi^{2/3}}{\beta E}v(y)\right) \qquad (2.22)$$

The current density in equation (2.22) is defined as the ratio of current (*I*) to the effective emission area (α) for a given surface:

$$J_c = \frac{I}{\alpha} \qquad (2.23)$$

In addition, the electric fielde in parallel plate configuration defind by the ratio of applied voltage to the anode-sample distance as:

$$E = V/d \qquad (2.24)$$

where, *V* is the applied voltage in volt and *d* is the distance between the sample and the anode.

By substituting equations (2.23) and (2.24) into equation (2.22) will give an expression of Fowler-Nordheim equation for the current as a function of applied voltage:

$$I = a\frac{V^2}{d^2}exp\left(\frac{-bd}{V}\right) \qquad (2.25)$$

$$a \equiv\propto \frac{A\beta^2}{1.1\Phi}exp\left(\frac{9.84}{\Phi^{\frac{1}{2}}}\right)$$

$$b \equiv \frac{0.95B\Phi^{\frac{3}{2}}}{\beta}$$

$$A = 1.54\times10^{-6}\text{A.eV.V}^{-2},$$

$$B = 6.83\times10^{7}\ (\text{eV})^{3/2}.\text{V.cm}$$

where, equation (2.25) is the fitting equation and *a* and *b* are constants that are used to fit the field emission (*I*-*V*) data in this thesis (chapters 4-8).

The following equation is used in experiment for plotting the field emission data in what is termed F-N plot, namely $\ln(I/V^2)$ versus $(1/V)$.

$$\ln\left(\frac{I}{V^2}\right) = \ln\left(\frac{a}{d^2}\right) - \frac{bd}{V} \tag{2.26}$$

The F-N plot yealids a straight line with slope (-b) and intercept ln(a)

$$-b = \frac{B\Phi^{\frac{3}{2}}}{\beta} \tag{2.27}$$

2.6 Electron emission sources

Thermionic emission and field emission are the two most common methods that are being implemented effectively in charged particle technology/industry.

2.6.1 Thermionic emission source

In thermionic emission, electrons from the Fermi level E_F acquire sufficient energy to overcome the surface potential barrier of the cathode (the work function). This is typically accomplished via passing an electric current through the filament to increase its temperature. The nuclia vibrates due to the excessive thermal energy and hence electrons gain sufficient energy initiating the thermionic emission. The dependence of the emission current density J_c on the temperature and the work function is given by the Richardson-Dushman equation[62]:

$$J_c = AT^2 \exp(-\Phi / kT_c), \tag{2.28}$$

where:

T: is the temperature of the cathode tip in Kelvin,

k: is Boltzmann constant (8.6×10^{-5} eV/K) and

A: is a constant depending on the cathode material.

Just below the melting point T_m, the emission current density is sufficiently optimised.

Another formula is given by Nordheim, which considers possibility of electrons being reflected back into the metal as they reach the emitter surface[52].

$$J_c = A(1-r)T^2 \exp(-\Phi / kT_c), \tag{2.29}$$

where, r is the probability factor that counts for electrons that are reflected back.

As a device, a basic thermionic electron gun essentially consists of two elements. The cathode is the source of electrons, and the anode (which is biased positive with respect to the cathode), attracts the generated electrons. The anode has a small

(≈1mm) central aperture to allow the extracted electrons to passes through. In 1909 a third cylindrical elements locates between the cathode and the anode, was introduced to the electron gun structure by Wehnelt[63]. This is known as the Wehnelt cap and has a smaller central aperture (≈ 500μm) which applies a negative electric field to converge the electron beam towards the anode's aperture as well as controlling the emitting area at the cathode. This is illustrated in figure 2.6.

Several materials have been utilized as thermionic electron sources albeit among all, the tungsten cathode is typically the most ancient and widely used. A conventional thermionic tungsten cathode that is formed as a bent wire has a work function of ≈4.8 eV, operates at ≈ 2850K and can produce a stable emission at low vacuum environment of $\approx 1\times10^{-4}$ mbar. The drawbacks, on the other hand are, short lifetime of ≈50 hrs and moderate current density of ≈ $5x10^4$ A/m^2 coupled with brightness ≈$1.5x10^5$ $Am/cm^2.sr$ due to the high operation temperature and high work function respectively[64].

In comparison, the single crystal lanthanum hexboride (LaB_6) operates at a lower temperature of ≈ 1800K with a lower work function of 2.8 eV. This yields a higher current density combined with 10 times higher brightness of ≈ $5x10^6$ $Am/cm^2.str$ and a lifetime of ≈ 1000hrs. Nonetheless, LaB_6 emitter requires more stringent environment than the tungsten in which necessitates high vacuum of ≈ 1×10^{-6} mbar[65, 66].

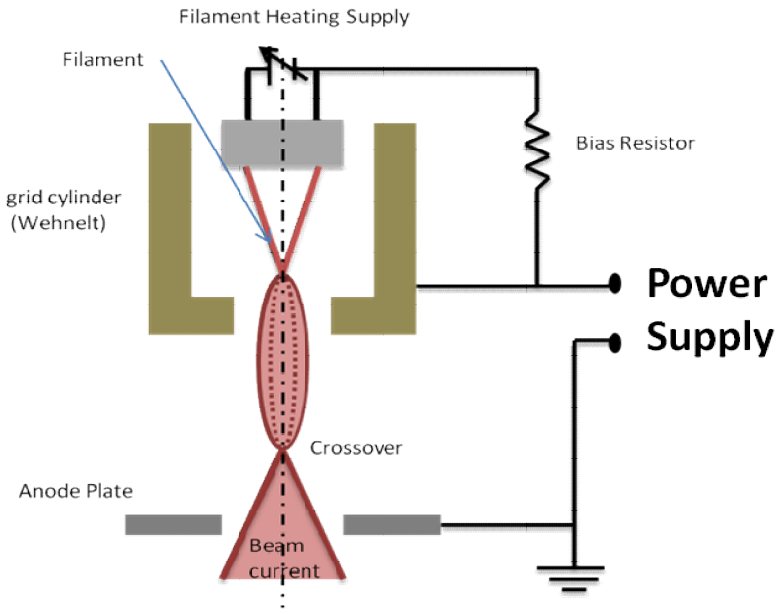

Figure 2.6 The configuration of thermionic electron gun.

2.6.2 Field emission electron source

As explained in section (2.3), the field emission process involves applying high electric field (on the order of 2-5x10^7 V/cm) for lowering and thinning the potential barrier. The thinning process is sufficient enough at the degree where the width of the barrier is less than or similar to the electrons' wavelength. It is hence possible for an electron with energy near the Fermi level to penetrate (tunnel) through the barrier[65].

Field emission electron gun also has a triode configuration structure based on the design of Crewe *et al.*[67]. The electron source (cathode) consists of a very sharp single crystal tungsten tip. The other two anodes locate below the cathode as figure 2.7 shows. The extractor (first anode) is held at positive potential of ≈ 3-5 kV (with respect to the cathode) through which the electric field is applied to the cathode's surface. The lens (second anode) is responsible for accelerating the electrons towards the target (column or sample) by applying a positive electrostatic field with respect to the cathode. The accelerating voltages used in electron microscopes for instance can range from 5-30 kV in the SEM and up to 200 kV in the TEM.

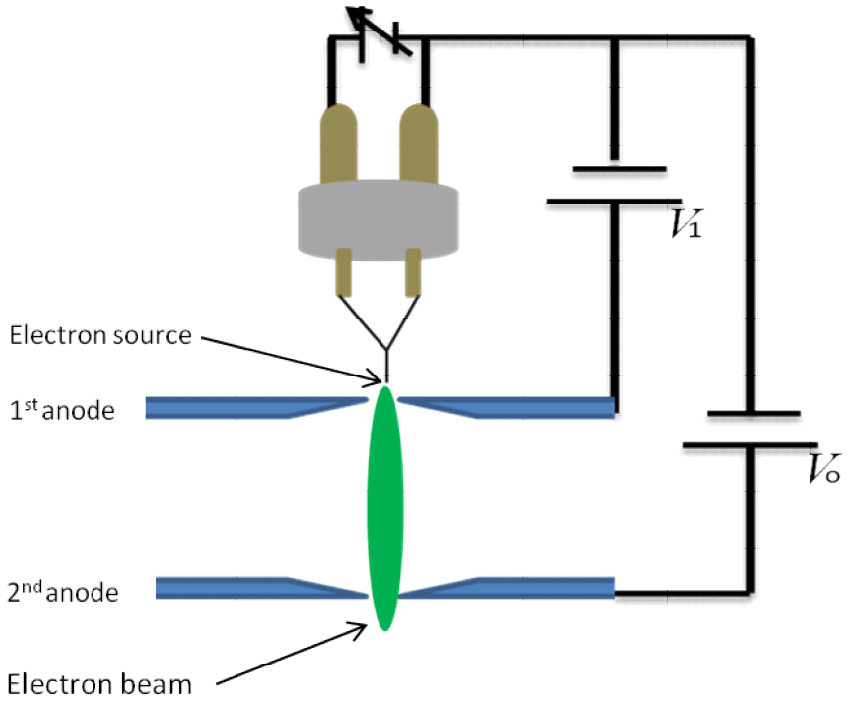

Figure 2.7 The configuration of field emission electron gun.

2.7 Basic field emission characteristics

Since, the work function, the operating temperature and the melting point are the prerequisite factors in refereeing the cathode's material in thermionic emission, the material of field emission cathode also needs to meet some requirements. Several important characteristics and properties can be used as guide to determine the FE properties of the source material.

1. The turn on field and the threshold field

As an external field is applied, the turn on field and threshold field are essential indicators of determining the field emission efficiency of the source material. The turn on field is the field strength corresponding to the current density equal (10 μA/cm^2) and the threshold of emission, defined as the electric field necessary to achieve a minimum current density (10 mA/cm^2) for the application in industry.

The lower the characteristic value of these two fields, the more prompt the field emission occurs. This is experimentally demonstrated as the *I-V* curve where (*I)* is the field emitted current and (*V*) is the applied voltage which determines the electric field. The emission current values (*I*) are recorded as applied voltage is increased. The values of the turn on voltage and the threshold voltage can be determined by plotting the emission current (*I*) versus the applied voltage (*V*).

2. The stability of the emission current

The stability of the emission is defined as the variation of the emission current against time. An instable emission current fluctuates more frequently over a span of time. Such fluctuation is considered to be induced by the timely change of the local work function and/or the field strength on the atomic scale. These are due to adsorption, desorption, ion bombardment of ambient molecules and surface migration. The two major observed current instabilities are the flicker noise type and the step and spike type current fluctuations. Flicker type is more severe in metals, while in carbon related materials, the step and spike type is the dominant type that is caused by ion bombardment[68].

3. The field enhancement factor

The field enhancement factor β is defined as the ratio of the local field F_{local} to the macroscopic field (the average applied field) F as follow:

$$\beta = \frac{F_{local}}{F}, \tag{2.30}$$

The field enhancement factor can be estimated from the slope of F-N plot according to equation (2.27)

2.8 Conclusion

This chapter describes the theory of electron emission in which various topics such as the band theory of solids, the surface potential barrier, the electron emission and the work function, modification of the surface potential barrier, Fowler-Nordheim theory, electron emission sources and basic field emission characteristics are discussed in length. Therefore, the field emission data in chapters 4-8 will be discussed and analyzied within the frame of the Fowler-Nordheim theory.

CHAPTER3

EXPERIMENTAL TECHNIQUES

3.1 Introduction

Several techniques and methods were used to fabricate and characterise the zinc oxide nanomaterials. This chapter is dedicated to equip the readers with the basic knowledge of the used methods and techniques.

3.2 Synthesis techniques used for this work

The hydrothermal growth and the thermal evaporation techniques have been successfully employed to synthesize doped and undoped zinc oxide nanostructures.

3.2.1 The hydrothermal growth technique

Pure ZnO nanostructure is hydrothermally grown in a tightly-sealed autoclave, shown in figure 3.1. The thick-walled steel is lined with Teflon, which sustains high temperatures and pressures. In a typical synthesis process, the crystal growth is carried out in a queues solution of zinc chloride $ZnCl_2$, hexamine (HMTA), ammonium hydroxide NH_4OH and deionised water. A clean substrate is immersed within the thoroughly mixed former solution in the 100 ml size autoclave. Using an ordinary laboratory oven, the autoclave was then heated to an operating temperature of 110°C. At the end of the experiment, the substrate was taken out and washed with acetone, then dried in air, and kept for further characterisations.

Figure 3.1 Arepresentitive image of the different parts of the autoclave.

3.2.2 The thermal evaporation process

In synthesising a variety of nanostructures, the thermal evaporation is less complex and more versatile than the hydrothermal technique. This is due to its flexibility and control of growth. There are several modifications of this method depending on precursors used. Generally, this method utilizes a high temperature thermal furnace to vaporize the source material and facilitates the deposition of the nanostructures. The vapors of the source materials are generated first by physical or chemical methods, which are delivered into the growth zone by the carrier gas. The resultant vapors are condensed under certain conditions such as temperature, pressure, substrate and atmosphere.

Figures 3.2 and 3.3 are a schematic illustration of the instrumental setup of evaporation process and a photographic image of the real set-up used respectively. The system is made of a 100 cm long quartz tube arranged horizontally to serve as a reactor chamber that is combined with a rotary pump. The gas inlet is connected to one side while the rotary pump is attached to the other side of the quartz tube. Both ends of the quartz tube are sealed by rubber rings with vacuum grease. The temperature and gas flow rate are controlled by temperature controller and mass flow controller, respectively. The exact reaction temperature during synthesis is monitored by a movable thermocouple.

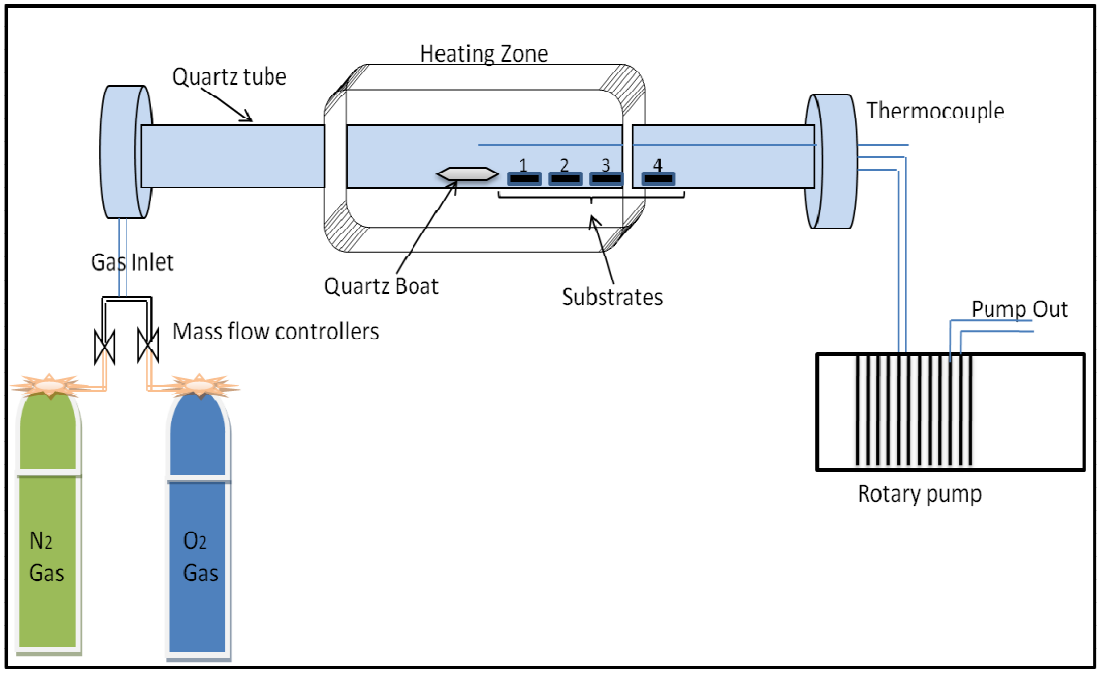

Figure 3.2 Schematic for the instrumental setup for the thermal evaporation process used for the growth of ZnO nanostructures.

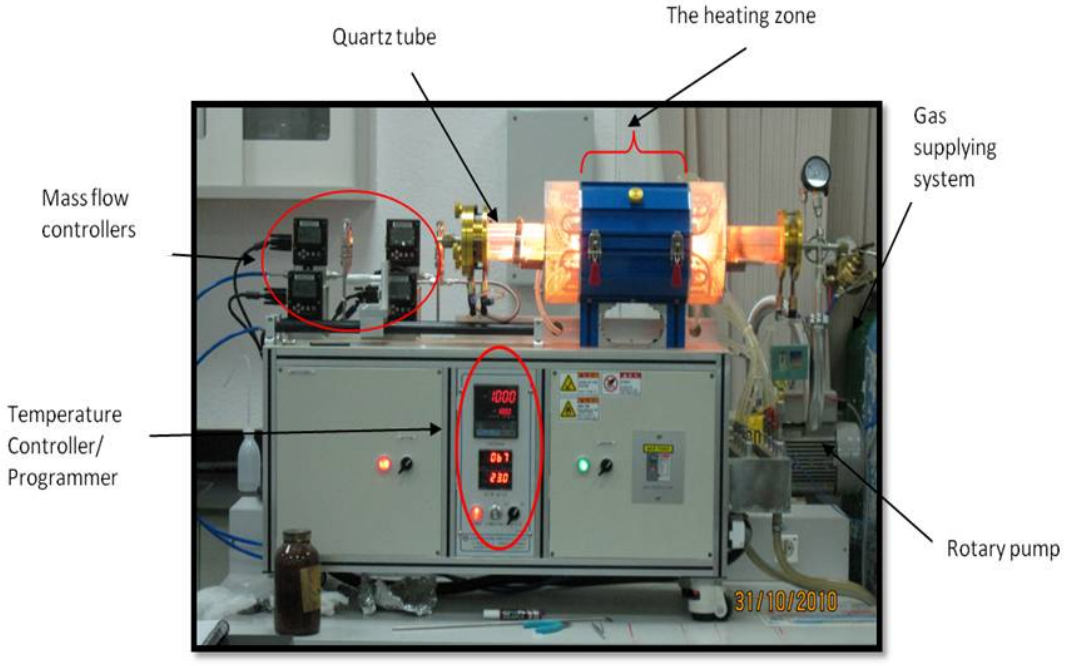

Figure 3.3 Real photograph of the horizontal tube furnace used for the growth of ZnO nanostructures.

3.3 Characterization techniques

3.3.1 Structural characterizations techniques

3.3.1.1 X-Ray diffraction (XRD)

X-ray diffraction is a powerful and common technique for determining the crystallographic structure of the material. X-ray diffraction techniques are based on the elastic scattering of X-rays from structures that have long range order. When a monochromatic X-ray beam is incident on the atoms in a crystalline material they get scattered and due to the periodicity associated with the arrangement of atoms of a crystal for certain angles of incidence (θ), they will interfere constructively or destructively. The constructive interference occurs from a plane of atoms is called diffraction. By knowing the wavelength (λ) of the X-ray beam and the angles at which the constructive interference occurs (termed angle θ_B), it is possible to understand the geometrical ordering of the atoms inside the crystal. In 1912, W. L. Bragg recognized a predictable relationship among several factors. These factors are combined in Bragg's law[69]:

$$2dsin\theta = n\lambda, \qquad (3.1)$$

where the integer n is the order of the diffracted beam, λ is X-ray wavelength, d is the distance between adjacent planes of atoms (the d-spacing) and it is of the order of X-ray wavelength, and θ is the angle of the incidence of the beam. The intensity of the diffracted X-rays is measured as a function of the diffraction angle 2θ and the specimen's orientation. Important information about the structural properties of the material emerge from the XRD pattern depending on the peak positions, intensities, peak width and peak shape. A sharp peak with high scattering intensity indicates that the sample has good crystallinity.

Since the wave length of the X-ray source is known and the angle (θ) can be determined from the XRD spectra, the lattice spacing (d) can be calculated using Bragg's law (equation 3.1). Moreover, the lattice parameters can be also calculated using Miller Indices (hkl) that describe the orientation of planes with respect to different crystal axis and the lattice spacing d_{hkl} for *hcp* crystal is given by the following equation[69]

$$\frac{1}{d_{hkl}^2} = \frac{4}{3}\left(\frac{h^2 + hk + k^2}{a^2}\right) + \frac{l^2}{c^2} \quad (3.2)$$

In the present work, a *PANalytical* X-ray diffractometer (*PANanalytical* Xpert Pro) was used to record the XRD pattern of ZnO nanostructures.

3.3.1.2 Field emission scanning electron microscopy (FESEM)

The field emission scanning electron microscope (FESEM) is a vastly informative tool to characterize nanomaterials and nanostructures. The technique utilizes electrons instead of light waves as the illumination source to realize/examine the micro and nano structure of the sample's surface.

Owing to its exceptionally short wavelength (disproportional to kinetic energy of electrons) which is few nanometres, scanning electron microscopy is regarded as high resolution microscopy.

Conventional light microscopes use glass lenses for magnification to create images, while electromagnetic lenses in SEM are not part of the image formation system; they instead focus the electron probe on the sample. Alternatively, the magnification in SEMs is accomplished and increased by scanning the electron probe over small and smaller areas, respectively. In SEM, electrons are generated by either field emission or thermally assisted field emission sources that is formed in a very sharp tungsten tip with radius of order of tenth and hundreds of nanometres respectively. The primary electron beam is accelerated toward the anode using high electric field and is focused by a combination of a condenser and objective lenses and scanned using a pair of scanning coils in the objective lens. An electronic interaction occurs as electrons hit the sample material, transferring their energy to other atomic electrons within an interaction volume known as the teardrop-shaped volume. This interaction between the electron probe and the sample gives rise to emission of electrons (secondary, backscattered and Auger electrons) and electromagnetic radiation (X-rays) which can be detected using various detectors. The secondary electron (SE) and backscattered electrons (BSE) are used to image the sample and the x-rays and Auger electrons are normally used for qualitative and quantitative spectroscopy.

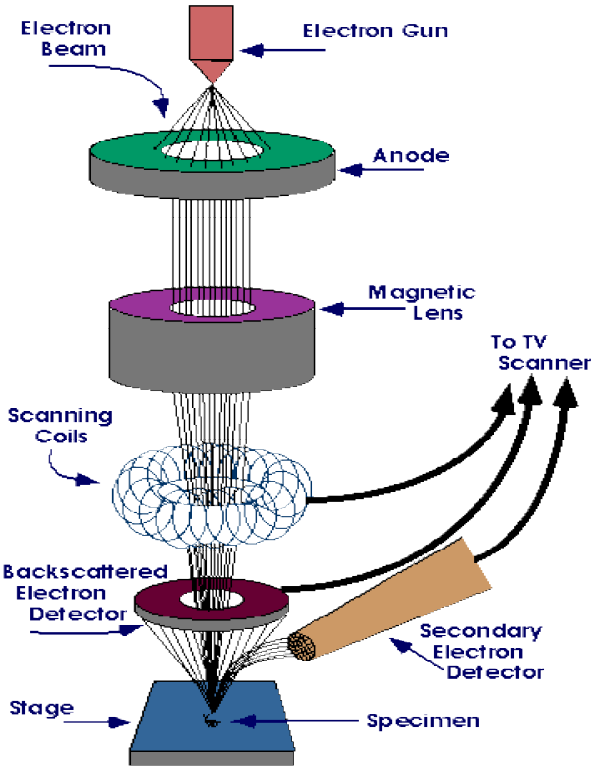

Figure 3.4 Schematic diagram of Field Emission scanning electron microscope (FETEM)[70].

3.3.1.3 Energy dispersive X-rays spectroscopy

Energy dispersive X-ray spectroscopy (EDS or EDX) is a powerful analytical technique that is commonly attached to SEM or TEM columns. It identifies the elemental composition or the chemical characterization of materials with a sensitivity of >0.1% for elements heavier than C from an area as small as several hundred of nanometres of the sold under investigation[55].

The principle of EDS is based on sample bombardment by an electron probe in either an SEM or TEM columns, in which electrons are expelled from the inner shell leaving vacancies behind. Successively electrons from outer shells fall into the lower vacant level by conceding a specific amount of their energy to occupy the vacant gaps in the inner shell. Finally, the excessive conceded energy is emitted either as a form of X-ray (equivalent to energy difference between the two electrons' state), or as electron, if the energy is transmitted to an electron from either the same shell or a higher energy one;

referred to as the Auger electron. The X-ray (or Auger electron) energy is characteristic of the element from which it was emitted.

Energy-dispersive spectrometry is employed to detect the X-ray photons energies. As an X-ray photon hit the lithium drifted silicon detector, Si (Li), it creates electron-hole pairs which is amplified by a sensitive preamplifier located close to the detector, resulting in pulses proportional in height to the X-ray energy. The pulses are counted and analysed through a multichannel analyser and displayed as a function of energy.

3.3.1.4 Transmission electron microscopy (TEM)

The transmission electron microscope (TEM) is a powerful instrument for detailed information about the structure of nanomaterials and its column is somewhat arranged similarly as a light microscope but using electrons as a source of illumination instead of light. Since the electrons' wavelength is dependent on their velocity, emitted electrons from an electron source are accelerated via a potential difference of 100-200 kV with reduced wavelength of few pico-meters ($\lambda \approx$ 0.002 nm). This allow them to easily penetrate through a thin sample and diffracted by the sample's atomic planes forming therefore a transmission electron diffraction patterns which then can be focused to be imaged[71].

Ultra-high resolution is easily achieved as at higher energies (velocities), the wavelength is even smaller and in most electron microscopes the wavelength of the electrons is about 10,000 times smaller than that of visible light.

The basic structure of the TEM consists of an electron gun at the top of the microscope with an electron emitter, which can be either a thermionic source or a field emission source. The TEM uses a series of electromagnetic lenses above and under the sample (first condenser lens, second condenser lens, objective lens, first intermediate lens, second intermediate lens and projector lens) as figure 3.5 shows. This is to focus electrons into a very fine probe which travels through the sample under investigation and generate the beam signals to the detector. Depending on the density of the material, some electrons will transmit (penetrate) through the sample and some scatter and as a result of this interaction the un-scattered electrons hit a fluorescence screen which gives rise to a "shadow image" of the sample that is finally captured by CCD camera.

TEM is a complementary tool to conventional crystallographic methods such as x-ray diffraction. A crystalline material interacts with the electron beam mostly by diffraction rather than absorption. If the planes of atoms in crystal are aligned at certain angles to the electron beam, the beam is transmitted strongly while at other angles the beam is diffracted. For TEM study presented in this thesis, a JEOL 2011F with LaB_6 therionic was used.

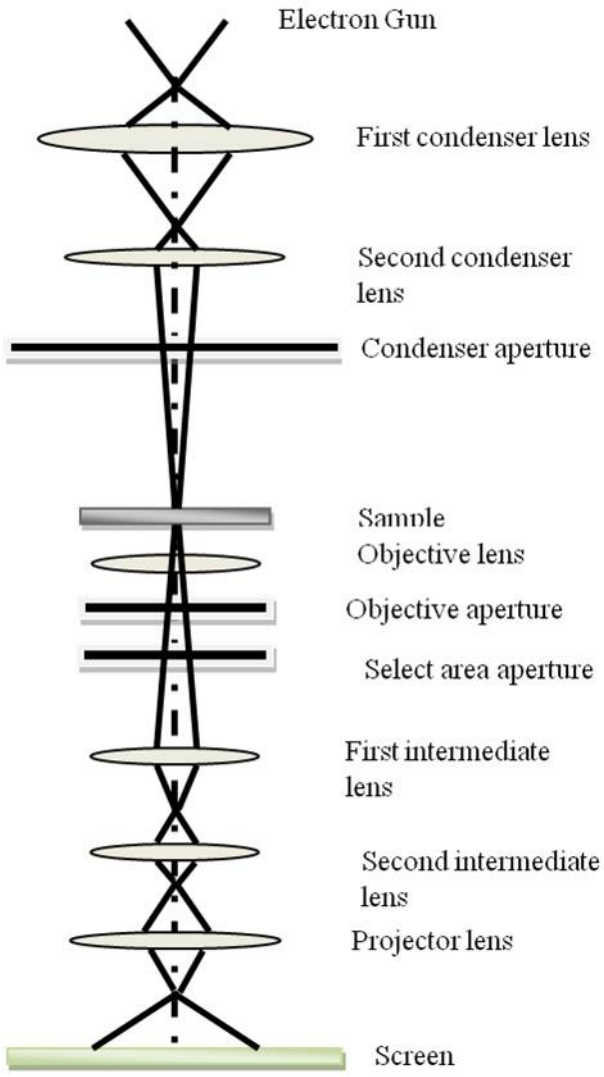

Figure 3.5 Schematic diagram of transmission electron microscope (TEM).

3.3.2 Optical characterization techniques

3.3.2.1 Room-temperature photoluminescence spectroscopy

The optical properties of ZnO nanostructures, reported in this work were investigated by photoluminescence (PL) spectroscopy. Photoluminescence (PL) is defined as the spontaneous emission of light from a material under optical excitation. An inherited limitation of PL analysis is its reliance on radiative events. Materials with poor radiative efficiency, such as low-quality indirect band gap semiconductors, are difficult to study via ordinary PL.

As light of sufficient energy is incident on a material, photons are absorbed and electronic excitations are created. Eventually, these excitations relax and the electrons return to the ground state. If radiative relaxation occurs, the emitted light is called PL. Room temperature PL spectra of ZnO typically consist of an ultra violet (UV) emission and possibly one or more visible bands due to defects and /or impurities in the sample being studied. The UV emission generally originate from the direct recombination of free excitons through an exciton-exciton collision process and this is called near band edge emission (NBE) while the appearance of the visible emission also known as deep level emission is due to the impurities and structural defects (oxygen vacancies and zinc interstitials) in the case of ZnO crystals. Green emission is the most commonly observed defect emission in the ZnO nanostructures. Regarding the origination of green emission, several different hypotheses are proposed[72]. But the commonly cited mechanism regarding the green emission suggests that intrinsic defects, especially oxygen vacancies, play a key role for this emission and also emission generated by the recombination of electrons in singly occupied oxygen vacancies with photo-excited holes in the valance band.

The photoluminescence (PL) measurements of ZnO nanostructures presented in this report were measured using a He-Cd laser line of 325 nm as excitation source with the excitation power of 30 mW at room temperature.

3.3.2.2 Raman-scattering spectroscopy

Unlike most other chemical analysis techniques, Raman spectroscopy exhibits high specificity requires no special sample preparation, and short experimental timescale. Raman spectroscopy is based on the Raman effect, which is the inelastic scattering of photons by molecules[73]. The difference in energy between the incident photon and the Raman scattered photon is equal to the energy of vibration of the scattering molecule. The Raman Effect occurs due to change in vibrational, rotational or electronic energy when light impinges upon a molecule and interacts with the electron cloud of the bonds (electric dipole) of that molecule, in other words the Raman bands arise from a change in the polarizability. The vibrational energy is ultimately dissipated as heat. Because of the low intensity of Raman scattering, the heat dissipation does not cause a measurable temperature rise in a material. Since vibrational information is very specific to chemical bonds, Raman spectra are considered fingerprints by which molecules can be identified. A Raman spectrum is a plot of the intensity of Raman scattered radiation as a function of its frequency difference from the incident radiation (usually in units of wave numbers, cm^{-1}). This difference is called the Raman shift[73,74].

A typical Raman spectrometer consists of four basic components: firstly, the excitation source (laser source). In order to achieve a coherent beam of monochromatic light, a laser source, which must exhibit decent wavelength stability and low background emission, is utilised to generate the Raman spectra. The second component is a collection probe device, which collects the scattered photons, filters out the Rayleigh scatter and any background signal from the fibre optic cables to be sent through interference filter or spectrophotometer. Finally, the intensity of the Raman signals at each wavelength is captured by a detector.

The Raman measurements presented in this work were measured at room-temperature with Ar^+ laser line of 514.5 nm as the excitation source.

3.4 Field emission measurements system

3.4.1 Vacuum system layout

Since the field emitters are vacuum nano/microelectronics devices, it is essential to be operated under vacuum conditions. A system that can obtain high vacuum is necessary in order to prevent the arc between the anode and the cathode that might cause damage to the nanoemitters.

In order to investigate the field emission properties of the ZnO nanostructures, a system consists of a stainless steel vacuum chamber with two pumps (turbo and rotary pumps) and baking unit has been used. The rotary is used to pump the system down to bring the pressure up to 10^{-3} mbar and then the turbo pump is used to get high vacuum in the order of $1x10^{-8}$ mbar. An ion gauge and pirani gauge are used to measure the pressure in the stainless steel vacuum chamber and the backing line respectively. The vacuum chamber is normally baked out at 180ºC over 24 hrs to improve the vacuum and, i.e. To achieve ultra high vacuum (UHV) conditions, the chamber then is allowed some time to cool down up to room temperature naturally.

The field emission pattern is observed and imaged using a digital camera through a glass window fixed on the front side of the vacuum chamber.

The field emission measurements were performed using a manually controlled high voltage power supply unit for creating a high electric field between the anode and the cathode and a picoammeter to measure the current emission. The emission current stability measurements were recorded with respect to the time for different times under different fixed anode voltages. A national instruments card connected parallel with a 10 MΩ resistor was used to interface to a PC. The data acquisition was carried out using "Labview" software supplied by YPS Ltd.

3.4.2 Design of the sample holder and the field emission experimental setup

The field emission property of ZnO nanostructures is measured using a triode configuration in order to achieve a relatively low control voltage. The sample holder consists of several components as shown in figure 3.7. A flat stainless steel plate is placed in the centre of a U shaped peek and hold together through two screws from sides. The sample is mounted on the stainless steel plate using silver paste and kept at negative potential. A grid is placed on the U shaped peek base and kept at ground potential to be used as extractor. An Yttrium Aluminium Garnet (YAG) is used as

viewing screen and kept at positive potential. The YAG screen is separated from the extractor using peek sheet spacer with a thickness of about 1mm

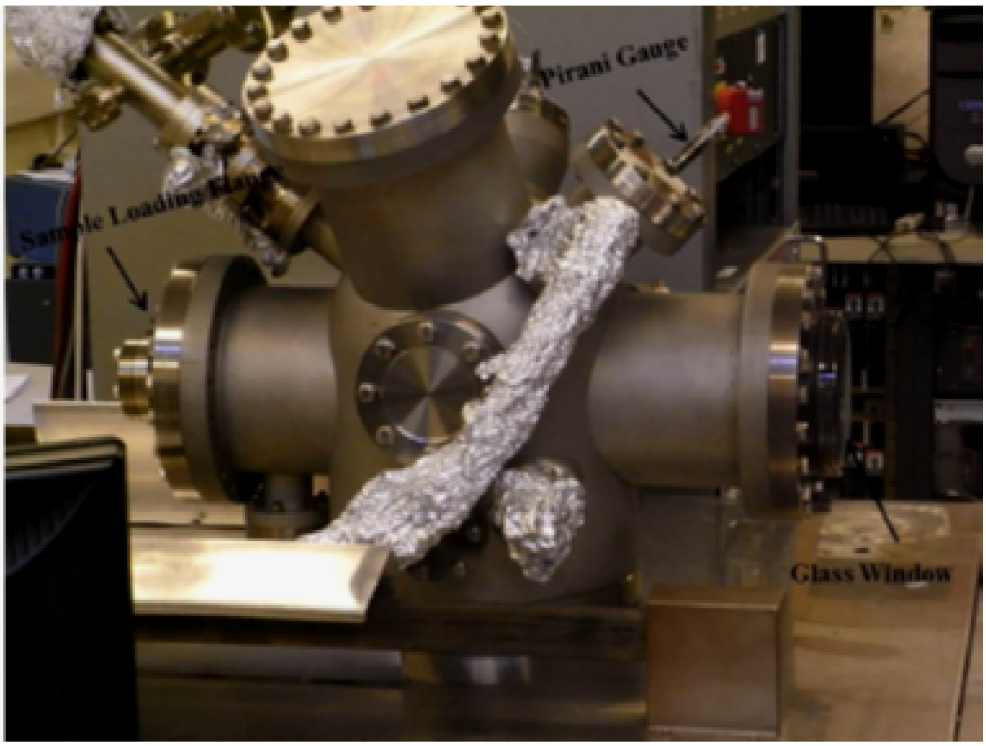

Figure 3.6 A photograph of the Renta-Port system used for the field emission experiments.

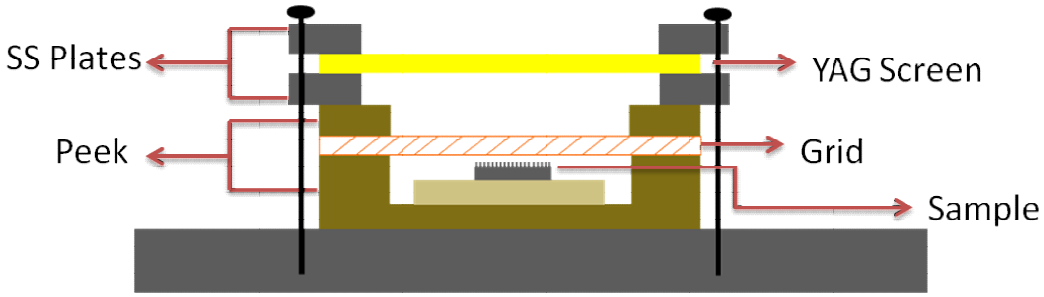

Figure 3.7 Schematic of the triode configuration stage for field emission.

3.5 Conclusion

A brief description of the experimental apparatus and basic concepts of the synthesis techniques were introduced. Particularly, factors that influence the performance of the growth were described in this chapter, which are vital for Chapters 4-8. Since the scope of this study also revolves around improving the field emission performance of the ZnO nanostructures, it was equally important to briefly describe the characterization techniques to help interpreting the experimental results.

CHAPTER4

ZnO NANOSHEETS INTERCONNECTS: GROWTH, CHARACTERIZATIONS AND FIELD EMISSION PROPERTIES

4.1 Introduction

Due to its physical and chemical properties that can be utilized in several applications, the II-VI group semiconductor zinc oxide (ZnO) with the wurtzite hexagonal structure is regarded as one of the most multifunctional materials amongst various metal oxides. For instance, it's exotic property of wurtzite (B4) crystal structure which is the most stable and thus most common under ambient conditions. Moreover, its large-exciton binding energy of 60 meV exceeds that of other predominant semiconductor materials such as ZnSe and GaN.

In addition, the wide band gap as well as high-exciton energy of ZnO allows it to be utilized in room temperature ultraviolet laser diodes[75-77]. Also, the ZnO exhibits various attractive properties; unique piezoelectric and pyroelectric properties, high mechanical strength, chemical and thermal stability, biocompatibility, low-cost, easy fabrication, non-toxic to name but a few.

Nonetheless, the preference of ZnO in a wide variety of high-technological applications is attributable to its aforementioned characteristics. To name some of these applications; light emitting diodes, photo-detectors, piezoelectric transducers and actuators, piezoelectric generators, hydrogen storage, chemical and biosensors, surface acoustic wave guides, solar cells, photo catalysts, field emission devices and so forth[78-85].

Various techniques have been implemented to synthesize 1D, 2D and 3D ZnO nanostructure, such as hydrothermal process, solution process, thermal evaporation process, sol-gel process, PLD process, electrochemical deposition process, MOCVD process and so on[75-99]. The dimensional forms of these structures is defined in the introduction chapter section (1.1) in which examples of nanowires, nanotubes, nanorods, are deemed 1D, whereas, nanosheets are 2D. However, among several morphologies of ZnO, the 2D sheet-like nanostructures exhibited distinct physical properties compared to the 1D nanomaterials. Normally, the nanosheets possess higher surface area (if the thickness is in nanometers) compared to nanowires and hence

demonstrating better performance for some of the promising applicatons such as catalysis, chemical, bio and gas sensors, Li-ion batteries, solar cells, and so on[75]. As a result, the sheet-like nanostructure is regarded to be a promising potential candidate for several applications such as sensing, energy storage, solar cells, field emission, catalysis and photo-catalysis and so on. Several reported studies discussed the growth and the properties of crystalline ZnO nanosheets, some of which a micrometer-sized nanosheets were grown by reduction of ZnS powders[92].

Whereas Umar *et al*. fruitfully utilized the thermal evaporation technique with $ZnCl_2$ and O_2, to grow well-crystalline ZnO nanosheets and nanodisks[93]. Recently and for the fabrication of dye-sensitized solar cells, Heniti *et al*. demonstrated the growth of nanocrystalline ZnO nanoflakes by solution process with the as-synthesized nanoflakes being the anode of dye-sensitized solar cells[94]. Lao *et al*. reported grown ZnO nano-walls also by thermal evaporation onto Au-coated sapphire substrate[95]. Although, the above methods are commonly dedicated to growth, their results, on the other hand vary in terms of simplicity, purity well-crystalline repeatability, high throughput and cost effectiveness.

This chapter is divided into two parts, where firstly reports a simple and cost-effective growth of nanocrystalline thin ZnO nanosheets interconnects on zinc foil via hydrothermal process. In addition, the growth mechanism of ZnO nanosheets interconnects is discussed and analysed in section 4.3 this involved using zinc chloride, hexamethylenetetramine (HMTA) and ammonium hydroxide at low-temperature.

On the second part, the morphological, structural, optical and field emission properties of the as-synthesized nanostructures were characterized and then the annealing effect on the morphologies of as-synthesized ZnO nanosheet interconnects was also investigated.

4.2 Experimental work

4.2.1 Synthesis of nanocrystalline thin ZnO nanosheets interconnects on zinc foil

Nanocrystalline thin ZnO nanosheet interconnects on zinc foil were synthesized at low-temperature by simple and facile hydrothermal process. For the synthesis of nanosheet interconnects, zinc chloride ($ZnCl_2.2H_2O$; **≥98%**), hexamethylenetetramine (HMTA; $C_6H_{12}N_4$; **≥99%**) and ammonium hydroxide (NH_4OH; 28.0-30.0% NH_3 basis) were provided by Sigma-Aldrich and used as received without any further purifications.

In a typical reaction process, particular concentrations of zinc chloride (0.1 M), HMTA (0.1 M) and ammonium hydroxide (0.01 M) were thoroughly mixed in 100 mL de-ionized (DI) water under continuous stirring for 10 minutes. The resultant solution was transferred to a Teflon-lined stainless steel autoclave. The ZnO nanostructures were deposited on Zinc foils substrate of 1 x 1 cm^2 as the foil had been ultrasonically cleaned in DI water, ethyl alcohol and acetone, then dried with nitrogen gas and finally immersed into the resultant solution. The autoclave was tightly sealed and heated up to 110°C for 12 hrs, to allow the reaction to be terminated and then the autoclave was naturally cooled down to room-temperature. The substrates were removed from the aqueous solution which were gently rinsed with DI water and dried overnight at 35°C. White colored products deposited over the substrates were observed which were characterized in detail in terms of their morphological, structural and optical properties. A concise summary of the growth parameters of ZnO nanosheet interconnects are presented in table 4.1.

Nanomateial Type	ZnO nanosheet Interconnects
Growth Technique	Hydrothermal growth process
Reactants	Zinc Chloride, hexamethylenetetramine (HMTA) and ammonium hydroxide
Substrate	Zinc foil substrate
Reaction Temperature	110°C
Reaction Time	12 hrs

Table 4.1 Summary of the growth parameters of ZnO nanosheet interconnects.

4.2.2 Characterization of nanocrystalline thin ZnO nanosheet interconnects on zinc foil

Detailed morphological, structural as well as optical characterizations of the grown ZnO nanostructures on zinc foil were carried out.

The morphologies were imaged by the field emission scanning electron microscopy (FESEM) and transmission electron microscope (TEM). The crystallinity and crystal orientations of the grown ZnO nanostructures were examined by X-ray diffraction (XRD) pattern measured with Cu-Kα radiations (λ=1.54056 Å) and 2θ at a range of 10° to 60° with scanning rate of 2°/sec.

Room-temperature photoluminescence (PL) spectroscopy, measured with He-Cd laser line (325nm) as the exciton sources, was carried out to investigate the optical properties of synthesized nanostructures. Raman-scattering spectroscopy technique with Ar^+ laser line (513.4 nm) was implemented to study the scattering properties at room-temperature. Finally, the field emission properties of the as grown nanosheets were investigated.

4.3 Results and discussion

4.3.1 Morphological, structural and compositional properties of grown ZnO nanosheets interconnects

Being uniform and densely grown on the entire substrate surface, the ZnO structures appear to be formed in sheet-like morphologies. This was revealed by the low-magnification FESEM images as figures 4.1 (a) and (b) show.

The nanosheets are randomly distributed in partially aligned manner and interconnected with each other, forming a network like structures. For this reason, from now on it will be referred at, as ‘the nanosheet interconnects’.

A physical penetration between some of the adjacent nanosheets was also observed. This formed a specific shaped triangular trench. The average size of the grown nanosheets is ≈3–4 μm, however some smaller were also observed as (figures 4.1 (c) and (d) show. The nanosheets thickness is ≈ 60-70 nm hence exhibiting higher surface area for the grown structures (inset figure 4.1 (d)).

The flower-shaped structures composed of thin ZnO nanosheets which are grown at the edge vicinity of the substrate are shown in figure 4.2. These striking-looking blended mixtures of nanostructures appear to be densely grown and arranged themselves around the vicinity of the substrate's edge forming flower-shaped morphologies.

It is predicted that the nanosheets are mingled and agglomerated due to the long range electrostatic interactions among the polar charges of the {0001} planes of ZnO[93]. The typical dimensions of each nanosheet petals of flower-shaped structure are ≈ 2-4 μm while the thickness is ≈50-70 nm. However, the full array of flower-shaped structures is in the range of 3-4 μm.

To examine the crystallinity and crystal phases of as-grown thin ZnO nanosheet interconnects, X-ray diffraction technique was used and the result is demonstrated in figure 4.3 (a). The observed XRD pattern exhibits well-crystalline nature and mixed phases of ZnO and Zn. Various well-defined XRD reflections related with ZnO (1010), (0002), (1011), (1012) and (1120) were observed in the pattern which are similar to bulk ZnO and correspond to wurtzite hexagonal phase of ZnO and show good agreement with the standard JCPDS data card No 36-1451. In addition to presence of ZnO, few reflections related with Zn (100), (101), (102) were also observed in the obtained pattern data. The Zn reflections were justified due to the presence of zinc foil substrates. Interestingly, it was seen that two diffraction reflections, i.e. (0002) and (1011) are dominant reflections compared to any other observed ZnO reflections in the XRD pattern which revealed that the prepared nanosheets are grown in two crystal planes. The lattice parameters of ZnO nanosheets were also calculated from the XRD peaks (0002) and 1011) using the formula for a hexagonal crystal structure (see equation 3.2) and were found to be a=0.324 nm and c=0.52 nm. Moreover, the crystallite size for the dominant peak of the XRD pattern representing the (1011) plane in figure 4.3(a) was calculated using the well known scherrer's formula given by equation 4.1[94] and found to be 33.3 nm.

$$D = \frac{0.9\lambda}{\beta(rad)cos\theta} \tag{4.1}$$

where D is the crystallite size, λ the wavelength of X-rays used, $ß$ the full width of diffraction peak at its half maximum intensity (FWHM) in radians and θ the angle of

diffraction. More essentially, the origination of sharp and strong XRD reflections, confirms that the grown nanosheet interconnects are well-crystalline.

To further identify the composition of as-grown ZnO nanosheet interconnects, point EDS analysis was carried out and the result is demonstrated in figure 4.3 (b). Only zinc and oxygen peaks were observed in the obtained EDS spectrum which clearly reflects that the synthesized materials are made of zinc and oxygen. In line with the detection limit of EDS technique, no other peaks that can be related to impurities than the Zn and O peak were observed. This further confirms that the synthesized nanosheet interconnects are made of zinc and oxygen.

The detailed structural characterizations of as-synthesized ZnO nanosheet interconnects were examined by TEM. To prepare the specimen for the TEM measurements, the as-grown ZnO nanosheet interconnects on zinc foil was ultrasonically treated in acetone for 5 min, and then it was detached from the zinc substrate and mixed with the acetone. A drop of acetone which contains the ZnO nanosheets was dried on a TEM grid to be examined. Figure 4.4 (a) shows the low-magnification TEM image of the fragment of ZnO nanosheet dispersed from the substrate. The obtained nanosheet morphology is random due to the ultrasonic fracture.

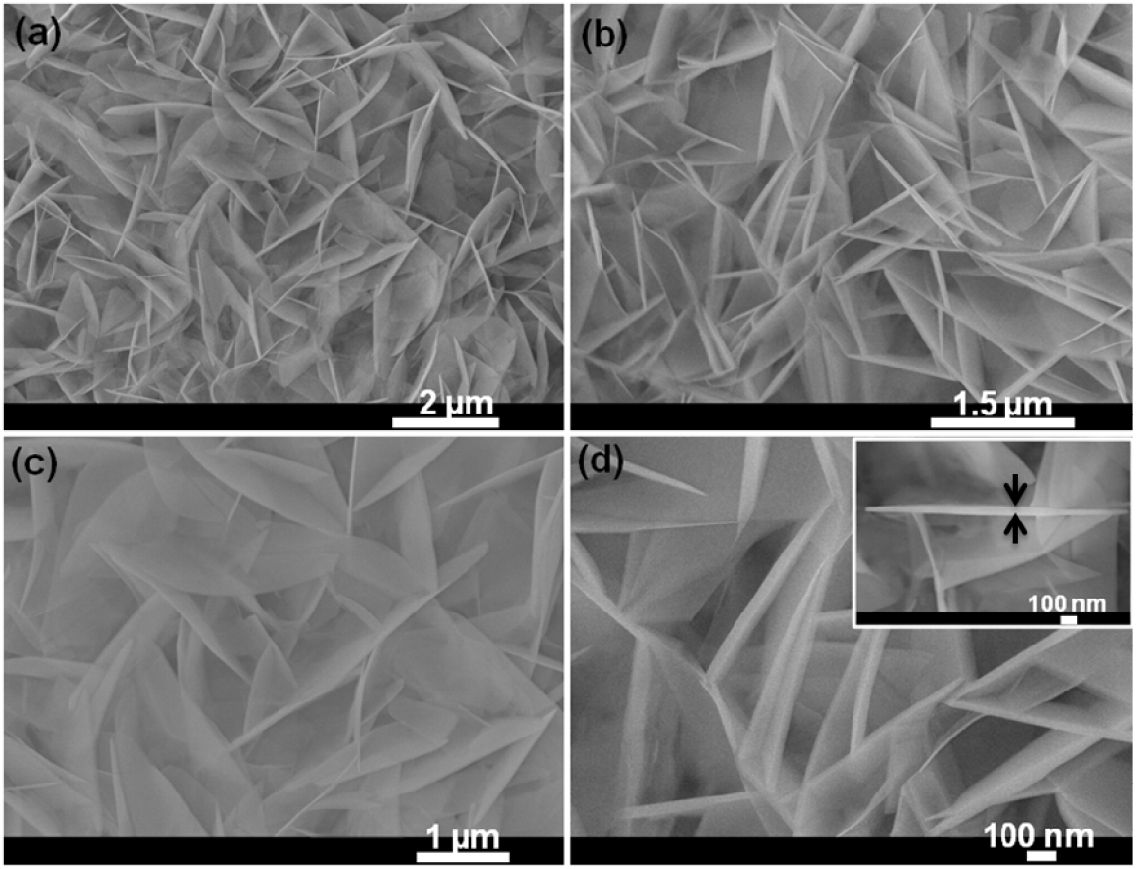

Figure 4.1 Typical (a and b) low-magnification, and (c and d) high-resolution FESEM images of the as-grown thin ZnO nanosheet interconnects on zinc foil grown at 110ºC.

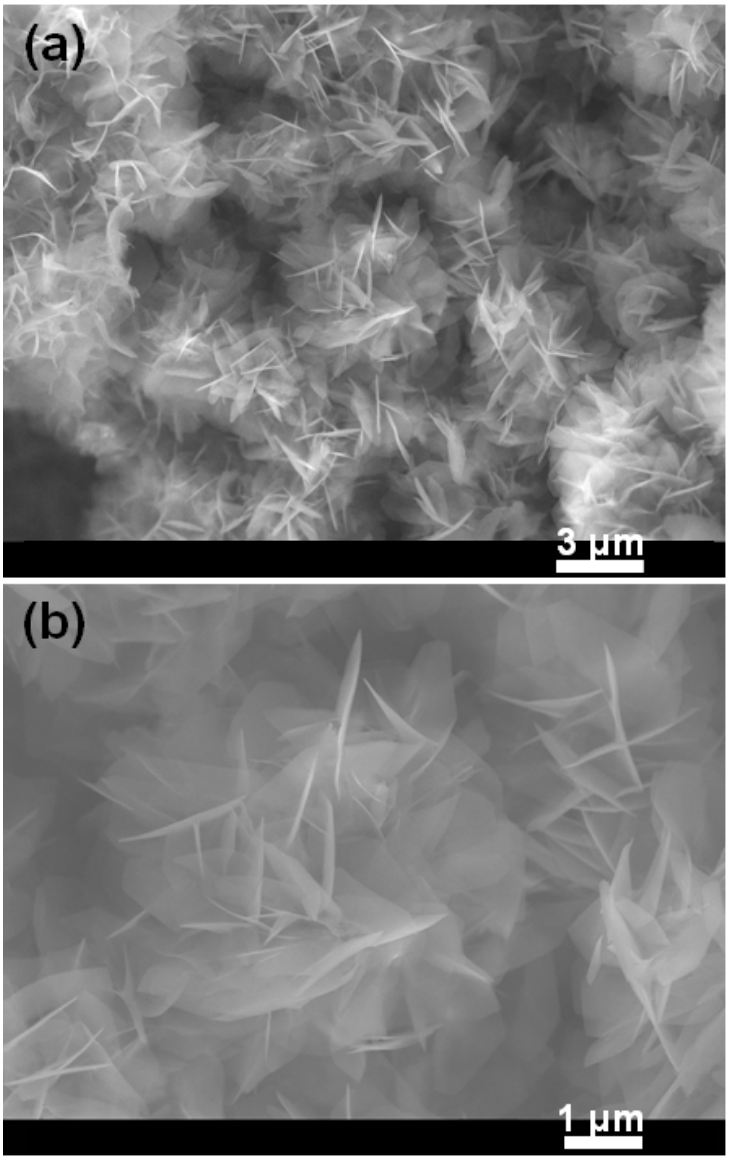

Figure 4.2 Low (a) and high (b) magnification FESEM images of flower-shaped structures composed of thin ZnO nanosheets, obtained from the edge portion of the zinc foil substrate grown at 110ºC.

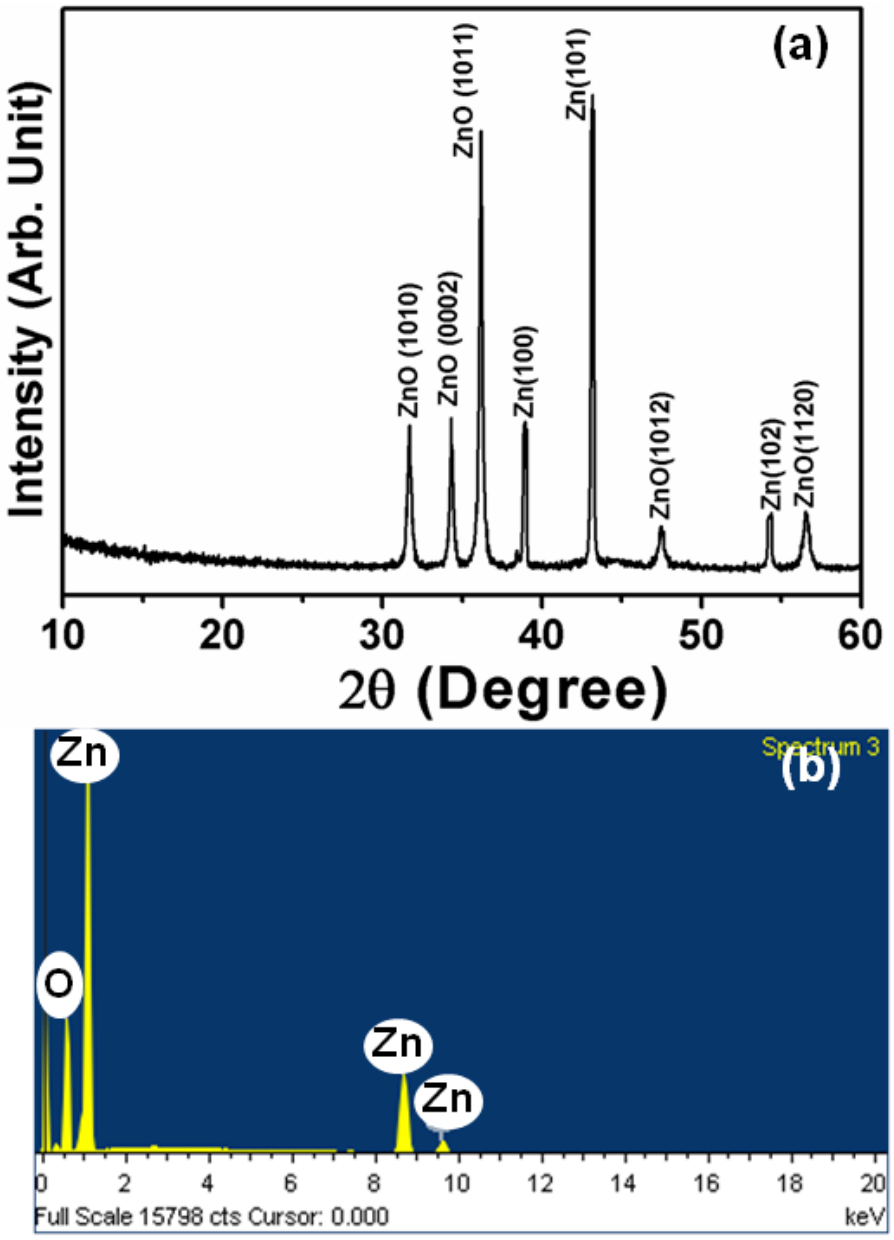

Figure 4.3 Typical (a) XRD pattern and (b) EDS spectrum of thin ZnO nanosheet interconnects grown on zinc foil at 110ºC.

The grown nanosheets are well-crystalline as confirmed by HRTEM observation. Figures 4.4 (a) and (b) show the typical HRTEM image of circled portion of ZnO nanosheet. The HRTEM image (b) shows well-defined lattice fringes with an interplanar distance of 0.28 nm, which is in agreement with the interspacing of the $\{10\bar{1}0\}$ planes. These observations confirmed the 2D sheet-like morphology formed with {0001} exposed surfaces[95].

To examine the effect of annealing on the morphologies of the as-synthesized ZnO nanosheet interconnects, the as-prepared samples were annealed at 200°C. Figures 4.5 (a) and (b) are low-magnification images of the annealed sample, in which the nanosheets are grown in very high density and randomly arranged manner covering most of the substrate surface. This observation is consistent with the observed FESEM images of the as-grown ZnO nanosheet interconnects and confirms that the morphological structure remains intact as well as hardly encounters only a minor structural alteration. In addition to some nanosheets being fractured, it is realized that by annealing, two or more adjacent nanosheets encountered a surface engagement with each other by retaining the parent morphologies as figure 4.5 (c) shows. The typical dimensions of the annealed nanosheets are in the range of 2–3 μm, with the thickness of≈ 60 nm as figures 4.5 (c) and (d) show.

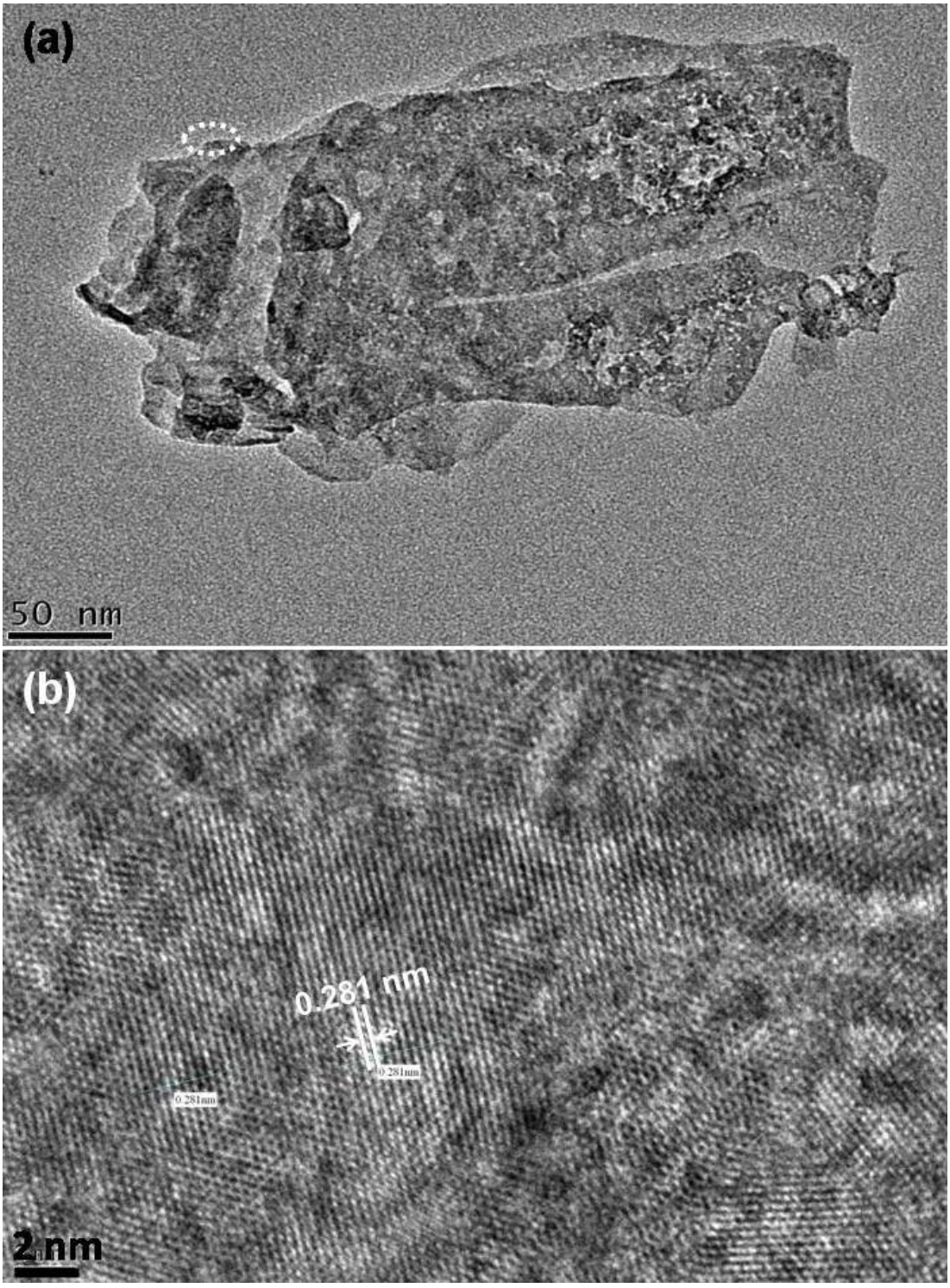

Figure 4.4 Typical (a) Low-magnification and (b) high-resolution TEM images of as-grown thin ZnO nanosheet interconnects grown on zinc foil at 110ºC.

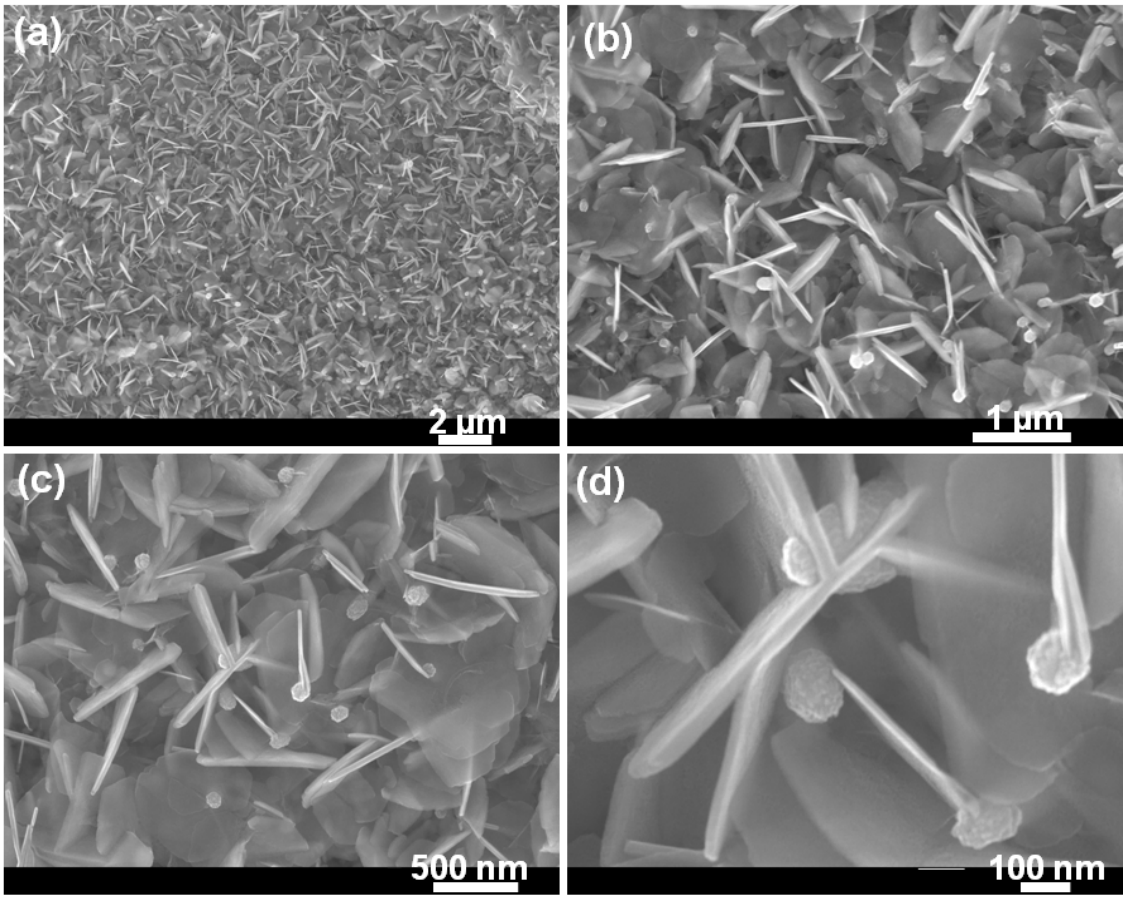

Figure 4.5 Typical (a and b) low-magnification, and (c and d) high-resolution FESEM images of the 200 ºC annealed thin ZnO nanosheet interconnects grown on zinc foil at 110ºC.

4.3.2 Room-temperature photoluminescence (PL) properties of grown ZnO nanosheets interconnects

The optical properties of the as-grown thin ZnO nanosheet interconnects were investigated by using room-temperature photoluminescence spectroscopy and the result is shown in figure 4.6. Generally, two peaks have appeared in the room-temperature PL spectrum of ZnO nanostructures; i.e. in the UV region and visible region. The UV-region peak is known as near band edge emission (NBE) and originated due to the recombination of the free-excitons through an exciton-exciton collision process. The origination of the visible-region peak, which is known as either the green emission peak or the deep level emission (DLE), is somehow controversial. However, the most agreed upon cited explanation for its origin in the spectrum is due to radial recombination of the photo-generated hole with the electrons which belongs to oxygen vacancies[98]. In the case of ZnO nanosheet interconnects, the PL spectrum exhibits a strong and sharp UV emission at 381 nm and a suppressed and broad green emission at 525nm. These were reported as being indicative of good crystal quality, less structural defects (such as less oxygen vacancies and zinc interstitials) and low impurities in the synthesized nanostructures[87,89,99]. In addition to this, the calculated NBE/DPE intensity ratio is ~5.36. Therefore, it can be concluded that the synthesized ZnO nanostructures possess good crystal quality and exhibits very less structural defects.

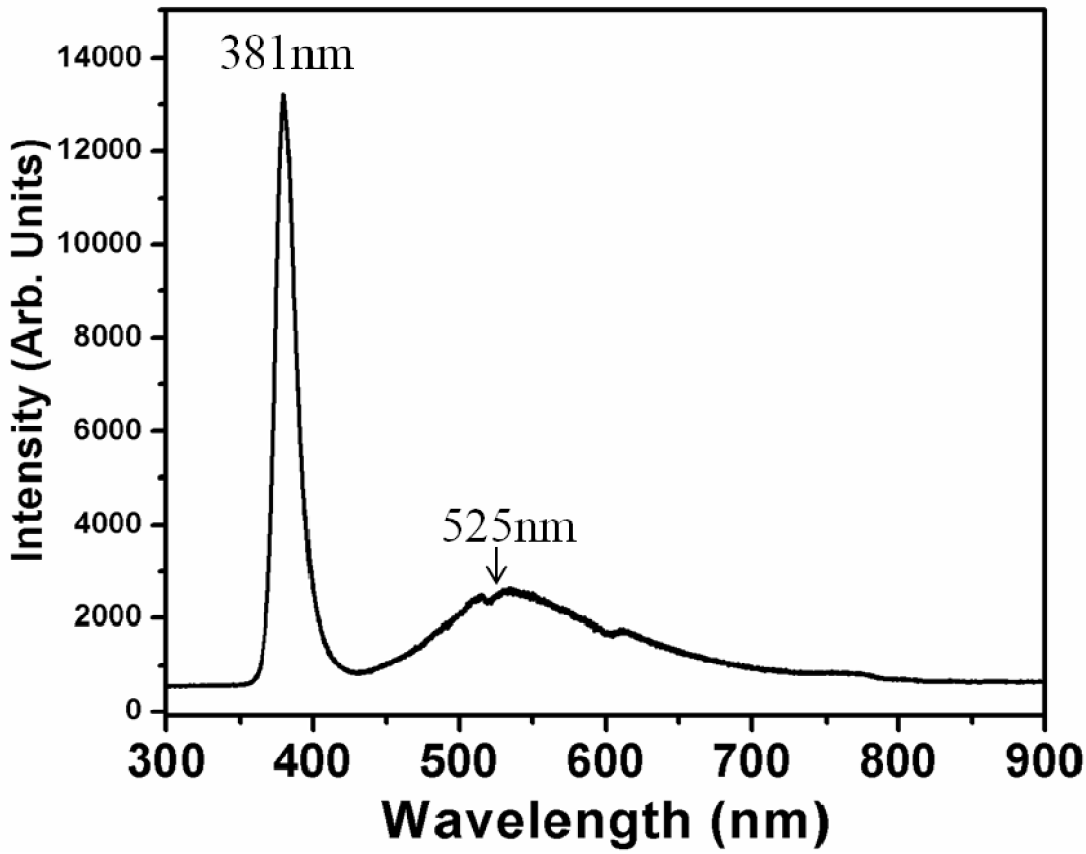

Figure 4.6 Typical room-temperature photoluminescence (PL) spectrum of thin ZnO nanosheet interconnects grown on zinc foil at 110ºC. A strong UV emission with a suppressed green emission confirmed the well-crystallinity of the prepared ZnO nanosheets interconnects.

4.3.3 Room-temperature Raman-scattering properties of as-grown thin ZnO nanosheets interconnects

To investigate the vibrational properties of as-synthesized ZnO nanosheet interconnects, Raman-scattering measurements were carried out at room temperature. Figure 4.7 shows the typical room-temperature Raman-scattering spectrum of as-grown ZnO nanosheet interconnects on zinc foil in which few well-defined bands were observed. The presence of a strong and dominated band at 437 cm^{-1} is attributed to the Raman-active non-polar optical phonon E_2 (high) mode, a significant band for the wurtzite hexagonal phase of pure ZnO[89].

In addition to the optical phonon E_2 (high) mode, two small bands appeared at 332 cm^{-1} and 378 cm^{-1} that are assigned as E_{2H}-E_{2L} (multi-phonon process) and A_1T

modes, respectively[89]. Furthermore, a broad band at 535 cm^{-1} is also observed in the spectrum which could be identified as E_{1L} mode. Such mode is believed to appear in the spectrum due to the presence of structural defects and impurities of the grown nanostructures. In summary, the presence of the sharp and strong E_2 (high) mode as well as the suppressed and broad E_{1L} mode in the Raman-scattering spectrum confirms that the grown nanosheets are of good crystal quality and less structural defects and impurities. This is also in agreement with the PL results.

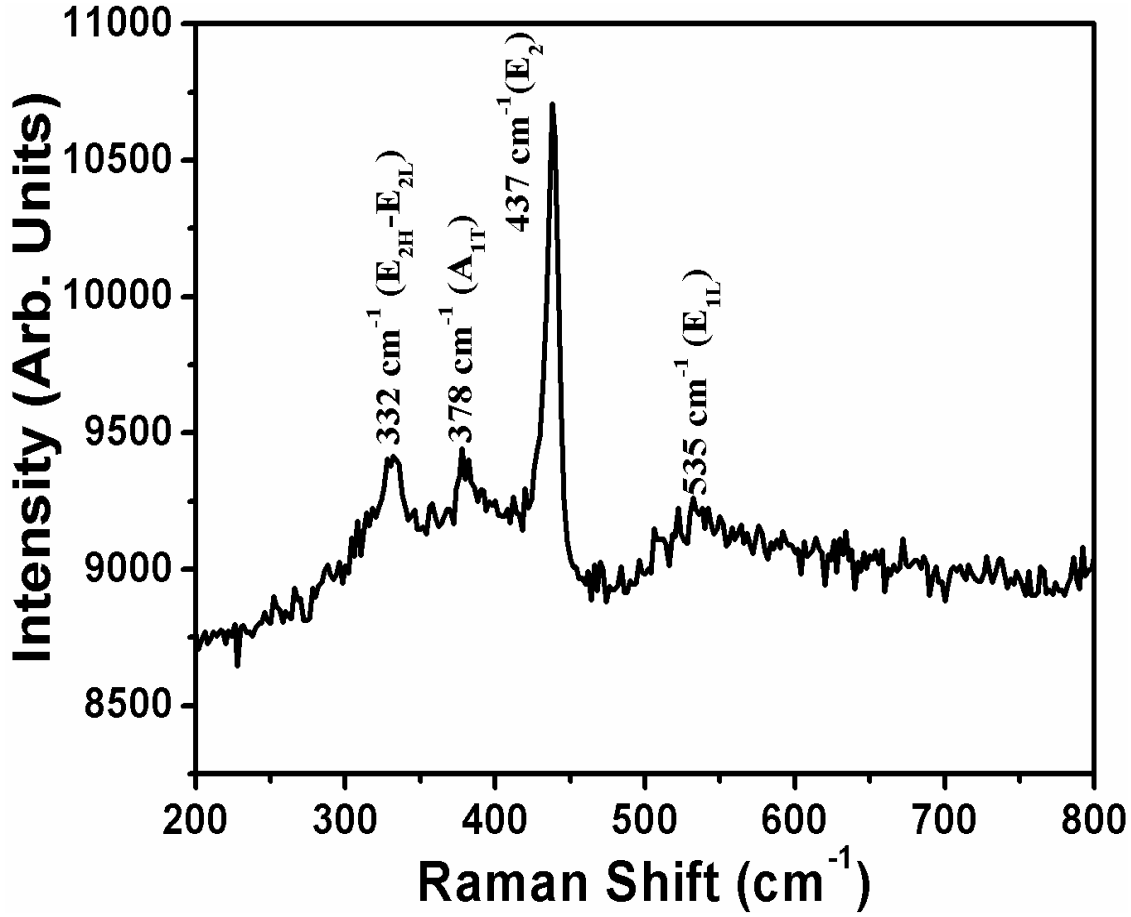

Figure 4.7 Typical room-temperature Raman-scattering spectrum of thin ZnO nanosheet interconnects grown on zinc foil at 110ºC showing a strong E_2 peak and a suppressed E_{1L} which are indicative of a good quality crystal.

4.3.4 Plausible growth mechanism for as-grown thin ZnO nanosheets interconnects

The growth of as-grown thin ZnO nanosheet interconnects can be understood by the chemical reactions involved and the crystal growth habits of ZnO. Figure 4.8 shows the schematic mechanism for the formation of ZnO nanosheet interconnects on zinc foil. For the growth of ZnO nanosheets, a zinc foil was used as substrate (fig. 4.8(a)). Initially, the cleaned zinc foil was dipped in a well-mixed 100 mL solution of zinc chloride, HMTA and ammonium hydroxide.

During the reaction, the $ZnCl_2$ was initially dissociated to Zn^{2+} and Cl^- while ammonium hydroxide (NH_4OH) was dissociated into NH_4^+ and OH^-. These components reacted with each other yielding $Zn(OH)_2$ and NH_4Cl according to the following chemical reaction:

$$\mathbf{ZnCl_2.\ 2H_2O\ (aq) + NH_4OH\ (aq) \longrightarrow Zn\ (OH)_2\ (s) + NH_4Cl\ (aq)} \qquad (4.2)$$

The HMTA was mainly used for two purposes, firstly to acts as a source for OH^- and secondly as an additive. At appropriate reaction temperature the HMTA dissociates according to the following chemical reaction:

$$\mathbf{(CH_2)_6N_4 + 6H_2O \longrightarrow 6HCHO + 4NH_3} \qquad (4.3)$$

$$\mathbf{NH_3 + H_2O \rightleftharpoons NH_4^+ + OH^-} \qquad (4.4)$$

These reactions breed the Zn^{2+} and OH^- ions as simplified in (fig.4.8(b)). Once the concentration of the Zn^{2+} and OH^- ions exceeds a critical value, the precipitation of $Zn(OH)_2$ nuclei starts (fig. 4.8(c)) according to chemical reaction:

$$\mathbf{Zn^{2+} + 2OH^- \longrightarrow Zn(OH)_2} \qquad (4.5)$$

The $Zn(OH)_2$ can be transformed into the ZnO seed nuclei according to the simple following reaction (fig. 4.8(d)):

$$\mathbf{Zn(OH)_2 \xrightarrow{110^\circ C} ZnO + H_2O} \qquad (4.6)$$

These formed ZnO seed nuclei are the building blocks for the formation of final ZnO products and hence the continuous formation of ZnO nuclei leading finally to the formation of ZnO nanosheets via facile hydrothermal process (fig. 4.8(e)). With prolonged reaction time, the branched of as-grown nanosheets on zinc foil started to mingle with each other and finally nanosheet networks were obtained.

In addition to the chemical reactions involved, the growth of nanosheet can also be well-understood by the crystal habits of ZnO. With the wurtzite hexagonal phase, the crystals of ZnO possess polar surfaces in which the zinc and oxygen atoms are tetrahedrally coordinated along the hexagonal axis. The ZnO crystals has Zn-terminated (0001) and O-terminated surfaces in which the Zn-terminated (0001) surfaces are catalytically active, while the O-terminated (000$\bar{1}$) surfaces are chemically inert[100,101]. It is reported that the morphologies of the ZnO nanostructures are greatly affected by growth velocities of the ZnO crystals in different directions. According to the crystal habits of ZnO, the growth velocities of ZnO crystals are [0001] > [01$\bar{1}$ $\bar{1}$] > [01$\bar{1}$0] > [01$\bar{1}$1] > [000$\bar{1}$] under hydrothermal conditions[101]. Therefore, the fastest growth in the ZnO crystals are along the [0001] direction (*c*-axis direction) which leads to the growth of 1D nanostructure. For the growth of ZnO nanosheets, it is assumed that under our experimental conditions, the growth was along two directions, i.e. {0001} and {10$\bar{1}$1} planes, hence two directional growth resulted the formation of sheet-like structures. This phenomenon is also confirmed by the observed XRD pattern in which the dominated diffraction reflections are (0002) and (1011). Thereofore, with increasing the reaction time, the growth of ZnO nanosheets increases effectively and eventually the nanosheets were mingled with each other, due to the long range electrostatic interactions among the polar charges of the {0001} planes of ZnO, in such as special way that they made the networks of grown nanosheets[93].

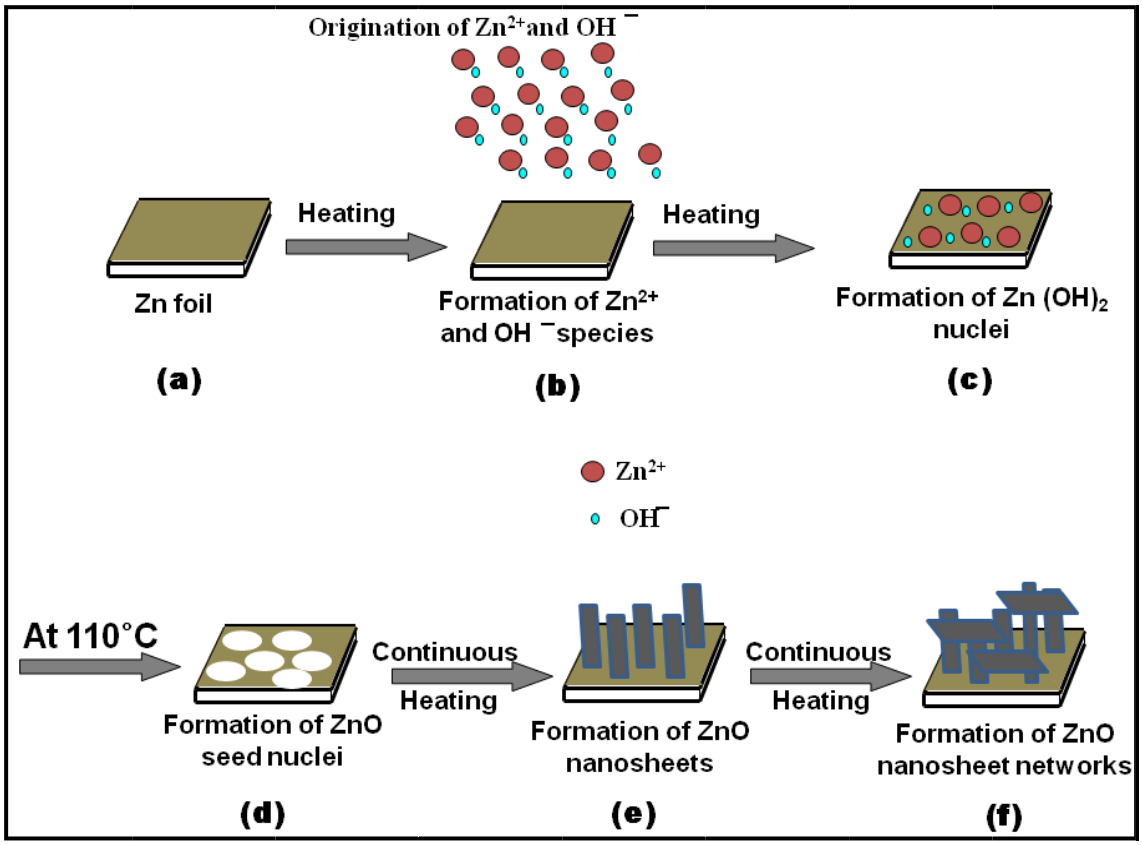

Figure 4.8 Plausible schematic for the growth mechanism for the synthesis of ZnO nanosheet interconnects grown on zinc foil at 110ºC.

4.3.5 Field emission studies

4.3.5.1 Current –voltage characteristic of ZnO nanosheets

The field emission measurements of ZnO nanosheet interconnects were performed under high vacuum environment of ≈ $3x10^{-8}$ mbar. The *I-V* characteristics were carried out from ZnO nanosheets grown on 25 mm^2 zinc foil substrate; however, the cathode surface area is not necessarily the effective emission area. Therefore, the emission current, not the current density, is shown and this due to ambiguity in the effective emission area. The experimental data of current-voltage curve of ZnO nanosheets were fitted using the Fowler-Nordheim equation (chapter 2, equation (2.25)) and shows the classic Fowler-Nordheim behaviour (see figure 4.9(a)). The turn-on voltage was set as the applied voltage that corresponds to an emission current of ≈ 0.1 μA. A turn-on voltage equal to 4600 volt which corresponds to an emission current of ≈ 0.12 μA was observed. The emission current reaches a maximum value of ≈ 2.08 μA under an applied voltage of 5500 volt. In this thesis, the applied voltage which corresponds to the maximum current emission is considered the threshold voltage (5500 volt; in this case). Any further voltage increase results in no extra emission gain, instead, voltage break-down occurred causing the power supply to trip off. An image of the field emission pattern at the break down voltage event (5800 volt) is shown in figure 4.11.

The relatively high turn-on voltage and low current emission of ZnO nanosheets emitters was attributed to the geometrical aspects as they are not designed to offer large field enhancement.

The corresponding F-N plot is shown in figure 4.9(b), in which the experimental data is represented by the plotted black dots and the straight line is the best linear fitting to the experimental data. The work function of ZnO nanosheets was assumed to be 5.3 eV[16]. The calculated field enhancement factor β was estimated to be 896.15. The obtained F-N plot is not an ideal straight line; however, there can be several causes of such linearity deviation. The first possible reason is that, the ZnO nanosheets emitters inherently suffer from relatively large and non-uniform emission areas that can vary some of the main F-N plots dependents such as the work function (Φ) and the enhancement factor (β)[102]. The variations in the local work function value which is inherently uncontrollable over large emission areas will affect the slopes in the F-N plot

and consequently produce nonlinearity. The other possible reason that may cause this deviation is the presence of the adsorbates which cause instability in the emission current and thus deviation from linearity in F-N plot[103].

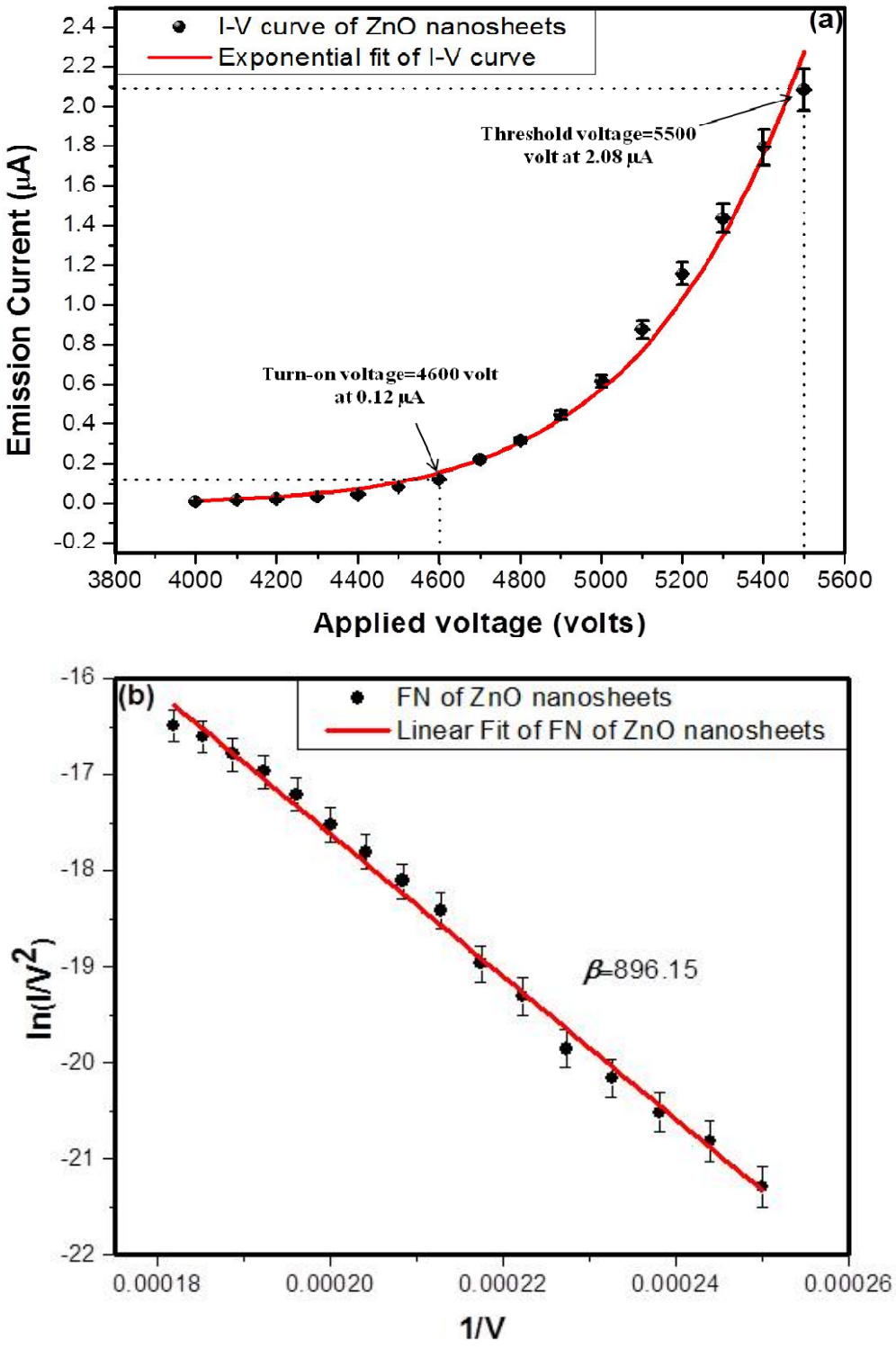

Figure 4.9 (a) The field emission electron *I-V* characteristic of ZnO nanosheets interconnects. (b) The corresponding F-N plot.

4.3.5.2 Current emission stability of ZnO nanosheets

The field emission stability of ZnO nanosheets interconnects was tested at base vacuum of $3x10^{-8}$ mbar.

Figure 4.10 shows, the behavior of the field emission current over a span time of 2 hrs at fixed extraction voltage of 4.6 kV. Initially and over the first 15 min, an emission current of an average of ≈130 nA with high fluctuation (116.9%) was recorded. In this thesis, the fluctuation is estimated as:

$$fluctuation = \left(\frac{I_{max} - I_{min}}{I_{av}}\right) \times 100 \quad (4.7)$$

The emission current severely surged to the maximum recoded value of > 230nA, combined with a dramatic fluctuation (≥ 50%) with an average of ≈ 120nA over the next 25 minutes.

Similar current fluctuation was reported by Pradhan *et al*[104] (i.e. the increase and fluctuation in the emission at the initial stage of operation) and attributed to sample's surface cleaning which most likely could be the reason in our case as well[28]. After the self-cleaning process, the emission current sharply dropped to its lowest recorded value of 45 nA (less than 50% of its initial value). The sharp edges of the ZnO nanosheets are mainly responsible for the field emission, and they are more susceptible to the damage caused by ions bombardment which led to a sharp degradation in the emission current.

Apart from few spikes the emission current stability highly improved with a fluctuation of (44.44%) at an average current of 45 nA over a span of 40 min as figure 4.10 shows. The most likely reason of the constant periodic increase and decrease that was clearly recorded over the last 60 minutes is the adsorption and desorption of some species which alter the material's work function along as the time elapse.

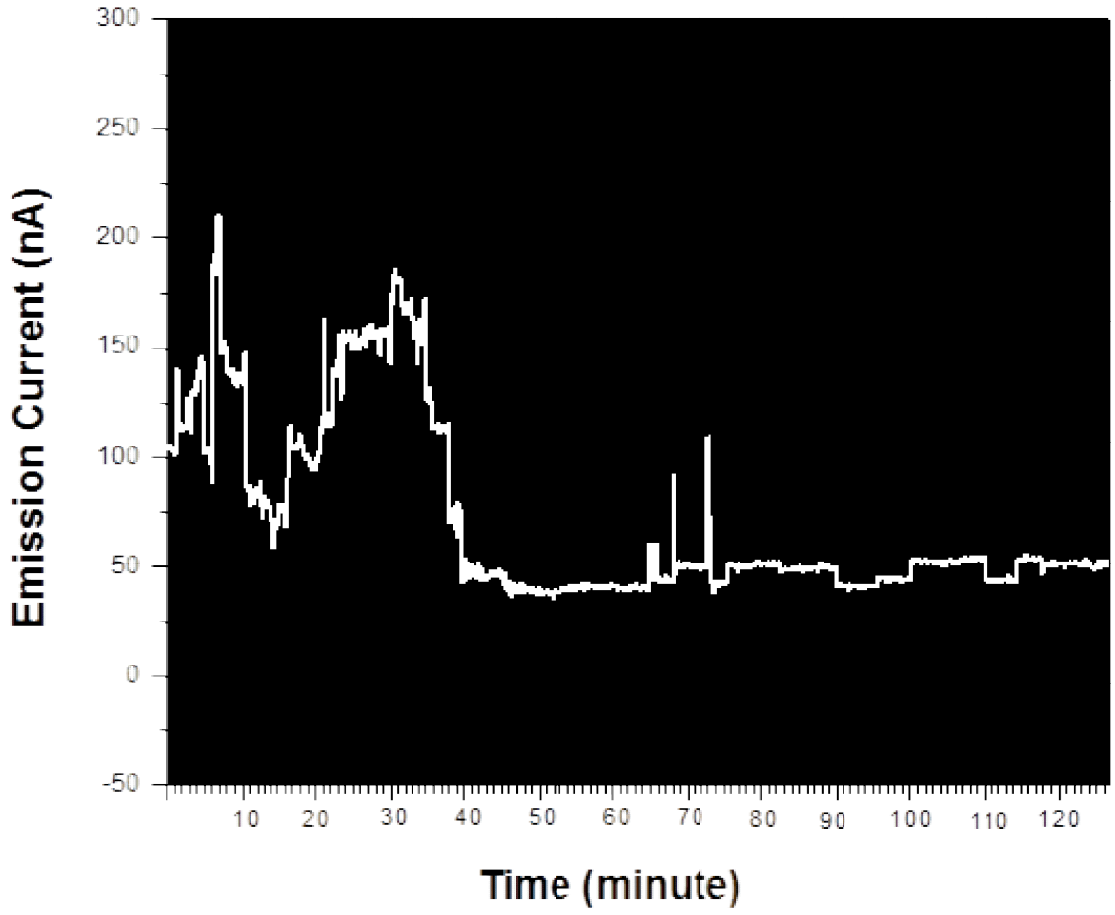

Figure 4.10 Emission current stability graph of ZnO nanosheets interconnects as a function of time.

4.3.5.3 Field emission pattern of ZnO nanosheet at different voltages

The images of emission pattern of ZnO nanosheets were captured by a digital camera during the first test of the sample. First image represent the emission pattern at an applied voltage of 4.4 kV. Increase in the emission sites and the luminescence with increasing the applied voltages as can be seen from figures 4.11 (4.4 kV, 5 kV, 5.5 kV and 5.8 kV).

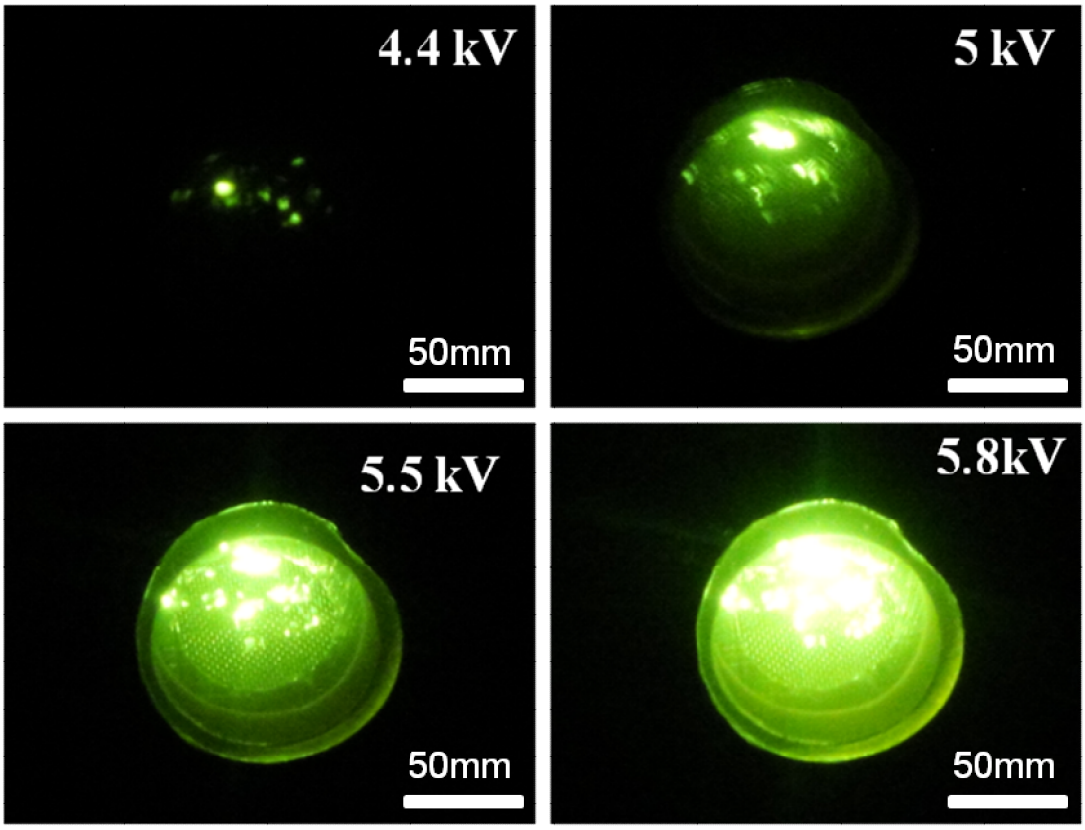

Figure 4.11 Field emission patterns of ZnO nanosheets interconnects grown on Zn foil as a function of the applied voltage. The last image at an applied voltage of 5.8 kV shows the breakdown flash.

4.4 Conclusion

The nanocrystalline thin ZnO nanosheets interconnects were grown on zinc foil by facile hydrothermal process at low-temperature. The detailed structural properties of as-prepared nanosheet interconnects revealed that the synthesized products were well-crystalline and possessing wurtzite hexagonal phase. The optical property was examined by room-temperature PL, of as-grown ZnO nanosheet interconnects and confirmed to be sound. The annealing impact of up 200°C on the morphological integrity of the nanosheets was minute. A plausible mechanism based on the crystallographic habits of ZnO has also been discussed. The field emission properties of the as synthesized nano-crystalline thin ZnO nanosheets were investigated. The limited success of ZnO nanosheets based field emission devices opens a way to prepare and utilize one dimensional (1D) ZnO and sharp edges compared to 2D nanomaterials. For this purpose, in the next work, aligned ZnO nanorods were grown on Ti substrate with the aim that these nanomaterials will exhibit excellent field emission properties.

CHAPTER5

NON-CATALYTIC GROWTH OF HEXAGONAL SHAPED ZnO NANORODS ON TITANIUM SUBSTRATE: STRUCTURAL, OPTICAL AND FIELD EMISSION PROPERTIES

5.1 Introduction

Recently, the researches on 1D semiconductor nanomaterials have received a great attention due to their unique morphologies and wide applications in various high-technological areas including photovoltaics, electronics, sensors and actuators, and so on[75]. The 1D nanomaterials of ZnO such as nanorods, nanowires, nanofibers, nanoneedles, etc are very attractive due to their tunable electronic and optoelectronic properties and various high-technological applications, for instance, nanoscale electronic and optoelectronic devices, sensors and actuators, solar cells, nanogenerators, laser operating at room-temperature and so on[105]. ZnO nanorods/nanowires were synthesized by various techniques such as solution process, hydrothermal process, chemical vapor deposition process, metal–organic chemical vapor deposition process, electro-deposition process and so on and reported in the literature[105-114]. Recently, the use of various substrates for the growth of 1D ZnO nanomaterials has received a great attention as particular substrates are needed for specific applications. The substrates used for the growth of ZnO nanorods/nanowires are various orientations of silicon chips[115-117], stainless steel grid[118], indium tin oxide substrates[119], nylon fibers[120], alumina[121], anodized aluminum oxide[122], CaF_2[123], steel alloy substrates[100], and so on.

In this section, attempts have been made to grow well-crystalline ZnO nanorods on Ti substrate. Titanium is a paramagnetic and refractory metal with relatively high melting point (more than 1,650°C). Moreover, the prepared aligned ZnO nanorods on Ti substrate were examined in detail in terms of their morphological, structural, optical and field emission properties. To the best of the author knowledge, this is the first report in which vertically aligned and well-crystalline hexagonal ZnO nanorods were grown on Ti substrate by facile thermal evaporation of metallic zinc powder in the presence of oxygen at moderate temperature.

5.2 Experimental details

For the growth of aligned ZnO nanorods, commercially available Ti substrates were used. Prior to the growth, the substrates were ultrasonically cleaned with DI water, alcohol and acetone, sequentially. The growth of nanorods on Ti substrate was done by facile thermal evaporation process by using highly pure metallic zinc powder (99.98%) in the presence of oxygen (99.99%). The thermal evaporation system consists of 70 cm long quart tube furnace with the halogen lamp heating system with heating rate of 20°C/s. For the growth of ZnO nanorods, a 2 cm long ceramic boat filled with high-purity metallic zinc powder was placed at the middle of the furnace and several pieces of $1x1cm^2$ Ti substrates were placed adjacent to the source boat. After loading the source materials and substrates, the chamber pressure was evacuated down to 2 mbar using a rotary vacuum pump and the same pressure was maintained during the whole reaction. The reaction temperature was 750°C. During the reaction, high purity nitrogen (20 sccm) and oxygen (100 sccm) gases were flown inside the quart tube furnace. The reaction was completed in 1.5 hr. After completing the reaction, the furnace was naturally cooled to room-temperature and white colored deposited products were seen on the Ti substrate. A concise summary of the growth parameters of hexagonal-shaped ZnO nanorods are presented in table 5.1. The deposited products were analyzed in terms of their morphological, compositional, structural, optical and field emission properties.

The morphologies and compositions of the deposited materials were investigated using the field emission electron microscopy (FESEM) and energy dispersive X-ray (EDX) spectroscopy, respectively. The detailed structural characterization was done using transmission electron microscope (TEM) and selected area electron diffraction (SAED) pattern. The crystallinity and crystal phases of the deposited nanorods were examined by the X-ray diffraction (XRD) pattern measured with Cu-Kα radiation. Room temperature Raman scattering and photoluminescence (PL) spectroscopy with the Ar^+ (513.4 nm) and He-Cd (325 nm) laser lines as the exciton sources were used to know the optical properties of as-prepared ZnO nanorods.

Nanomateial Type	Hexagonal shaped ZnO nanorods
Growth Technique	Thermal evaporation process using horizontal quartz tube furnace
Reactants	High-purity metallic zinc powder, oxygen and nitrogen gases
Substrate	Titanium foil substrate
Reaction Temperature	750°C
Reaction Time	1.5 hr

Table 5.1 Summary of the growth parameters of hexagonal shaped ZnO nanorods.

5.3 Results and discussion

5.3.1 Morphological and structural properties

The general morphologies of as-deposited ZnO products on Ti was examined by field emission scanning electron microscopy (FESEM) and results are shown in figures 5.1(a-c). From the observed FESEM analyses, it is confirmed that the deposited products are nanorods which are grown in high density in vertically aligned manner on the whole substrate surface (figure 5.1(a)). By clear observations, it is seen that the nanorods possess perfectly hexagonal shape throughout their lengths and hence confirms the epitaxial growth and single crystalline nature of as-grown ZnO nanorods (figure 5.1(b)). The typical lengths (observed from titled images of nanorods; not shown here) and diameters of as-grown nanorods are in the range of 1.0 ± 0.25 μm and 50 ± 10 nm, respectively (figure 5.1(c)). Interestingly, due to high density growth of the nanorods, it was also observed that two or more nanorods are joined to each other through one of their surfaces and the increased the diameters of the nanorods as can be seen clearly in figure 5.1(c). The elemental composition of the as-prepared ZnO nanorods was examined by energy dispersive x-ray spectroscopy (EDS) which is shown in figure 5.1(d). As can be seen from the EDS spectrum, only zinc and oxygen peaks are observed which confirmed that the prepared nanorods are made of Zinc and oxygen. No other peak related with any impurity was observed from the EDS spectrum which further shows the purity of the as-prepared nanorods and confirms that the synthesized nanorods are pure ZnO.

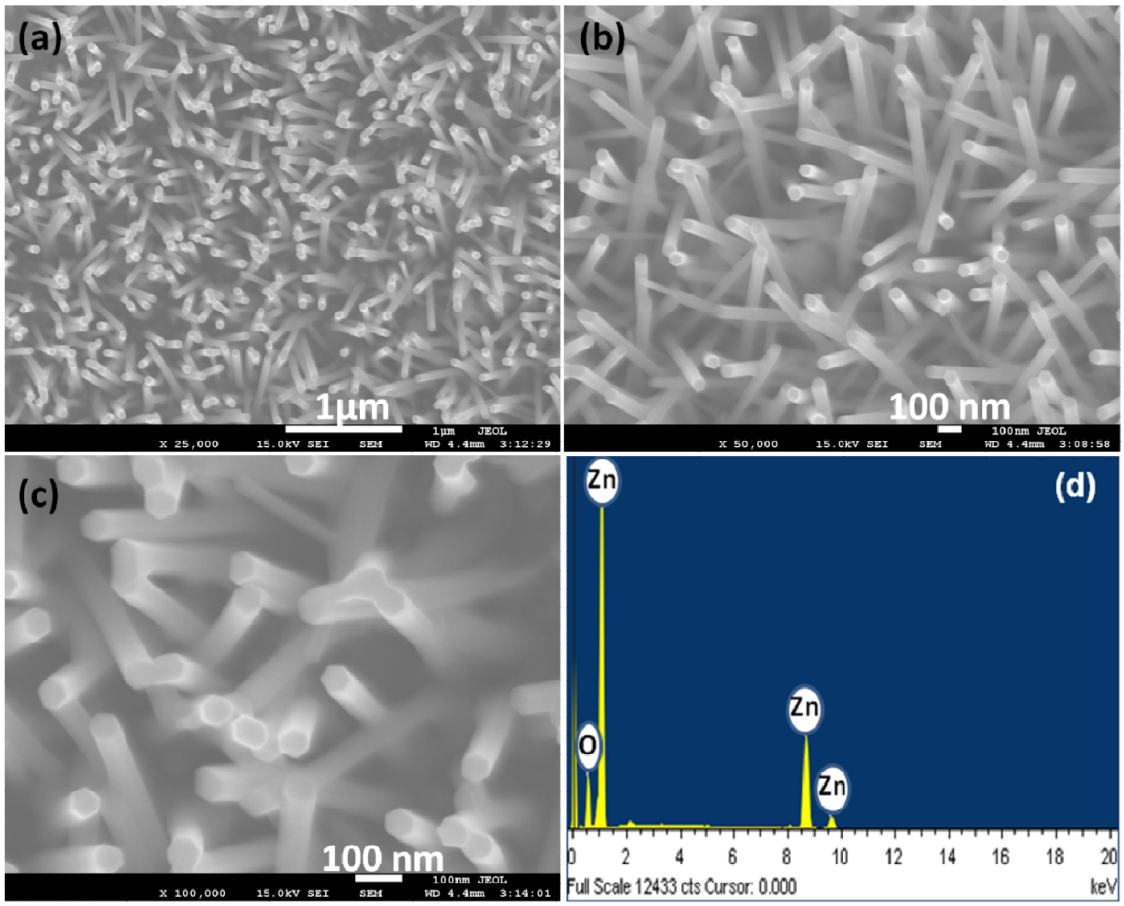

Figure 5.1 Typical (a) low-magnification and (b) and (c) high-magnification FESEM images, and (d) EDS spectrum of as-grown ZnO nanorods on Ti substrate.

For further and detailed structural characterizations, the as-prepared ZnO nanorods grown on Ti substrate were examined by transmission electron microscopy (TEM). Figure 5.2(a) exhibits the typical low-magnification TEM image of the as-grown ZnO nanorods which exhibits the full consistency with the FESEM observations in terms of their morphological and dimensional aspects. The nanorods exhibit clean and smooth surfaces and uniform diameter throughout their lengths. The inset of figure 5.2(a) shows the corresponding SAED pattern of the nanorod shown in figure 5.2(a). The observed SAED pattern shows very well defined, ordered diffraction pattern which confirmed that the grown nanorods are well-crystalline and preferentially grown along the *c*-axis direction. Figure 5.2(b) exhibits the typical TEM image of the nanorods shown in figure 5.2 (a). The TEM image shows the well-defined lattice fringes with the inter-planar distance of 0.52 nm, equal to the lattice constant of crystalline ZnO. This fact clearly confirms that the prepared nanorods are well-crystalline ZnO.

To examine the crystallinity and crystal phases, the as-prepared ZnO nanorods were examined by X-ray diffraction (XRD) pattern. Figure 5.3(a) exhibits the typical XRD pattern of as-prepared ZnO nanorods. All the observed diffraction reflections in the XRD pattern are well matched with the wurtzite hexagonal phase of pure well-crystalline ZnO and hence confirm that the prepared nanorods are well-crystalline and possessing wurtzite hexagonal phase of ZnO. Some small diffraction reflections at 38.4°, 40.3°and 53.1° are also seen in the observed XRD pattern of ZnO nanorods which are related with the Ti substrate as was confirmed by measuring the XRD pattern of pure Ti substrate (figure 5.3(b)).

The average crystallite size and lattice parameters of the ZnO nanorods were calculated from different XRD peaks (100) and (002) and summarised in table 5.2. The estimated lattice constants of the ZnO nanorods are fully agreed with the TEM observation.

Crystallite size (*D*) (nm)	Lattice constants (nm)
38	*a*= 0.3233 *c*= 0.521

Table 5.2 crystallite size and lattice constant of the ZnO nanorods grown on Ti substrate.

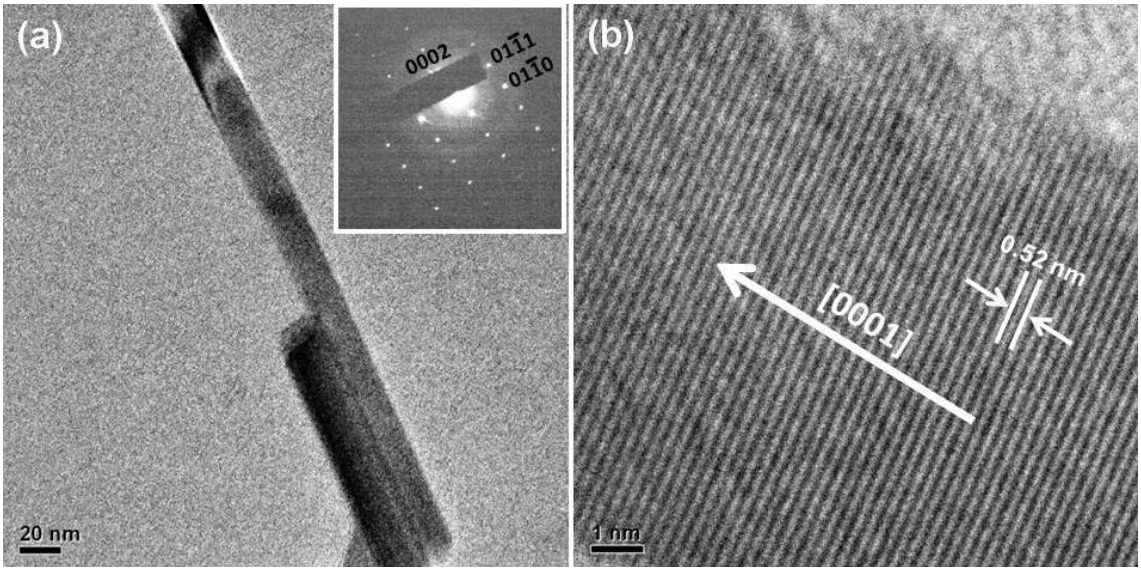

Figure 5.2 Typical (a) low-magnification and (b) high-magnification TEM images of as-grown ZnO nanorods on Ti substrate. Inset (a) exhibits the corresponding SAED pattern.

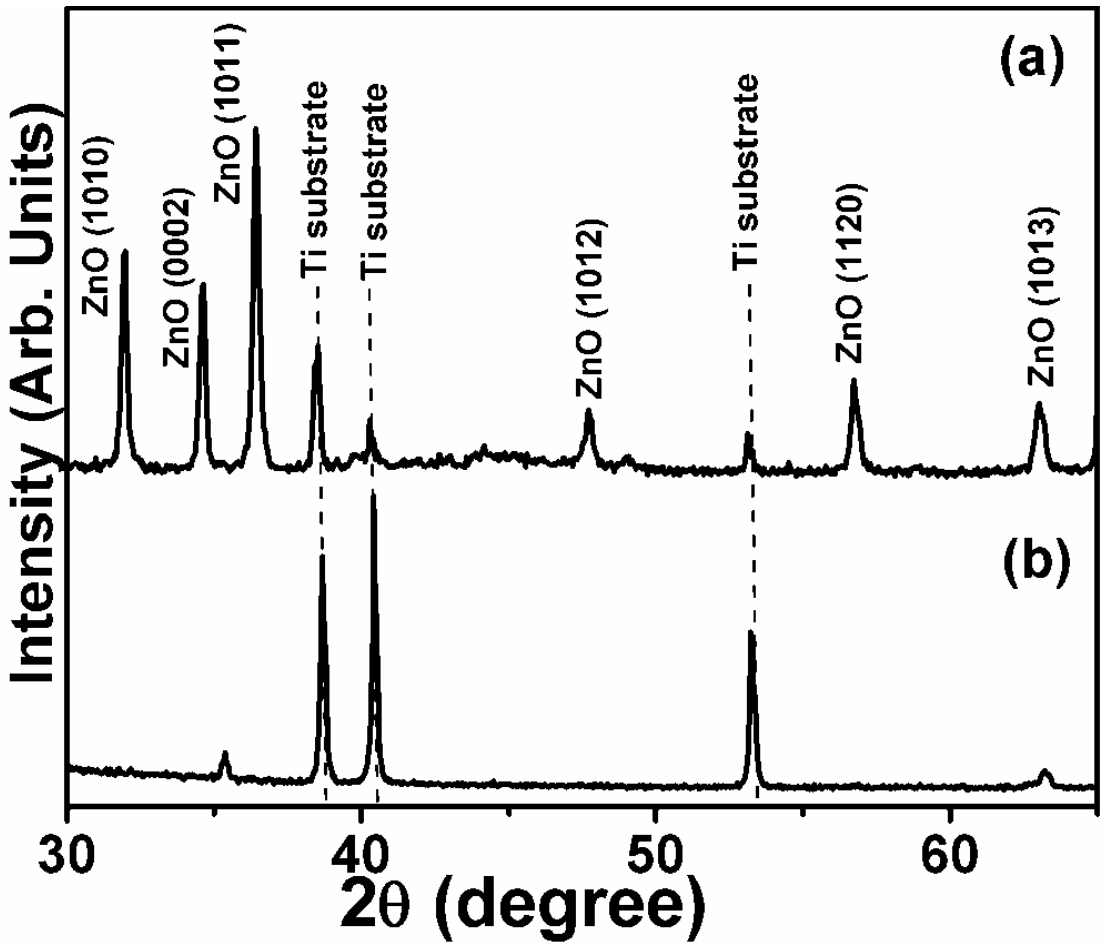

Figure 5.3 Typical (a) XRD pattern of as-grown ZnO nanorods on Ti substrate and (b) XRD for pure Ti substrate.

5.3.2 Optical properties

To examine the optical properties, the as-grown ZnO nanorods on Ti substrate were examined by photoluminescence (PL) spectroscopy measured using He-Cd (325 nm) laser line as the exciton source at room temperature. Figure 5.4 exhibits the typical room-temperature PL spectrum of as-grown ZnO nanorods. Generally, two bands are appearing in the room-temperature PL spectrum of ZnO nanostructures; a band in the UV region, also called as near band edge emission (NBE), originated due to the free-exciton recombination[108], and in the visible region, also called as green emission or deep level emission (DLE). The theory behind the origination of green emission or DPE is controversial but the most accepted theory reveals that the green emission appearing in the spectrum mainly due to the impurities and structural defects in the crystal such as oxygen vacancies, zinc interstitials, etc[108]. The calculated NBE/DLE intensity ratio is ~ 3.77 and hence, it is concluded that the appearance of strong UV emission as compared to DPE in the PL spectrum reveals the well-crystallinity of the grown ZnO nanostructures. Interestingly, the room-temperature PL spectrum of the as-grown ZnO nanorods exhibits a strong UV emission at 385 nm and a suppressed and broad DPE at 627 nm. As, the PL spectrum of as-grown nanorods exhibited a sharp and strong UV emission and suppressed visible emission which confirmed that the obtained nanorods possess good crystal quality and optical properties.

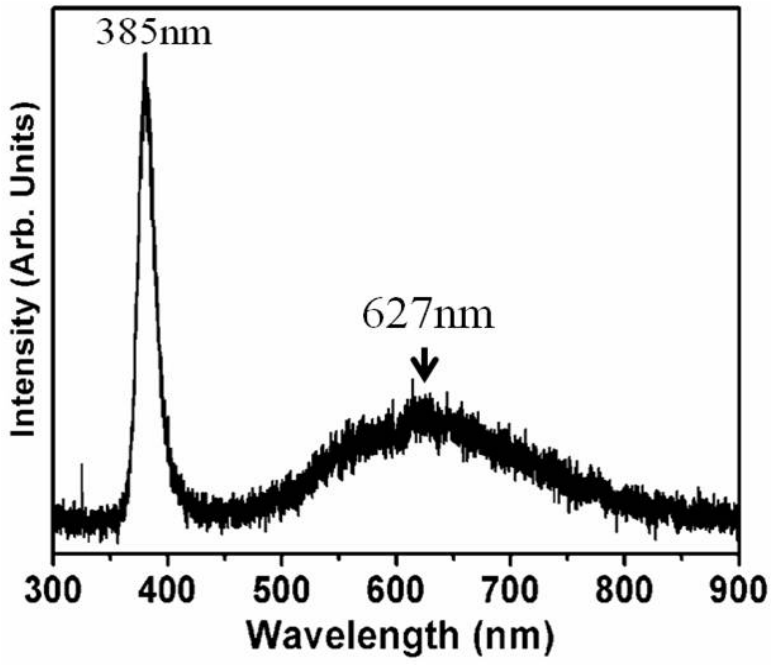

Figure 5.4 Typical room-temperature PL spectrum of the as-grown ZnO nanorods on Ti substrate.

The Raman-scattering property of the as-grown ZnO nanorods was also examined as Raman-scattering is excellent tool to determine the crystallinity of the grown nanomaterials. Figure 5.5 exhibits the typical Raman-scattering properties of the as-prepared ZnO nanorods. With the wurtzite hexagonal phase, the II-VI semiconductor ZnO belongs to the C^4_{6v} with two formula unit primitive cells where all the atoms occupy the C_{3V} sites. ZnO possess eight sets of optical modes in which A_1, E_1, and E_2 modes are Raman active. As can be seen from the observed Raman-scattering spectrum, only two well-defined bands are seen, i.e. at 332 cm^{-1} and 438 cm^{-1}. The weak and suppressed band appearing at 332 cm^{-1} is attributed to $E_{2H} - E_{2L}$ (multi phonon) mode and it appears only when the ZnO nanomaterial is single crystalline[100]. Another dominated and strongest band in the spectrum appears at 438 cm^{-1} which is assigned as Raman-active E_2 mode and reported as a characteristic band for the hexagonal wurtzite phase of ZnO[100]. It is important to note that the absence of E_{1L} band as copmeared to the ZnO nanosheets in chapter 4 (section 4.33) is an indicator of less structural defects and/or lower impurities of the grown ZnO nanorods.

Furthermore, due to the presence of high intensity and strongest Raman active E_2 mode in the observed Raman-scattering, it could be concluded that the prepared ZnO nanorods are well-crystalline and possessing wurtzite hexagonal phase.

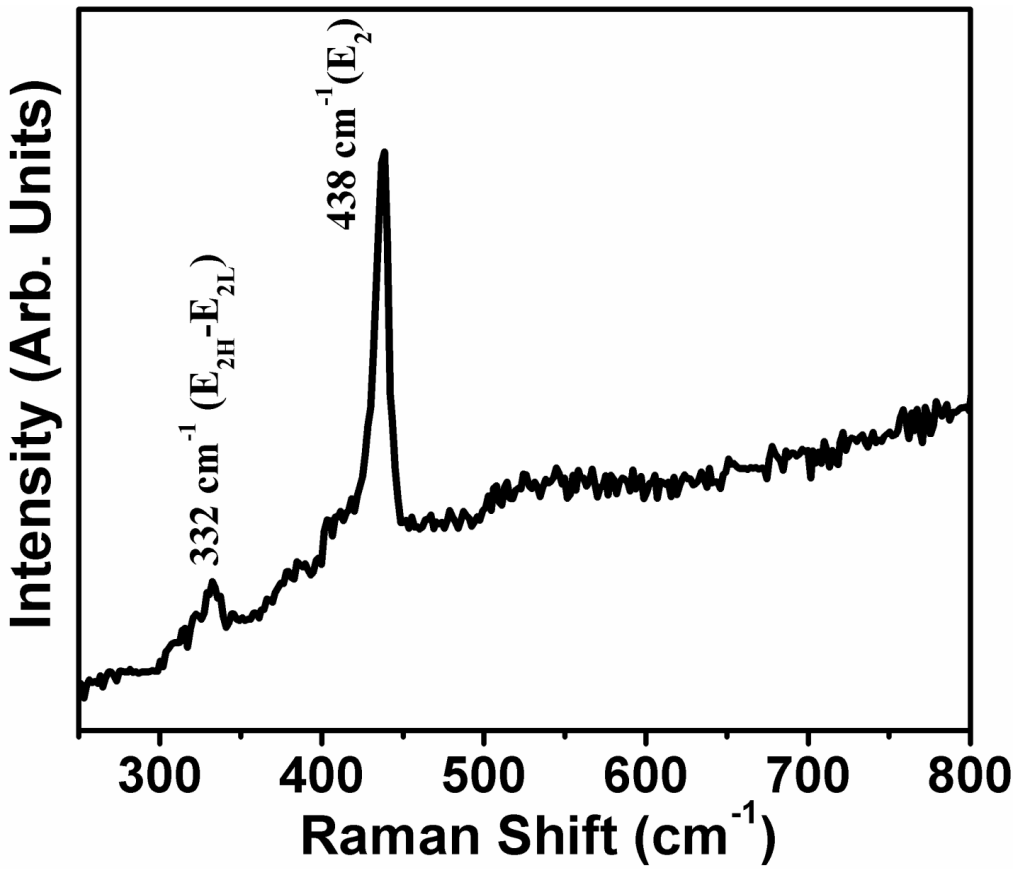

Figure 5.5 Typical Raman-scattering spectrum of as-grown ZnO nanorods on Ti substrate.

5.3.3 Plausible growth mechanism

Based on the observed FESEM and TEM images, a plausible growth mechanism for the formation of ZnO nanorods is proposed. Normally, two kinds of growth mechanisms are reported in the literature regarding the growth of nanomaterials, i.e. vapor-solid (VS) mechanism[100] and vapor-liquid-solid (VLS) mechanisms[124]. The important characteristic of VLS mechanism is the appearance of metal particles on the tips of nanomaterials. However, in case of the growth of ZnO nanorods on Ti substrate no metal particles were seen on the tips of nanorods which suggest that the growth of nanorods follows the VS mechanism and not VLS mechanism. Figure 5.6 shows the schematic of the growth of hexagonal ZnO nanorods grown on Ti substrate. The growth of nanorods follows two steps, i.e. nucleation and growth. During the nucleation step, once the furnace was heated above the melting point of zinc powder (melting point of Zn = 419.5°C), the zinc vapors were generated and transferred to the substrate surface

as depicted in figure 5.6(a). Once the furnace temperature reached ~750°C, the oxygen gas was introduced into the reaction chamber which interacted with the originated zinc vapors and formed ZnO vapors which were condensed on the substrate and formed ZnO nuclei. As the basic characteristic of ZnO is the formation of hexagonal crystals hence during condensation hexagonal nuclei were formed on the substrate. This could be called as nucleation process (figure 5.6(b)). With continuous supply of zinc and oxygen in the presence of nitrogen gas, the formed nuclei started to grow and small nanorods are formed (figure 5.6(c)) and at particular reaction time, perfectly hexagonal shaped ZnO nanorods are formed on the Ti substrate. The formed ZnO nanorods exhibited top and bottom ±(0001) planes and surrounded by six crystallographic {01$\bar{1}$0} planes (figure 5.6(d)).

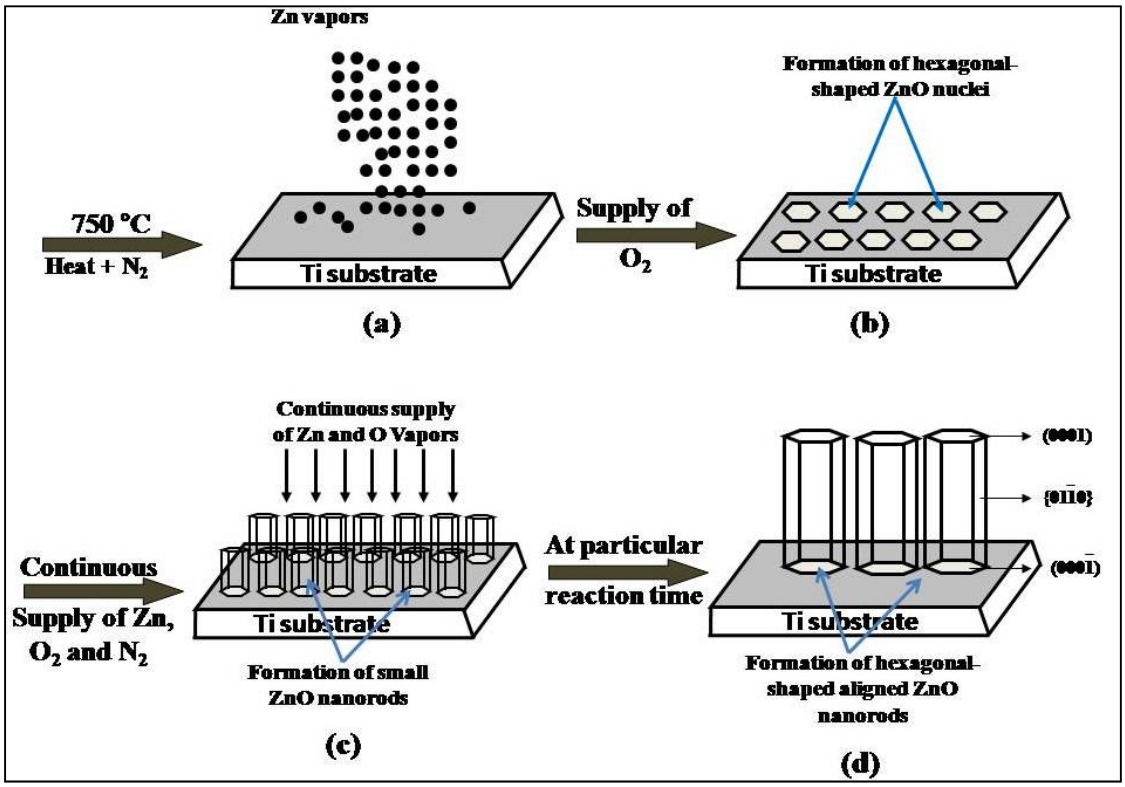

Figure 5.6 Schematic growth mechanism for the formation of the as-grown ZnO nanorods on Ti substrate.

5.3.4 Field emission studies

5.3.4.1 Current –voltage characteristic of ZnO nanorods

Further, the field emission properties of ZnO nanorods were also investigated under pressure of $5x10^{-8}$ mbar. The cathode's surface area is 1 cm^2, however, as was mentioned in chapter 4 this is not necessarily the effective emission area as it is usually smaller compared to the actual cathode's area in case of flat substrate. For the FE measurements, two runs were carried out.

Figure 5.7(a) (black dots) exhibits the typical *I-V* curve (measured current as a function of applied voltage) of the ZnO nanorods. It is seen that in the initial scan, referred to as first scan, the emission current increased exponentially with increasing the applied voltage showing the classical Fowler-Nordheim behaviour as described in equation (2.25). The initial turn on voltage is 2.55 kV with the observed emission current of ~100 nA. An emission current of 13 µA was recorded at an applied voltage of 4.56 kV. The corresponding F-N plot of the first scan is shown in figure 5.7(b). In the first scan, the emission current was quite unstable. Moreover, the *I-V* curve of the first scan usually appears to be noisy and this is attributed to the surface contamination such as carbon and H_2O[125]. Therefore, repeated scans are necessary to achieve stable and reproducible emission current.

A much stable and less noisy *I-V* curve was obtained in case of the second FE measurement which can be attributed to the removal of the surface's contaminants during first FE scan. However, slightly higher voltage was required for the same emission current. The interpolated value of the turn on voltage for an emission current ~100 nA is ~2.65 kV. Fitting the data using F-N plots showed linear behavior indicating that the field emission process is dominant. The (*I-V*) curve and F-N plot are shown in figures 5.7(a) and (b) respectively and referred to it as second scan (the red dots). The estimated field enhancement factor β=3185 assuming the work function of ZnO nanorods is 5.3 eV[16].

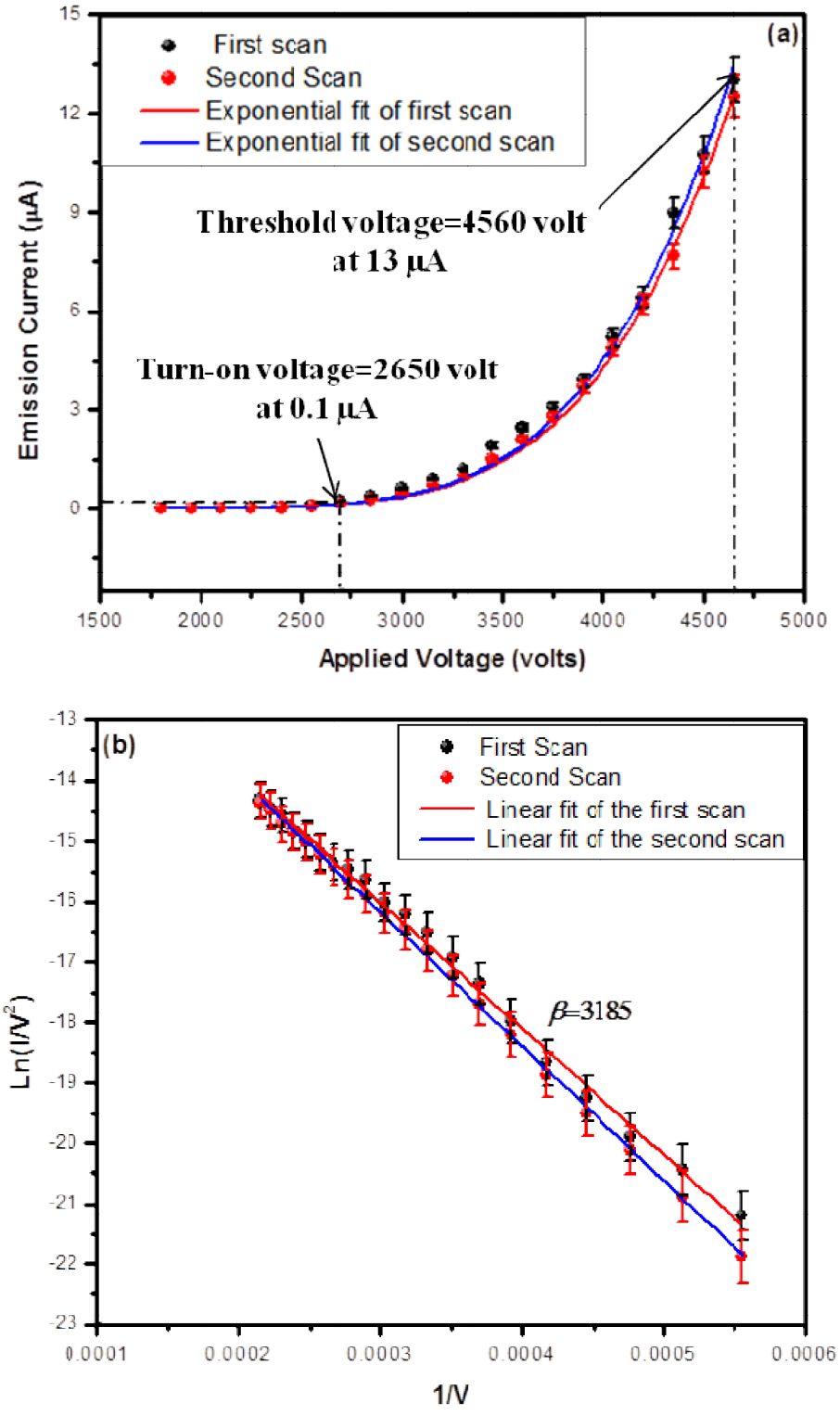

Figure 5.7 (a) Current-voltage (*I-V*) characteristic of the as-grown ZnO nanorods on Ti substrate (first scan black symbols) and (second scan red symbols). (b) The corresponding F-N plots.

The influence of the pressure on the field emission properties of the ZnO nanorods was also checked. Figure 5.8(a) shows the *I-V* characteristic of ZnO nanorods at different air pressure i.e. ($5x10^{-7}$ and $5x10^{-6}$ mbar). It has been found that, with the increase of pressure, the turn on voltage shifted to higher values from 2.55 kV at $5x10^{-8}$ mbar to ~3kV at $5x10^{-7}$ mbar, and further to 3.5 kV at $5x10^{-6}$ mbar. Further the field emission current decreases as pressure increases. At the same applied voltage of 4.65 kV, the emission current at $5x10^{-7}$ mbar drops to ~75 % (9.36 µA) of the emission current at pressure of $5x10^{-8}$ mbar (12.5 µA) and to only ~38% when vacuum decreases to $5x10^{-6}$ mbar. The corresponding F-N plots of two different pressures (i.e. 10^{-7} and 10^{-6} mbar) are presented in figure 5.8(b). The linear fitting of the data measured at 10^{-7} mbar indicates the little influence of the pressure in this range on the field emission properties of ZnO nanorods. However, the F-N plot at higher pressure i.e. 10^{-6} mbar exhibits strong deviation from linearity indicating the strong effect of the pressure on the field emission properties in this range.

The above analysis shows the pressure dependence of the field emission properties of ZnO nanorods. The influence of the pressure on the field emission process may be attributed to the effect of adsorbates on the surface of the ZnO nanorods[126-127]. Different gas species such as H_2, O_2, N_2 and H_2O normally exist in vacuum chamber which alter the electrical properties of semiconductors and hence their field emission properties. With the increase of the pressure, the concentration of these gas species increases in the vacuum chamber. The oxygen and nitrogen gases are known with their negative impact on field emission performance of ZnO due to filling of the oxygen vacancies which is dominating the surface electronic properties and thus decreasing the carrier concentration of ZnO nanomaterials[127]. Moreover, based on first principle study that has been done by Dardona and his co-worker, the calculated work function of ZnO increased in the presence of these adsorbates which means higher applied voltage is required to extract the same amount of the emission current[127]. This could explain the increase in the turn on voltages at higher pressures. Similar undesirable effect of O_2 on the field emission properties (i.e. the emission current suppression) of carbon nanotubes was also reported[128,129].

Based on the F-N fitting a deviation from the linearity is more noticeable in the data that is collected at a pressure of $5x10^{-6}$ mbar and this to some extent could be related to the electron collision with air molecules in the gap between the two electrodes[127].

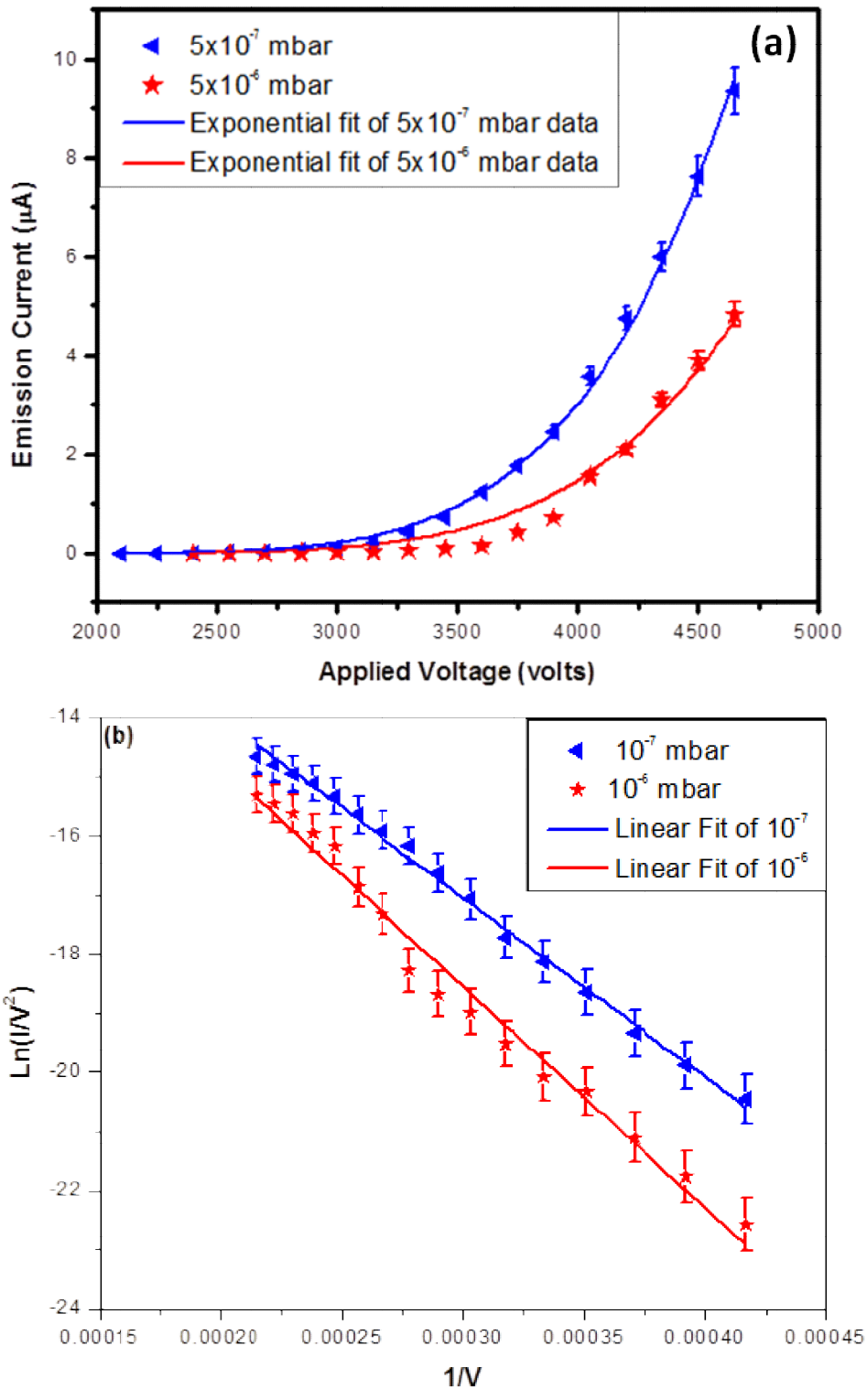

Figure 5.8 (a) Current-voltage (*I-V*) characteristic of as-grown ZnO nanorods on Ti substrate at different air pressures. (b) The corresponding F-N plots.

5.3.4.2 The field emission stability of ZnO nanorods

The field emission stability of ZnO nanorods was tested at base vacuum of $3x10^{-8}$ mbar. Initially, repeated scan runs were required to clean the sample's surface and removing the adsorbates until a smooth and reproducible field emission curve was obtained. After that, the field emission stability measurement was carried out at fixed extraction voltage of 2.7 kV.

Figure 5.9 shows, the emission current profile of the ZnO nanorods as a function of the time over a period of 7 hours. Stable current emission of an average of 100 nA with a fluctuation of 28.6% was recorded and persisted for about 7 hours without any tendency of gradual decrease in the emission under the applied voltage of 2.7 kV. The present stability in the emission current is attributable to the fact of ZnO being an oxide material which is inherently more stable under harsh environments. Moreover, the emission current stability strongly depends on several elements that are related to the emitters' properties and geometry such as the crystallinity, uniformity (i.e. shape and size) and alignment[130-131]. Evidently, these ZnO nanorods are well crystalline and posses the same shape length and diameter as well as aligned assembly as illustrated in previous section (3.1). An improvement in the emission current stability (28.6%) and longer life time (7 hours) of the ZnO nanorods was achieved this time in comparison with previously recorded emission current stability and life time (i.e. 44.44% and 2.2 hours) of ZnO nanosheets (section 4.3.5.2). Therefore, this result indicates that ZnO nanorods are promising materials for fabrication of efficient field emission devices.

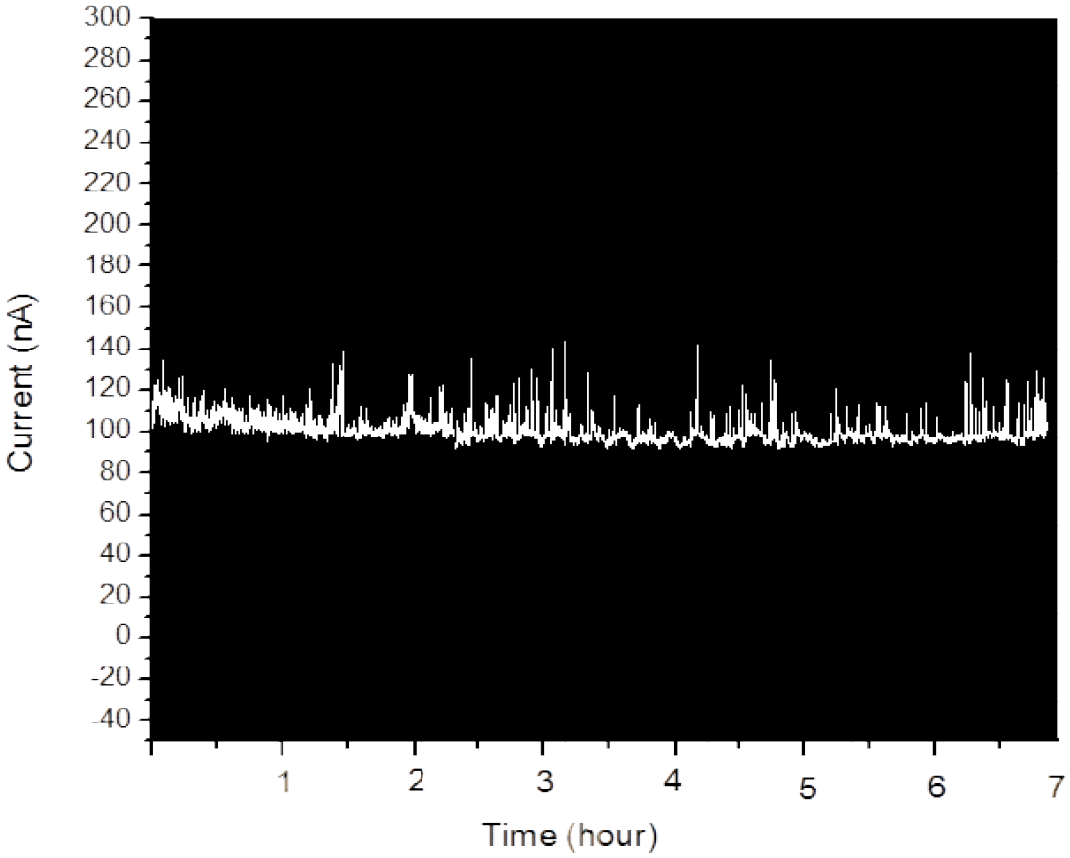

Figure 5.9 The emission current stability profile of ZnO nanorods under a constant applied voltage of 2.7 kV.

5.3.4.3 Field emission patterns from ZnO nanorods

The converted electron to light emission patterns from ZnO nanorods on a YAG scintillator were captured by a digital camera at different applied voltages and are shown in figure5.10. Several emission spots appeared on the YAG screen at 1.4 kV with a current of about 22 nA. These spots were getting intense and more emission sites were encouraged with increasing the applied voltages until the breakdown occurred at an applied voltage of 5 kV.

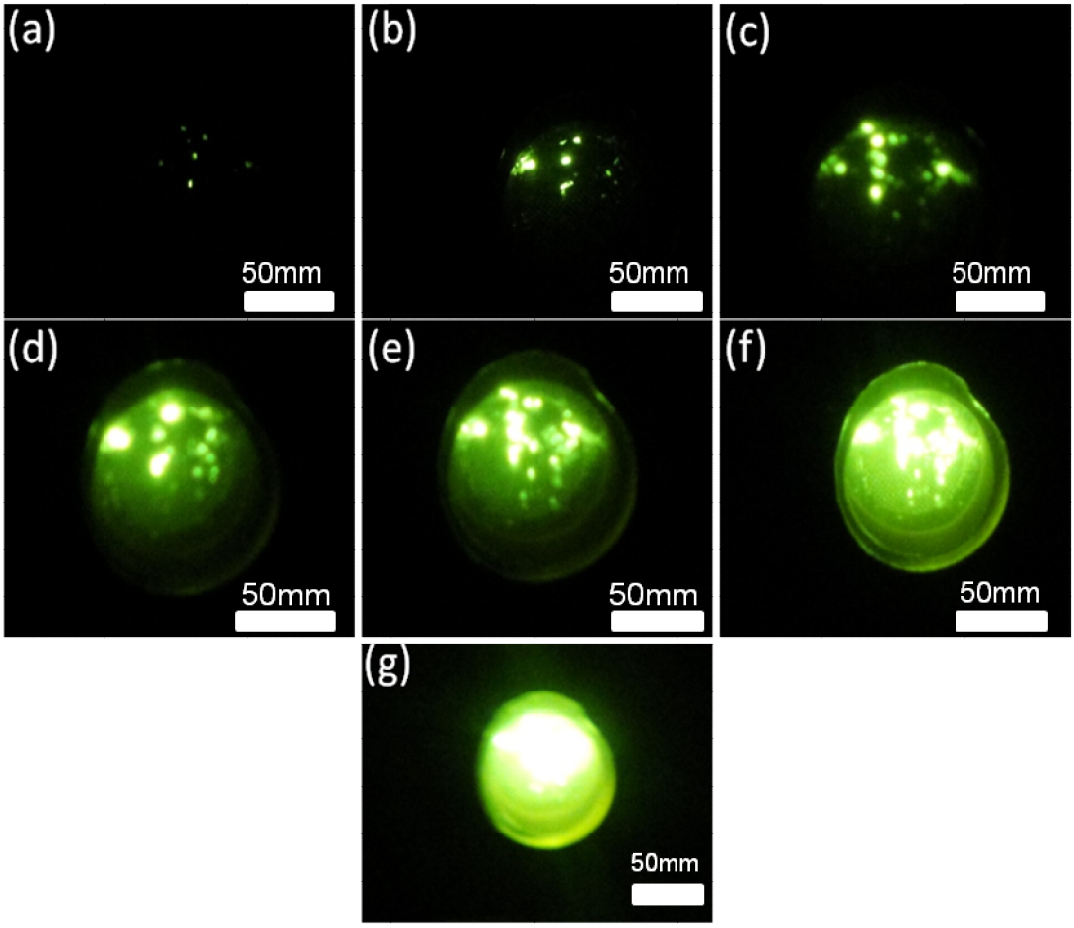

Figure 5.10 Field emission patterns of ZnO nanorods grown on titanium substrate. The patterns show the emission current as a function of increasing voltage: (a) 2.1kV, (b) 2.4 kV (c) 2.7 kV (d) 3 kV (e) 3.3kV (f) 3.9 kV and (g) shows the breakdown flash at 4.65kV.

5.4 Conclusion

In summary, perfectly hexagonal-shaped ZnO nanorods were grown on Ti substrate by simple and facile thermal evaporation process using metallic zinc powder in the presence of oxygen. The detailed morphological and compositional properties of the as-grown products revealed that the prepared nanomaterials are "ZnO nanorods" which are aligned to the substrate surface. The structural studies revealed that the prepared nanorods are well-crystalline and possessing wurtzite hexagonal phase. A strong UV emission was observed in the room-temperature PL spectrum of as-prepared nanorods compared to the deep level emission which confirmed that the grown nanorods possess good optical properties. Finally, the field emission performance of the vertically aligned ZnO nanorods on Ti substrate was investigated under various pressure regimes ($5x10^{-7}$, $5x10^{-6}$ and $5x10^{-8}$ mbar) and presented in this chapter.

CHAPTER6

GALLIUM-DOPED ZnO NANOSTRUCTURES: GROWTH, OPTICAL AND FIELD EMISSION PROPERTIES

6.1 Introduction

Due to these excellent properties, ZnO is widely used for a variety of electronic and optoelectronic applications such as optical devices and switches, field emission displays, UV-lasers, light emitting diodes, photo-detectors, surface acoustic wave guides, solar cells and so on. Due to its piezoelectric nature, ZnO is used for the fabrication of piezoelectric transducers and actuators, piezoelectric generators, etc. The environmental benign, bio-safe and bio-compatible nature of ZnO makes it a particularly promising material for applications in chemical sensors and biosensors, catalysts, medicines, sun creams and cosmetics[132-142]. It is because of such excellent properties and wide applications that a variety of ZnO nanomaterials such as nanowires/nanorods, nanotubes, nanobelts, nanoneedles, nanorings, nanosprings, nanoflowers, nanowalls, nanoballs, nanosheets, nanodisks, were synthesized by using various synthetic techniques that have been reported in the litertuare[132-161]. To tailor the physical and chemical properties of ZnO nanomaterials, the morphologies, chemical composition and sizes need to be tuned. It is reported that doping ZnO nanomaterials with various elements such as Gallium (Ga), Indium (In), Phosphorous (P), Tin (Sn), Antimony (Sb), Bismuth (Bi), can affect various physical and chemical properties of ZnO and hence greatly enhance its electrical, optical and magnetic properties[1]. Therefore, by choosing the appropriate dopant, the properties of ZnO nanomaterials can be tailored for their utilization in specific applications[75]. Several dopant elements such as aluminium (Al), Germanium (Ge), Sulphur (S), Tin (Sn), Antimony (Sb), Gallium (Ga) and Indium (In) were doped with ZnO nanomaterials by our group however, due to optimized morphologies for efficient field emission device applications, only Ga- and In-doped ZnO nanomaterials are presented in this thesis.

Amongst the various dopant elements, the doping of ZnO with Ga has various advantages due to the similar atomic radii of Ga and Zn by which the gallium is highly soluble in ZnO. It is also observed that doping of group III-A elements such as Al and Ga into ZnO may lead to the reduction in its electrical resistivity (as low as 10^{-4} Ω cm)

which makes Ga-doped ZnO a promising candidate for a transparent conducting material[1]. Moreover, it is also reported that Ga doping of ZnO leads to a reduction in the ZnO work function which is advantageous for field emission applications[143].

In this chapter, a facile and simple synthesis method and detailed morphological, structural and optical characterizations of Ga-doped ZnO nanoneedles and multipods will be reported. The Ga-doped ZnO nanostructures were grown on a silicon substrate by thermal evaporation process. Moreover, the effect of gallium ion concentrations (0.5 and 2%) on the morphologies, structural and optical properties of the grown nanostructures were also studied and presented.

6.2 Experimental details

6.2.1 Synthesis of Ga-doped ZnO nanostructures on a Si(100) substrate

Ga-doped ZnO nanostructures were grown on a Si (100) substrate by facile and simple thermal evaporation process by using metallic zinc (99.98%) and Ga powders (99.99%) in the presence of oxygen. Several ratios of Ga powder concentrations (0.5, 1.0, 1.5 and 2.0%) were examined in order to determine the proper composition of the source materials for obtaining ZnO nanomaterials with best desirable characteristics which could be used for future field emission device applications. Interestingly, it was found that vertical and high-aspect ratio Ga doped ZnO nanoneedles were obtained in the case of 0.5% concentration of gallium which could be excellent candidates for the fabrication of efficient field emission devices. Moreover, thorny branched structures were obtained when using 2% of gallium whilst other concentrations gave random morphologies. In this regard, the detailed structural and optical characterizations of the best structures, i.e aligned nanoneedles and thorny branched structures were investigated and reported here.

In a typical reaction process, commercially available high purity (99.99%) metallic Zn was thoroughly mixed with Ga powder and put into a ceramic boat and placed at the centre of the quartz tube furnace. Small (1cm x 1cm) pieces of Si(100) wafers were used as substrates which were washed and cleaned in DI water, ethanol and acetone, sequentially, prior to material deposition in the furnace. For the deposition, several pieces of Si(100) were placed adjacent to the source boat which was placed at the middle of the furnace. After loading the source materials and substrates, the

chamber pressure was evacuated down to 1.33 mbar using a rotary vacuum pump and this pressure was maintained during the whole reaction process. For the reaction, the furnace was heated up to 950ºC under the continuous flow of highly-pure nitrogen (purity= 99.999%; 30 sccm) and oxygen (purity= 99.999%; 70 sccm) gases. The reaction lasted about 1 h and after the growth the furnace was allowed to be naturally cooled to room-temperature. Whitish-grey coloured products were observed onto the surfaces of the substrate placed 2 cm away from the source boat. A concise summary of the growth parameters of Ga-doped ZnO nanoneedles and thorny branched structures are presented in table 6.1 and 6.2, respectively. The as-deposited Ga-doped ZnO nanomaterials were characterized in detail in terms of their structural and optical properties.

Nanomateial Type	Ga-doped ZnO nanoneedles
Growth Technique	Thermal evaporation process using horizontal quartz tube furnace
Reactants	High-purity metallic zinc and 0.5% Ga powders, oxygen and nitrogen gases
Substrate	Silicon substrate
Reaction Temperature	950°C
Reaction Time	1.0 hr

Table 6.1 Summary of the growth parameters of Ga-doped ZnO nanoneedles with Ga concentration of 0.5%.

Nanomateial Type	Ga-doped ZnO thorny branched (multipods) nanostructures
Growth Technique	Thermal evaporation process using horizontal quartz tube furnace
Reactants	High-purity metallic zinc and 2.0% Ga powders, oxygen and nitrogen gases
Substrate	Silicon substrate
Reaction Temperature	950°C
Reaction Time	1.0 hr

Table 6.2 Summary of the growth parameters of Ga-doped ZnO thorny branched (multipods) nanostructures with Ga concentration of 2%.

6.2.2 Characterization of Ga-doped ZnO nanostructures on Si (100) substrate

The detailed morphological properties of as-prepared Ga-doped ZnO nanostructures were examined by field emission scanning electron microscopy (FESEM) and transmission electron microscopy (TEM) both equipped with energy dispersive X-ray spectroscopy (EDS). The crystallinity and crystal phases of the prepared nanostructures were characterized by X-ray diffraction (XRD; PANanalytical Xpert Pro) with Cu-Kα_1 Radiation (λ=1.54056 Å) operating at 35 kV and 15 mA with a scanning rate of 0.02°/s and 2θ at a range of 10° to 60°. The optical properties of the deposited nanostructures were evaluated by room-temperature photoluminescence (PL) measurements excited by the He-Cd laser line (325 nm).

6.3 Results and discussion

6.3.1 Morphological, compositional and structural properties of Ga-doped ZnO nanostructures grown on Si(100) substrate

Figures 6.1 (a-b) exhibit the general morphologies of the as-prepared Ga-doped ZnO material with a gallium concentration of 0.5% (atomic). It is clear from the observed FESEM images that the deposited material possesses needle shaped morphologies and is grown over the entire silicon substrate in high density. The nanoneedles are significantly vertically aligned to the substrate surface and the diameters of the nanoneedles were dwindling with the extension of its length which results in the origination of needle-shaped morphologies. The typical diameters of the grown structures at their roots and tips are in the range of 120 ± 30 nm and 20 ± 5 nm, respectively. The typical lengths of the grown nanoneedles are in the range of 4-5μm. Careful inspection of the inset of figure 6.1(b) shows that the nanoneedles are made by the accumulation and stacking of several hexagonal disks. The diameters of these nanodisks get smaller moving vertically leading to fine nanoneedle shaped morphology. Recently, Yan *et al*. have reported that, in the growth process of ZnO nanomaterials, the mean free path controlled by the reagent vapour pressure is considered as the crucial factor which is determining the formation of the layer-by-layer structure and needle or tower-shaped morphologies[149-151]. In the present experiment the reaction was performed at high temperature (950°C), which results in a higher reactant (zinc) vapour pressure,

and this consequently leads to a smaller mean free path. In addition, during the reaction and the high vapor pressure of Zn, the consumption and instability of the Zn source increased which leads to a reduction in the periods of metastable states. Therefore, the growth time for each layer was reduced which led to the formation of thin hexagonal nanodisks during the reactions. Further, it is also believed that the resulting smaller diameter of the nanodisks may be due to a reduced supply of the source material with time during the synthesis process. Moreover, as the Zn vapors have smaller mean free path which obstruct long-space migration, consequently at each step of the growth, the grown nanomaterial suffered with the fewer amount of source material, and hence the lateral growth of the hexagonal nanodisks was deterred and the axial growth was promoted[149-151]. As a result of high axial growth rate, the diameter of nanomaterial decreased as growth proceeds, hence finally nanoneedle shaped morphologies are formed.

Figure 6.1(c) exhibits a typical EDS composition of the pointed structures of the as-grown Ga-doped ZnO nanoneedles shown in figure 6.1(a). The EDS spectrum reveals the appearance of several well defined peaks for zinc, oxygen and Ga which clearly confirms that the synthesized products are made of these materials. The presence of a small peak of Si is due to backscattering from the substrate. The obtained spectrum shows that Ga was doped into the lattices of ZnO with (0.46 ± 0.01)% atomic, which is in very good agreement with the starting values of 0.5%.

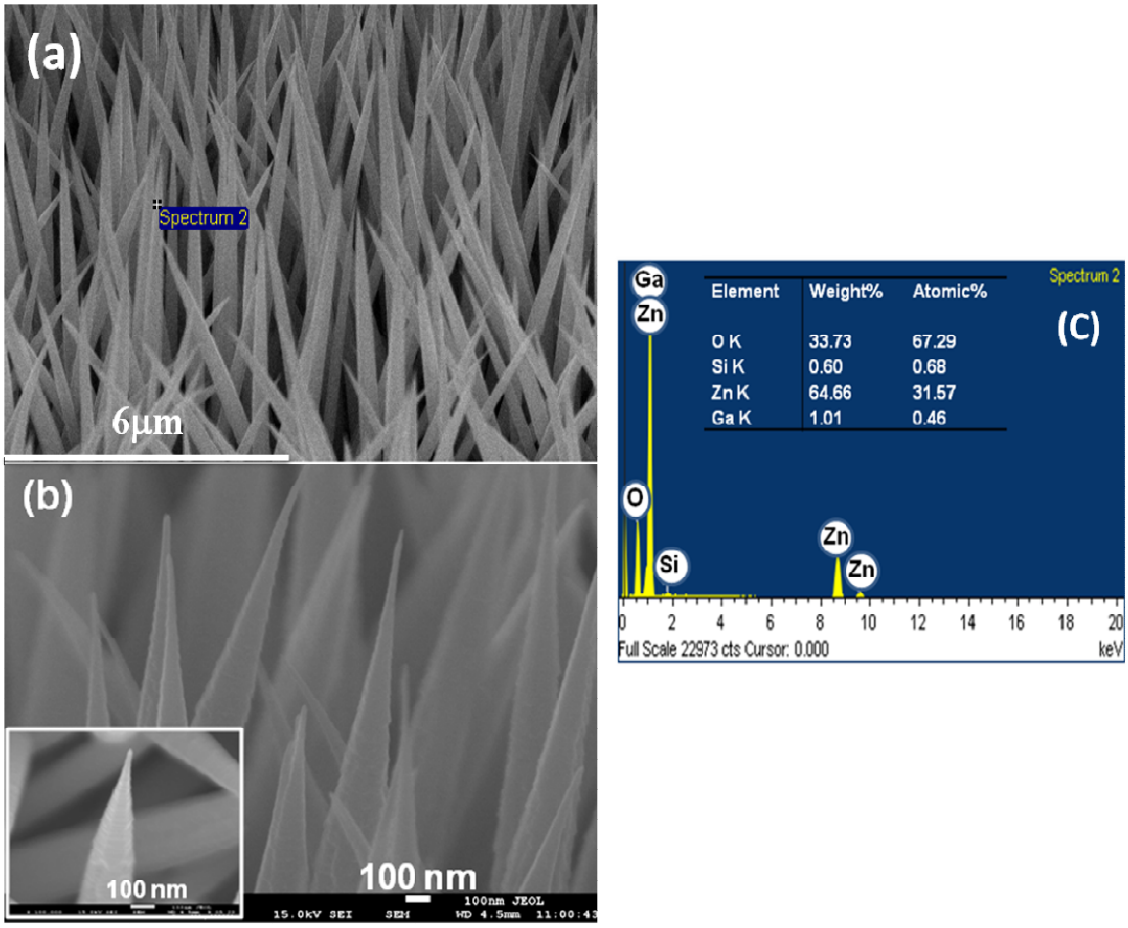

Figure 6.1 Typical (a) low-magnification, (b and inset) high-resolution FESEM images and (c) the corresponding EDS spectrum of the as-grown Ga-doped ZnO nanoneedles with Ga concentration of 0.5%.

With increasing the concentration of Ga up to 2% (atomic), the morphology of the synthesized materials was changed. Figures 6.2(a-b) show the general morphologies of the as-grown Ga-doped ZnO material with the gallium concentration of 2%. Figure 6.2(a) exhibits a low-magnification image which reveals that the deposited materials possess thorny branched morphologies in which hexagonal needles are radically grown. It was interesting to note that there was secondary growth on the tips of the needles as was confirmed by high-magnification FESEM (figure 6.2(b)). The results obtained show that the basic structure of the needles is almost the same as was observed in the case of the 0.5% Ga-doped nanoneedles shown in figures 6.1(a) and (b). However, increasing the Ga concentration leads to secondary growth of small nanoneedles grown on the outer surface of the tip of the needle shaped structures. It is predicted that the secondary growth might be due to the fact that the ionic radius of Ga (~0.62 Å) is smaller than the ionic radius of the Zn (~0.74 Å) so when a large number of Ga ions is incorporated into the lattice of the ZnO they cause strain and hence distortion of the primary growth [158-161]. This distortion helps in the formation of multipod structures as the distorted sites of the crystal act as the active sites for the secondary growth.

The typical diameter of the grown structures at their roots and tips are in the range of 500 ± 100 nm and 100 ± 20 nm, respectively. The typical lengths are in the range of 8-10 μm. Moreover, the diameters of the nanoneedles grown on the tips of the needles at their top and bases are in the range of 50 ± 20 nm and 120 ± 30 nm, respectively. The length of the secondary grown nanoneedles are about 1~1.5 μm.

Figure 6.2(c) shows a typical EDS spectrum of the as-synthesized multipod Ga-doped ZnO structures shown in figure 6.2(b). The observed spectrum exhibits several well-defined peaks related to zinc, oxygen and gallium which clearly reflects that the synthesized products are made of these materials and hence confirms that the prepared multipods are Ga-doped ZnO. In addition, the atomic percentage concentration for the Ga into the lattices of ZnO was estimated by EDS to be (1.67±0.02)% in very good agreement with the starting value of 2%.

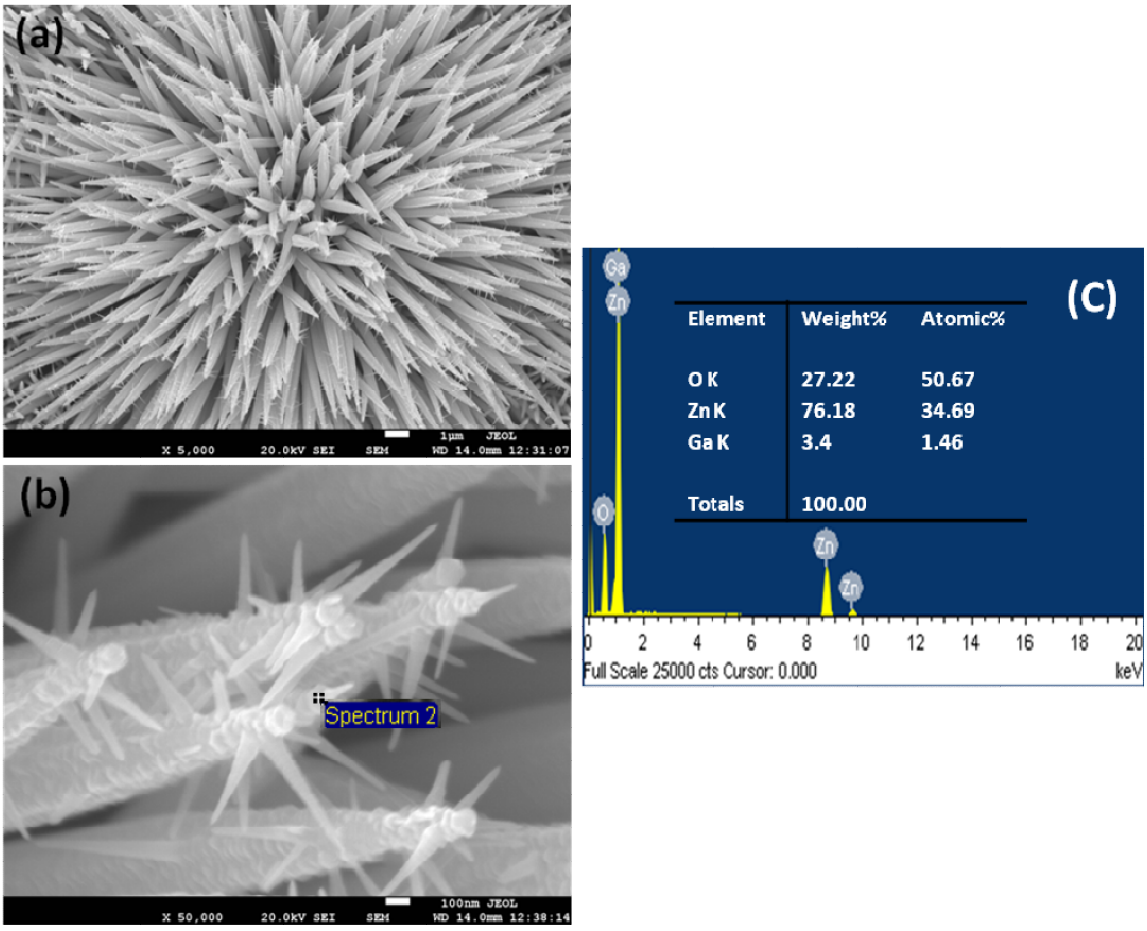

Figure 6.2 Typical (a) low-magnification, (b) high magnification FESEM images and (c) the corresponding EDS spectrum of the as-grown Ga-doped ZnO multipodswith Ga concentration of 2%. The high magnification image (b) shows the presence of two groups; the small tips that result from the secondary growth (will be referred to as group1) and the big base needles (will be referred to as group2).

Figure 6.3(a) exhibits the low magnification TEM images of the Ga-doped ZnO nanoneedles with Ga concentration of 0.5%. The observed TEM image is fully consistent with the obtained FESEM images in terms of morphological and dimensional view points. The nanoneedles possess wider bases and thinner tips. From the observed TEM image of single nanoneedle the tip diameter is about 15 nm. It is clear from the high-magnification TEM image that the nanoneedles are formed with the accumulation and stacking of several hundreds of hexagonal nanodisks. The nanodisks are stacked in such a manner that they clearly made nanoneedles shaped morphologies (figures 6.3(b) and inset).

A further investigation of chemical composition of the as-grown Ga-doped ZnO nanoneedles has been carried out by using TEM-EDS. Figure 6.3(c) shows a typical spot analysis TEM-EDS spectrum of the as-grown single Ga-doped ZnO nanoneedles shown in figure 6.3(b). The observed spectrum exhibited several well-defined peaks related to zinc, oxygen and gallium which confirm that the as-deposited nanoneedles are made of these materials. It is believed that the origin of the copper peaks in the spectrum is from the TEM copper grid. To confirm the presence of these materials in the grown structures, several TEM-EDS spectra were recorded from different areas of various nanoneedles and similar results were obtained which further confirm that the gallium atoms were efficiently included (i.e. doped) into the lattice of the ZnO.

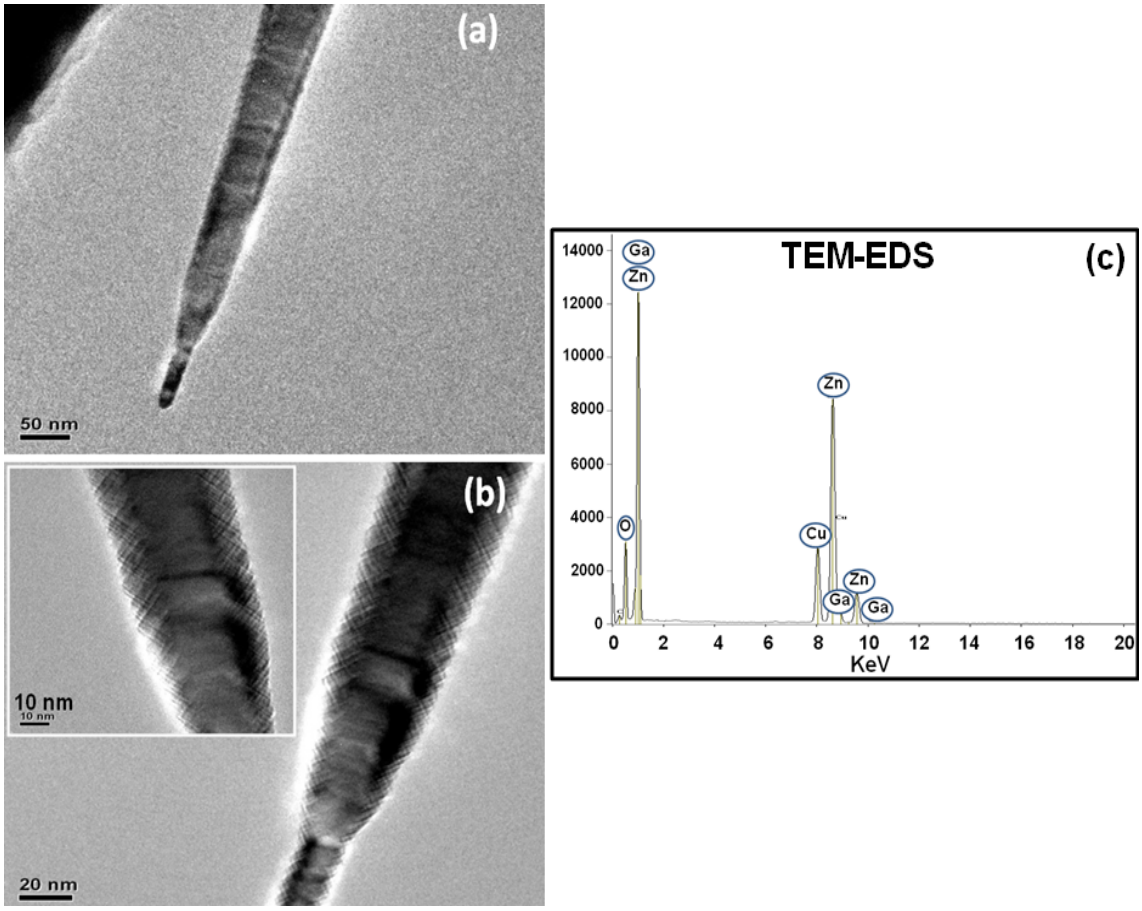

Figure 6.3 Typical (a) low-magnification, and (b and inset) high-resolution TEM images and (c) TEM-EDS of the as-grown Ga-doped ZnO nanoneedles with Ga concentration of 0.5%.

Figure 6.4 exhibits the (a) low-magnification and (b) high-magnification TEM images of the as-grown Ga-doped ZnO multipods with the nominal Ga concentration of 2%. The observed low-magnification TEM image confirmed that the synthesized product is multipod in which the small nanoneedles appear to originate from the tip of the big base needle (figure 6.4(a)). The observed TEM image is consistent with the examined FESEM results shown in figures 6.2(a-c) in terms of morphology and dimensionality. Figure 6.4(b) reveals the high magnification TEM image of the corresponding nanoneedles shown in fig 6.4(a). The calculated lattice spacing between two adjacent lattice fringes was found to be 0.52 nm which is in good agreement with the lattice constant of ZnO and indicates that the deposited materials have wurtzite structure.

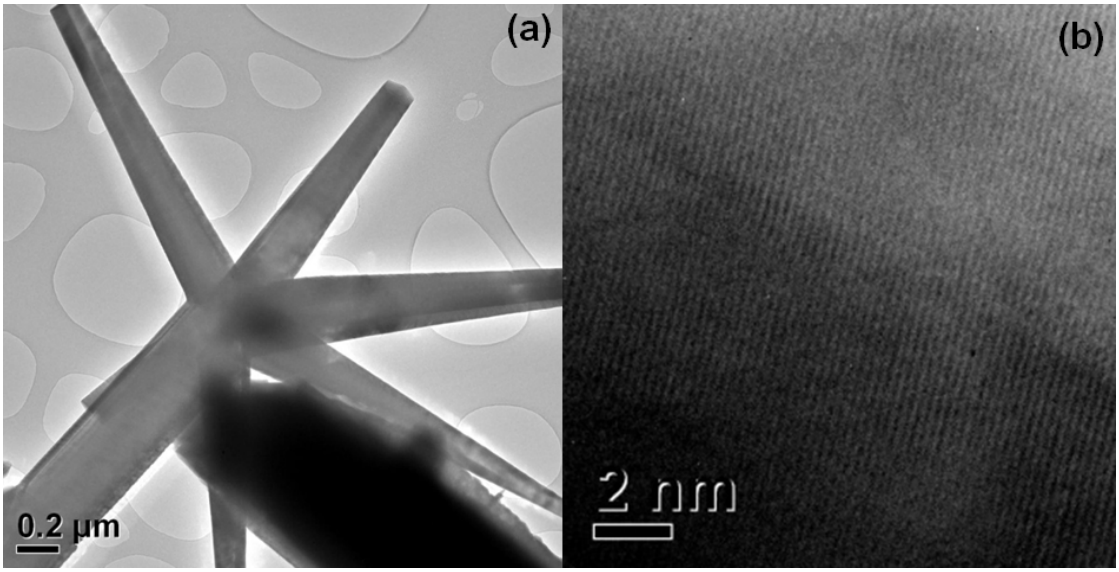

Figure 6.4 Typical (a) low-magnification, and (b) high-resolution TEM images of the as grown Ga-doped ZnO multipods with nominal Ga concentration of 2%.

To examine the crystallinity and crystal phases of the as-prepared Ga-doped ZnO nanostructures, X-ray diffractions analysis were performed. Figure 6.5 exhibits the typical XRD pattern of the as-synthesized; (a) Ga-doped ZnO nanoneedles and (b) multipod Ga-doped ZnO structures prepared on silicon substrate by simple thermal evaporation process. All the diffraction reflections appearing in the XRD pattern for both the nanostructures belong to wurtzite-structured hexagonal phase single crystalline bulk ZnO. The diffraction reflection appearing at 34.3º, in both cases and assigned as ZnO(002) phase, exhibit the highest intensity among all the observed reflections which

show that the synthesized Ga-doped ZnO nanomaterials are preferentially grown along the [002] direction. A small reflection appearing at 32.9º, in both cases, are due to the silicon substrate and assigned as Si(002). It is interesting to note that no reflection related with Ga or gallium oxide was seen in the observed XRD pattern which was due to the fact that the atomic radii of Zn (1.38 Å) and Ga (1.41 Å) are almost the same. Therefore, due to the similar atomic radii of Zn and Ga, no considerable lattice distortion was seen in the observed XRD pattern. In addition, it is seen that with increasing the Ga-doping concentration, the intensities of the XRD reflections are also increased which is similar to the reported literature[144].

The crystallite size for the dominant peak representing (002) plane of the XRD patterns in figures 6.5 (a and b) were calculated using Scherrer's formula given by equation (4.1) and the lattice parameters were also calculated from different XRD peaks (100) and (002) using the formula for a hexagonal structure given by equation 3.2 and the results of both samples (i.e. the Ga-doped ZnO nanoneedles (with0.5% Ga) and Ga-doped ZnO multipods (with 2.0% Ga) are listed in table 6.3. The estimated lattice constants of both samples (i.e. the Ga-doped ZnO nanoneedles (with0.5% Ga) and Ga-doped ZnO multipods (with 2.0% Ga) agree with the lattice constants of the hexagonal unit cell of ZnO wurtzite structure[20].

sample	Crystallite size (*D*) (nm)	Lattice constants (nm)
Ga-doped ZnO nanoneedles (0.5% Ga)	72.3	*a*=0.325 *c*=0.521
Ga-doped ZnO multipods (2.0% Ga)	120	*a*=0.325 *c*=0.521

Table 6.3 crystallite size and lattice constants as-synthesized Ga-doped ZnO nanoneedles with Ga concentration of 0.5%.and multipods Ga-doped ZnO structures with Ga concentration of 2%.

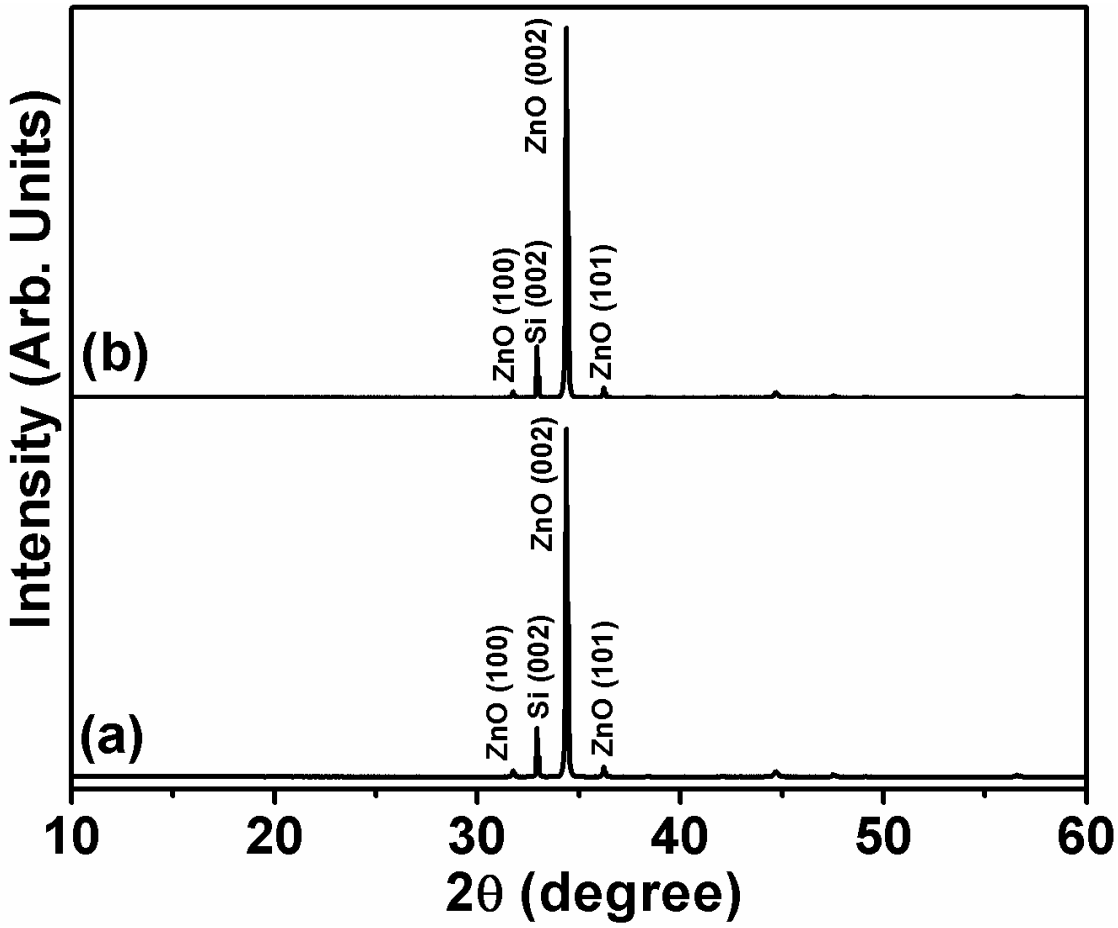

Figure 6.5 Typical XRD pattern of as-synthesized; (a) Ga-doped ZnO nanoneedles with Ga concentration of 0.5%.and (b) multipods Ga-doped ZnO structures with Ga concentration of 2%.

.

For the growth of nanomaterials, generally two mechanisms are known, i.e. vapor-solid (VS)[100] and vapor-liquid-solid (VLS) mechanisms[162,163]. In the case of VLS mechanism, normally, metal catalysts are used which form the eutectic alloys in the molten phase with the source materials and considered as a seed or nucleation site for the growth of nanomaterials. The main characteristic of the VLS mechanism is the existence of metal nanoparticles at the tips of the nanomaterials. As the grown Ga-doped ZnO nanomaterials, i.e. aligned nanoneedles and thorny branched structures, do not possess metal caps on their tips, hence the VLS mechanism for the growth of these nanomaterials can be ruled out. It is expected that the growth of these nanomaterials follow two steps: i) nucleation and ii) growth. In the first step, the source materials i.e. metallic zinc powder (melting point of zinc = 419.6°C) and Ga powder (melting point of gallium = 29.8°C) were mixed and heated up to the desired reaction temperature. During the heating process, the zinc and gallium source vapors were generated and transferred through the nitrogen carrier gas to the substrate surface and forms small metal alloy droplets which play an important role in the nucleation of the Ga-doped ZnO nanomaterials. This is the nucleation process. In the next step, in the presence of oxygen gas, the formed metal alloy droplets converted into oxide and lead to the formation of Ga-doped ZnO nanomaterials. It is assumed that in the case of low-amount of Ga (0.5% Ga), the number of nuclei were limited hence facilitate the growth of 1D nanomaterials while when Ga concentration was increased (2.0% Ga), the number of nuclei were also increased which contributed significantly in the formation of branched Ga-doped ZnO nanomaterials. The proposed mechanisms for the formation of Ga-doped ZnO nanomaterials are just plausible and hence more studies are needed to find more conclusive evidences.

6.3.2 Room-temperature photoluminescence (PL) properties of Ga-doped ZnO nanostructures grown on a Si(100) substrate

The optical properties of the as-deposited Ga-doped ZnO nanostructures were characterized by using room-temperature photoluminescence (PL) spectroscopy. Figures 6.6 and 6.7 are the PL spectra of the as-grown Ga-doped ZnO nanomaterials. Typically, two peaks are appearing in the room-temperature PL spectrum of ZnO based nanomaterials, i.e. a peak in the UV region, also referred to as the UV emission of near band edge emission (NBE) and a peak in the visible region, also referred to as visible emission or deep level emission (DLE). It is reported that the origin of the near band emission in the PL spectrum are due to the recombination of the free-excitons through an exciton-exciton collision process[164]. However, the appearance of green emission or deep level emission is because of the radial recombination of the photo-generated hole with the electrons[165]. It is also reported that with increasing the structural defects and impurities, the intensity of deep level emission increases while decreasing the defects and impurities, the intensity of the near band emission increases[166].

Figure 6.6 exhibits the room-temperature PL spectrum of lightly (0.5 atomic %) Ga-doped ZnO nanoneedles which shows a strong UV emission (NBE) at 383 nm and a suppressed and broad green emission (DLE) at 545 nm with NBE/DLE intensity ratio of ~ 2.66. Therefore, due to strong NBE and suppressed green emission in the PL spectrum of Ga-doped ZnO nanoneedles, it could be concluded that the synthesized nanoneedles possess good optical properties and exhibiting very low structural defects and impurities (low amount of Ga-doping). The observed PL results for Ga-doped ZnO nanoneedles are consistent with already reported literature[167-169].

Figure 6.7 demonstrates the room-temperature PL spectrum of heavily (2 atomic %) Ga-doped ZnO multipods structures. The observed PL spectrum exhibits a strong and sharp deep level emission (DLE) at 533 nm and a suppressed UV emission (NBE) at 385 nm NBE/DLE intensity ratio is ~ 0.075. The origin of the strong deep level emission was due to the heavy doping of gallium ions into the lattices of ZnO which reflect the origination of some defects in the ZnO lattice by gallium ions doping.

The PL results shown in figures 6.6 and 6.7 are in line with earlier observations i.e. the significant difference in the intensity ratios of the deep level emission peak, which is usually attributed to impurities and structural defects (oxygen vacancies and zinc interstitials) in the ZnO crystals, to the near band edge emission peaks[165,166]. In the

case of lightly doped Ga ions (0.5%), an enhanced UV emission was observed in the PL spectrum of Ga-doped ZnO nanoneedles, however, when Ga ions were heavily doped (2%) into the lattices of Ga-doped ZnO multipods, a strong deep level emission was seen in the PL spectrum. This is clear from the observed results that increasing the impurity in the ZnO lattices, the green emission intensities in the room-temperature PL spectra are increases. Also by comparing the pure ZnO nanomaterials (figures 4.6 and 5.4), the Ga-doped ZnO exhibited much enhanced DLE due to the addition of Ga ions into the lattices of ZnO.

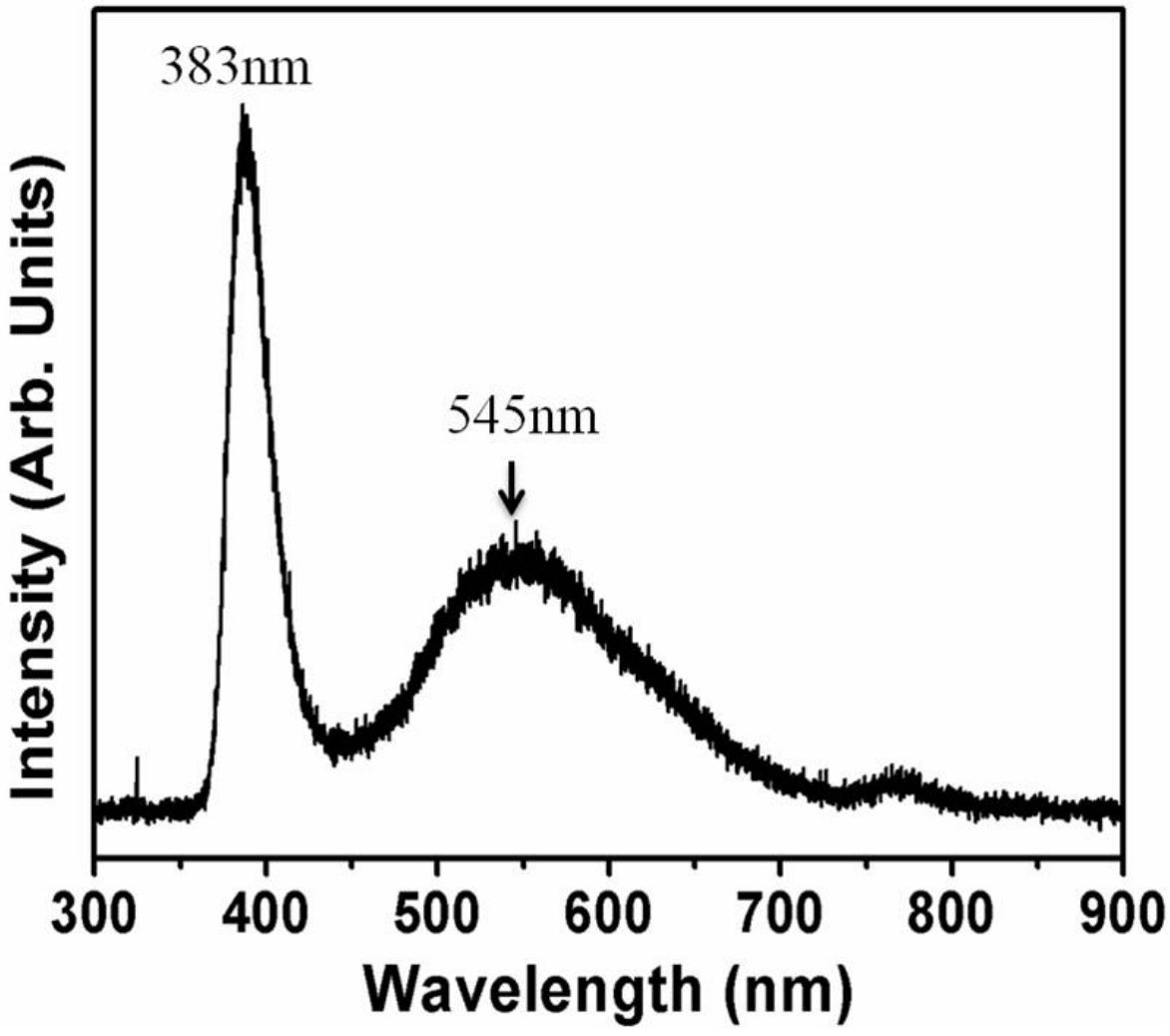

Figure 6.6 Typical room-temperature photoluminescence spectrum of the as-grown Ga-doped ZnO nanoneedles with Ga concentration of 0.5%.

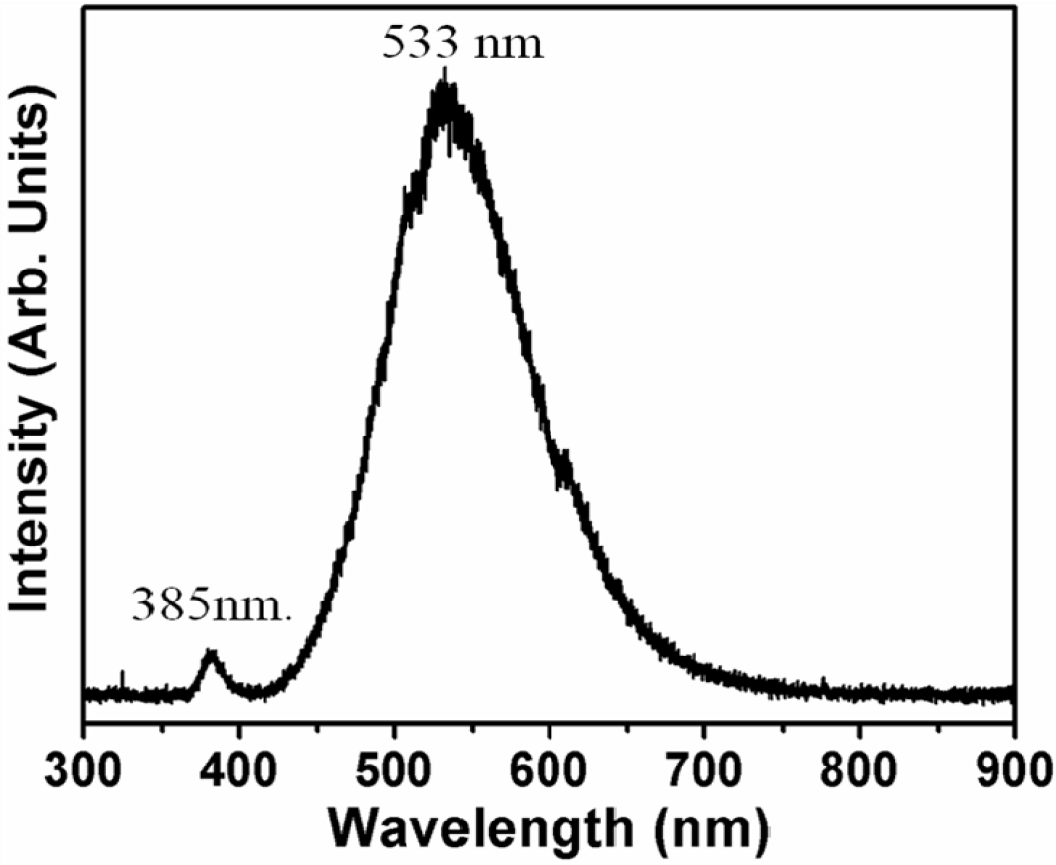

Figure 6.7 Typical room-temperature photoluminescence spectrum of the as-grown Ga-doped ZnO multipods with Ga concentration of 2%.

6.3.3 Field emission studies

6.3.3.1 Current –voltage characteristic of Ga doped ZnO nanostructures

The field emission properties of Ga doped ZnO nanoneedles (0.5% Ga) were investigated under pressure of $3x10^{-8}$ mbar. After a number of emission current measurements scans (not shown for brevity), figure 6.8(a) shows a reproducible and stable *I-V* curve of Ga doped ZnO nanoneedles with Ga concentration of 0.5%. It is clearly seen from the *I-V* curve that the emission current increases exponentially with increasing the applied voltage. The turn on voltage and threshold voltage are 1.7 kV with observed emission current of 110 nA and 2.7 kV with emission current of 20 μA, respectively. The corresponding F-N plot is shown in figure 6.8(b). The experimental data are almost fitted into straight line supporting the field electron emission mechanism (tunneling process). However, since the work function of the Ga-doped ZnO nanoneedles is unknown, it is not possible to estimate the field enhancement factor (β) from the linear fitting.

The interpretation of the excellent field emission performance of the Ga-doped ZnO nanoneedles with Ga concentration of 0.5% will stand on two grounds (i.e. geometry and properties of the Ga doped ZnO nanoneedles). Firstly, the tip morphology (needle shape) and high aspect ratio of the Ga doped ZnO nanoneedles gives rise to huge enhancement of the local electric field on the apex of the ZnO emitters[170] which result in low turn on voltage (1.7 kV) compared with the ZnO nanorods with flat end which was 2.55 kV (see chapter 5 section 4.3). Secondly, doping of gallium into ZnO has two major effects on field emission properties: the first one is that the Ga-doping reduces resistivity of the ZnO nanoneedles leading to voltage drop along the nanoneedle which results in an enhancement of the effective field at nanoneedle tips[144]. The second effect is that, n-type doping lifts the Fermi level up and hence lowering the work function of the ZnO nanoneedles[144]. Due to the combined effect of these two elements (i.e. sharp tip morphology and doping effect) as well as the vertical alignment, the Ga doped ZnO nanoneedles exhibit excellent field emission performance and therefore, can serve as an efficient electron source in vacuum electronic and flat panel display.

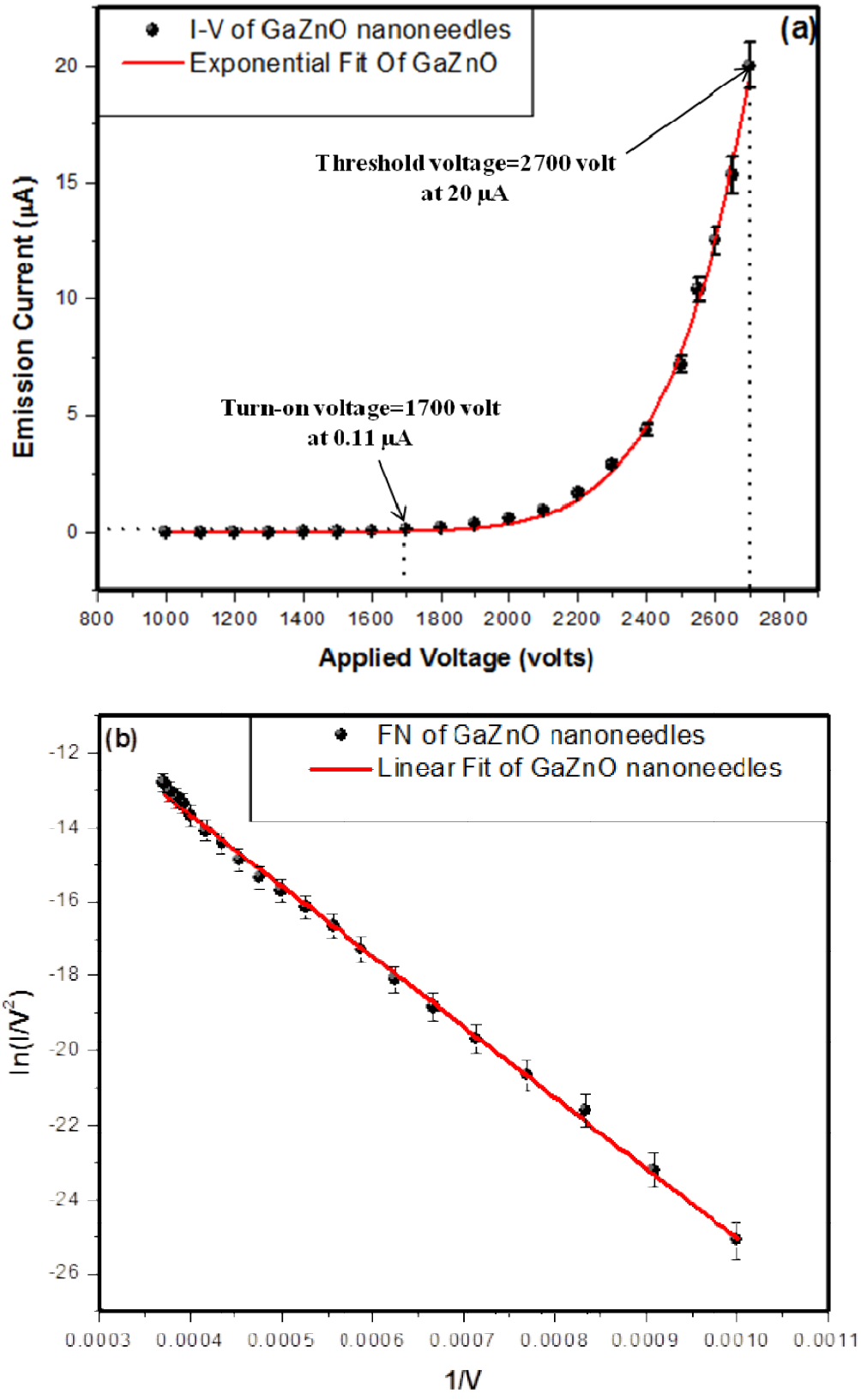

Figure 6.8 (a) Current-voltage (*I-V*) characteristic of of the as-grown Ga-doped ZnO nanoneedles with Gaconcentration of 0.5%. (b) The corresponding F-N plot.

The field emission properties of the as-grown Ga-doped ZnO multipods with Ga concentration of 2% were also tested under pressure of $3x10^{-8}$ mbar. Figure 6.9(a) shows the *I-V* characteristics of these structures. The emission current increased with the systematic increase in the applied voltage and the turn on voltage was found to be 2 kV with observed emission current of 83 nA. An emission current of 18 µA was recorded at threshold voltage of 2.95 kV.

The corresponding F-N plot is shown in figure 6.9(b). Interestingly, the experimental data can not fit into one straight line, but instead two straight lines with different slopes. At low electric field region, the slope of the linear fitting is lower than that in the high electric field region. This phenomenon presumably occurred due to the nonuniformity in the field enhancement factors of this sample[171]. The Ga doped ZnO multipods consists of two groups; the small tips as a result of the secondary growth (will be referred to as group1) and the big base needles (will be referred to as group2) as was reveled by FESEM and TEM images (see previous section (3.1) figures 6.2 and 6.4). Group1 and group2 have different field enhancement factors β_1 and β_2 respectively, where $\beta_1 > \beta_2$. It is well known that the slope of the F-N plot is inversely proportional to the field enhancement factor β. At low electric field region (1.3 kV-2.5 kV) electron emission only comes from the small tips (group1) with the larger field enhancement β_1, which corresponds to the part of the FN plot with a small slope, while at high electric field region, the big base needles (group2) start to emit electrons in addition to the small tips. Moreover, with increasing the field the contribution from group2 becomes comparable to those in group1. Therefore, at high electric field region the total emission is determined by the contribution from both groups with an expected field enhancement factor to be smaller than β_1 and thus larger slope of the F-N plot at this region (i.e. from 2.5 kV to 2.95 kV). Similar behavior has been reported by Zhou *et al.* and was attributed to the differences in the field enhancement factor due to various shapes of tungsten oxide nanotips[172]. On the other hand, several studies attributed the feature of two lines to the two-band FE mechanism[173,174] (i.e. emission from the conduction band at low field region and from the valance band as well as the conduction band at high field region).

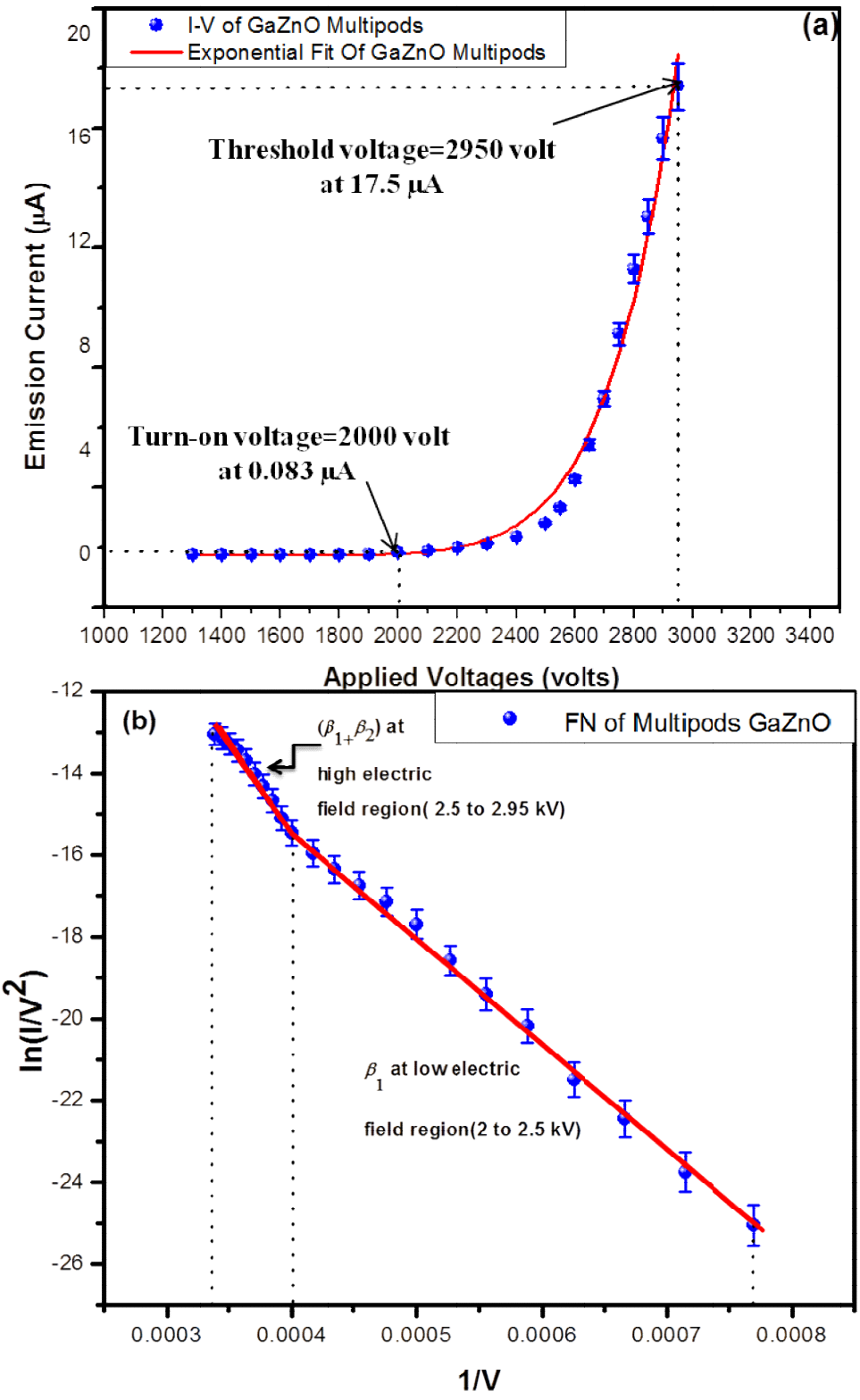

Figure 6.9 (a) Current-voltage (*I-V*) characteristic of of the as-grown Ga-doped ZnO multipods with Ga concentration of 2%. (b) The corresponding F-N plot.

6.3.3.2 The field emission stability of the Ga-doped ZnO nanoneedles

The emission current stability of the Ga-doped ZnO nanoneedles with Ga concentration of 0.5% was tested at different fixed voltages. Figure 6.10(a) shows the emission current stability profile of the Ga doped ZnO nanoneedles for a period of 10.5 hours at the anode voltage of 1.7 kV. Initially and over the first hour, the emission current exhibited step like current fluctuations of ~ 18.18% ranging between 100 nA and 120 nA as was clearly shown in the enlarged part in figure 6.10(b). Such fluctuations could be induced by the alteration of the work function and/or the local electric field due to several reasons such as the self cleaning process and the adsorption and desorption effect. After that, the present stability shows a stable emission current for a continuous operation of about 9.5 hours of an average corrent of about 95 nA with only 10% current fluctuation.

When the extraction voltage was increased to be 2 kV, the average emission current increased to be about 300 nA and recorded for only 18 minutes as shown in figure 6.11. The fluctuation of the emission current is as high as 85%. The higher fluctuation and short life time is believed to be due to the resistive heat as well as the ion bombardment as the collision between the electrons and surrounding molecules in the gap between the anode and the cathode become significant at higher emission current creating positively charged ions which are accelerated toward the negatively charged emitters and causing damage to them.

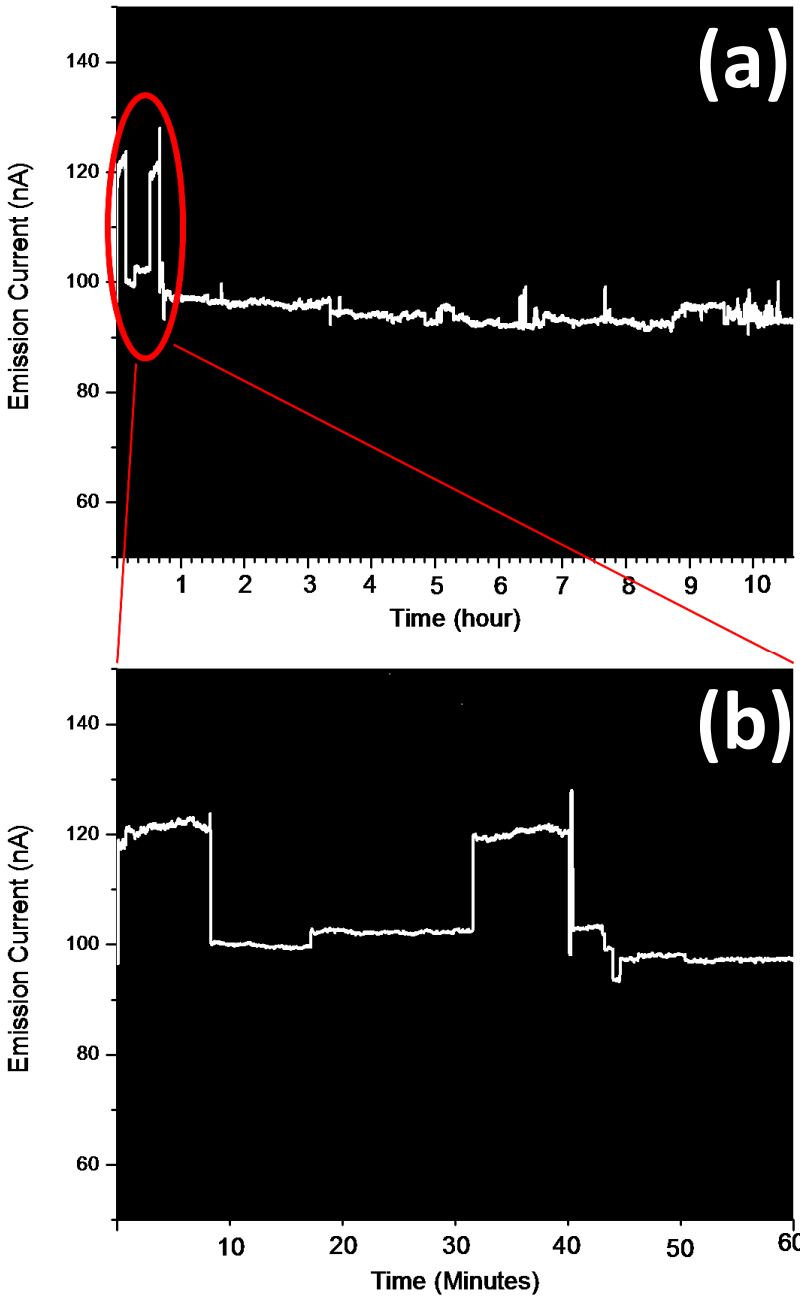

Figure 6.10 the emission current stability profile of Ga-doped ZnO nanoneedles with Ga concentration of 0.5% under a constant applied voltage of 1.7 kV.

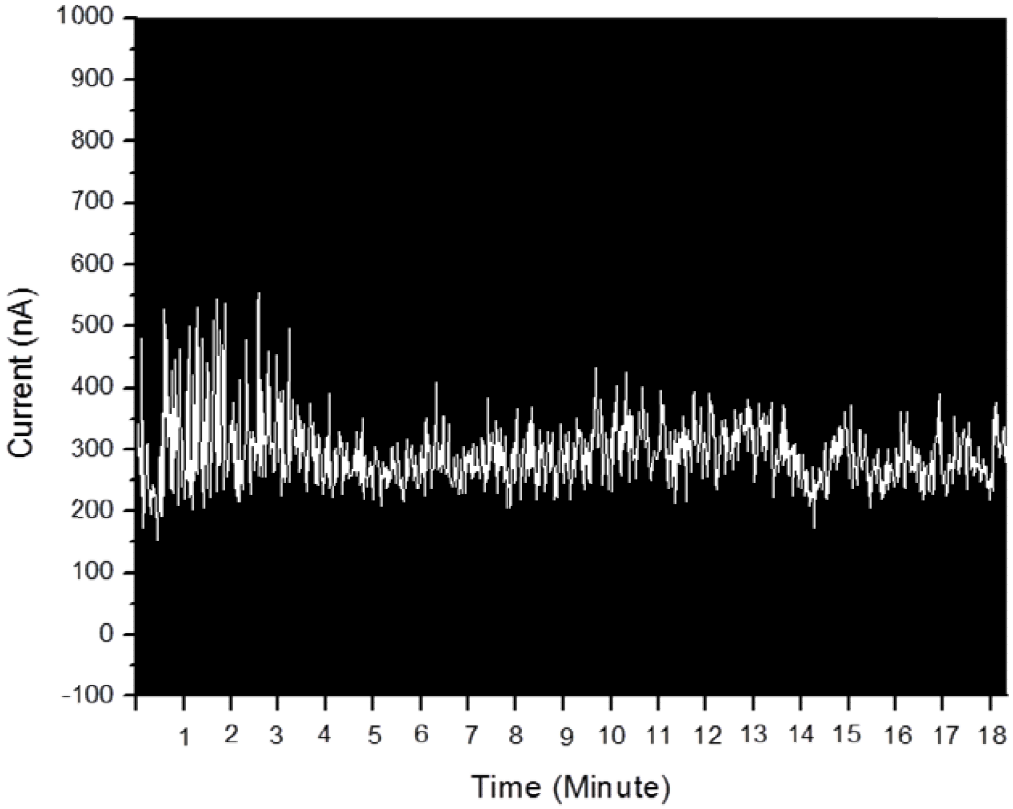

Figure 6.11 the emission current stability profile of Ga-doped ZnO nanoneedles with Ga concentration of 0.5% under a constant applied voltage of 2 kV.

6.3.3.3 Field emission patterns from Ga-doped ZnO nanoneedles

The field emission images of the Ga-doped ZnO nanoneedles with Ga concentration of 0.5% as a function of applied voltages are shown in figure 6.12. Several emission sites were observed and captured at an applied voltage of 1.6 kV with an emission current of about 35 nA. As can be seen clearly, at higher applied voltages (1.9 kV, 2.2 kV, 2.5 kVand 2.7 kV), these spots were getting intense and more emission sites appeared with corresponding emission current of 0.6 µA, 2.9 µA, 7.2 µA and 20 µA respectively.

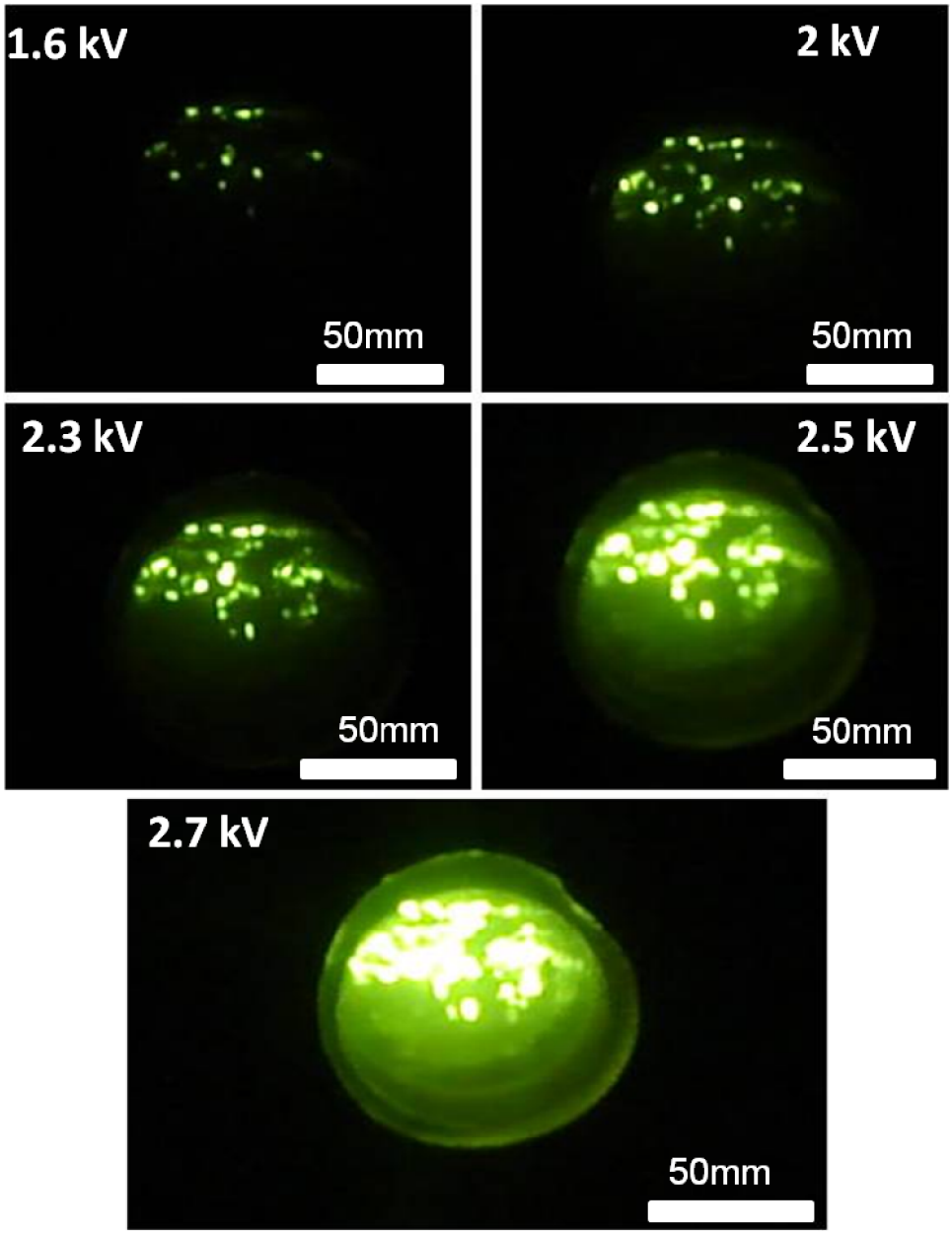

Figure 6.12 Field emission patterns of Ga-doped ZnO nanoneedles with Ga concentration of 0.5% grown on Si substrate.

6.4 Conclusion

In summary, the effect of gallium ion concentrations (0.5 and 2%) on the morphologies, structural and optical properties of Ga-doped ZnO nanostructures have been studied and presented in this chapter. The Ga-doped ZnO nanomaterials were synthesized by simple thermal evaporation process and interestingly it was observed that by varying the concentration of Ga from 0.5% to 2%, different morphologies, i.e. nanoneedles to multipod structures were observed. This research demonstrates that simply by controlling the concentration of Ga, the morphologies of Ga-doped ZnO nanomaterials can be controlled for specific applications. The field electron emission characteristics of the samples were investigated. The Ga-doped ZnO nanoneedles sample exhibits excellent field emission properties owing to their sharp tip morphology, good electrical properties and vertical alignment. In addition, the nonlinearity in the F-N plot in the case of Ga-doped ZnO multipods was attributed to the nonuniform field enhancement factors (β). At the low macroscopic electric field region, emission mainly comes from the small tips (thorns) with large field enhancement factor (β_1), which correspond to an F-N plot part with small slope. At high macroscopic electric field region, big base needle with low field enhancement factor (β_2) also become emission sites, which reduce the average of field enhancement factor leading to increase in the slope of corresponding part of the F-N plot. The field emission stability of the Ga-doped ZnO nanoneedles with Ga concentration of 0.5% was tested at different applied voltages and presented. The Ga-doped ZnO nanoneedles exhibit better field emission performance in comparison with the Ga-doped ZnO multipods due to better alignment and uniformity.

CHAPTER7

INDIUM-DOPED ZnO NANOPENCILS: GROWTH, CHARACTERIZATIONS AND FIELD EMISSION PROPERTIES

7.1 Introduction

The tip morphology plays an important role in the field emission properties of ZnO nanostructures. Various morphologies of ZnO nanostructures such as nanosheets networks, nanorods and nanoneedles have been synthesized using various fabrication techniques and their optical and FE properties have been checked and demonstrated in the previous chapters. Moreover, detailed study of the effect of metal doping on the morphology and the field emission properties of ZnO nanomaterials was also examined and reported. Conventionally, one of the possible routes for improving the field emission performance of an emitter is to increase the geometrical enhancement factor near the tip apex. In the case of the tungsten FE emitter, this is typically achieved by electrochemically etching the tip to very sharp end of ≈ several nanometers, Obviously, the 1D Nano-structure has the advantages of both high aspect ratio and large throughput particularly if the ZnO nanostructures, are further enhanced by being fabricated with specific shape and size.

It has been reported that pencil-like nano-tips, which is being formed in two step configuration growth can be promising candidates for the field emission applications[175]. To further investigate this hypothecs, the growth, characterizations and field emission properties of In-doped ZnO nanopencils will be presented in this chapter. Theses nanopencils emitters are grown on silicon substrate by simple and facile thermal evaporation process.

7.2 Experimental details

In-doped ZnO nanopencils were grown on silicon substrate by facile thermal evaporation process, using metallic indium (99.99%) and zinc powders (99.98%) in the presence of oxygen. Silicon wafers (1 x 1 cm) were used as substrates for the deposition of In-doped ZnO nanopencils which were ultrasonically cleaned with DI water and isopropyl alcohol and finally rinsed with acetone. In a typical reaction process, high-

purity metallic indium and zinc powders were thoroughly mixed in 1:10 ratio (5.0 % atomic) and transferred into quartz boat and placed at the centre of the quartz tube furnace. Consequently, the cleaned substrates were placed adjacent to the source material. Prior to heating, the quartz tube furnace was evacuated to 10^{-1}~ 10^{-3} Torr and kept under vacuum throughout the entire synthesis process. After evacuation of the quartz tube, the furnace was heated up to 800°C using a halogen lamp heating system in the presence of high purity nitrogen and oxygen gases. Once the temperature of the furnace reached over 500°C, indium and zinc vapors were generated (as the melting point of indium and zinc powders are less than 500°C) which were transferred to the substrate by nitrogen carrier gas. The oxygen gas was reacted with the generated zinc and indium vapors and finally the growth was carried out. The reaction was completed in 1 hr. A concise summary of the growth parameters of In-doped ZnO nanopencils are presented in table7.1.

After completing the reaction, the furnace was very slowly cooled down (15°C/min) to room-temperature and the deposition of a grayish white coloured product was observed on the entire substrate surface. The deposited material was characterized in terms of their morphological, structural and optical characterizations by using various analytical tools.

The detailed morphologies of as-prepared doped ZnO material was examined by field emission scanning electron microscopy (FESEM; JEOL-JSM-7600F) and transmission electron microscopy (TEM). The composition of as-prepared material was investigated by energy dispersive spectroscopy (EDS) attached to FESEM. The structural properties of the prepared material was examined by X-ray diffraction (XRD; PANanalytical Xpert Pro.) with Cu-Kα radiation (λ=1.54178 Å) in the range of 2θ between 20° to 65°. To investigate the crystal purity, the prepared material was studied by Raman-scattering measured with the Ar^{+} laser lines (513.4 nm) as the exciton source. The optical properties was examined by room-temperature photoluminescence (PL) measured with He-Cd laser lines (325 nm) as the exciton source.

Nanomateial Type	In-doped ZnO nanopencils
Growth Technique	Thermal evaporation process using horizontal quartz tube furnace
Reactants	High-purity metallic zinc and In powders, oxygen and nitrogen gases
Substrate	Silicon substrate
Reaction Temperature	800°C
Reaction Time	1.0 hr

Table 7.1 Summary of the growth parameters of In-doped ZnO nanopencils.

7.3 Results and discussion

7.3.1 Morphological, compositional and structural properties of In-doped ZnO nanopencils

The general morphologies of the as-prepared material was examined by field emission scanning electron microscopy (FESEM) as figure 7.1 shows, the resultant fabricated nanostructures are of pencil-shaped morphologies. The nanopencils are grown in very high density as was confirmed from the low-magnification image shown in figure 7.1(a). It is interesting to see that the nano-pencils are made of two parts; i.e. a nanorod as well as a nanoneedle which are connected in such a manner that the base of the nanoneedle is attached to the head of the nanorod. Very interestingly, the nanopencils are exhibiting smooth and clean surfaces throughout their lengths (figure 7.1(b)). The typical diameters of the base nanorods in nanopencils are 80 ± 10 nm while the lengths are in the range of 3 ± 0.5 μm. The diameters for the tips of the nanopencils are ~15 ± 3 nm (figure 7.1(c)).

The elemental composition of the as-prepared In-doped ZnO nanopencils were examined by energy dispersive spectroscopy (EDS) attached to FESEM. Figure 7.1 (d) exhibits a typical EDS spectrum of an as-prepared In-doped ZnO nanopencils which confirms that the nanopencils are made of zinc, indium and oxygen as spectrum exhibits peaks only related to these elements. No other peak related to any other element is observed in the EDS spectrum. This further reveals that the nanopencils are In-doped ZnO without any significant impurity, up to the detection limit of the EDS method.

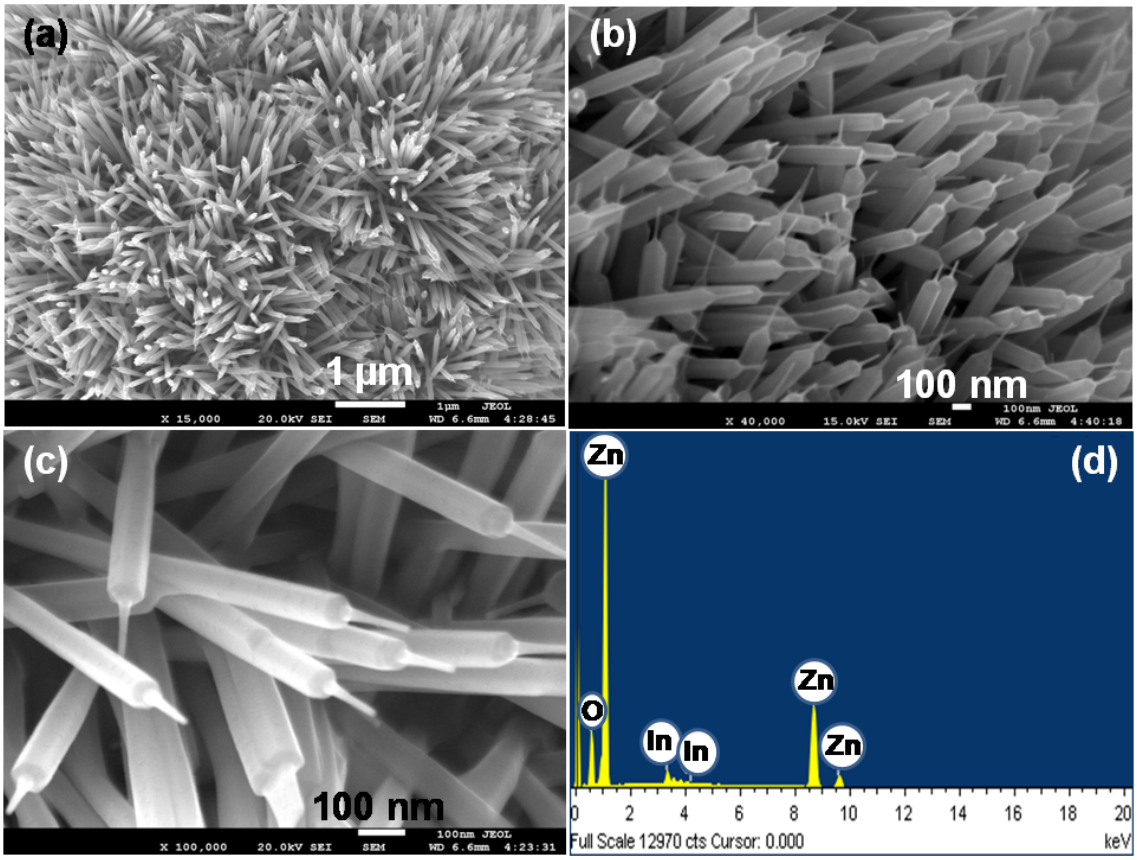

Figure 7.1 (a-c) FESEM images showing the morphology of the In-doped ZnO nanopencils on silicon substrate prepared by thermal evaporation process. Image (a) shows the dense growth of In-doped ZnO nanostructures. (b and c) images show that the In-doped ZnO nanostructures are made of two parts: ultra fine tip connected to a base of ZnO nanorods. (d) Shows the EDS spectrum showing the constituent elements found on the grown structures.

The crystallinity and crystal phases of the ZnO nanopencils were examined by X-ray diffraction (XRD) and the results are shown in figure 7.2. Several well defined diffraction reflections at 31.8°, 32.9°, 34.49°, 36.4°, 47.6°, 54.5°, 56.6° and 62.9° are seen in the observed XRD pattern. The diffraction reflections appeared at 31.8°, 34.2°, 36.3°, 47.6°, 56.6° and 62.9° are related with the wurtzite hexagonal phase of ZnO and assigned to be ZnO(100), ZnO(002), ZnO(101), ZnO(102), ZnO(110) and ZnO(103), respectively. A small diffraction reflection originated at 54.5° is related with In and assigned as In(112). In addition to zinc and In reflections in the diffraction pattern, a small reflection appeared at 32.9° is due to the silicon substrate and can be attributed to Si(002). The crystallite size was estimated from dominant peak of the XRD pattern in figure 7.2 using Scherrer's formula given by equation (4.1). In addition, the lattice parameters of the In-doped ZnO nanopencils were also calculated using the formula for a hexagonal structure given by equation (3.2) from two XRD peaks positioned at 34.49°and 36.4° representing (002) and (101) planes, respectively. The crysrtallite size and the estimated lattice constants of the In-doped ZnO nanopencils are summarised in table 7.2. The estimated lattice constants agree with the TEM observation in figure 7.3(b).

Crystallite size (D) (nm)	Lattice constants (nm)
36.4	a= 0.324 c= 0.52

Table 7.2 crystallite size and lattice constant of the In-doped ZnO nanopencils grown on Si substrate.

Finally, due to the presence of a small indium peak with other wurtzite ZnO reflections in the pattern reveals that the indium atoms are efficiently incorporated into the lattices of grown nanopencils. Moreover, no characteristic diffraction reflection related with any impurity was detected in the pattern within the detection limit of the X-ray diffractometer, further revealed that the synthesized nanopencils are well-crystalline and are pure In-doped ZnO.

The detailed structural characterizations of the as-deposited In-doped ZnO nanopencils were carried out by transmission electron microscopy (TEM) and shown in figure 7.3. For the TEM analysis, the prepared In-doped ZnO nanopencils grown on silicon substrate were ultrasonically dispersed in acetone and a drop of acetone solution, which contains the In-doped ZnO nanopencil, was placed on a copper grid and

examined. Figure 7.3(a) exhibits the low magnification TEM image of tip portion (nanoneedle) of the as-prepared single In-doped ZnO nanopencil. As can be seen from the TEM image, the tip of the nanopencil exhibits the same morphology as was observed in FESEM. The nanoneedle diameter gradually decreases with increasing the length and finally a needle-shape is formed. The typical diameter of the nanoneedle at its tips and root are in the range of 13-15 nm and 16-18 nm, respectively. The nanoneedles possess smooth and clean surfaces throughout their length and the roots exhibit wider diameters while the tips show narrow diameter. Figure 7.3(b) exhibits the high resolution image of the nanoneedle shown in figure 7.3(a). The HRTEM image shows well-defined lattice fringes with the distance between two fringes are ~0.52 nm, which is equal to the lattice constant of crystalline ZnO and indicates that the deposited materials have wurtzite structure. Thus far, one can conclude that In atoms are efficiently and appropriately incorporated into the lattices of ZnO in such a way that these doped (In) atoms does not affect the crystal structure of the parent crystal, i.e. wurtzite hexagonal phase ZnO.

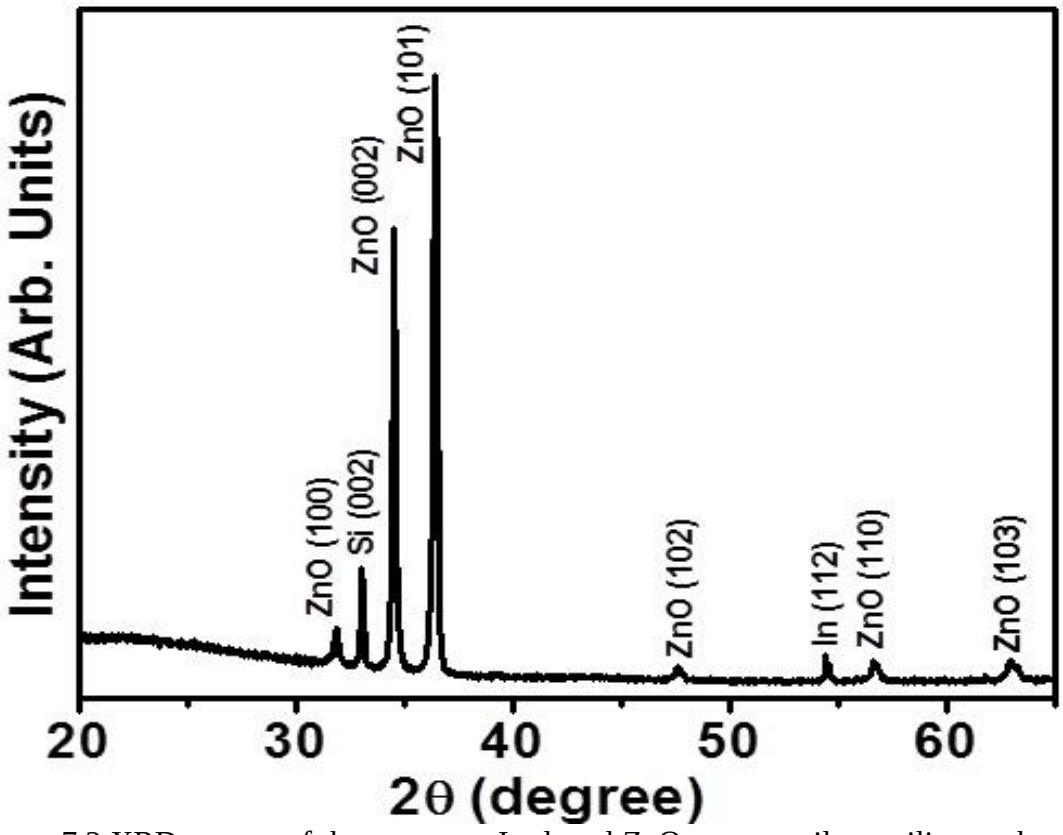

Figure 7.2 XRD pattern of the as-grown In-doped ZnO nanopencils on silicon substrate prepared by thermal evaporation process showing a well crystalline wurtzite hexagonal phase of ZnO. The small peak at 54.5° indexed to In(112).

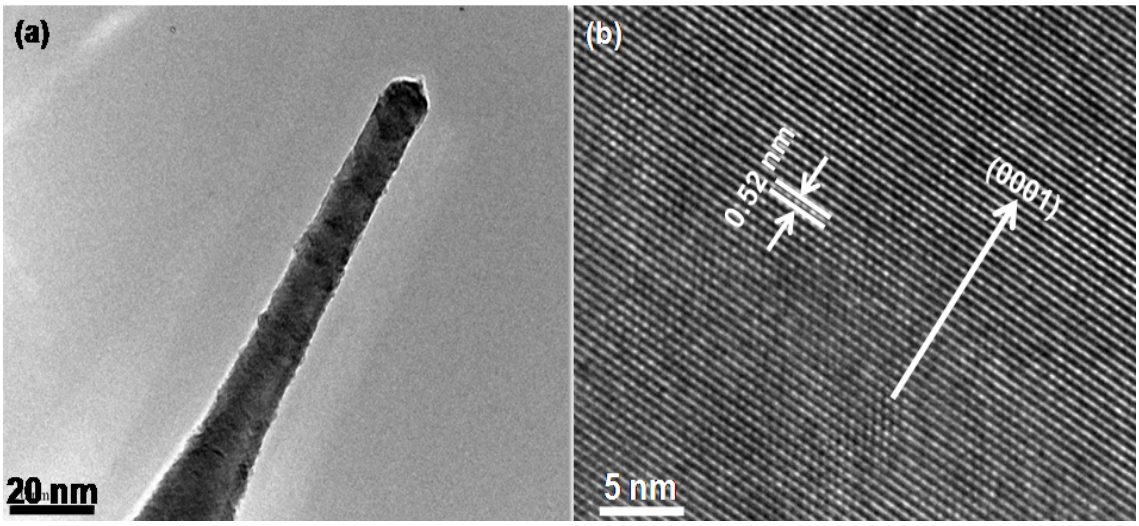

Figure7.3 (a) low magnification TEM image of the ultra fine tip (nanoneedle) of the as-grown In-doped ZnO nanopencil with a diameter in the range of 13-15 nm and (b) high-magnification TEM images of as-grown In-doped ZnO nanopencils on silicon substrate showing well-defined lattice fringes with *d* spacing equal to the lattice constant of crystalline ZnO (~0.52 nm).

7.3.2 Optical and Raman-scattering properties of In-doped ZnO nanopencils

The optical properties of as-prepared In-doped ZnO nanopencils were characterized at room-temperature using photoluminescence (PL) spectroscopy and presented in figure7.4. Normally, ZnO based nanomaterials exhibits two bands in the room-temperature PL spectrum, i.e. a band in the UV-region and a band in the visible region. The band which is indicated by the UV-region is called the 'near band edge emission' and according to the literature this band appears in the PL spectrum of ZnO based materials due to the free-exciton recombination[100]. The visible region band is called the 'deep level emission' and there are several theories reported in the literature regarding the origination of this band in the PL spectrum of ZnO based nanomaterials[1,4]**.** Among various theories, the most commonly reported one regarding the origination of deep level emission is that it ascribed to the single ionized oxygen vacancy and arises from the recombination of a photo-generated hole with the single ionized charged state of the defect in ZnO[177]. In addition, it is also reported that deep level emission result from the radiative transitions between shallow donors (related to oxygen vacancies) and deep acceptors (zinc vacancies)[178]. It is well known that with the addition of foreign element (i.e. dopant) into the lattices of a ZnO crystal, the intensity of the deep level emission increases while by decreasing the defects and impurities, the intensity of the near band emission increases[179]. These facts are well-mentioned and discussed in chapters 4-6 in which pure ZnO nanomaterials and Ga-doped ZnO nanostructures are demonstrated. Figure 7.4 exhibits the typical room-temperature PL spectrum of In-doped ZnO nanopencils and shows a sharp and strong UV emission (NBE) at ~391 nm with a suppressed and broad deep level emission (DLE) at ~560 nm. The calculated NBE/DLE intensity ratio is ~ 1.88. Because of the presence of deep level emission in the room-temperature PL spectrum of In-doped ZnO nanopencils, one can conclude that this band results due to the doping of indium which leads to some defects in the lattices of ZnO and hence enhance the green emission. The observed PL spectrum for In-doped ZnO nanopencils is in line with earlier observation in PL results of Ga-doped ZnO nanomaterials demonstrated in chapter 6.

Raman-scattering is an excellent tool to determine the vibrational and crystal quality of prepared nanomaterials. Therefore, the as-prepared In-doped ZnO nanopencils were examined by the Raman-scattering spectroscopy at room-temperature and the results are shown in figure 7.5. The II-VI wurtzite hexagonal phase ZnO belongs to C^4_{6v} space group and according to the Γ point of the Brillouin zone, it

possess various optic modes: $\Gamma = A_1 + 2B_1 + E_1 + 2E_2$ in which A_1, E_1, and E_2 modes are Raman active. Among these, the E_2 modes are Raman active only while the A_1 and E_1 are also infrared active[180]. Figure 7.5 exhibits the typical Raman-scattering spectrum of as-prepared In-doped ZnO nanopencils grown on silicon substrate.

Three well-defined peaks appear in the Raman-scattering spectrum, i.e. at 332 cm^{-1}, 437 cm^{-1} and 577 cm^{-1}. The most dominant peak appears at 437 cm^{-1} and can be assigned as Raman-active optical-phonon E_2 mode, a characteristic peak of wurtzite hexagonal ZnO, and confirms that the base material is ZnO[89]. A small peak appears at 332 cm^{-1} and can be attributed to $E_{2H} - E_{2L}$ (multi phonon) and it was observed that this peak appear in the Raman-scattering spectrum when the material is well-crystalline[93]. The presence of a peak at 577 cm^{-1} can be assigned as E_{1L} which originates due to the insertion of impurities in the lattices of ZnO as In is doped into the lattices of ZnO. The presence of most dominated optical-phonon E_2 mode and a suppressed E_{1L} mode in the observed Raman spectrum, leads one to conclude that In is efficiently doped into the lattices of ZnO and that the as-deposited In-doped ZnO nanopencils possess a good crystalline structure.

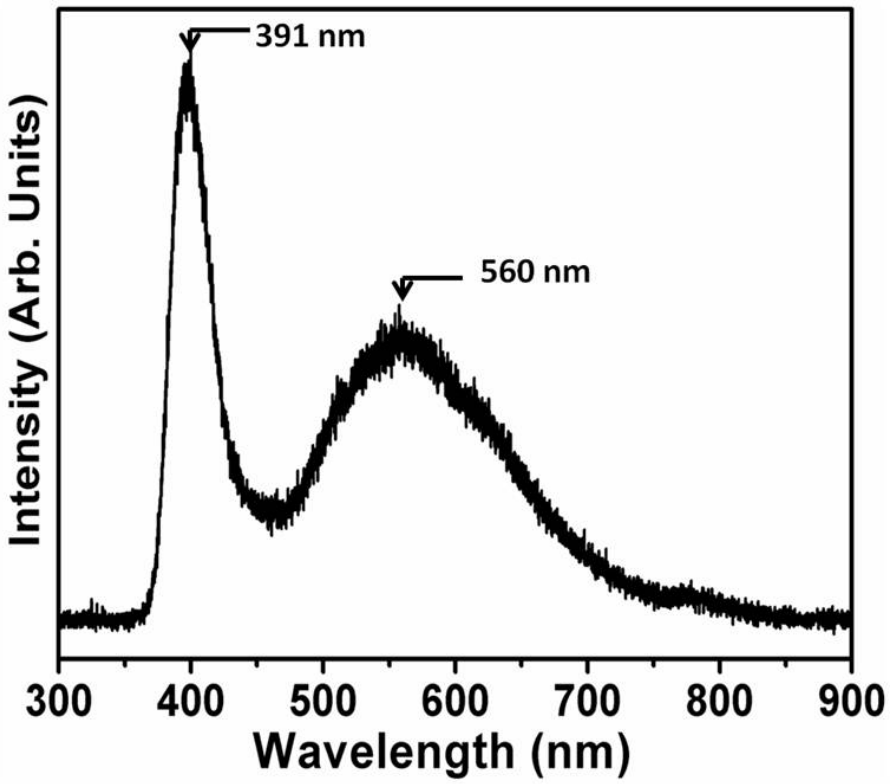

Figure 7.4 Room-temperature photoluminescence (PL) spectrum of as-grown In-doped ZnO nanopencils on silicon substrate prepared by thermal evaporation process. See text for detailed discussion and assignments of the peaks.

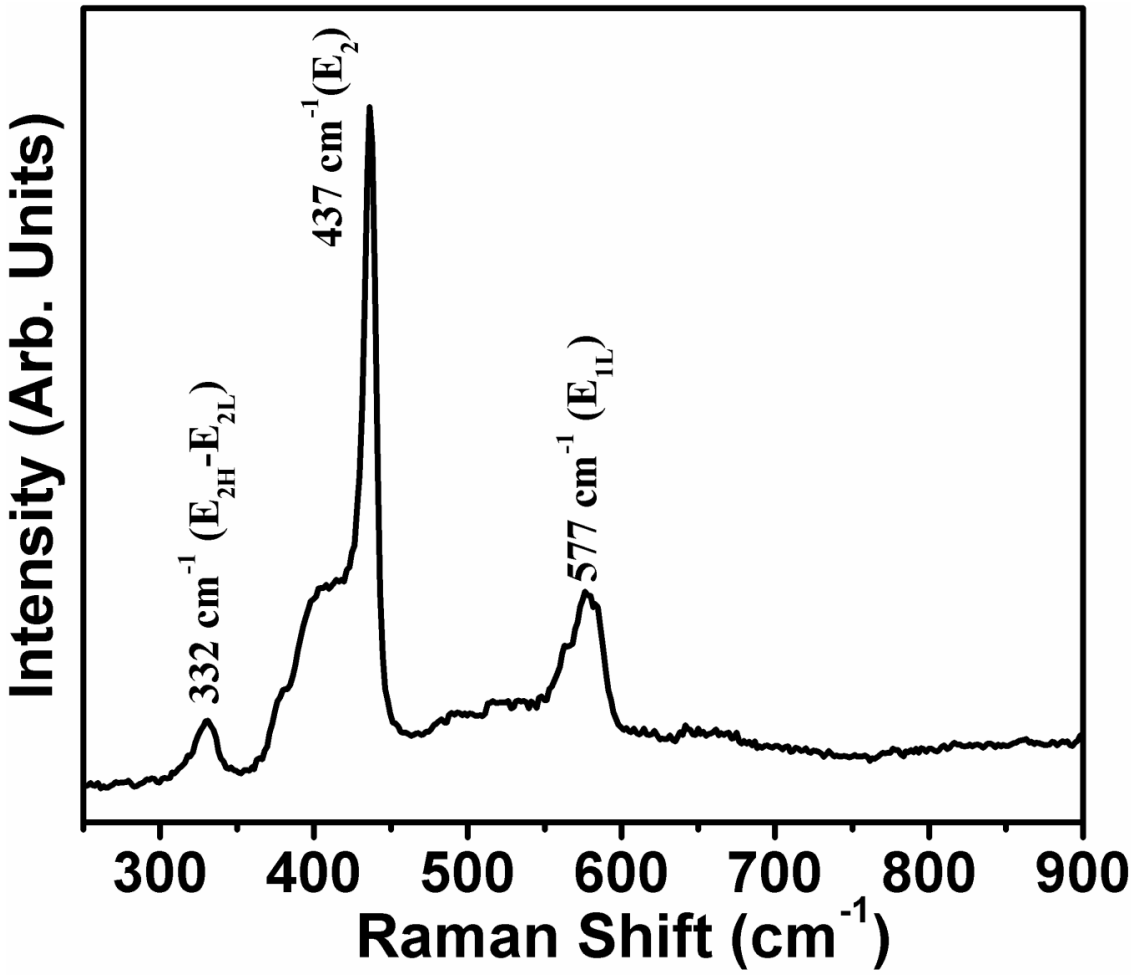

Figure 7.5 Raman-scattering spectrum of as-grown In-doped ZnO nanopencils on silicon substrate prepared by thermal evaporation process**.**

7.3.3 Plausible growth mechanism of In-doped ZnO nanopencils

Based on the observed FESEM and TEM images, a plausible mechanism for the formation of In-doped ZnO nanopencils can be explained. The mechanism can be explained based on the chemical reaction involved and the crystal growth habits of the prepared nanomaterial.

For the growth of 1D nanomaterials, normally two kinds of mechanisms have been proposed in the literature, i.e. vapor-liquid-solid (VLS)[24] and vapor-solid (VS)[167]. The VLS mechanism involves the utilization of metal nanoparticle as a catalyst and as initial nuclei which leads to the formation of 1D growth of nanomaterials. The main characteristic of VLS mechanism is the presence of metal a nanoparticle at the tip of the nanomaterial. For the growth of In-Doped ZnO nanopencils, no metal particles are used

during the reaction and no metal particles are observed on the tips, hence the VLS mechanism for the growth of nanopencils can be ruled out.

Basically, the growth of In-doped ZnO nanopencils can be divided into two sections, i.e. in the first part, the formation of hexagonal nanorods while the second part lead to the growth of nanoneedles on the head of grown nanorods. For the first step growth, initially when the furnace temperature was increased up to 800°C in the presence of high-purity N_2 and oxygen gases, the In and Zn powders melted (melting points: In= 156.59°C, Zn= 419.5°C) and consequently generated In and Zn vapors and reacted with oxygen gas in the gaseous phase (figure 7.6(a)). The gaseous InZnO species formed the InZnO hexagonal nuclei as the reaction proceeds (figure 7.6(b)). It is important to mention that the nuclei of InZnO follow the crystal behavior of ZnO due to the high content of Zn during the reaction. The formed nuclei exhibit (0001) top and $(000\bar{1})$ bottom surfaces. According to the crystal growth behaviors of ZnO, various shapes of ZnO or ZnO based nanomaterials depend upon the relative growth rates of different crystal facets which is $[0001] > [01\bar{1}\bar{1}] > [01\bar{1}0] > [000\bar{1}]$ under hydrothermal conditions[100,101,181]. It was realized that the basal hexagonal nanorod identically follows the ideal growth behavior of ZnO in which the nanorods are grown along the [0001] direction while the top and side surfaces are formed by the ±(0001) and six crystallographic equivalent $\{01\bar{1}0\}$ planes, respectively. During the ZnO crystal growth, the surface diffusion is the most important rate limiting process; therefore, the (0001) plane disappears and capped with the lower surface energy facet but higher miller indices of $[01\bar{1}1]$ surfaces and after the growth of $[01\bar{1}1]$ facet, the (0001) plane is the most likely remaining facet. This crystal behavior of grown In-doped ZnO nanorods fully follows the crystal behavior of ZnO crystals (figure 7.6(c))[181]. The exposed (0001) surfaces in the grown hexagonal nanorods are catalytically active and hence these provide the preferred growth sites for the second step growth of InZnO nanopencils. The second step growth is formed during the very slow cooling process of the furnace during which, the absorbed reactant vapors on the catalytically active (0001) surfaces, is still sufficient enough. However, during cooling, which is combined with continuously temperature reduction, the grown structures are purposely deprived from the source material. This leads to reducing the diameter of nanomaterial and the nanoneedle are eventually have shaped morphologies that is constructed over hexagonal nanorods,

forming the InZnO nanopencils. It is important to mention that the proposed mechanism is plausible and to draw an exact mechanism more experimental data is needed.

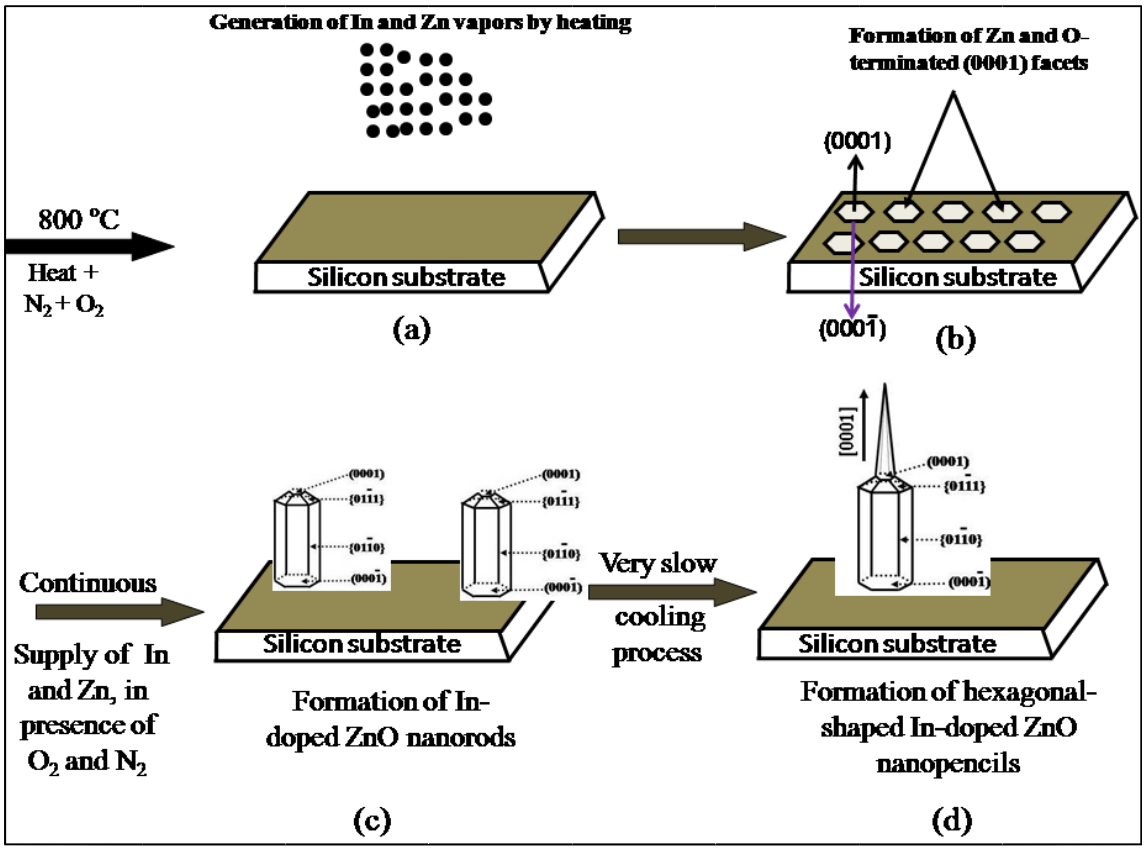

Figure 7.6 Schematic growth mechanism for the formation of as-deposited In-doped ZnO nanopencils on silicon substrate prepared by thermal evaporation process.

7.3.4 Field emission properties of In-doped ZnO nanopencils

7.3.4.1 Current-voltage characteristics of In-doped ZnO nanopencils

To verify the field emission properties of the In-doped ZnO nanopencils, field emission measurement was carried out in a vacuum chamber at pressure environment of $3x10^{-8}$ mbar. Field electron emission was obtained from In-doped ZnO nanopencils grown on 5×5 mm Si substrate. The applied voltage was increased from 0 to 3 kV at 0.1 kV increment. The *I-V* characteristics curve of FE from the In-doped ZnO nanopencils along with the corresponding F-N plot are shown in figure 7.7. The turn-on and threshold voltages were found to be ~1.3 kV with emission current of 80 nA registered and 3 kV with emission current of 17.15 μA registered, respectively. Since the distribution of the electric field around an emitter depends on its apex gometry[182], therefore, the low turn on voltage of the In-doped ZnO nanopencils can be an indication of their distinctive geometrical configuration. It is believed that, the pencil-like feature of ZnO emitters is beneficial in terms of performance due to large enchantment of the local electric field. Moreover, the two step configuration localize the electric field on of the emitter eliminating unwanted emission from off axis sites specially the thick base of the emitters[175].

Additionally, the impact of the doping is equally important as the geometry of the tip, and cannot be disregarded. Doping of indium into the ZnO leads to improvement in the electrical properties (i.e. conductivity and carrier concentration) and therefore lowering the work function which enhance the FE performance and prolong the life time of the tip[183].

On the other hand, the relatively high threshold voltage is believed to be due to the screening effect. Since, the growth is highly dense and randomly oriented, some of the nanopencils emitters are physically shadowed by others, failing therefore to emit because of the absence of electric field[175]. Clearly then, a vertically oriented growth of In doped ZnO nanpencils will improve the field emission performance of these emitters by eliminating the shadowing effect and strengthens the local electric field by being perpendicular to it.

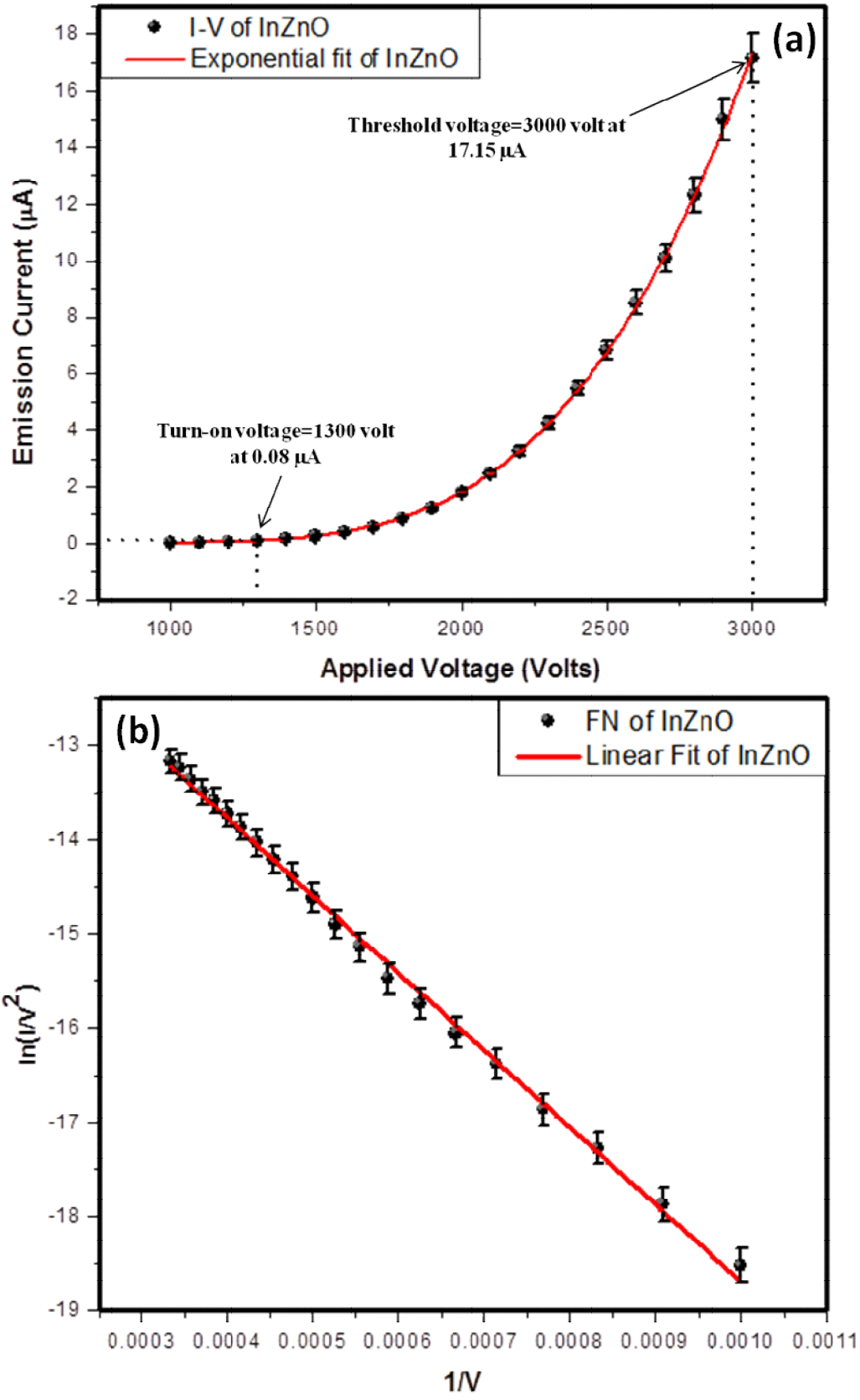

Figure 7.7 (a) Current-voltage (*I-V*) characteristic of of the as-deposited In-doped ZnO nanopencils. (b) The corresponding F-N plot.

7.3.4.2 The field emission current stability of In-doped ZnO nanopencils

To investigate the practical applications of the In-doped ZnO nanopencils as field emitter candidate, the field emission current stability was measured at constant voltage under base pressure of $3x10^{-8}$ mbar.

Figure 7.8 shows the variation of the emission current versus time for a period of time of over 3 hours at an applied voltage of 1.5 kV. In the present experiment, an emission current of about 120 nA was recorded at the beginning. The field emission current exhibits steady decrease to be about 40% of the initial value after 3 hours of continuous operation. In the second hour of operation, the emission current exhibits reasonable stability with a fluctuation of about 60% at an average of ~ 76 nA, however, in the last hour the current fluctuation increased and combine with many sharp spikes which could be attributed to the adsorbates effect.

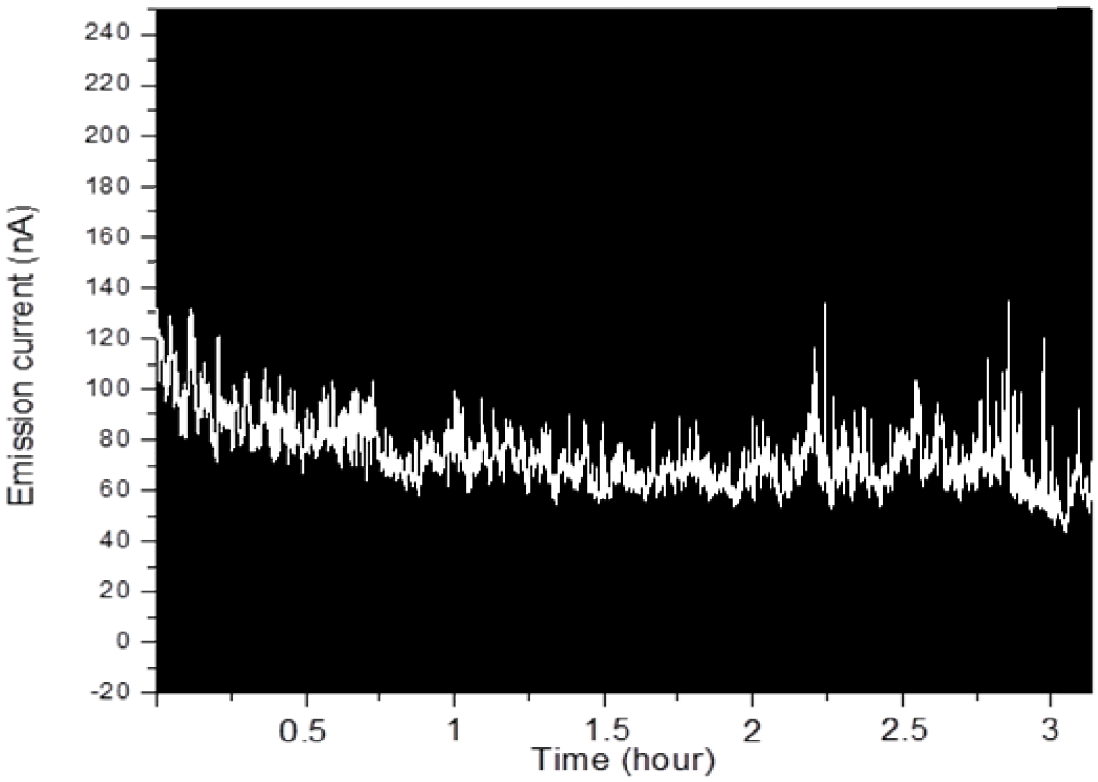

Figure7.8 the emission current stability profile of In-doped ZnO nanopencils at fixed voltage of 1.5 kV.

7.3.4.3 Field emission patterns of In-doped ZnO nanopencils

Several representative images of the emission pattern of the In-doped ZnO nanopencils were captured by digital camera at different applied voltages and shown in figure 7.9. As can be seen, the emission sites gradually immerged and were getting intense with increasing the applied voltage. The corresponding emission current is (0.55 µA, 2.46 µA, 6.82 µA and 17.15 µA) at applied voltages of (1.7 kV, 2.1 kV, 2.5 kV and 3 kV) respectively.

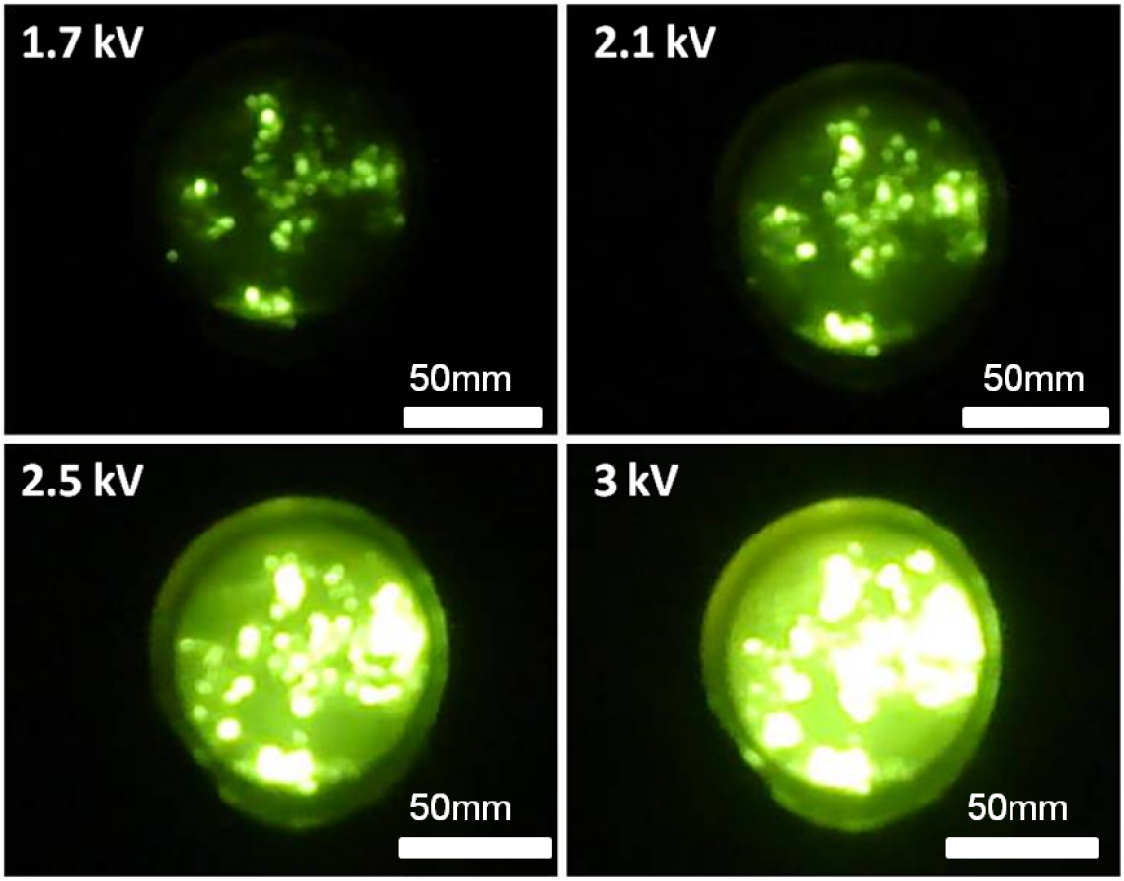

Figure 7.9 Field emission patterns of In-doped ZnO nanopencils grown on Si substrate as a function of applied voltage.

7.4 Conclusion

In summary, In-doped ZnO nanopencils were grown on silicon substrate by facile thermal evaporation process using metallic indium and zinc powders in the presence of oxygen. The detailed morphological and structural properties investigations revealed that the high density prepared nanomaterials are wurtzite hexagonal phase nanopencils. Raman-scattering studies also confirmed the well-crystallinity and wurtzite hexagonal phase of the nanopencils. The presence of a sharp and strong UV emission in the room-temperature PL spectrum is an indication of good optical properties for the examined material. The field emission properties of the grown nanopencils on silicon substrate were also investigated. The main advantage of the In-doped ZnO nanopencils is the lower turn-on voltage of 1.3 kV compared to ZnO nanorods (2.65 kV) (see section 5.3.4.1) and Ga-doped ZnO nanoneedles (1.7 kV) (see section 6.3.3.1). On the other hand, the field emission current stability experiment revealed that the In-doped ZnO nanopencils exhibited poor current stability of 60% for only 1 hour compared to the Ga-doped ZnO nanoneedles (with only 10% current fluctuation) as well as shorter life time of 3 hours compared to 10 hours in the case of Ga-doped ZnO nanoneedles.

CHAPTER8
GROWTH AND FIELD EMISSION STUDIES OF ZnO NANOSTRUCTURES GROWN ON MICROFABRICATED TUNGSTEN EMITTERS

8.1 Introduction

Field electron emission is an important application of nanomaterials, particularly the 1D nanomaterial as their emitting efficiency can be enhanced by being fabricated perpendicularly aligned to the anode surface and for their flexible geometry[184-189]. The carbon nanotube is one of the most extensive materials that have been studied over the last two decades for field emission device applications, due to its several exotic properties, such as good conductivity, chemical stability, easy and cost-effective growth etc[53,54,190,191].

However, recently the metal oxide nanomaterials are also considered a promising field emission material as well, owing to their excellent stability in oxygen environment and at high-temperatures[75]. Moreover, the electronic properties of the oxide nanomaterials can also be controlled by several techniques. Among the oxide family of nanomaterials, the zinc oxide material turned out to uniquely possesses excellent properties[75]. The field emission application of ZnO nanowires is rarely investigated, contrary to being utilized in a variety of high-technological applications, to name a few, electronic and optoelectronics, gas sensors, field emission devices, piezoelectric nano-generators, mechanics, sensors, actuators and solar cells[192-196].

In this chapter, a novel fabrication of a facile growth of ZnO nanowires on pre-fabricated micro tungsten emitters provided by York Probe Sources (YPS) Ltd, York, UK, is demonstrated. In addition, the field emission properties of the grown ZnO nanowires are also investigated in this chapter.

8.2. Direct growth of ZnO nanowires on micro-fabricated tungsten emitters

ZnO nanowires were grown on pre-fabricated micro tungsten emitters provided by YPS, in which a 100 μm diameter tungsten wire is spot welded to a bent tungsten wire and mounted on a ceramic base of the type used in electron microscopy cathodes.

The end of the tungsten wire is electrochemically etched to a sharp tip-needle with a radius in the range of 0.5-1.0 μm. For all the experiments, high purity metallic zinc (99.98%), oxygen (99.99%) and nitrogen (99.99%), were used.

8.3 Experimental work of the growth of ZnO nanowires on the W emitters

The growth of ZnO nanowires on the micro tungsten emitters was carried out by horizontal quartz tube furnace using high-purity metallic zinc powders in the presence of oxygen and nitrogen as Figure 8.1 shows.

A special experimental assembly was made in which an alumina boat containing metallic zinc powder is placed at the centre while the tungsten emitter is placed at a certain distance away from the source material boat in the horizontal quartz tube furnace and the quartz tube furnace was evacuated to 10^{-3} mbar. This pressure was preserved constant during the entire reaction process. After evacuation, a flow rate of 100 sccm of high-purity nitrogen gas is maintained in the reactor over a span time of 20 min, while, the furnace temperature was very slowly (10°C/min) increased up to the growth temperature (ranging from 550°C to 750°C) using a halogen lamp as a heating element.

Once the temperature of the furnace reached the growth temperature, a high purity oxygen gas (35 sccm) is then introduced to the reactor furnace. At this stage the growth is believed to be initiated as the zinc vapors is generated then transferred to condense on the tungsten tip. The reaction time was varied from 1 to 3 hrs period over a set of experiments. After the reaction is completed, the furnace was slowly cooled down to room-temperature (20°C/min) and a deposition of grayish to white colored layer is observed by the naked eye on the surface of the tungsten tips. The deposited material's structure was examined by using field emission scanning electron microscopy (FESEM; JEOL-JSM-7600F). Furthermore, the field emission properties of the ZnO nanowires grown on tungsten emitters were examined and demonstrated in section (8.5.2).

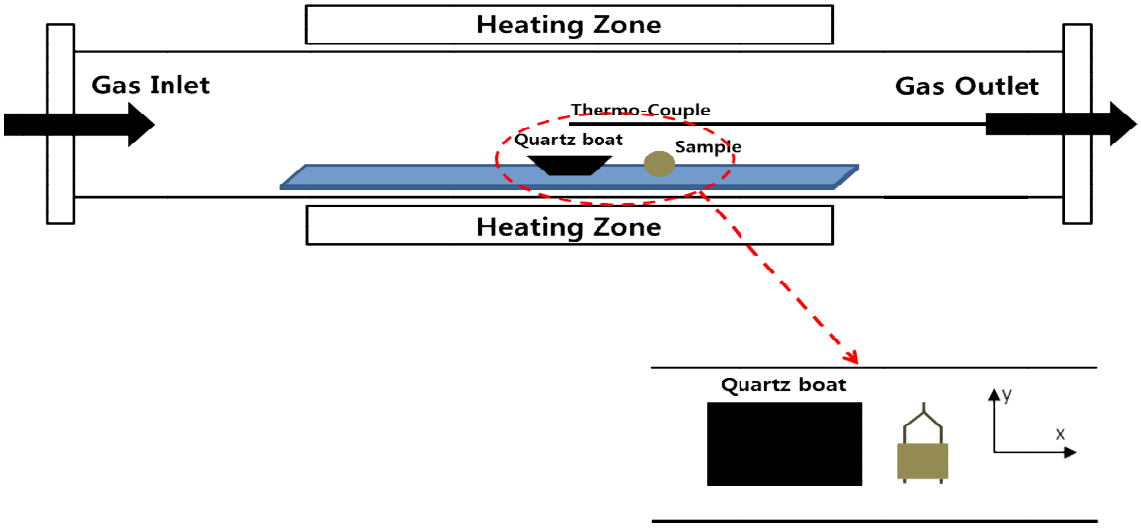

Figure 8.1 Schematic for the direct growth of ZnO nanowires on pre-fabricated micro tungsten emitters provided by York Probe Sources (YPS) Ltd., York, UK.

Nanomateial Type	Growth Technique	Substrate Type	Reaction Time	Zinc powder amount	Distance between source material and w tip	Growth Temperature
Tip-1: ZnO Microrods	Thermal evaporation	YPS- W emitter	3 hrs	1.5 gm	5 cm	600°C
Tip-2: ZnO Nanowires	Thermal evaporation	YPS-W emitter	2.5 hrs	1.5 gm	5 cm	650°C
Tip-3: ZnO Nanowires	Thermal evaporation	YPS- W emitter coated with ZnO thin film (200 nm)	2.0 hrs	1.5 gm	5 cm	650°C
Tip-4: ZnO Nanowires	Thermal evaporation	YPS- W emitter coated with ZnO thin film (200 nm)	1.5 hrs	1.5 gm	5 cm	700°C
Tip-5: ZnO Nanowires	Thermal evaporation	YPS- W emitter coated with ZnO thin film (200 nm)	1.0 hrs	0.5 gm	3 cm	750°C

Table 8.1 Summary of the growth parameters for the growth of ZnO nanomaterials on YPS- tungsten (W) emitters.

8.3.1 The effect of temperature, the distance between the tip and source material and reaction time

The best results obtained of any recognizable growth of ZnO structures in Figures 8.2 are resultant of implementing a growth condition of 3hrs reaction time, using 1.5 gm of metallic zinc powder at 600°C. These conditions were arrived at by varying the temperature by ≈50°C increment, starting from 500°C. Likewise the source materials were increased by 0.5 g increment by which, several experiments were carried out to define the appropriate amount of the source material that is needed to achieve the growth. Experimentally, it turned out that the impact of changing the amount of the source materials is not as crucial as the temperature. However, a 5 cm distance between source material and emitter had to be initially guessed or somewhat based on trial and error approach.

Figure 8.2(a) is a low-magnification image of the resultant structures which are not nanowires. They are instead micro-rods being randomly grown and distributed on the tip. The high-resolution images figures 8.2(b and c) show that the deposited ZnO micro-rods have diameters of 1.5-2 µm and typical lengths of ~8-10 µm.

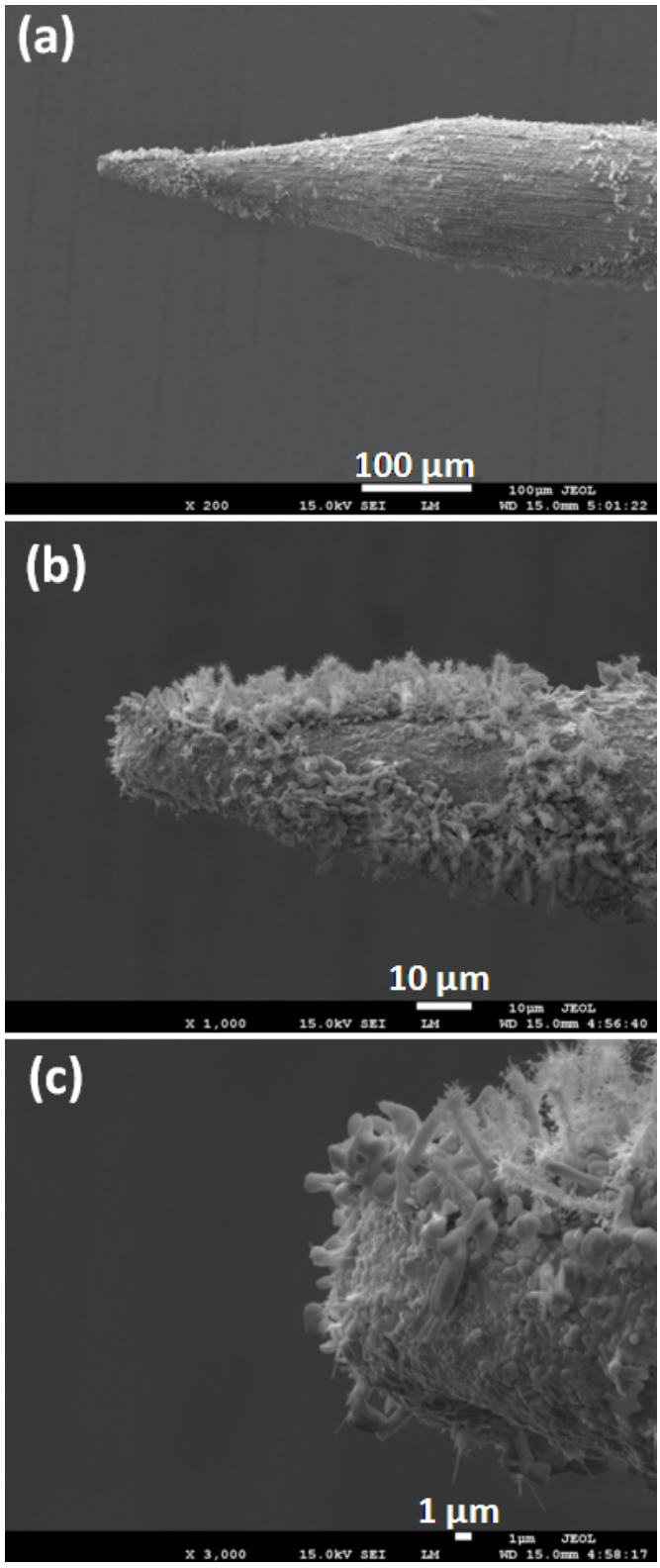

Figure 8.2 FESEM images of ZnO growth on the YPS tungsten emitters (Tip-1) (Reaction time: 3 hrs, Zn amount = 1.5 g; distance between source material and emitter: 5 cm; growth temperature: 600°C).

To realize our objective, which is obtaining aligned nanowires, a second set of experiments was performed, and the resultant FESEM images are shown in Figure 8.3.

For these set of experiments, the reaction conditions were altered by reducing the reaction time to 2.5 hrs, amount of metallic zinc powder remained intact at 1.5 g, reaction temperature set at 650°C while the distance between the source material and the emitter being fixed at and 5 cm.

The ZnO nanowires growth is achieved this time though, it is over their outer surfaces as shown by the SEM images in figure 8.3. Although, these are the best results achieved from few tenths of experiments, the nanowires are still randomly distributed in all directions around the tips. A much improved aligned structures are observed on both sides of the tip in which the nanowires are perpendicular to the surface and distant from each other by 10-20 nm as figure 8.3(c) shows. Although the growth density has considerably increased, but the quality of the growth is still unsatisfactory as the nanowires are mixed and interconnected with thin ZnO nanosheets at the tip apex (figure 8.3(d)). Therefore, the decision was made to introduce an interface layer on the tungsten to improve the growth.

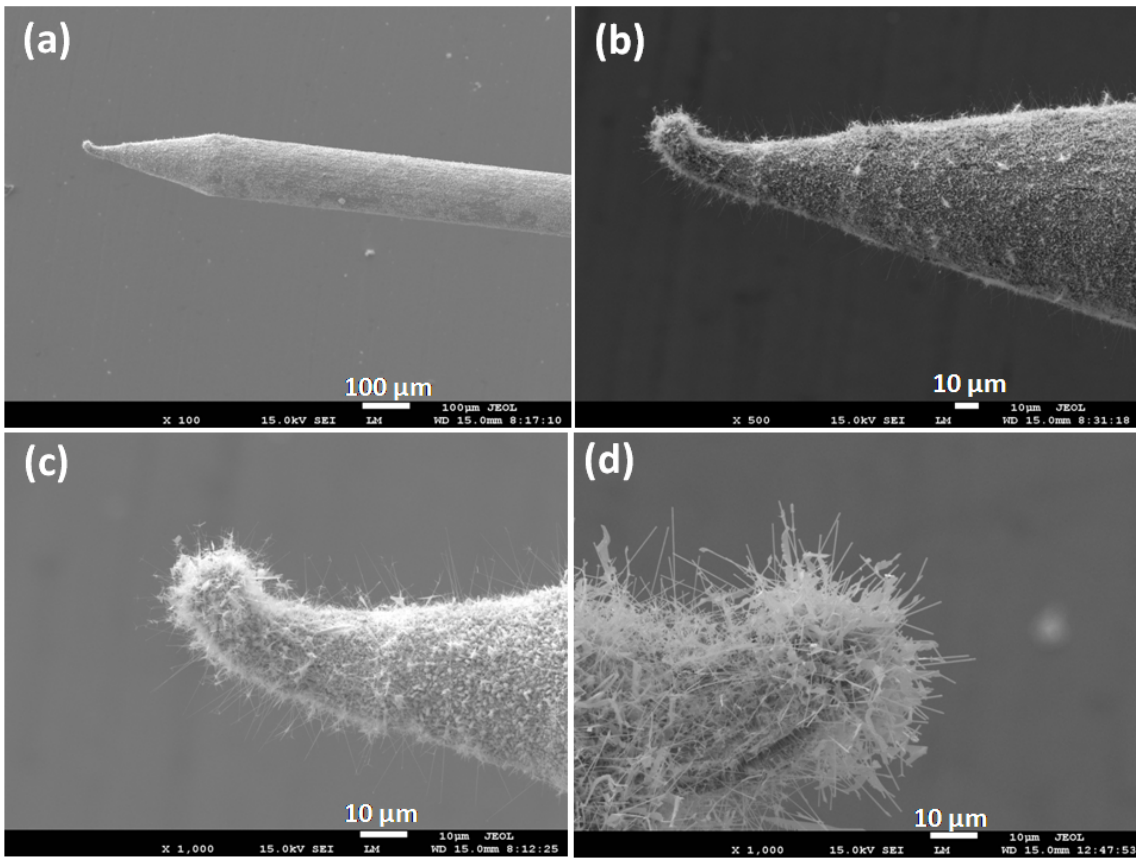

Figure 8.3 FESEM images of ZnO nanowires grown on the YPS micro tungsten emitters (Tip-2). (Reaction time 2.5 hrs, amount of metallic zinc powder =1.5g, reaction temperature 650°C; and distance between source material and emitter was set to 5 cm). The bent end-form has most likely been caused during handling the emitter while loading it in the furnace. This does not affect the experimental results discussed here, though as some nanorods are indeed grown along the optical axis of the tungsten emitter.

8.3.2 Improving the alignment of the nanowires by adding an interface layer

To get an aligned structure of ZnO nanowires and being located on the tip apex a new strategy was applied. Instead of directly growing on tungsten, an interface layer of thin ZnO film (200 nm) was sputtered using a magnetron sputtering on the tips' surface in advance. This is to reduce the lattice mismatch and to act as seed layer for the growth. Figure 8.4 exhibits FESEM images of ZnO nanowires grown on the ZnO film coated on the tungsten emitters over a span of time of 2 hrs, 1.5 g of metallic zinc powder, 650°C and 5 cm distance between source material and emitter.

As can be seen from the observed FESEM images, the entire surface of the emitter is covered with ZnO nanowires as figures 8.4(a), (b) and (c) show and interestingly, some over growth of the ZnO nanowires were also seen. To eliminate this over growth problem, several other experiments have been carried out and presented in next section. The decision was made here to slightly alter the growth conditions that had been established in section 8.3.1.

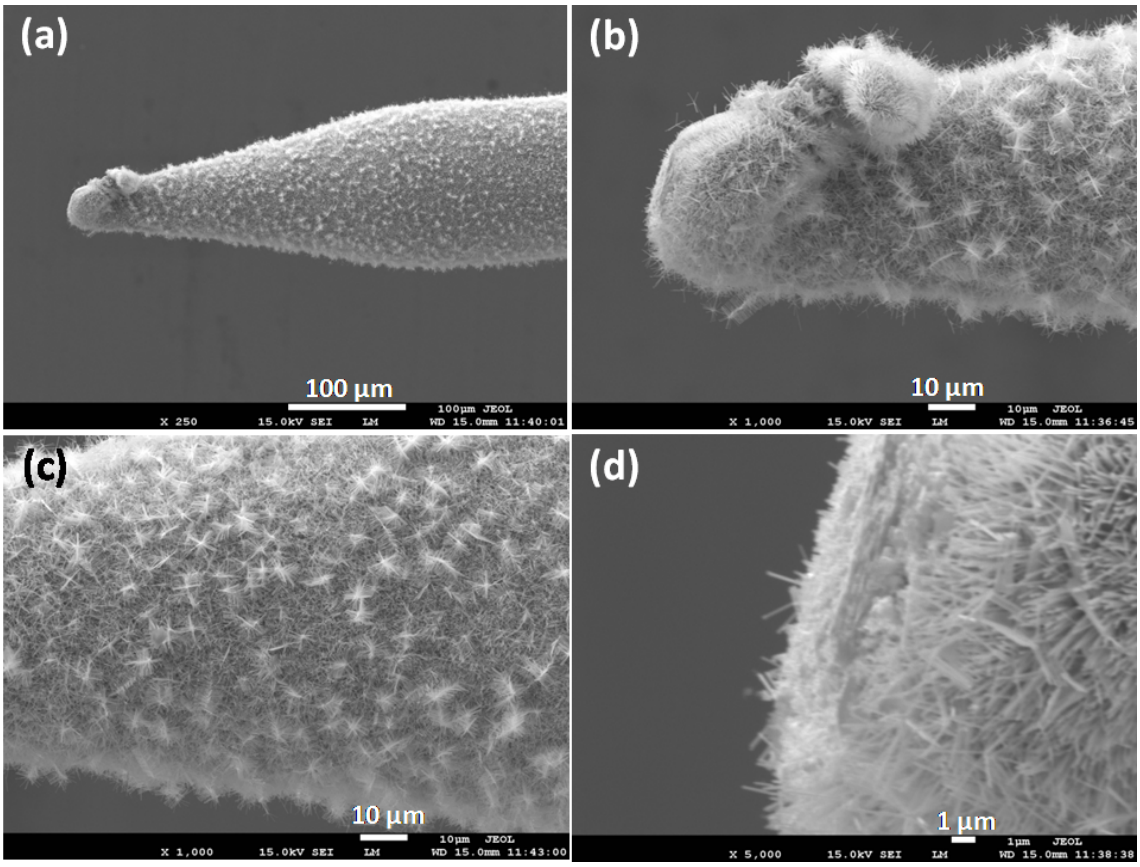

Figure 8.4 FESEM images of ZnO nanowires grown on the ZnO film (200 nm) coated pre-fabricated micro tungsten emitters provided by YPS (Tip-3). (Reaction time 2 hrs, amount of metallic zinc powder =1.5 g, reaction temperature 650°C; and distance between source material and emitter was set to 5 cm)

8.3.3 The elimination of the overgrowth phenomenon

Several other experiments have been carried out in which the growth conditions needed to be tuned for obtaining low density, high-aspect ratio and aligned ZnO nanowire with smooth surfaces.

After several experiments, it was found that the best results were obtained by reducing the reaction time to be 1.5 hrs and increasing the growth temperature to 700°C. The amount of the source material and the distance between source material and emitter remained intact at 1.5 g and 5 cm respectively.

Figure 8.5 demonstrates the FESEM images of ZnO nanowires grown on ZnO film (200 nm) coated tungsten emitter under aforementioned growth conditions. As seen from the FESEM images the entire tungsten emitter tip is covered with high-aspect ratio

ZnO nanowires. The nanowires are grown almost aligned to the surface of the tungsten tip with lengths and diameters of about 20-25 µm and 150-200 nm, respectively as shown in figure 8.5(d). However, unpredicted growth of tetrapod shaped ZnO nanowires emerged from the tip-end of the nanowires.

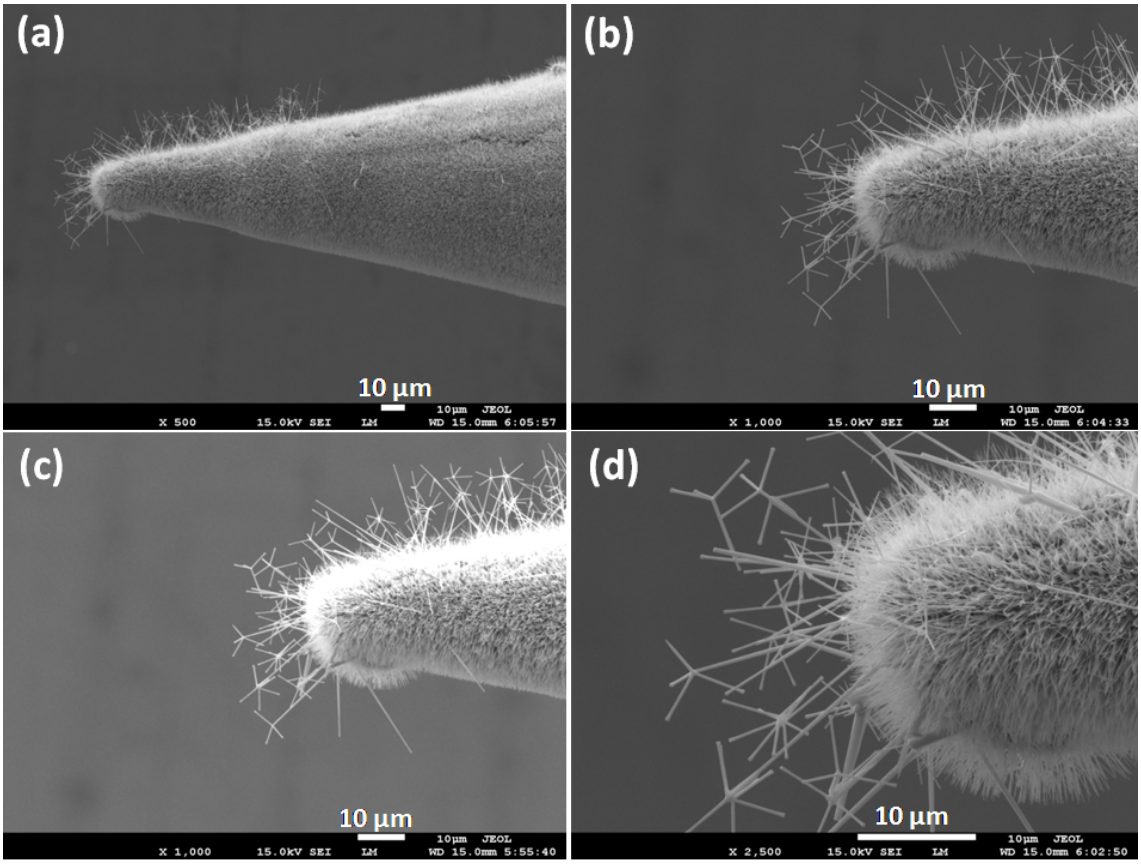

Figure 8.5 FESEM images of ZnO nanowires grown on ZnO film (200 nm) coated pre-fabricated micro tungsten emitters provided by YPS (Tip-4). (Reaction time 1.5 hrs, amount of metallic zinc powder = 1.5 g, reaction temperature 700°C; and distance between source material and emitter was set to 5 cm)

Although the coincident tetrapod shaped growth is worthy of further investigation, it is beyond the scope of this study to do so. In order to eliminate the tetrapods overgrowth, the growth conditions that had been established in section 8.3.3 must be slightly altered. Several sets of experiments have been designed and carried out in which each growth factor was solely modified. As a result reducing the reaction time to 1hr as well as the source materials to 0.5 g seemed to cure the overgrowth phenomenon. The reaction temperature and the distance between source material and emitter were also altered to be 750°C and 3 cm respectively. Figure 8.6 exhibits the typical FESEM images of ZnO nanowires grown on ZnO thin film (200 nm) deposited tungsten emitter tip when applying these growth conditions.

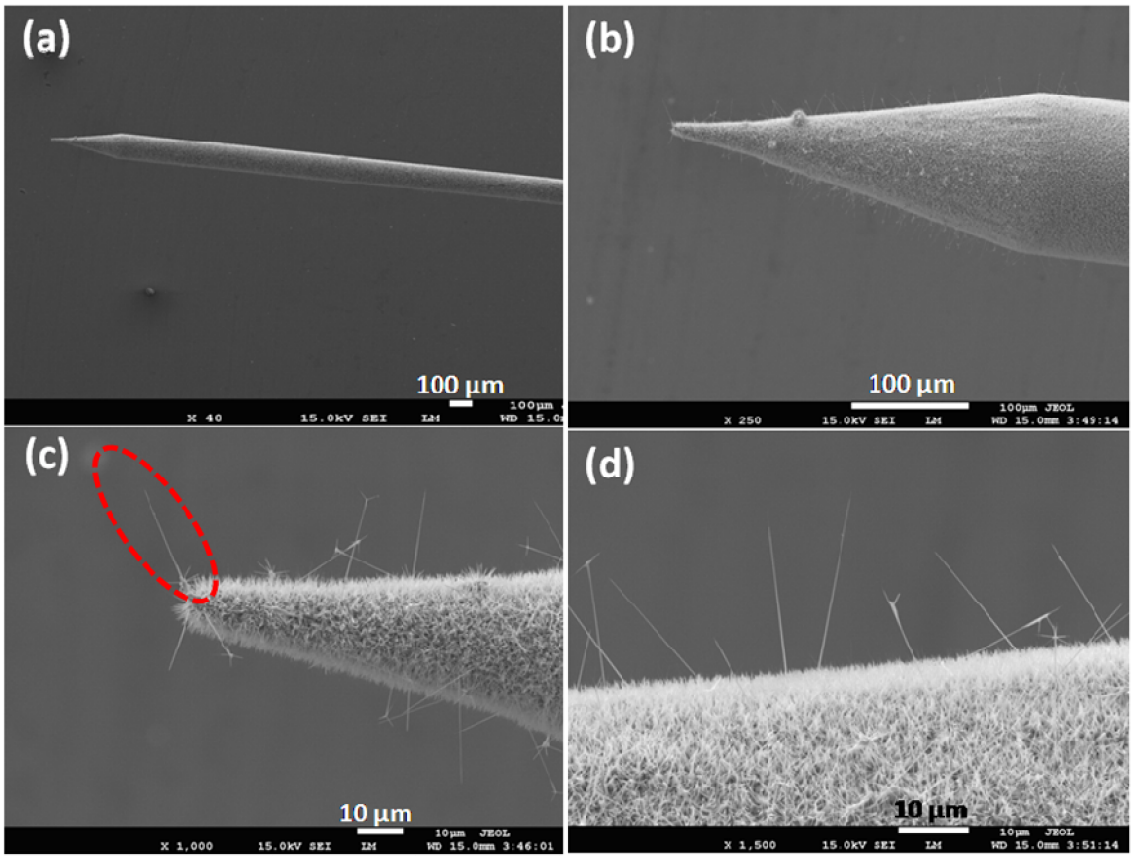

Figure 8.6 FESEM images of ZnO nanowires grown on ZnO film (200 nm) coated pre-fabricated micro tungsten emitters provided by YPS (Tip-5). (Reaction time 1 hr, amount of metallic zinc powder = 0.50 g, reaction temperature 750°C; and distance between source material and emitter was set to 3 cm). Note the ZnO nanowire, identified by the red circle in image (C), is significantly higher than the others grown on the tip's apex.

8.4 Discussion

A novel growth fabrication of ZnO nanowires on (YPS) pre-fabricated micro tungsten emitters is carried out to study the field emission properties of the nanowires. The horizontal quartz tube furnace shown in figure 8.1 is used and all results are examined by the JEOL FESEM.

It is important to note that for the optimum nanowires growth on the tungsten tip, various factors such as reaction time, amount of source material, position of substrate/tips with regard to the source material, growth temperature, the increased rate of temperature, cooling rate, etc are very important and need to be taken into consideration. Some of the former initial growth conditions were established based on work from the literature whereas others are based on trial and error approach. However, it is noteworthy that, fundamentally the growth can significantly differ even when applying the same conditions reported in the literature, due to some minor discrepancy of the gas purities, instrumental settings and measurements accuracy. For this reason the decision was made to independently alter some of the former growth conditions and monitor their impact on the growth.

In section 8.3 a brief portrayal of the initial growth conditions is presented. A very stringent cleaning procedure was established in which Acetone and DI water are used to remove any surplus depositions on the quartz tube form preceding experiments. This was to ensure that the growth is only governed by the reaction conditions that were then defined throughout the experimentation sections 8.3.1, 8.3.2, and 8.3.3.

In section 8.3.1 the effect of the temperature, the distance between the tip and source material and the reaction time were investigated. Although, the obtained results in figure 8.2, from implementing the initial conditions are not in the form of nanostructure, they still represent the origination of 1D mirco/nano structure. The best results obtained were due to implementing growth conditions of 3hrs reaction time, using 1.5 gm of metallic zinc powder at 600°C. Over several experiments, a 5 cm distance between source material and emitter is chosen whereas, the temperature was varied by ≈50°C increment, starting from 500°C and the source materials were increased by 0.5 g increment . The later factor seemed to have less influence on the growth in comparison to the temperature. Even when the ZnO nanowires growth is achieved, it was over their outer surfaces and randomly distributed in all directions around the tips as shown in figure 8.3. Another disappointing growth aspect was the fact

that the nanowires are mixed and interconnected with thin ZnO nanosheets (figure 8.3(d)). Nonetheless, on the sides of the tip, the nanowires were perpendicular and of a superior quality than those on the tip apex. Therefore, the decision was made to introduce an interface layer on the tungsten to improve the growth.

In section 8.3.2, an enhanced alignment is gained as new approach was adapted. An interface layer of thin ZnO film (200 nm) was sputtered on the tips' surface rather than growing directly on tungsten. This was to reduce the lattice mismatch and to act as seed layer for the growth and the results are shown in figures 8.4(a), (b) and (c). Here, the ZnO nanowire grown in very high density and low aspect ratio. Unfortunately, some over growth of the ZnO nanowires were also seen in which, some of the original ZnO nanowires acted as substrates for a secondary growth of new ZnO nanowires on their surfaces. The over growth phenomenon might have been due to the long reaction time, therefore to eliminate this over growth problem; the reaction conditions were slightly altered.

In section 8.3.4, the reaction time was reduced to 1.5 hrs and the temperature is increased to 700°C. The alignment is further enhanced and the lengths and diameters of the nanowires are 20-25 μm and 150-200 nm, respectively as shown in figure 8.5(d). Unpredicted as well as surpluses growth of tetrapod shaped ZnO nanowires is also seen, which again necessitated further modifications to the growth conditions. Reducing the reaction time to 1 hr, the source materials to 0.5 g, the source material to emitter distance to 3 cm and by increasing the temperature to 750ºC seemed to eliminate the overgrowth phenomenon.

Finally the result of applying the above optimum conditions that have been investigated in sections 8.3.1, 8.3.2 and 8.3.3 is shown in figure 8.6. The resultant nanowires are vertically aligned to the tip surface, possess very high aspect ratio and grown in a very smooth manner in all directions on the entire surface of the tip. The typical lengths and diameters of the grown nanowires are in the range of 15-20 μm and 150-200 nm, respectively. Moreover, due to well-aligned nature and good aspect ratio, the grown ZnO nanowires on tungsten tip can be very useful for field emission device applications.

8.5. Field emission properties of ZnO nanowires directly grown on micro-fabricated tungsten emitters provided by York Probe Sources (YPS), Ltd.

8.5.1 Experimental design: sample holder layout

In order to study the field emission properties of the ZnO nanorods grown on micro-fabricated tungsten emitters a special sample mount needed to be designed. Firstly, I used a stage which would allow for easy alignment and positioning of the emitters. The stage consists of two parts as follows ***i) the mounting plate***, an aluminum disc of 100 mm diameter and 4 mm in thickness. It has a big hole through its centre for electrical connections and other six screw holes as can be seen in figure 8.7. ***ii) the emitter holder***, it was made from two pieces, an emitter mount ring suspended inside a U shaped aluminum holder by two screws, which allow for adjusting the angle of the emitter while the U shaped aluminum holder has the ability to move in ±Y axis allowing for repositioning and centering the emitter. The emitter holder is isolated from the mounting plate by placing it on an insulating base of peek materials of thickness of 4mm. the emitter holder is mounted on the mounting plate through two screws each side. The emitter acts as the cathode so the emitter and the holder are kept at negative potential. For more illustrations please figure 8.8.

Secondly, the anode is made of 100 mm circular disc of aluminum with 500 µm diameter hole at the centre (see figure 8.9). A thin layer of phosphor powder was deposited on the whole surface of the anode and coated by very thin layer of gold (20 nm) and is used as viewing screen and for imaging the emission pattern. For measuring the angular current density, a faraday cup was connected to the back of the anode plate behind the opening hole and connected to a picoammeter. Figure 8.10 shows schematic diagram of the field emission assembly.

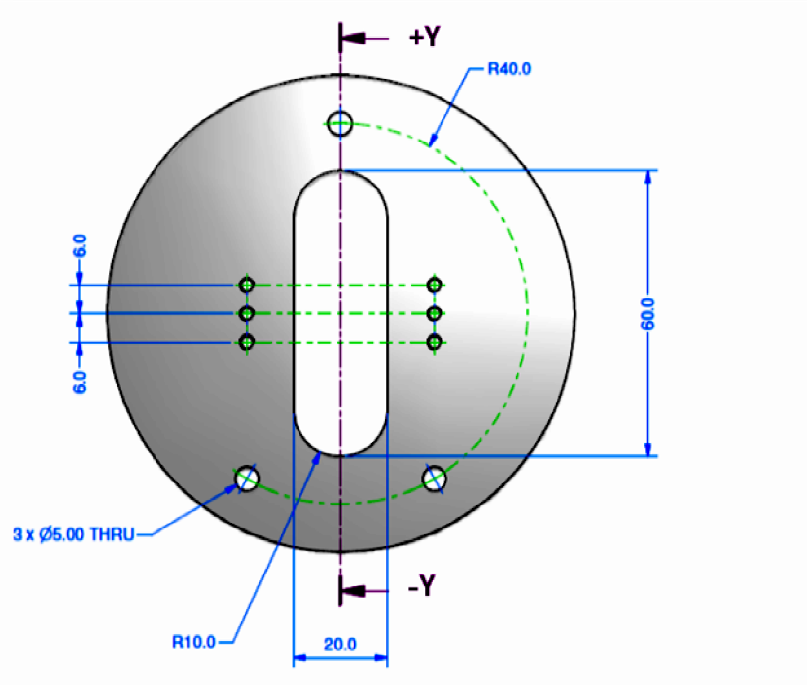

Figure 8.7 Schematic diagram of the mounting plate showing the clearance hole through its centre for electrical connection purpose.

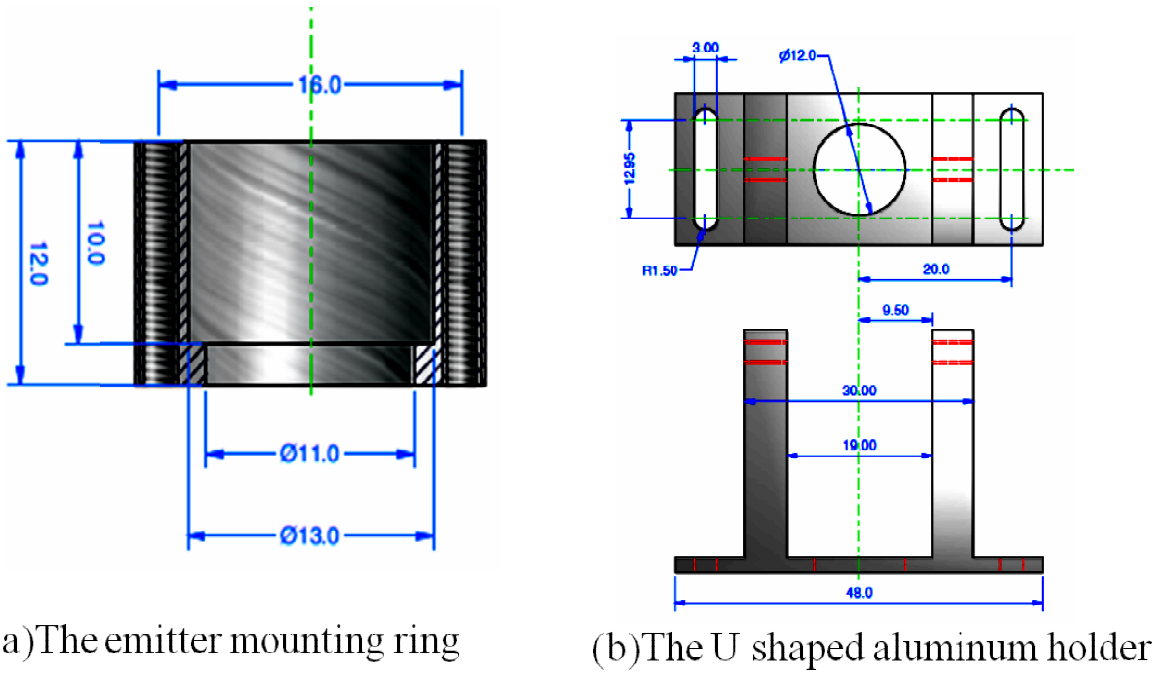

Figure 8.8 Schematic diagram of the emitter holder showing (a) the emitter mounting ring (b) the axial and side view of the U shaped aluminum holder.

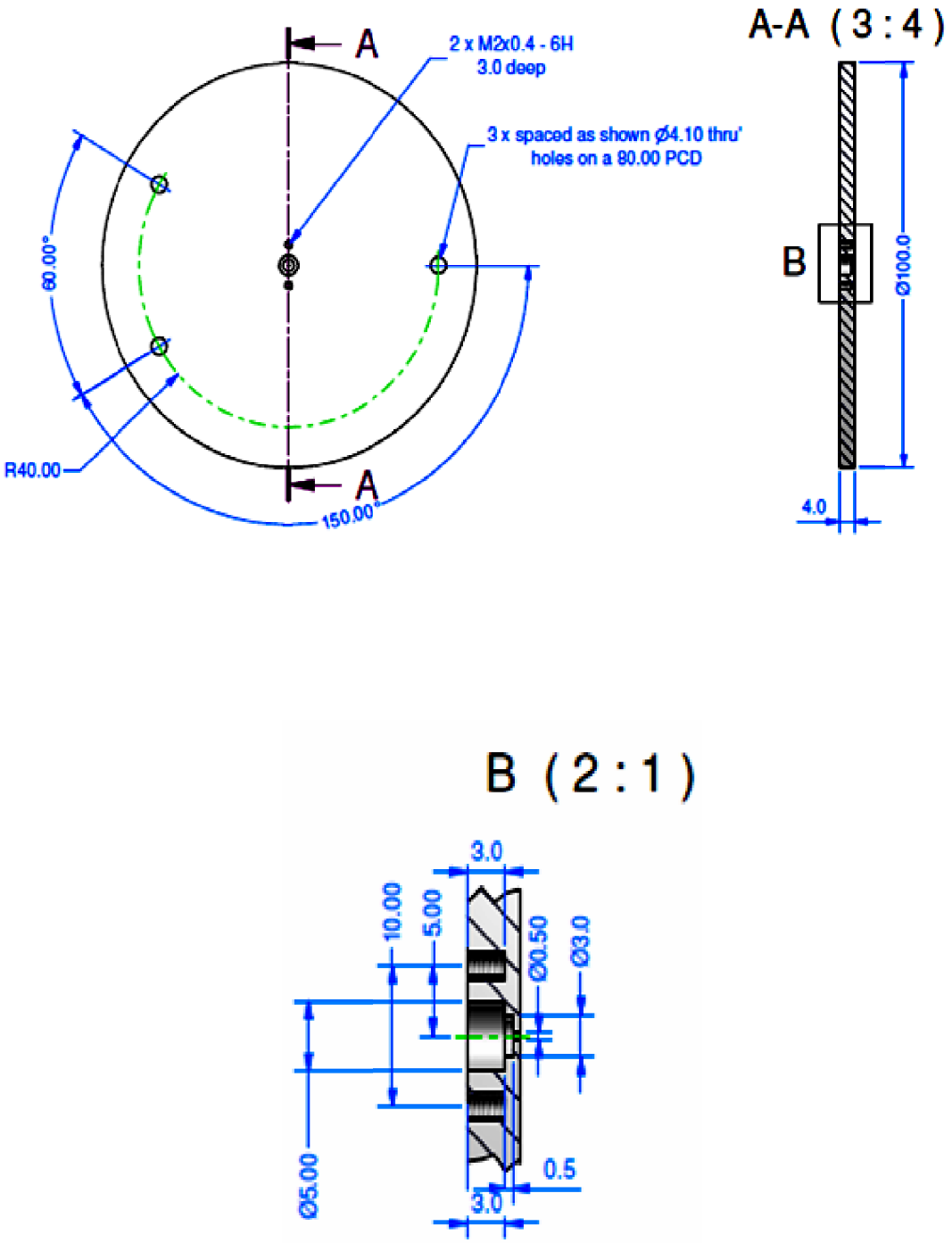

Figure 8.9 Schematic diagram of the anode plate showing the 500 µm aperture hole at the centre of the plate for measuring the emission current from small spot through a Faraday cup connected to the back of the anode plate.

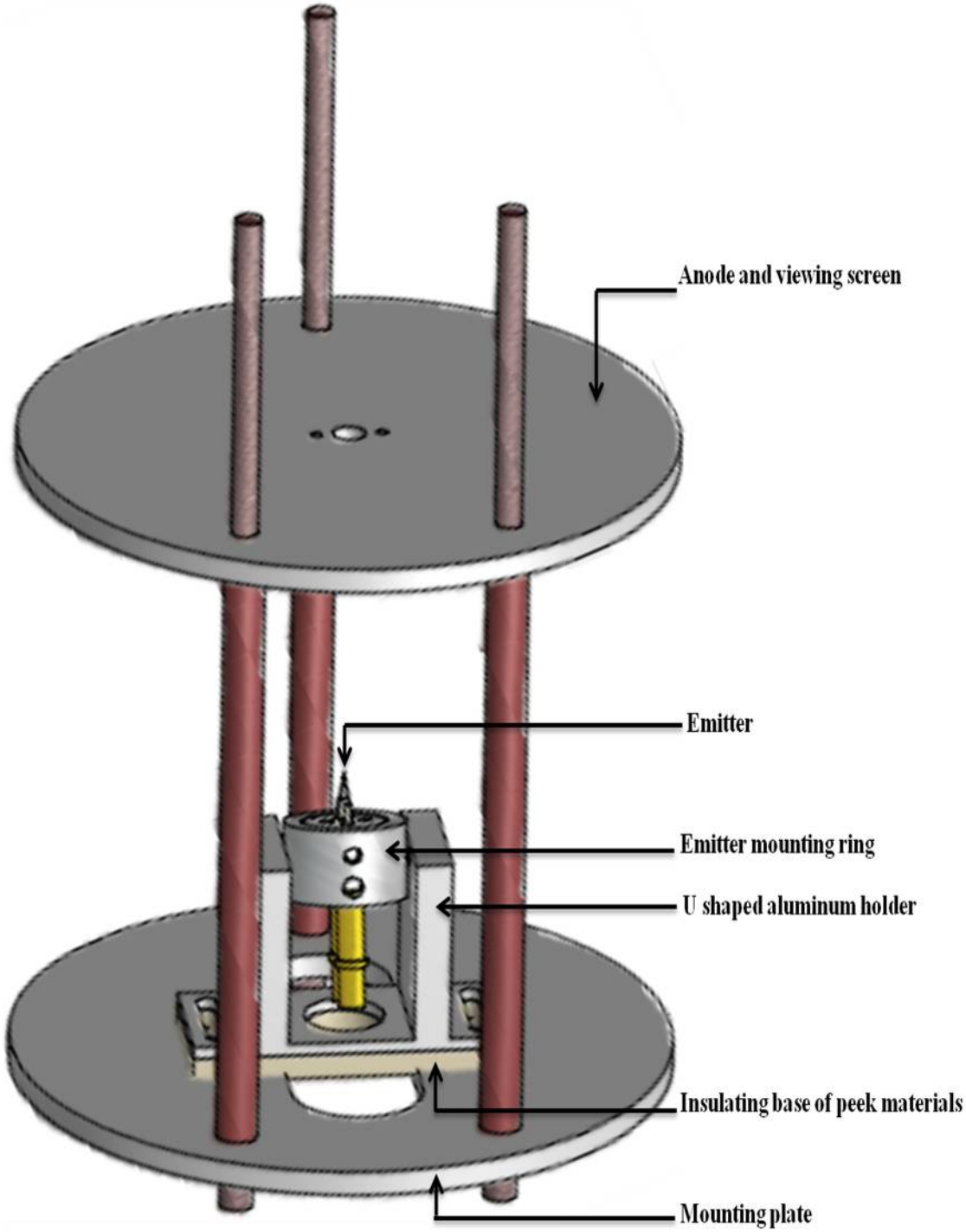

Figure 8.10 Schematic diagram of the field emission assembly.

8.5.2 Field emission results

For measuring the field emission properties of ZnO nanowires grown on tungsten emitters, initially, the emitter was mounted and adjusted to the center of the mounting plate of the field emission set-up then installed in the Renta-Port system (described in chapter 3 section 3.4.1). The system was then pumped down to 10^{-6} mbar and baked at 180ºC for 24 hour to establish UHV conditions and same procedure has been followed for all the measurements presented in this section.

Before testing the ZnO nanowires emitters, a high voltage test was necessary to be carried out in which the emitter holder without any emitter being mounted was gradually taken to 10 kV with respect to ground. This is for two purposes; firstly, to make sure that these components could withstand the voltages to be applied. Secondly, it was necessary in order to remove sharp objects or absorbed particles from these components.

The first field emission data was collected from Tip-3 as shown in figure 8.4. Figure 8.11 shows the I-V characteristics of the ZnO nanowires and the corresponding F-N plot. Several scans were necessary for obtaining a reproducible *I-V* curve. The first field emission pattern was observed on the screen at an applied voltage of 4 kV corresponds to an emission current of 10 nA. This value is considered very high compared of that reported by Dong *et al*[14]. The high turn on voltage could be attributed to the very high density growth and low aspect ratio of ZnO nanowires which results in screening the electric field as well as a reduction in the local amplification of electric field at the emitter apex. Then the emission current increased exponentially with increasing the applied voltage flowing the Fowler-Nordhiem theory descriped in equation (2.25) to reach its value of about 290 nA at threshold voltage of 5.5kV.

Figure 8.12 shows the most stable field emission pattern at the centre of the fluorescent screen. The field emission pattern is believed to come from a “bunch/cluster” of ZnO nanowires grown on the apex of the W tip. The circular feature of the emission pattern indicates that the field emission comes from the ZnO nanowires rather than the tungsten tip. As in the case of the tungsten emitter, the crystal facets of the tungsten would be observed instead. Moreover, higher applied voltage is required for obtaining field emission from the tungsten tip.

The field emission current stability of ZnO nanowires (Tip-3) was also investigated. Figure 8.13 shows the total screen emission current as a function of time

for a period of 10 hours. A higly fluctuated emission current with a fluctuation of 107.7% was recorded and persisted for a period of 10 hours with an average of about 60 nA without any noticeable degradation. The field emission current stability from very small spot (500 μm) was also measured through a Faraday cup. An emission current with an average of 1.5 nA with a fluctuation of 133.33% was recorded for a span of 14 hours. Both current emission measurements show very high instability in the emission current of the ZnO nanowires under a moderate pressure of 1.1×10^{-8} mbar.

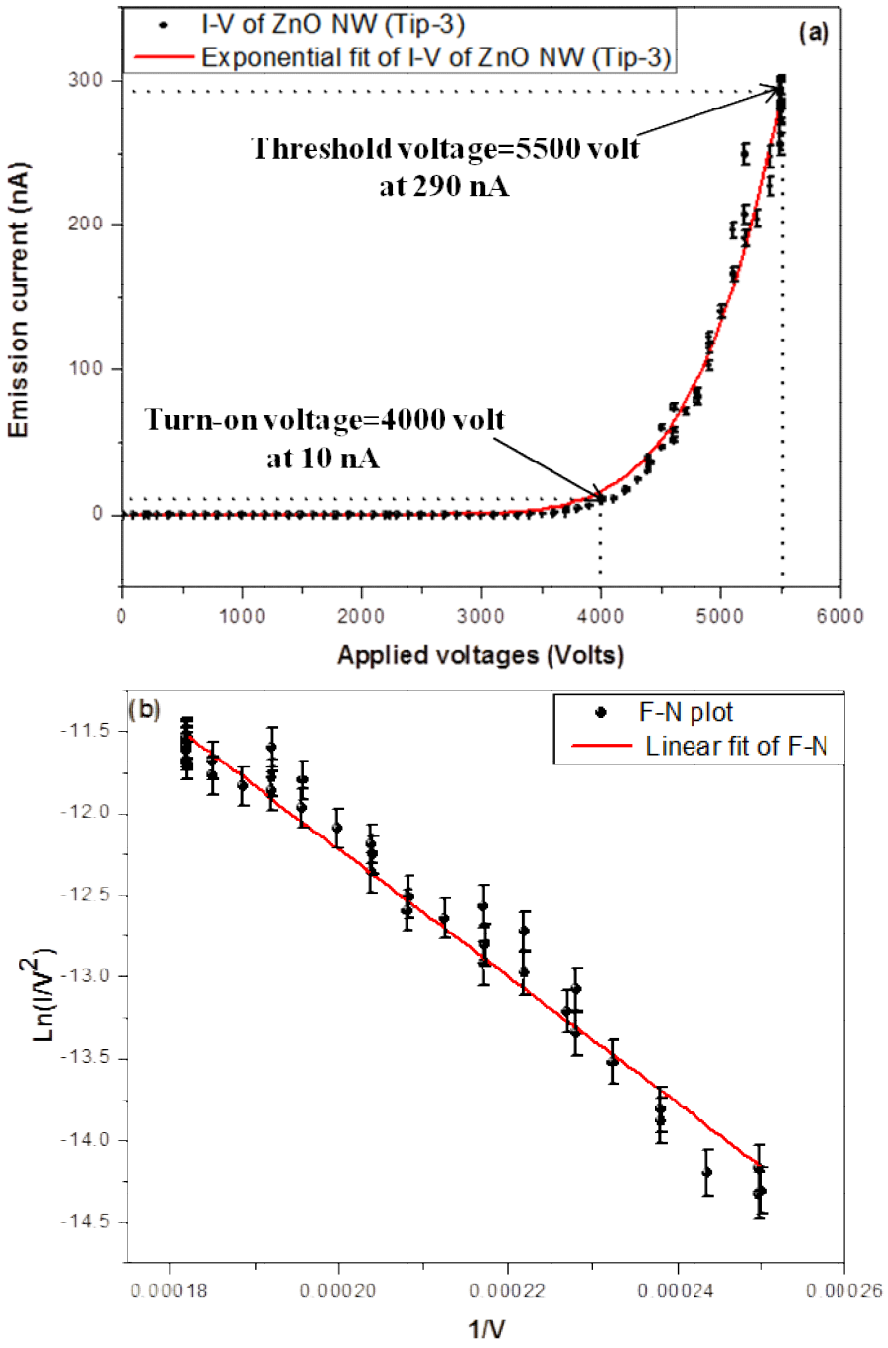

Figure 8.11 (a) Current-voltage (*I-V*) characteristic of of ZnO nanowires grown on the ZnO film (200 nm) coated pre-fabricated micro tungsten emitters (Tip-3). (b) The corresponding F-N plot.

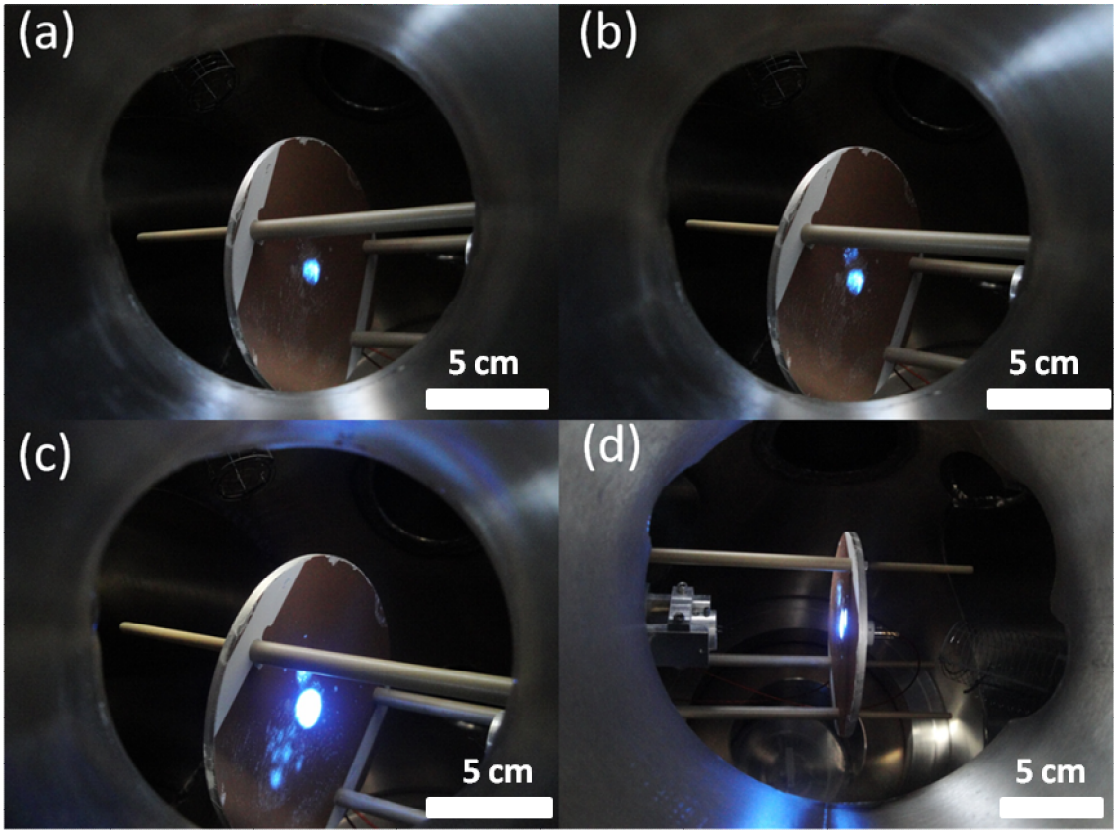

Figure 8.12 The field emission pattern of ZnO nanowires grown on the ZnO film (200 nm) coated pre-fabricated micro tungsten emitters (Tip-3). This field emission pattern was obtained after several voltage ramps. (a) shows that the emission pattern starts as one circular spot at the centre of the phosphor screen. (b) and (c) images show that the emission pattern gets intense with increasing voltage and some other emission sites were also appeared. (d) shows the emission pattern from different angle at the centre of the phosphor screen facing the Faraday cup.

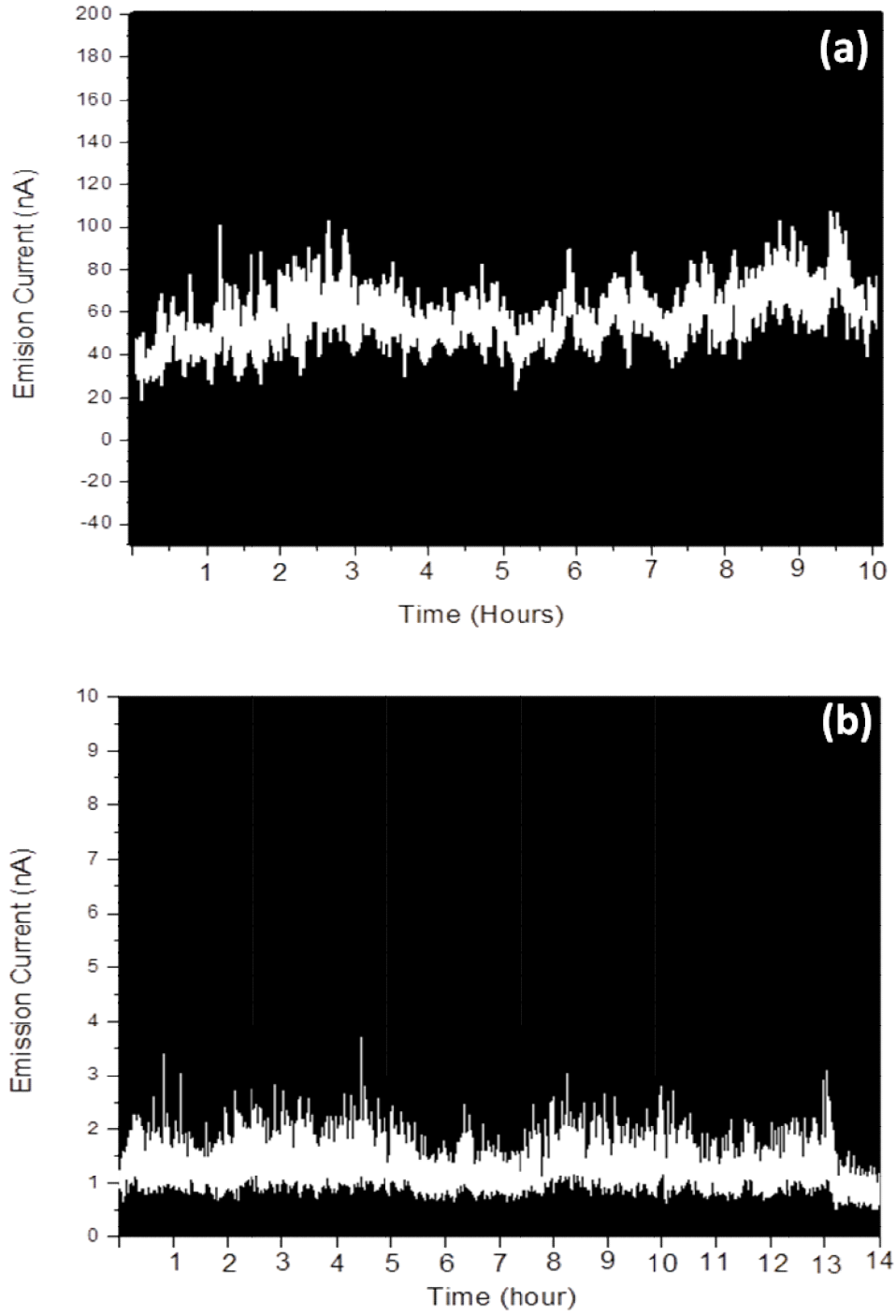

Figure 8.13 The emission current stability profile of ZnO nanowires grown on the ZnO film (200 nm) coated pre-fabricated micro tungsten emitters (Tip-3). (a) shows the total screen current as a function of time. (b) shows the field emission current stability of small spot (500 µm) measured by faraday cup through an opening hole at the centre of the viewing screen.

The second field emission experiment was carried out using Tip-4 as shown in figure 8.5. In this experiment, the applied voltage was gradually increased with steps of 50 volts per second. Unsurprisingly, several field emission patterns start to occur on the fluorescent screen at an applied voltage higher than 2 kV. This is because several ZnO nanowires grew on the tungsten tip's apex in all inclinations. Although, several ZnO nanowires started to emit at same applied voltage, a more intense field emission pattern was observed at the centre of the fluorescent screen and it is believed to be from the ZnO nanwires that grew along the tungsten tip's axis, as they have more exposure to the applied electric field than that grown not aligned to the tip's axis. The typical field emission patterns of ZnO nanowire Tip-4 is shown in figure 8.14.

After several scans, figure 8.15 shows the most stable and reproducible *I-V* curve. The emission current starts at voltage of about 2.448 kV and increased exponentially to reach 290 nA at an applied voltage of about 3kV. The corresponding F-N plot is shown in figure 8.15(b) and exhibits reasonable linearity.

The stability of the field emission current as a function of time is recorded for both, the total screen emission current (I_{total}) and from a small spot of 500 μm through a Faraday cup at the centre of the screen. The measurement of the emission current stability of the total screen emission current (I_{total}) was carried out at an applied voltage of 3 kV for a span of 3 days. Figure 8.16 (a) shows the emission current stability of ZnO nanwires grown on Tip-4 for the first 11 hours. The emission current started at 800 nA and persisted for about an hour and then rapidly decreased to ~ 50% of its initial value during the next two hours. The emission current continued its decrease steadily to be as low as 200 nA after a period of 7 hours of continues operation. The degradation in the emission current is believed to be due to the resistive heat. The extraction of high emission current from ZnO nanowire heats or even melts the emitter which can degrade the emission current. Another possible reason is that the deformation of the tip of the ZnO nanowire that is induced by ion bombardment could diminish the field emission performance of the emitter. The emission current stability over the next 50 hours is shown in figure 8.16(b). An average of emission current of 150 nA was recorded with fluctuation of about 133%.

The field emission stability of the field emission pattern at the centre of the screen highlighted with the red arrow in figure 8.14(c) was also measured using a Faraday cup and shown in figure 8.17. An emission current with an average of 3.3 nA

was recorded for a span of 16 hours with a fluctuation of 155% and after that, the emission current decreased to be as low as ~ 0.5 nA in average with a fluctuation of 90% at this value. The high fluctuation in the first 16 hour is believed to be due to self cleaning process.

The field emission stability measurements display very poor emission current stability of ZnO nanowires (Tip-4) for a reliable electron source emitter. A plausible explanation of the high instability is that the total emission current is a summation of emissions from multiple emitters of ZnO nanowires emitting at the same time. These ZnO nanwires are not identical in terms of their dimensional uniformity, tip radius, separation distance and alignment to the tip's apex which results in different emission stabilities and hence the total emission current remains unstable.

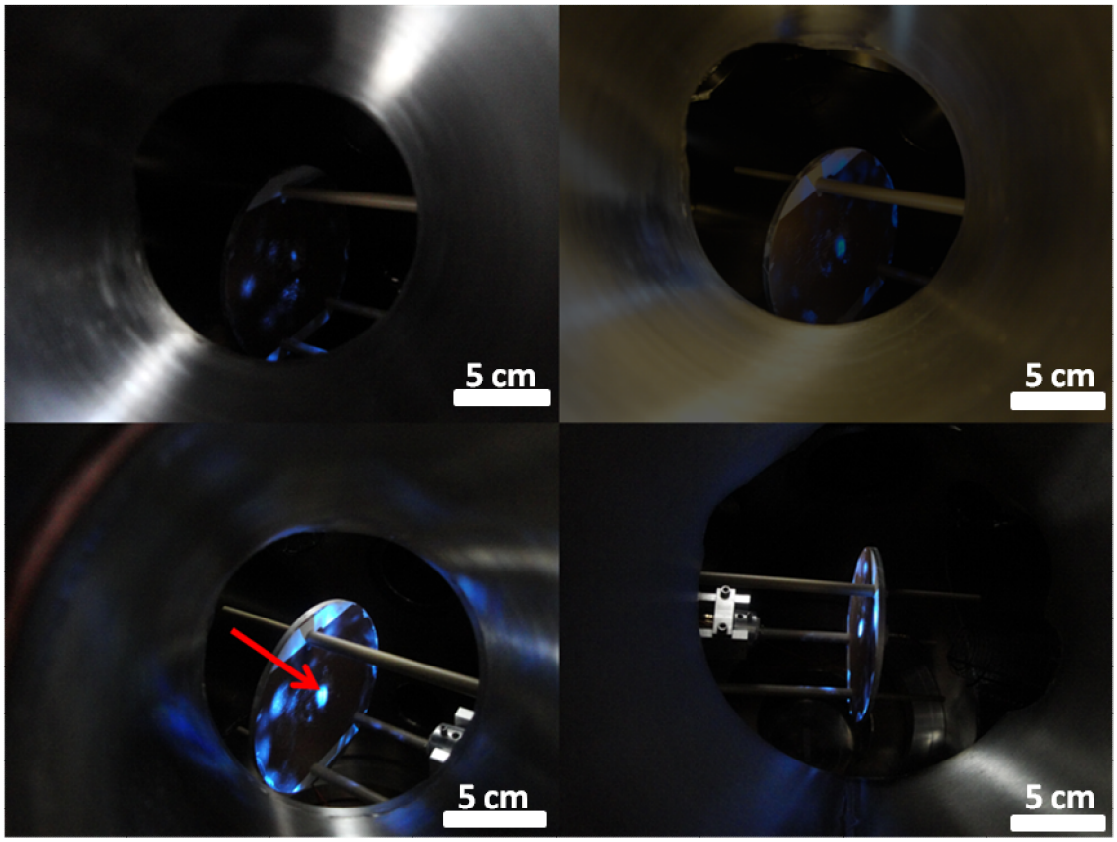

Figure 8.14 The field emission pattern of ZnO nanowires grown on the ZnO film (200 nm) coated pre-fabricated micro tungsten emitters (Tip-4) as a function of applied voltages. (a) shows several emission patterns at an applied voltage of 2.5 kV. (b) and (c) images show that the emission patterns at 2.7 kV and 3 kV respectively. (d) shows the emission patterns from different angle.

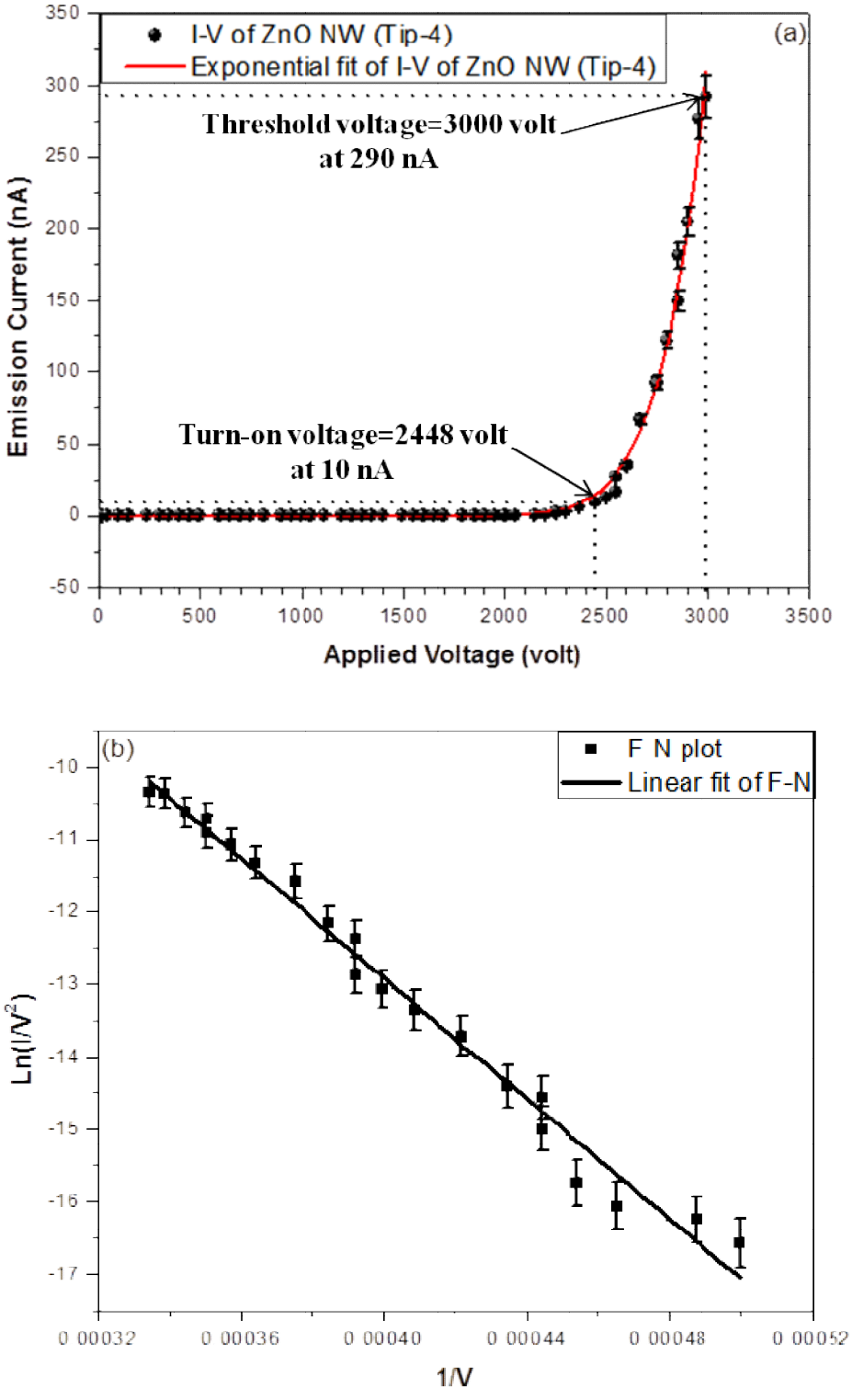

Figure 8.15 (a) Current-voltage (*I-V*) characteristic of of ZnO nanowires grown on the ZnO film (200 nm) coated pre-fabricated micro tungsten emitters (Tip-4). (b) The corresponding F-N plot.

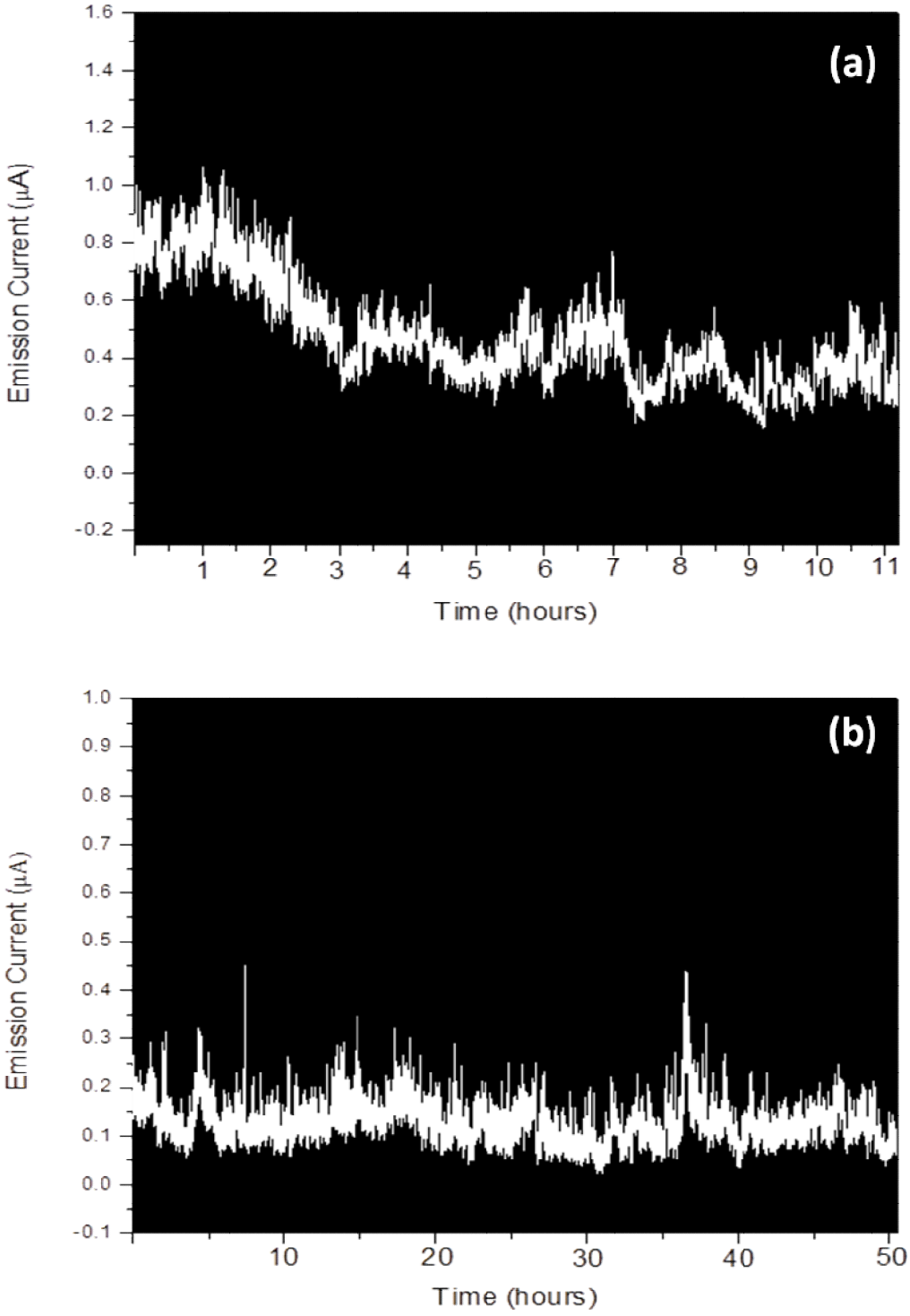

Figure 8.16 The emission current stability profile of ZnO nanowires grown on the ZnO film (200 nm) coated pre-fabricated micro tungsten emitters (Tip-4). (a) shows the total emission current as a function of time for the first 11 hours of continues operation. (b) shows the stability of total emission current for span of another 50 hours.

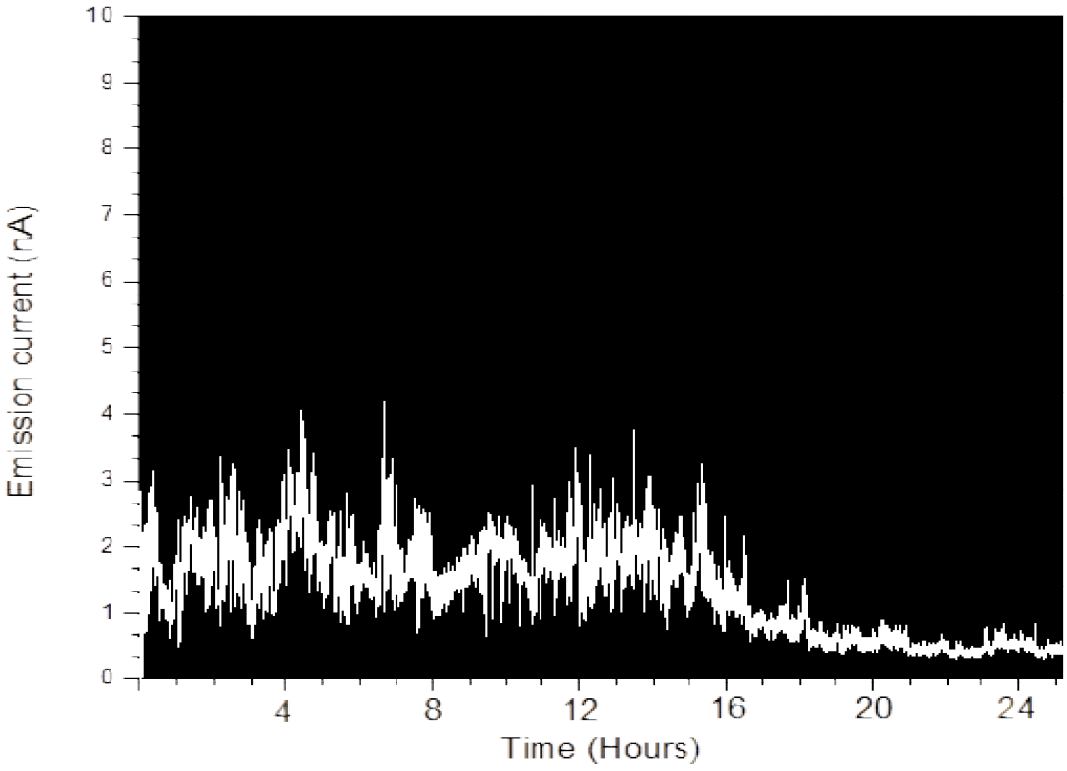

Figure 8.17 The emission current stability profile of the field emission pattern at the centre of the screen highlighted with the red arrow in figure 8.14(c). The emission current stability was measured through a Faraday cup for a span of more than 24 hours.

For the use of ZnO nanowires as electron source in electron microscopes, it is necessary that beam originates from a single nanowire. This is because beams from multiple nanowires will interfere and have different energies[54] as well as different source size(s). In the present experiment, field electron emission from a single ZnO nanowire, identified by the red circle in figure 8.6(c) was achieved. Although the ZnO nanowire was not aligned to tip axis, we were able to align it by tilting the emitter mount ring to an angle of about 60 degree and adjusting the emitter to the centre by moving the emitter holder in ±Y axis (see figure 8.7).

For the determination of the field emission properties of ZnO nanowire, the applied voltage was gradually increased and the emission current was recorded. Figure 8.18(a) shows the *I-V* characteristics of single ZnO nanowire. An emission current of ~ 12 nA was recorded at an applied voltage of 2.1 kV and then the emission current increased exponentially as the applied voltage increased to reach its maxmum value of about 200 nA at an applied voltage of 3 kV. Figure 8.18(b) shows the corresponding F-N plot for the data where electron emission occurs. The linear fitting indicates that field emission process "tunneling" is dominant.

Single field emission pattern was observed on the fluorescent screen suggesting that emission current from a single ZnO nanowire. Figure 8.19 shows the field emission pattern of single ZnO nanowire as a function of applied voltages. The emission pattern was getting intense with increasing the applied voltage. It is important to note that even at an applied voltage of 3 kV, no other emission patterns were observed confirming that the other ZnO nanwires are not contributing to the emission process. This is due to the fact that the ZnO nanowire, identified by the red circle in figure 8.6(c), has a very large aspect ratio and extends significantly higher than the neighboring nanowires.

Finally, the emission current stability of single ZnO nanwire was also investigated. Figure 8.20 shows the emission current as a function of time at fixed voltage of 3 kV over a period of about 34 hours. The result shows that, the emission current is quite unstable and consists of many spikes for the first 15 hours with a fluctuation of 175%. Such fluctuation is believed to be due to self cleaning process. After the ZnO nanowire cleans itself and most of the contaminants were removed, the emission current stability slightly improved and an average emission current of ~100 nA with a fluctuation of 135% was recorded for the next 19 hours with a lot less variations. A field emission stability test of muti-walled carbon nanatube attached to a tungsten needle was carried out by Mann *et al*[197]. The stability measurement of the CNTs was carried out at an ultra

high vacuum level (5×10^{-11} mbar) and exhibited a very poor emission current stability with a fluctuation of ~175%. It is noteworthy that the field emission experiments of ZnO nanwire grown on tungsten tip were carried out at only high vacuum level of 5×10^{-8} mbar which is three orders of magnitude lower than that in the case of CNTs. This confirms that the ZnO nanowire could be used as field emitter in harsh environments. Howere, the present stability measurement suggests that much more work is required in order to bring the ZnO nanowires for the practical operation as field emission electron source. Next section will shed the light on the required emission current stability for field emitter for electron microscopy and ways of how to improve the emission current stability.

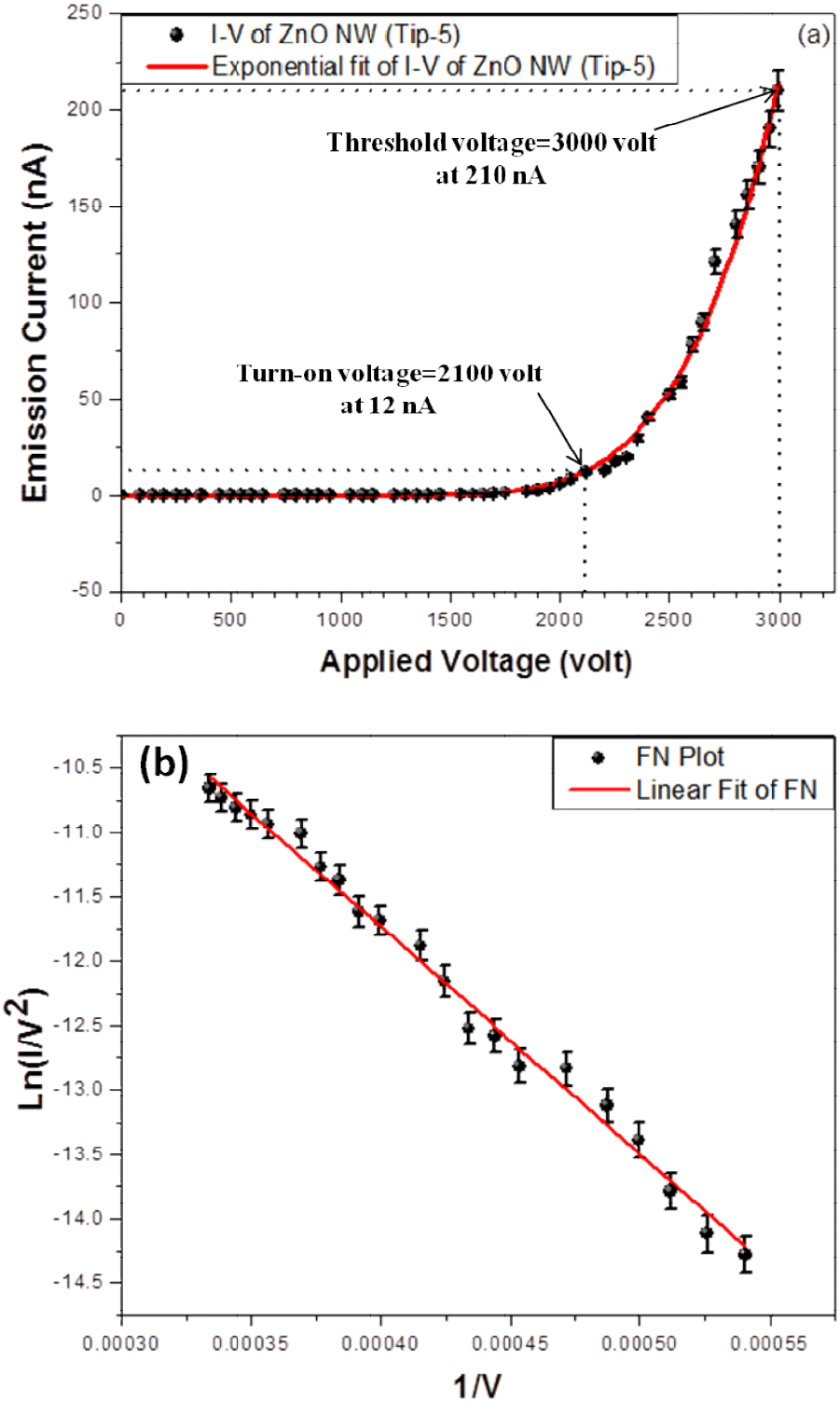

Figure 8.18 (a) Current-voltage (*I-V*) characteristic of single ZnO nanowires grown on the ZnO film (200 nm) coated pre-fabricated micro tungsten emitters (Tip-5). (b) The corresponding F-N plot.

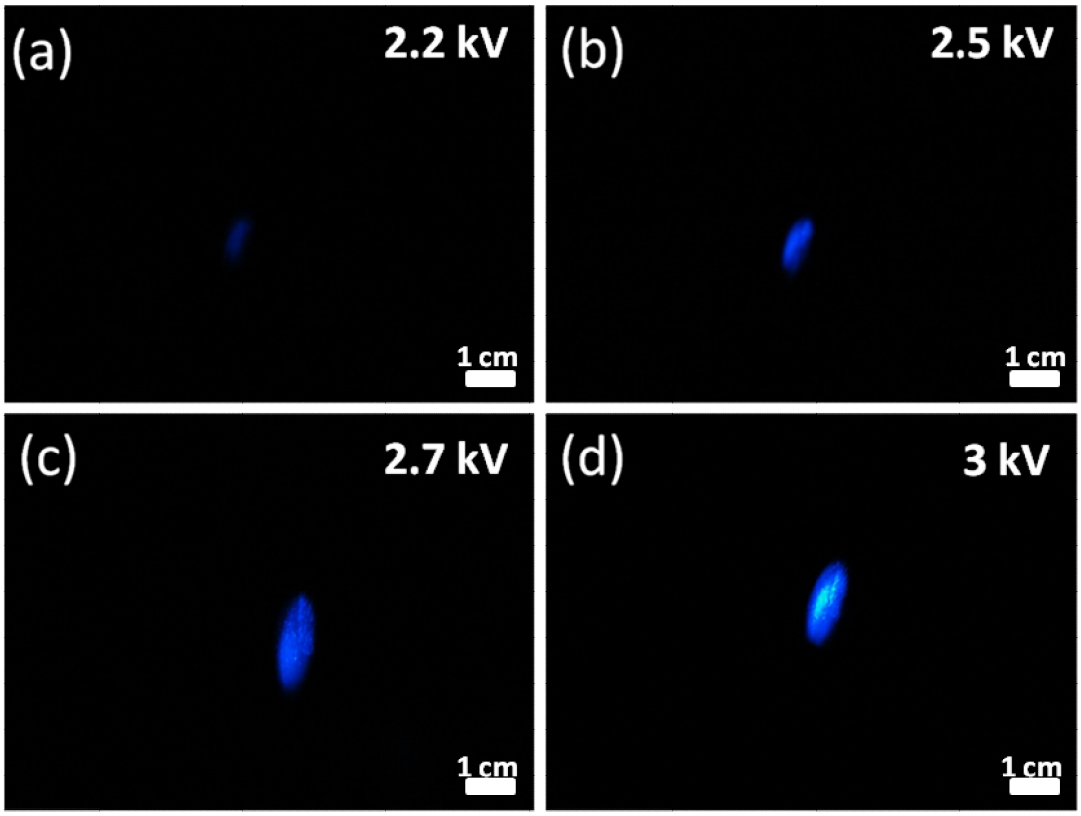

Figure 8.19 The field emission pattern of single ZnO nanowires grown on the ZnO film (200 nm) coated pre-fabricated micro tungsten emitters (Tip-5) as a function of applied voltages.

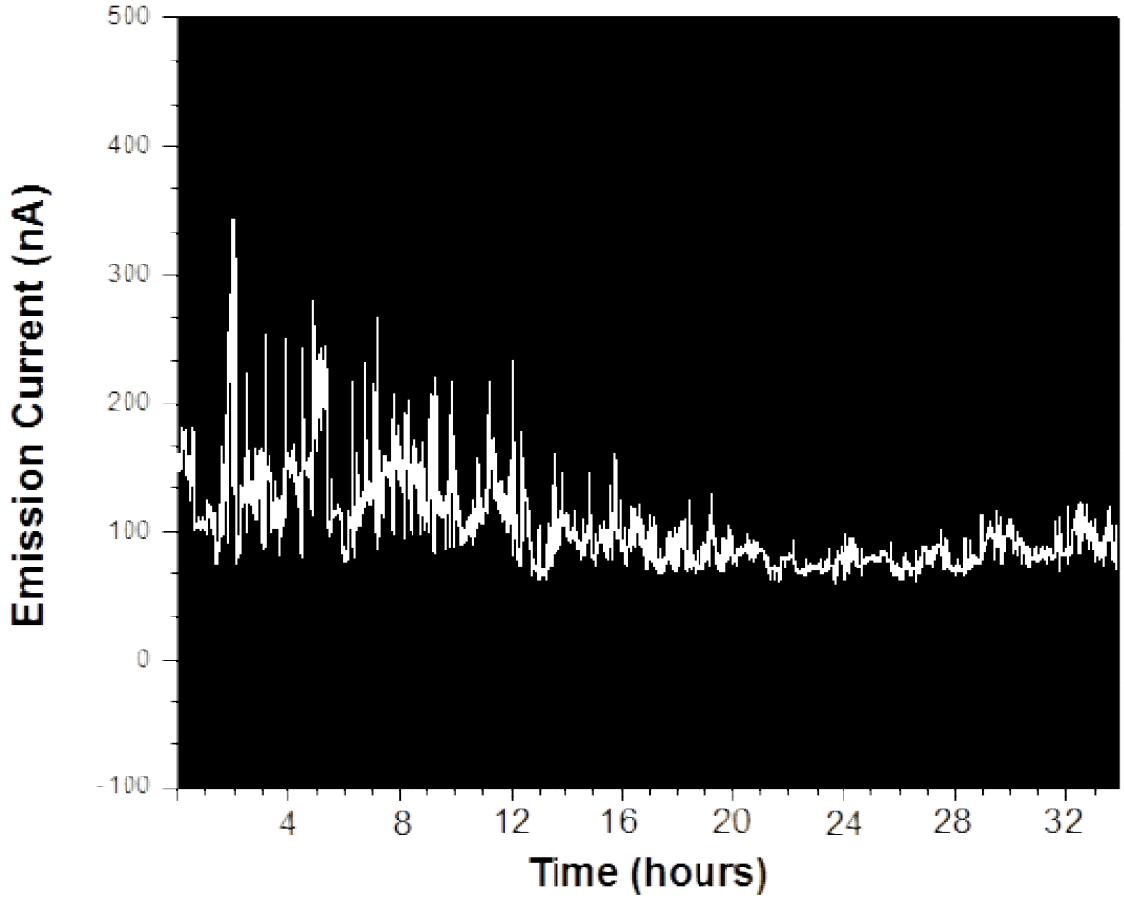

Figure 8.20 The emission current stability profile of single ZnO nanwire grown on the ZnO film (200 nm) coated pre-fabricated micro tungsten emitters (Tip-5) as a function of time at fixed voltage of 3 kV over a period of about 34 hours.

8.6 Requirment for emission current stability of cold field emitter for electron microscopy

The ultimate performance of any electron optical system is dependent on the quality of electron source (i.e. material properties and geometry). To acquire a decent image, the emission current stability is one of the major concerns among those characteristics. An emission current stability of ~5%[198] is required for a scanning electron microscope equipped with conventional tungsten cold field emitters. However, the cold field emitters exhibit high emission current fluctuation ×10~×100 times worse than the requirement. In the case of ZnO nanowires emitters grown on modified tungsten tip, the fluctuation in their emission current was very high compared to the required stability ranging between 90 to 175%. Several causes for such fluctuation were discussed throughout this thesis such as residual gases, different source sizes, ion bombardment and contaminants absorbed on emitter surface, etc. Nevertheless, the instability of the emission current has to be reduced to the required stability of less than 5% if the ZnO nanowire is to be practically utilised in electron microscopy application. Several methods have been reported in the literature for improving the emission current stability of cold field emitters. The use of high resistance feedback control has been reported as a simple method for improving the emission current stability. Muray *et al*. reported that emission current fluctuation was reduced from 20% to less than 1% with resistive feedback control, where a conventional tungsten cold field emitter was used[199].

Another solution to stabilise emission current is to use external electric feedback control circuit. This method was implemented successfully by El-Gomati group at the University of York and the experimental results showed that the emission current stability could be improved from 80% without the use of stabilizer to less than 1% with the use of stabiliser circuit[200].

Although the ZnO nanowires have been successfully grown and their emission behaviour has been experimentally studied, several issues such as emission current stability and optimization of the structure need to be carried out in the future work for reliable device performance.

8.7 Conclusion

In summary, in this chapter, a novel fabrication method have been presented for direct growth of ZnO nanowires on pre-fabricated micro tungsten emitters provided by York Probe Sources (YPS) Ltd. Several experiments have been performed to obtain aligned ZnO nanorods on the pre-fabricated emitters. By detailed experiments it was observed that the growth parameters such as temperature, the distance between the tip and source material and reaction time have deep impact on the growth of ZnO nanowires over pre-fabricated micro tungsten emitters. Moreover, it was observed that by controlling the source material, temperature and reaction time, optimised ZnO nanowires growth over micro tungsten emitters was obtained. The field emission behavior of ZnO nanowires grown over micro tungsten emitters was experimentally demonstrated. These preliminary results demonstrate that by ZnO nanowires grown over micro tungsten emitters can be used as effective field emitter.

CHAPTER9
CONCLUSIONS

The use of nanostructured materials for field emission device applications such as field emission arrays as well as electron microscopy has continued to be in high demand particularly, considering the current difficulties of using carbon nanotubes in such applications. These difficulties are thought to be due to several factors which indicate a lack of understanding the CNTs material for such applications. These include: fabrication difficulties, as well as inherent defects of CNTs such as emission instability. The definite conclusion on utilising CNTs in FE is yet to come and it is still under research even within the Electron Optics group at The University of York. However, it was also observed that the field emission properties of ZnO nanomaterials are strongly-dependent on both the properties (structural, optical, doping, compositions) and geometry of the fabricated nanomaterials. Therefore, the motivation was to investigate the ZnO nanomaterials but, to avoid disappointment, the three major factors behind the delay in realizing the CNTs in FE were simultaneously investigated for ZnO nanostructures.

The zinc oxide (ZnO) was chosen as it is perhaps the most promising material among the metal oxide semiconductor family where extensive research has been carried out on this material in the last few years. Some of the fascinating properties of ZnO are, the wide direct band gap (3.37 eV at T = 300K), high exciton binding energy (60 meV at T = 300K), high optical gain of 300 cm^{-1} (100 cm^{-1} for GaN), biocompatibility, piezoelectricity to name but few. Despite the fact that its use in field emission applications has not yet been realized, ZnO has recently been used for a variety of high-technological applications due to these various properties.

In spite of the intrinsic material properties, some questions of how to transform the ZnO to a practical FE device are addressed in this thesis. In order to fabricate ZnO emitters, the two typical fundamental challenges to be encountered by any growth mechanisms were addressed, i.e. the growth parameters and choosing the appropriate substrate. In this regard, detailed experimentations work were carried out in chapters 4, 5, 6, 7 and 8 to investigate various factors that significantly affect the morphologies and properties of ZnO nanomaterials such as synthesis techniques as well as reaction parameters such as temperature, and annealing. Despite the fact that most of these

parameters have been examined in the literature, it was imperative to do so here to fully understand the growth process and establish the final fabrication conditions that will lead to the development of ZnO as an electron source emitter. The experimental research in these chapters was divided into two main directions; growth and instantaneous characterisation for morphologies, structural and optical properties and the characterisation results are confirmed by FE study at the end of each chapter.

In chapter 4, nanocrystalline thin ZnO nanosheets interconnect were grown on zinc foils by facile hydrothermal process at low-temperature. The annealing impact on the morphological integrity of the nanosheets was also examined and finally a plausible mechanism based on the crystallographic properties of ZnO has been proposed and the results obtained had been published. The field emission properties of the as synthesized nano-crystalline thin ZnO nanosheets were also investigated and it was found that apart from few spikes the emission current stability was highly improved after an initial self-cleaning process took place which resulted in an emission current stability of ~40% for emission current of 44 nA which persisted for about 9.5 hours under pressure of $3x10^{-8}$ mbar at fixed applied voltage of 4.6 kV.

Chapter 5 investigated the appropriate growth substrate in which, a systematic study of well-crystalline and aligned ZnO nanorods grown on a flat titanium substrate without using any metal catalysts or additives via simple thermal evaporation process. The as-grown nanorods exhibit hexagonal surfaces and shows good structural and optical properties. The field emission properties of ZnO nanorods were also investigated at various pressure regimes ($5x10^{-6}$ mbar, $5x10^{-7}$mbar and $5x10^{-8}$ mbar). It has been found that, with increasing the pressure, the turn-on-voltage shifted to higher values from 2.55 kV at $5x10^{-8}$ mbar to ~3 kV at $5x10^{-7}$ mbar, and went further up to 3.5 kV at $5x10^{-6}$ mbar. Moreover, the field emission current decreases as pressure increases. The detailed discussion of this phenomenon is described in section (5.3.4.1). The field emission stability were also investigated under vacuum condition of $5x10^{-8}$ mbar, the ZnO nanorods exhibited reasonable emission current stability of an average of emission current of about 100 nA which outstandingly persisted for about 7 hours without any tendency of gradual decrease under a constant applied voltage of 2.7 kV. Low emission current stability suppressed to large extent the use of cold field emission form being utilized in many applications.

Once the growth process was established and the field emission characteristics were examined, the field emission properties of ZnO nanostructures were found to be enhanced by doping. These results are given in chapters 6 and 7.

It was also found that Ga-doping has significant effect on the morphology as well as the electrical properties and thus the field emission properties of the ZnO nano emitters. Ga-doped ZnO nanomaterials prepared by a thermal evaporation process and characterized in details in terms of their morphological, structural, optical and field emission properties in chapter 6. The effect of gallium ion concentrations on the Ga-doped ZnO nanostructures has been investigated by varying the concentration of Ga, from 0.5% to 2%. It was found that, these variations led to different morphologies, i.e. nanoneedles and multipod structures. This means that by controlling the concentration of Ga, the morphologies of Ga-doped ZnO nanomaterials can be controlled for specific applications.

With regard to the field emission performance of the Ga-doped ZnO nanostructures; it was found that field emission performance of the Ga-doped ZnO nanoneedles enhanced significantly compared with the undoped ZnO nanorods with flat end. This is attributed to the combined effect of the sharp tip morphology and doping effect. The detailed explanation regarding the role of the tip morphology and the doping effect can be found in section (6.3.3.1). Moreover, the Ga doped ZnO nanoneedles exhibited stable emission current with fluctuation of 22% at an average emission current of 90 nA for a continuous operation of about 9.5 hours at fixed voltage of 1.7kV.

It was also found that, the Ga-doped ZnO multipods structures exhibited nonlinearity in the FN plot. This is attributed to the non-uniform field enhancement factors (β) in the sample.

In chapter 7 Indium-doped ZnO (In-doped ZnO) nanopencils were grown on silicon substrate by simple thermal evaporation process using metallic Indium and zinc powders in the presence of oxygen. The fabricated nanopencils were examined in terms of their morphological, structural and optical properties which revealed well-crystallinity, the possession of wurtzite hexagonal phase and good optical properties. Regarding the field emission properties investigation, the nanopencils also exhibited a very low turn-on voltage of 1.3 kV and their emission current steadily decreased to be about 40% of the initial value after 3 hours of operation. Overall, the field emission results show that the In doped ZnO nanopencils emitters can be very efficient candidate in applications such as flat panel displays and high brightness electron sources.

Finally in chapter 8, a novel FE electron source emitter(s) is successfully fabricated by growing ZnO nanowires on standard tungsten emitter. To the best of the author knowledge, this is the first report for the systematic growth of ZnO nanowires on tungsten emitters using thermal evaporation process without the use of any catalysis. The FE properties from these emitters were also investigated and the preliminary results obtained are very promising, however, more experiments are needed especially to enhance of the emission current stability before its use in either the field emission display or electron microscopy.

CHAPTER10
SUGGESTIONS AND FUTURE DIRECTIONS

Over the last several decades, electron sources have been employed for a wide range of technologies such as displays, imaging equipment, telecommunications etc. Due to increased demands of electron sources for possible applications in flat-panel displays, microwave amplifiers, X-ray tubes, nanolithography, etc, recently there has been extensive research on this topic. For this, varieties of new materials are being tested in which carbon nanotubes are extensively studied due to their good conductivity, chemical stability, and cost-effective fabrication. Recently, the oxide nanomaterials are considered as one of the important field emission materials due to their better stability at high-temperature in an oxygen environment and better controllable electronic properties.

As ZnO is one of the most important materials in the metal oxide family, exploration of this material for the FE properties is one of the most important research areas. In the work presented in this thesis, a variety of ZnO based nanomaterials have been synthesized. A utilization of ZnO based nanomaterials for the field emission devices applications have also been tackled in this thesis. The future directions to utilize ZnO based nanomaterials for field emission device applications are seemingly boundless, but will obviously are driven by demand for the successful achievement of devices.

However, an extensive work is still needed to fully explore this material and here, some future research works have been proposed in terms of growth and field emission applications.

10.1 Growth of ZnO nanomaterials

There are several issues which we will focus upon in the future research regarding the growth of ZnO nanomaterials. A few important aims regarding the growth of ZnO nanomaterials are mentioned below:

- Growth of highly aligned ZnO nanomaterials on various conductive substrates for field emission device applications.
- Direct growth of single ZnO nanowire on the pre-fabricated micro-emitters is still a remaining challenge. There is still a lot of work to be conducted for optimizations

and fine-tuning of the growth conditions of the ZnO nanowires that is already established in order to fabricate single nanowire that is aligned to the tip axis.

- Systematic studies on the effects of doping on the growth and properties of ZnO nanomaterials are needed to be carried out in the future. In this regard, various dopants and their numerous concentrations will be used for the growth of nanomaterials.

10.2 Field emission properties of ZnO nanomaterials

Various field emission parameters will be studied for the grown ZnO nanomaterials.

- Growth of fewer/single ZnO nanowire on the pre-fabricated tips and directly use them as efficient emitters.
- It is a great concern as to how to align the grown emitter in the microscope (on the optical axis) and some work on this direction is needed as well.
- To examine the effect of pressure on the field emission properties of ZnO nanomaterials.
- To built up an external feedback circuit in order to establish a stable emission current from ZnO nanowire.
- To examine the electron optical measurements, such as, energy spread, source size, brightness, work function, etc.
- Try to utilize the grown ZnO nanomaterials on specific substrates for simple device applications such as scanning electron microscopy (SEM) or FE based sensor.

10.3 Theoretical studies

We have studied experimentally the behavior of the ZnO nanowires as field emitters; however, theoretical work needs to be carried out in future work.

- Theoretical studies need to be carried out to see the effect of dopant on the structural, optical and electrical properties of ZnO nanomaterials.
- To simulate electron trajectories with a number of emitters on a W tip but with different orientation to guide the growth. The SIMION electron-ion trajectory package can be used for this goal.

References

1. D. S. Yang, C. Lao, and A. H. Zewail, *Science* 321, 1660 (2008)
2. J. D. Meindl, Q. Chen, and J.A. Davis, *Science* 293, 2044 (2001)
3. C. M. Leiber, *Sci. Am.* 58 (2001)
4. J. R. Heath, P.J. Kuekes, G. S. Snider, and R. S. Williams, *Science* 280, 1716 (1996)
5. C. Joachim, J. K. Gimzewski, and A. Avrami, *Nature* 408, 541 (2000)
6. C. P. Collier, G. Mattersteig, E. W. Wong, Y. Luo, K. Beverly, J. Sampaio, F. M. Raymo, J. F. Stoddart, and J. R. Health, *Science* 289, 1172 (2000)
7. W. I. Milne, K. B. K. Teo, G. A.J. Amaratunga, P. Legagneux, L. Gangloff, J. P. Schnell, V. Semet, V. Thien Binhc, and O. Greening, *J. Mater. Chem.* 14, 933 (2004)
8. X. Bai, M. S. Wang, G. M. Zhang, J. Yu, Z. X. Zhang, D. Z. Guo, X.Y. Zhao, and Z. Q. Xue, *J. Vac. Sci. Technol. B,* 25, 561 (2007)
9. Y. H. Yang, C. Y. Wang, U. S. Chen, W. J. Hsieh, Y. S. Chang, and H. C. Shih, *J. Phys. Chem. C,* 111, 1601 (2007)
10. K. Dean, P. V. Allmen, and B. Chalamala, *J. Vac. Sci. Technol. B,* 17, 1959 (1999)
11. C. Kim, Y. S. Choi, S. M. Lee, J. T. Park, B. Kim, and Y.H. Lee, J. *Am. Chem. Soc.*,124, 9906 (2002)
12. A. R. Wadhawan, K. Stallcup, and S. J. Perez, *Appl. Phys. Lett.* 79, 1867 (2001)
13. R. H. Baughman, A. A. Zakhidov, and W. A. de Heer, *Science*, 297, 787 (2002)
14. L. Dong, J. Jiao, D. W. Tuggle, J. M. Petty, S. A. Elliff, and M. Coulter, *Appl. Phys. Lett.* 82, 717 (2003)
15. N. S. Xu and S. Ejaz Huq, *Mater. Sci. Eng., R*, 48, 47 (2005)
16. Ü. Özgür, Y. I. Alivov, C. Liu, A. Teke, M. A. Reshchikov, S. Doğan, V. Avrutin, S. J. Cho, and H. Morkoç *J. Appl. Phys.* 98, 41301 (2005)
17. P. Yang, H. Yan, S. Mao, R. Russo, J. Johnson, R. Saykally, N. Morris, J. Pham, R. He, and H. J. Choi, *Adv. Funct. Mater.,* 12, 323-331 (2002)
18. Q. Wan, Q. H. Li, Y. J. Chen, T. H. Wang, X. L. He, J. P. Li, and C. L. Lin, *Appl. Phys. Lett.,* 84, 3654-3656 (2004)

19. C. H. Liu, J. A. Zapien, Y. Yao, X. M. Meng, C. S. Lee, S. S. Fan, Y. Lifshitz, and S. T. Lee, *Adv. Mater.*,15, 838- 841(2003).

20. R. R. Reeber, *J. App. Phys.* 41, 5063 (1970)

21. O. Dulub, L. A. Boatner, and U. Diebold, *Surf. Sci.* 519, 201 (2002)

22. J. C. Phillips, *Bonds and Bands in Semiconductors*, Academic, New York (1973)

23. http://www.wikipedia.org/

24. R. S. Wagner and W. C. Ellis, *Appl. Phys. Lett.* 4, 89 (1964)

25. R. S. Wagner, W. C. Ellis, S. M. Arnold, and K. A. Jackson, *J. Appl. Phys.* 35, 2993 (1964)

26. Y. Wu and P. Yang, *J. Am. Chem. Soc.* 123, 3165 (2001)

27. S. Y. Bae, H. W. Seo, and J. H. Park, *J. Phys. Chem. B* 108, 5206 (2004)

28. Y. J. Chen and J. B. Li, *J. Cryst. Growth* 245, 163 (2002)

29. J. M. Wu, H. C. Shih, W. T. Wu, Y. K. Tseng, and I. C. Chen, *J. Cryst. Growth* 281, 384 (2005)

30. Z. R. Dai, J. L.Gole, J. D. Stout, and Z. L. Wang, *J. Phys. Chem. B,* 106, 1274 (2002)

31. Y. Xia, P. Yang, Y. G. Sun, Y. Y. Wu, and B. Mayers , *Adv. Mater.* 15, 353 (2003)

32. A. Thess, R. Lee, and R. E. Smalley. *Science* 273, 483 (1996)

33. A. M. Morales and C. M. Lieber, *Science* 279, 208 (1998)

34. C. Lauhon, L. J. Gudiksen, D. Wang, and C. M. Lieber, *Nature* 42057 (2002)

35. S. Han, C. Li and Z. Liu. *Nano Lett.* 4, 1241 (2004)

36. T. Karabacak and A. Mallikarjunan, *Appl. Phys. Lett.* 83, 3096 (2003)

37. L. M. Cao and Z. Zhang, *Adv. Mater.* 13, 1701 (2001)

38. L. M. Cao and K. Hahn, *Appl. Phys. Lett.* 80, 4226 (2006)

39. W. I. Park, D. H. Kim, S. W. Jung, and G. C. Yi, *Appl. Phys. Lett,* 80, 4232 (2002)

40. B. P. Zhang, N. T. Binh, Y. Segawa, K. Wakatsuki, and N. Usami, *Appl. Phys. Lett,* 83, 1635 (2003)

41. T. T. Kang, X. Liu, R. Q. Zhang, W. G. Hu, G. Cong, F. Zhao, and Q. Zhu, *Appl. Phys. Lett,* 89, 071113 (2006)

42. R. Kaur and A. V. Singh, *J. Non-Crys. Solids*, 352, 2565 (2006)

43. M. Zhang, Y. Bando, and K. Wada and J. Mater. *Sci. Lett.* 20, 167 (2001)

44. C. S. Rout and S. H. Krishna, *Chem. Phys. Lett.* 418, 586 (2006)

45. X. Wu, G. Lu, C. Li, and Shi, *Nanotechnology*, 17, 4936 (2006)

46. C. K. Xu and G. D. Xu, *Solid State Commun.* 122, 175 (2005)

47. A. Vantomme, Z. Y. Yuan, G. H. Du, and B. L. Su, *Langmiir*, 21, 1132(2005)

48. L. H. Thompson and L. K. Doraiswamy, *Ind. Eng. Chem. Res.*, 38, 1215 (1999)

49. B. Liu and H. C. Zeng, *J. Am. Chem. Soc.*, 125, 4430 (2003)

50. M. H. Cao and Y. H. Wang, *Nanosci. Nanotechnol.*, 4, 824 (2004)

51. Robert Gomer, "Field Emission and Field Ionization", American Institute of Physics, New York, (1993)

52. C. A. Spindt, I. Brodie, L. Humphrey, and E. R. Westerberg, *J. Appl. Phys*. 47, 5248 (1976).

53. S. Iacobucci, M. Fratini, A. Rizzo, F. Scarinci, Y. Zhang, M. Mann, C. Li, W. I. Milne, M. M. El Gomati, S. Lagomarsino, and G. Stefani. *Appl. Phys. Lett.* 100, 053116 (2012)

54. M. Mann, M. El Gomati, T. Wells, W. I. Milne, and K. B.K. Teo, Proc. SPIE, Vol. 7037, 70370P (2008)

55. Ed. R. W. Kelsall, I. W. Hamley, and M. Geoghegan, "Nanoscale Science and Technology", John Wiley & Sons Ltd (2005)

56. J. Bardeen, *Phys, Rev.* 49, 653 (1936)

57. J. Bardeen, *Phys, Rev.* 58, 727 (1940)

58. G. Gaertner and H. W. P. Koops "Vacuum Electron Sources and their Materials and Technologies", Springer-Verlag New York, LLC,432 (2008)

59. M. Cardona and L. Ley " Photoemission in Solid I–General Principles", Springer-Verlag, Berlin (1978)

60. L. W. Nordheim, *Proc. Roy. Soc. A* 121, 626 (1928)

61. R. H. Fowler, L. W. Nordheim, *Proc. R. Soc.* (London) 119, 173 (1928)

62. O.W. Richardson, *Proc. Roy. Soc. A*, 117, 719 (1928).

63. P.W. Hawkes and E. Kasper. "Principle of electron optics volum 2: applied geometrical optics", Academic press Ltd, (1989)

64. M. Prutton and M. M. El Gomati, "Scanning Auger Electron Microscopy", Wiley, (2006)

65. A. N. Broers, *J. Appl. Phys*. 38, 1991 (1967)

66. N. Broers, *J. Appl. Phys.* 38, 3040 (1967)

67. A. V. Crewe, J. Wall and L. M. Weller, *J. Appl. Phys*, 39, 5861 (1968)

68. S. Yamamoto. *Rep. Prog. Phys.* 69, 181-232 (2006)

69. Ch. Kittel "Introduction to Solid State Physics", 3rd. Ed. New York, London: Wiley, (1996)

70. http://www.purdue.edu/rem/rs/sem.htm

71. R. F. Egerton. "Physical Principles of Electron Microscopy", Springer, (2005)

72. K. Vanheusden, W. L. Warren, and C. H. Seager, *Appl Phys.* 79, 7983 (1996)

73. Ed. M. J. Pelletier "Analytical Applications of Raman Spectroscopy", Blackwell, Oxford, (1999)

74. Y. W. Heo, D. P. Norton, and S. J. Pearton, *J. Appl. Phys.* 98, 073502 (2005)

75. Ed. A. Umar and Y. B. Hahn, "Metal Oxide nanostructures and their applications", American Scientific Publishers , Los Angeles, USA (2010)

76. M. Huang, S. Mao, H. Feick, H. Yan, Y. Wu, H. Kind, E. Weber, R. Russo, and P. Yang, *Science* 292, 1897 (2001)

77. R. F. Service, *Science* 276, 895 (1997)

78. Y. Masuda and K. Kato, *Cryst. Growth Des.* 8, 275 (2008)

79. Y. Masuda and K. Kato, *Cryst. Growth Des.* 8, 2633 (2008)

80. A. Umar, M. M. Rahman, and Y. B. Hahn, *Electrochem. Commun.* 11, 118 (2009)

81. Z. L. Wang, *Mater. Today* 10, 20 (2007)

82. X. D. Wang, J. H. Song, J. Liu, and Z. L. Wang, *Science* 316, 102 (2007)

83. A. Umar, Y. K. Park, and Y. B. Hahn, *J. Nanosci. Nanotechn.* 9, 2692 (2009)

84. Y. Cui, Q. Q. Wei, H. K. Park, and C. M. Lieber, *Science* 293, 1289 (2001).

85. A. Umar, M. M. Rahman, A. Al-Hajry, and Y. B. Hahn, *Electrochem. Commun.* 11, 278 (2009)

86. S. H. Al-Heniti, *J. Nanosci. Nanotechnol.* 10, 6606 (2010)

87. A. Umar, A. Al. Hajry, A. A. Al-Ghamdi, and S. Al-Heniti, *J. Nanosci. Nanotechnol*. 10, 6659 (2010)

88. D. S. Lee, J. H. Lee, J. Luo, Y. Fu, W. I. Milne, S. Maeng, M. Y. Jung, S. H. Park, and H. C. Yoon, *J. Nanosci. Nanotechnol.* 9, 7181 (2009)

89. Y. K. Park, A. Umar, E. W. Lee, D. M. Hong, and Y. B. Hahn, *J. Nanosci. Nanotechnol.* 9, 5745 (2009)

90. A. Al-Hajry, A. Umar, Y. B. Hahn, and D. H. Kim, *Superlattices Microstruct.* 45, 529 (2009)

91. A. Umar, *Nanoscale Res. Lett.* 4, 1004 (2009)

92. J. Q. Hu, Y. Bando, J. H. Zhan, Y. B. Li, and T. Sekiguchi, *App. Phys. Lett.* 83, 4414 (2003)

93. A. Umar and Y. B. Hahn, *Nanotechnology* 17, 2174 (2006)

94. B. D. Cullity and S. R. Stock, "Element of X-ray diffraction", 3rd .Ed. Prentice hall (2001)

95. J. Chang and E. R. Waclawik, *CrystEngComm*, **14**, 4041-4048 (2012)

96. S. Al-Heniti, A.Umar, P. Singh, A. Sayari, A. Al-Hajry, and A. A. Al-Ghamdi, *Adv. Sci. Lett.* 3, 543 (2010)

97. J. Y. Lao, J. Y. Huang, D. Z. Wang, Z. F. Ren, D. Steeves, B. Kimball, and W. Porter, *Appl. Phys. A* 78, 539 (2004)

98. K. Vanheusden, C. H. Seager, W. L. Warren, D. R. Tallant, and J. A. Voigt, *J. App. Phys.* 79, 7983 (1996)

99. D. M. Bagnall, Y. F. Chen, Z. Zhu, T. Yao, S. Koyama, M. Y. Shen, and T. Goto, *Appl. Phys. Lett.* 73, 1038 (1998)

100. A. Umar and Y. B. Hahn, *Appl. Phys. Lett.* 88, 173120 (2006)

101. R. A. Laudise and A. A. Ballman, *J. Phys. Chem.* 64, 688 (1960)

102. B. Cao, X. Teng, S. H. Heo, Y. Li, S. O. Cho, G. Li, and W. Cai, J. *Phys. Chem. C* 111 2470 (2007)

103. K. A. Dean and B. R. Chalamala, *Appl. Phys. Lett.* 75, 3017-3019 (1999)

104. D. Pradhan, M. Kumar, Y. Ando, and K. T. Leung, *Nanotechnology*,19, 035603(2008)

105. Ed. H. S. Nalwa, "Encyclopedia of Nanoscience and Nanotechnology", 25-Volume Set, American Scientific Publishers (ASP), Los Angeles, USA (2011)

106. Z. L. Wang, *Materials Today*. 10, 20-28 (2007)

107. J. Zhou, N. S. Xu, and Z. L.Wang. *Adv. Mater.*18, 2432-2435 (2006)

108. A. Umar, S. Lee, Y. S. Lee, K. S. Nahm, and Y. B. Hahn. *J. Crystal Growth***.** 277, 479 (2005)

109. A. Umar, S. H. Kim, Y. S. Lee, K. S. Nahm, and Y. B. Hahn, *J. Crystal Growth***.** 282, 131 (2005)

110. B. P. Zhang, N. T. Binh, K. Wakatsuki, Y. Segawa, Y. Yamada, N. Usami, and H. Koinuma, *Appl. Phys. Lett*. 84, 4098 (2004)

111. Y. B. Li, Y. Bando, and D. Golberg, *Appl. Phys. Lett*.84, 3603 (2004)

112. Y. W. Heo, *Appl. Phys. Lett*. 85, 2002 (2004)

113. W. I. Park, D. H. Kim, S. W. Jung, and G. C. Yi, *Appl. Phys. Lett*., 80, 4232 (2002)

114. W. I. Park, J. S. Kim, G. C. Yi, M. H. Bae, and H. J. Lee, *Appl. Phys. Lett*.85, 5052(2004)

115. M. Ladanov, M.K. Ram, G. Matthews, and A. Kumar, *Langmuir*. 27, 9012 (2011)

116. P.Yang, H. Yan, S. Mao, R. Russo, J. Johnson, R. Saykally, N. Morris, J. Pham, R. He, and H. J. Choi, *Adv. Funct. Mater*. 12, 323 (2002)

117. Q. Wan, Q. H. Li, Y. J. Chen, T. H. Wang, X. L. He, J. P. Li, and C. L. Lin, *Appl. Phys. Lett.* 84, 3654 (2004)

118. X. Y. Xu, H. Z. Zhang, Q. Zhao, Y. F. Chen, J. Xu, and D. P. Yu, *J. Phys. Chem. B*.109, 1699 (2005)

119. H. K. Lee, M. S. Kim, and J. S. Yu, *Nanotechnology*. 22, 445602 (2011)

120. C. H. Xue, R. L. Wang, J. Zhang, S. T. Jia, and L.Q. Tian, *Mater. Lett*. 64, 327 (2010)

121. X. D. Wang, C. J. Summers, and Z. L. Wang, *Adv. Mater*. 16, 1215 (2004)

122. Z. Fang, Y. Wang, X. Peng, X. Liu, and C. Zhen, *Materials Letters*. 57, 4187 (2003)

123. Y. C. Liu, X. Y. Xu, R. Mu, D. O. Henderson, Y. M. Lu, J. Y. Zhang, D. Z. Shen, X. W. Fan, and C. W. White, *Appl. Phys. Lett*. 83, 1210 (2003)

124. E. I. Givargizov, *J. Crystal Growth* 32, 20 (1975).

125. E. E. Martin, J. K. Trolan, and W. P. Dyke, *J. Appl. Phys.* 31, 782 (1960)

126. Z. Liao, Z. Lv, Y. Zhou, J. Xu, J. Zhang, and D. Yu, *Nanotechnology*, 19,335204 (2008)

127. S. Dardona, A. Peles, G. Wrobel, M. Piech, and P. Gao, *J. Appl.Phys.* 108, 124318 (2010)

128. A. Wadhawan, R. E. StallcupII, and J. M. Perez, *Appl. Phys. Lett*. 78, 108 (2001)

129. D. Akdim, X. Duan, and R. Pachter, *Nano Lett*. 3, 1209 (2003).

130. Y. H. Yang, B. Wang, N. S. Xu, and G. W. Yang, *Appl. Phys. Lett.* 89 43108 (2006)

131. A. Umar, S. Kim, H. Lee, N. Lee, and Y. Hahn, *J. Phys. D: Appl. Phys.* 41, 065412 (2008)

132. G. N. Dar, A. Umar, S. A. Zaidi, S. Baskoutas, S. H. Kim, M. Abaker, A. Al-Hajry, and S. A. Al-Sayari, *Sci. Adv. Mater.* 3, 901-906 (2011)

133. E. Mosquera, J. Bernal, M. Morel, and R. A. Zarate, *J. Nanoeng. Nanomanuf.* 2, 253-258 (2012)

134. D. Gultekin, M. Alaf, M. O. Guler, and H. Akbulut, *J. Nanosci. Nanotechnol.* 12, 9175-9182 (2012)

135. J. Huang, M. Shao, and X. Xu, *J. Nanoeng. Nanomanuf*. 2, 175-178 (2012)

136. S. Singh, G. M. Ali, and P. Chakrabarti, *Sci. Adv. Mater*. 3, 926-931 (2011)

137. A. Kulkarni, R. Wahab, S. G. Ansari, T. S. Kim, S. S. Al-Deyab, and Z. A. Ansari, *J. Nanosci. Nanotechnol*. 12, 2406-2411 (2012)

138. A. Umar, M. S. Akhtar, S. H. Kim, A. Al-Hajry, M. S. Chauhan, and S. Chauhan, *Sci. Adv. Mater.* 3, 695-701 (2011)

139. P. K. Khanna, Kunal Kate, K. Dhanabalan, S. Banerjee, N. Reji, S. D. Shinde, and G. H. Jain, *J. Nanosci. Nanotechnol*. 12, 2791-2796 (2012)

140. F. Sheng, C. Xu, J. Guo, G. Zhu, and Q. Chen, *Sci. Adv. Mater.* 3, 709-718 (2011)

141. G. She, X. Chen, Y. Wang, X. Qi, L. Mu, and W. Shi, *J. Nanosci. Nanotechnol.* 12, 2756-2760 (2012)

142. S. H. Kim, A. Umar, S. H. Al-Heniti, A. Al-Hajry, and A. A. Al-Ghamdi, *Sci. Adv. Mater.* 3, 719-724 (2011)

143. J. Wu and D. Xue, *Sci. Adv. Mater.* 3, 127-149 (2011)

144. C. X. Xu, X. W. Sun, and B. J. Chen, *Appl. Phys. Lett*. 84, 1540 (2004)

145. A. Escobedo-Morales and U. Pal, *Curr. Appl. Phys*. 11, 525 (2011)

146. G. W. Ho, *Sci. Adv. Mater*. 3, 150-168 (2011)

147. L. S. Roselin and R. Selvin , *Sci. Adv. Mater*. 3, 251-258 (2011)

148. P. K. Samanta and P. R. Chaudhuri , *Sci. Adv. Mater*. 3, 107-112 (2011)

149. Y. Yan, X. Wang, H. Chen, L. Zhou, X. Cao, and J. Zhang, *J. Phys. D: Appl. Phys*. 46**,** 155304 (2013)

150. T. Melchior, N. Piatkowski, and A. Steinfeld, *Chem. Engg. Science* 64, 1095-1101 (2009)

151. Y. Yan, L. Zhou, Q. Xue, and Y. Zhang, *J. Phys. D: Appl. Phys*. 41, 195402 (2008)

152. Z. Jing, J. Wang, F. Li, L. Tan, Y. Fu, and Q. Li, *J. Nanoeng. Nanomanuf*. 2, 133-142 (2012)

153. J. X. Wang, G. W. Hyung, Z. H. Li, S.Y. Son, S. J. Kwon, Y. K. Kim, and E. S. Cho, *J. Nanosci. Nanotechnol*. 12, 5644-5647 (2012)

154. I. Khan, S. Khan, R. Nongjai, H. Ahmed, and W. Khan, *J. Nanoeng. Nanomanuf*. 2, 385-392 (2012)

155. J. Li, X. Fang, X. Wang, and Y. Zhang, *J. Nanoeng. Nanomanuf.* 2, 367-370 (2012)

156. P. Lu and D. Xue, *Mater. Focus* 1, 191-196 (2012)

157. P. K. Samanta and P. R. Chaudhuri, *Sci. Adv. Mater*. 3, 919-925 (2011)

158. G. W. Sears, R. Powell, and B. Donn, *J. Chem. Phys.* 39, 2248 (1963)

159. M. Kitano, T. Hamabe, S. Maeda, and T. Okabe, *J. Cryst. Growth,* 102, 965 (1990)

160. M. L. Fuller, *J. Appl. Phys.* 15, 164 (1944)

161. M. Yan, H. T. Zhang, E. J. Widjaja, and R. P. H. Chang, *J. Appl. Phys.* 94, 5240 (2003)

162. R. S. Wagner and W. C. Ellis, *Appl. Phys. Lett*. 4, 89 (1964)

163. X. F. Duan and C. M. Lieber, *J. Am. Chem. Soc*. 122, 188 (2000)

164. H. Algarni, M. M. El-Gomati, and M. S. Al-Assiri, *Sci. Adv. Mater.* 4, 961-968 (2012)

165. K.Vanheusden, C. H. Seager, W. L.Warren, D. R. Tallant, and J. A.Voigt. *J.Appl. Phys*. 79, 7983 (1996)

166. C. Zhang, K. Li, S. Song, and D. Xue, *Sci. Adv. Mater.* 4, 1148-1153 (2012)

167. A. Umar, B Karunagaran, E. Suh, and Y B Hahn, *Nanotechnology* 17, 4072 (2006)

168. A. Umar, H. W. Ra, J. P. Jeong, E. Suh, and Y. B. Hahn, *Korean J. Chem. Eng.* 23, 499 (2006)

169. J. J. Wu and S. C. Liu, *J. Phys. Chem. B*, 106, 9546 (2002)

170. C. J. Park, D. Choi, J.Yoo, G.Yi, and C. J. Lee. *Appl. Phys. Lett.* 90, 083107 (2007)

171. X. Lu, Q. Yang, C. Xiao, and A. Hirose, *J. Phys. D: Appl. Phys.* 39, 3375–3379 (2006)

172. J. Zhou, L. Gong, S. Z. Deng, J. Chen, J. C. She, R. Yang, N. S. Xu, and Z. L. Wang, *Appl. Phys. Lett.*, 87, 223108 (2005)

173. Y. Huang, Y. Zhang, Y. Gu, X. Bai, J. Qi, Q. Liao, and J. Liu, *J. Phys. Chem. C*, 111, 9039 (2007)

174. N. S. Ramgir, I. S. Mulla, K. Vijayamohanan, D. J. Late, A. B. Bhise, M. A. More, and D. S. Joag, *Appl. Phys. Lett*, 88, 042107 (2006)

175. N. Pan, H. Xue, M.Yu, X.Cui, X. Wang, J. G. Hou, J. Huang, and S. Z. Deng, *Nanotechnology*, 21, 225707 (2010)

176. D. M. Bagnall, Y. F. Chen, Z. Zhu, T. Yao, S. Koyama, M.Y. Shen, and T. Goto, *Appl. Phys. Lett.* 73, 1038 (1998)

177. G. Shen, Y. Bando, B. Liu, D. Golberg, and C. J. Lee, *Adv. Func. Mater*. 16,410 (2006)

178. H. J. Egelhaaf and D. Oelkrug, *J. Crystal Growth* 161,190 (1996)

179. W. I. Park, Y. H. Jun, S. W. Jung, and G. Yia, *Appl. Phys. Lett*., 82, 964-966 (2003)

180. J. M. Calleja and M. Cardona, *Phys. Rev. B* 160, 3753 (1977)

181. R. A. Laudise, E. D. Kolb, and A. J. Caporaso, *J. Am. Ceram. Soc.* 47, 9, (1964)

182. R. Gomer, "Field Emission and Field Ionization", Harvard Univ., Cambridge, Mass., (1961)

183. Y. Huang, Y. Zhang, Y. Gu, X. Bai, J. Qi, Q. Liao, and J. Liu, *J. Phys. Chem. C*, 111, 9039 (2007)

184. U. N. Maiti, S. Nandy, S. Karan, B. Mallik, and K. K. Chattopadhyay, *Appl.Sur. Science*, 254, 7266-7271(2008)

185. W. Lee, M. C. Jeong, M. J. Kim, and J. M. Myoung, *Physics Letters A*, 370, 345-350 (2007)

186. C. M. Yang, M. H. Hon, and I. C. Leu, *Ceramics International*, 38, 4277-4283 (2012)

187. F. J. Sheini, D. S. Joag, M. A. More, J. Singh, and O. N. Srivasatva, *Materials Chemistry and Physics*, 120,691-696 (2010)

188. M. K. Li, D. Z. Wang, Y.W. Ding, X.Y. Guo, S. Ding, and H. Jin, *Materials Science and Engineering: A*,452–453,417-421 (2007)

189. Z. Z. Ye, F. Yang, Y. F. Lu, M. J. Zhi, H. P. Tang, and L. P. Zhu, *Soli. Sta. Comm*. 142, 425-428 (2007)

190. L. Zhang, L. Chen, T. Wells, and M. El-Gomati. *J. Nanosci. Nanotechnol.* 8, 1–5, (2008)

191. M. Deng, G. Ding, Y. Wang, X. Cui, H. Wang, F. Zang, and H.Wu, *Vacuum,* 85, 827-832 (2011)

192. G. Qi, S. Zhao, and Z. Yuan, *Sensors and Actuators B: Chemical,* 184, 143-149 (2013)

193. Y. Tian, J. Li, H. Xiong, and J. Dai, *Applied Surface Science,* 258, 8431-8438 (2012)

194. G. Li and Y. Liu, *Materials Science in Semiconductor Processing,* 16, 792-796 (2013)

195. S. K. Arya, S. Saha, J. E. Ramirez-Vick, V. Gupta, S. Bhansali, and S. P. Singh, *Analytica Chimica Acta,*737, 1-21 (2012)

196. A. Umar, M. M. Rahman, A. Al-Hajry, and Y. B. Hahn, *Talanta,*78, 284-289 (2009)

197. M. Mann, K. B. K. Teo, W. I. Milne, T. Tessner, and M. Ovsyanko, *J. Nanoengineering and Nanosystems* 222, 095-09901(2008)

198. V. N. Tondare, N. J. van Druten, C. W. Hagen, and P. Kruit *J. Vac. Sci. Technol.* 21, 1602-1606 (2003)

199. L. P. Muray, U. Staufer, E. Bassous, D. P. Kern, and T. H. P. Chang *J. Vac. Sci. Technol*. 6, 2713 (1997)

200. L. Chen, and M. M. El-Gomati, *Microelectronics and Reliability,* 46, 1209-1213 (2006)